The Dissertation Committee for Parrish Clawson Brady
certifies that this is the approved version of the following dissertation:

Novel Laboratory Simulations of Astrophysical Jets

Committee:

Todd Ditmire, Supervisor

Rodger Bengtson

Herb Berk

Richard Hazeltine

Craig Wheeler

Novel Laboratory Simulations of Astrophysical Jets

by

Parrish Clawson Brady, B.S.

DISSERTATION

Presented to the Faculty of the Graduate School of
The University of Texas at Austin
in Partial Fulfillment
of the Requirements
for the Degree of

DOCTOR OF PHILOSOPHY

THE UNIVERSITY OF TEXAS AT AUSTIN
May 2008

Dedicated to my wife Rebecca.

Acknowledgments

First of all I would like to thank my advisor Professor Todd Ditmire for his direction and belief in my abilities. He was a great support and an example to follow in his energy and passion for pursuing physics. I appreciate Professor Roger Bengtson for his time, discussion, direction and most of all his ICCD camera. I am grateful for Dr. Prashant Valanhu, for his ideas for the experiment and his theoretical help. I also thank Professor Wendell Horton for his encouragement for the work on magnetospheres.

Second I would like to thank all of my coworkers who gave me a lot of help over the years. Greg Hays gave me priceless instruction in construct the YOGA laser, as well as his share of “elbow grease” in its construction. I would like to thank Allen Dalton for his help in assisting me with my experiment and for taking over the YOGA laser. The YOGA glass heads have served many generations of graduate students and may they continue to serve for generations to come. Matt McCormick gave valuable assistance during the critical part of this experiment. I am grateful for Hernan Quevedo for his priceless physics and experimental knowledge to help me push forward and finish my work. He gave me a lot of time and encouragement, without which many of the goals met in this thesis would not be achieve. Will Grigsby and Gillis Dyre were always willing to help me out with whatever in the lab, gave me useful Igor programs, and took the time to teach me their Igor secrets. Sean Keely gave me a lot of help with the electrical and software part of this project. Kort Travis helped me out with a lot of practical things in the lab

that really helped me get moving. Arron Edens started me out in the Thor lab and gave me a lot of experimental help. I would like to thank all the undergraduates that gave me a lot of good work in the experiment.

I would like to thank my parents, especially my mother for reading over much of my dissertation, and my wife for their support and prodding to get this degree finished. Thanks especially to my wife, Rebecca, who has helped me in many scientific ways in this experiment and for general support (and prodding) through the process. I would not be in graduate school if it were not for teachers in my life such as Dr. Atiya, Mr. Burnett, Mr. Mosely, Mr. Sakashita, and Dr. Tucker that guided me through my pre-graduate academic adventures. I appreciate the skill and the work ethic of the employees in the Physics Machine shop, especially Allan Schroeder, who spent many overtime hours to help finish my projects. I am also grateful to Keith Carter who helped me a lot with electronics aspect of the experiment and gave me plenty of supplies to build my experiment, and also for Mr. Meyer who continually encouraged me to finish this experiment. Last of all I would like to thank dumb luck, because without dumb luck there wouldn't be science or the discoveries made in this thesis.

Novel Laboratory Simulations of Astrophysical Jets

Publication No. ________________

Parrish Clawson Brady, Ph.D.
The University of Texas at Austin, 2008

Supervisor: Todd Ditmire

This thesis was motivated by the promise that some physical aspects of astrophysical jets and collimation processes can be scaled to laboratory parameters through hydrodynamic scaling laws. The simulation of astrophysical jet phenomena with laser-produced plasmas was attractive because the laser-target interaction can inject energetic, repeatable plasma into an external environment. Novel laboratory simulations of astrophysical jets involved constructing and using the YOGA laser, giving a 1064 nm, 8 ns pulse laser with energies up to $3.7 \pm 0.2\ J$. Laser-produced plasmas were characterized using Schlieren, interferometry and ICCD photography for their use in simulating jet and magnetosphere physics. The evolution of the laser-produced plasma in various conditions was compared with self-similar solutions and HYADES computer simulations. Millimeter-scale magnetized collimated outflows were produced by a centimeter scale cylindrically symmetric electrode configuration triggered by a laser-produced plasma. A cavity with a flared nozzle surrounded the center electrode and the electrode ablation created supersonic uncollimated flows. This flow became collimated when the center electrode changed from an anode to a cathode. The plasma jets were in axially directed permanent magnetic fields with strengths up to 5000 Gauss. The collimated magnetized jets were 0.1-0.3 cm wide, up to 2.0 cm long, and had velocities of $\sim 4.0 \times 10^6$ cm/s. The dynamics of the evolution of the jet were compared qualitatively and quantitatively with fluxtube simulations from Bellan's formulation [6] giving a calculated estimate of $\sim 2.6 \times 10^6\ cm/s$ for jet evolution velocity and evidence for jet rotation. The density measured with interferometry was $1.9 \pm .2 \times 10^{17}\ cm^{-3}$ compared with $2.1 \times 10^{16}\ cm^{-3}$ calculated with Bellan's pressure balance formulation [6]. Kinks in the jet column were produced consistent with the Kruskal-Shafranov condition which allowed stable and symmetric jets to form with the background magnetic fields. The Euler number for the laboratory jet was 9 compared with an estimate of 40 for young stellar object jets [135] which demonstrated adequate scaling between the two frames. A second experiment was performed concerning laboratory simulations of magnetospheres with plasma winds impinging on permanent magnetic dipoles. The ratio of the magnetopause measured with ICCD photography to the calculated magnetopause standoff distance was ~ 2.

Table of Contents

Chapter 1

Introduction

1.1 Introduction

Astrophysical phenomena have fascinated people since the dawn of time. The 20th century has been an unprecedented time of discovery in the astrophysical realm. We have walked on the moon and peered out near the beginning of time with the Hubble telescope. We have learned much about our place in this expansive universe. As our technology increases here on earth we yearn to explore and visit these extraordinary places in the universe. Since travel to these distant places is nearly impossible, great minds have postulated about bringing these astrophysical phenomena home to our laboratories on a much smaller scale to study and admire. This is the scientific field of laboratory astrophysics, where scientists recreate physics from space in the laboratory. I present in this thesis a discussion of our attempt to create two astrophysical structures in the laboratory: astrophysical jets and magnetospheres.

1.2 Laboratory Astrophysics

High powered lasers and z-pinches have tremendously helped the new field of laboratory astrophysics. Although astronomers have garnered much information over the years about the physics of many astrophysical phenomena, there is still much that is uncertain. Ryutov el at. [122][123] stated that physical phenomena will act in similar ways if the two regimes are scalable.

This means that we could learn about astrophysical phenomena by doing experiments the laboratory.

Remington et al. [117] has written an exhaustive review of the laboratory plasma physics performed by intense lasers and z-pinches. One example of an astrophysical phenomenon being studied in the laboratory is the supernova. Supernovas are one of the most energetic events in the universe, exploding because of the collapse of the core. The methods by which the supernovas are able to explode are still not fully understood. One of the ways laboratory astrophysics can help understand supernova explosions are through shockwave breakout through the He-H interface [117]. Laboratory experiments have simulated the hydrodynamics of core-collapse in supernova, allowing the measurement of the growth of Rayleigh-Tayor instabilities [117].

When supernovae explode to interstellar medium they leave a lot of structure in the radiative blast waves they produce as illustrated in figure 1.1. Vishniac predicted an overstability that could explain the structure in the radiative blast waves. Many laboratory experiments conducted by researchers Edens et al. [31] and Symes et al. [134] have produced radiative laboratory blast waves using intense lasers impinging on targets in the background gas to test Vishniac's theory as illustrated in figure 1.1.

Laboratory simulations have also been successful in studying magnetosphere physics [112], which is much closer to home than supernovas, and has the advantage that gravity does not play an important role in its formation. Experiments using intense lasers have been performed to study equations of state of planetary interiors [117]. Intense lasers and z-pinches can also simulate protostellar jets and high-mock number flows [117]. Such simulations are the central topic for this thesis.

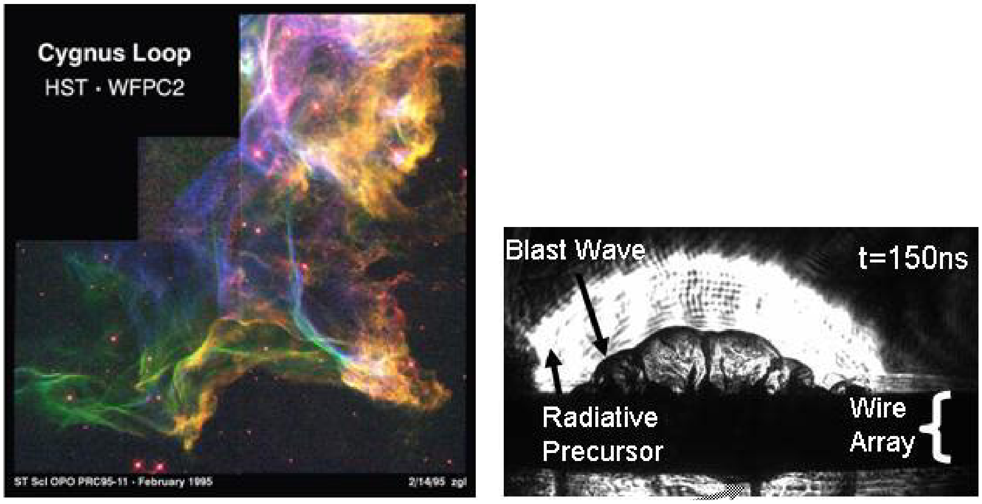

Figure 1.1: Visual comparison between the Cygus loop supernova remnants and blast wave created by Dr. Aaron Edens [30]

1.3 Astrophysical jets

Astrophysical jets are an enigmatic phenomena occurring in many different regimes of the universe. Their high velocities and collimation properties have made astrophysical jets of particular interest to the astrophysical community. Astrophysical jets can reach near the speed of light and remain collimated for thousands of light years [93]. Astrophysical jets almost always form out of accretion disks. Accretion disks form around massive astrophysical objects in relatively dense atmospheres. Angular momentum and gravitational attraction cause the atmosphere to rotate around the massive object and to collapse along the equatorial plane of rotation until a flat accretion disk forms. The mass of the object and the composition of the accretion disk determines the violence associated with the accretion mechanism. As matter accretes onto the central object, matter above a certain threshold of kinetic energy will be expelled along the axis of the accretion disk. Often these outflows create energetic collimated jets [135]. Astronomical images are shown in figure 1.2.

These collimated energetic outflows can form around many different kinds of objects in space. Table 1.1 list various parameters for four types of jets that I will discuss below. The most spectacular of these jets come from active galactic nuclei. Active galactic nuclei are nuclei of galaxies that are extraordinarily luminous and are thought to be powered by supermassive black holes. The astrophysical jets that emanate from these bodies are among the most energetic jets in the universe as seen in table 1.1 and their creation is the most mysterious of all jets. Energetic objects such as x-ray binaries and cataclysmic variables can also serve as sources for these jets. X-ray binaries are double pairs of stars rotating around each other that produce bright x-rays [135]. One of these stars is a compact object such as a black hole or neutron star. The dense star accretes matter from the less dense star, forming an accretion disk. The jets that emanate from X-ray binaries are smaller in spacial scale than active galactic binaries, but still produce very energetic jets [135]. They also have very strong magnetic fields that could explain the energies seen in the jets [135]. Cataclysmic variables are similar to x-ray binaries but are smaller and less energetic [100]. The compact star in a cataclysmic variable system is a white dwarf. Cataclysmic variables are not significant sources of x-rays, the defining characteristic of X-ray binary stars. The jets produced by Cataclysmic variable are similar to X-ray binary jets but are less energetic [135]. Jets may also emanate from less energetic objects, such as young stellar objects (YSO). YSOs are protostars in an accretion disk surrounding [135]. The jets that emanate from YSOs are among the least of the astrophysical jets as in table 1.1, but their value lies in the many images taken of YSOs that

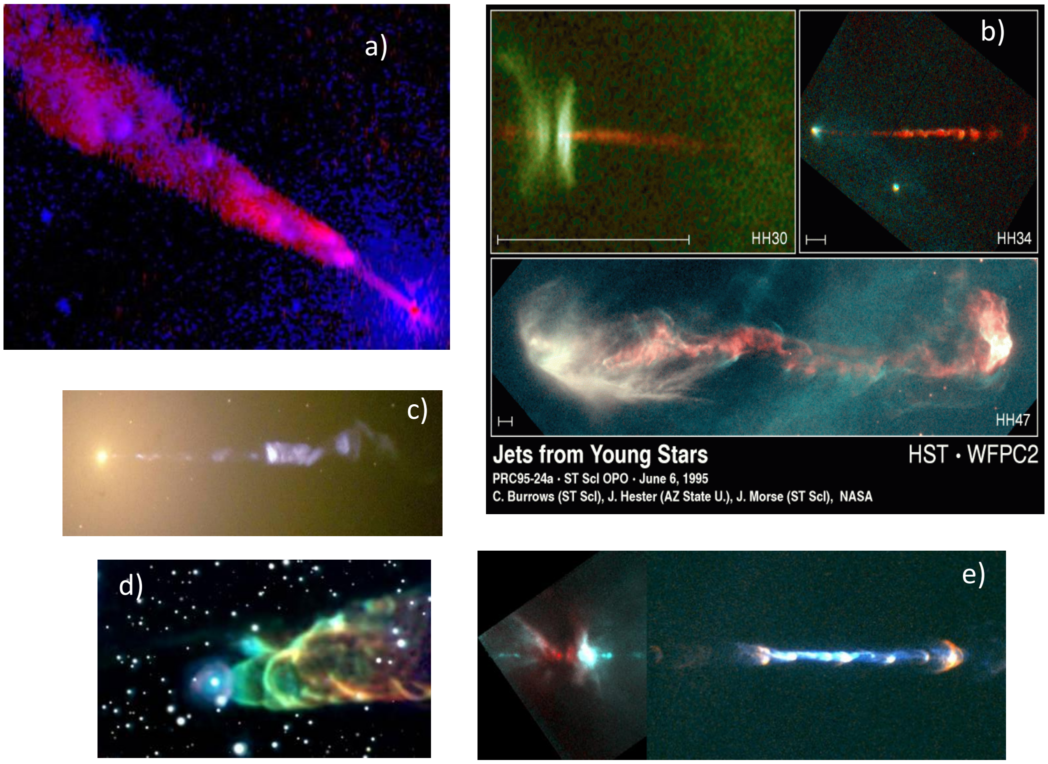

Figure 1.2: Images of astrophysical jets. a) is a combined image of the galactic jet from Centaurus A (NGC5128). The red is from the Hubble Space Telescope and the Blue is an x-ray image from the telescope Chandra [128]. b) are Hubble images of YSO jets HH30,HH34, and HH47 [124]. c) is a Hubble image of the M87 galactic jet (curtesy of NASA and STScI) [32]. d) is an image of a spiraling YSO jet from the star system HH49/50 [107]. e) is an image of a jet from the YSO HH111. There are actually three jets in this image from a system of three young stars. There are two smaller faint jets near the star system dwarfed by the main prominent jet [102].

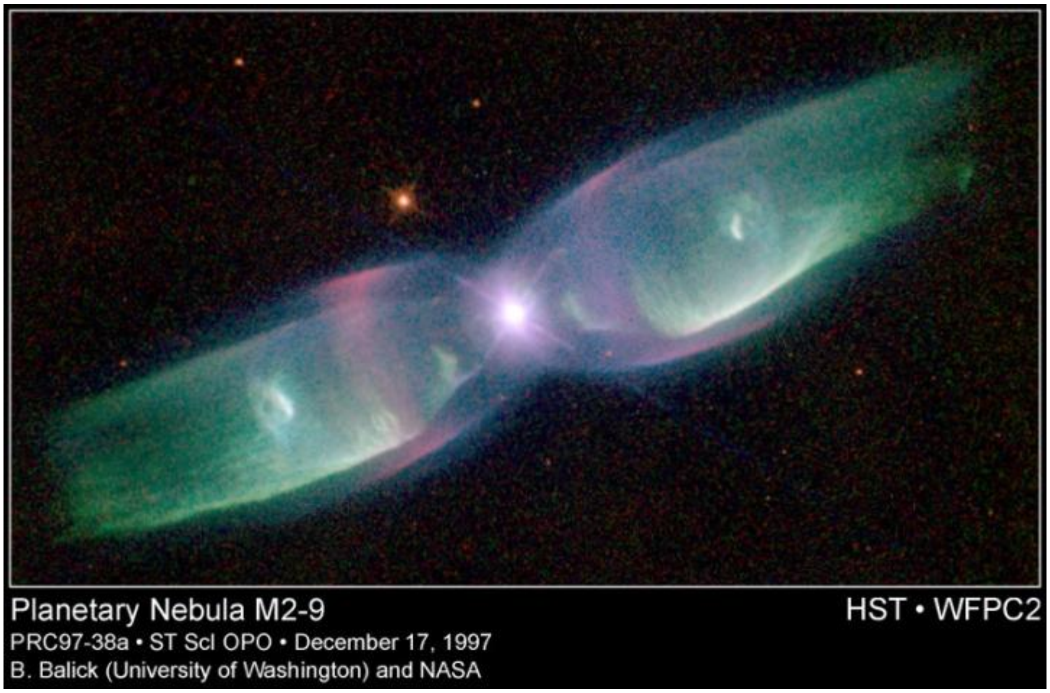

Figure 1.3: M2-9 Bipolar planetary nebula from the Hubble space telescope [17].

have shown great detail in their morphology as in figure 1.2 [135]. Planetary nebula have also been shown to produce jets as in figure 1.3 [17].

The Hubble space telescope has taken extraordinary images of the nearby M87 galactic jet, revealing that this jet stays collimated for very long time as in figure 1.2. Recent measurements of M87 using centimeter-wavelength very-long-baseline interferometry (VLBI) have revealed much about the collimation properties of this jet. Junor et al. [73] has describes this data showing that the jet leaves the accretion disk with an angle of 60°, but then collimates far away from the accretion disk as in figures 1.4 and 1.5.

Physical quantities central objects	AGN BH	YSO protostar	XRB BH/NS	CV WD
V_j/c	1	10^{-3}	0.3	10^{-2}
V_{esc}	1	10^{-3}	0.3	10^{-2}
$L_j(erg/s)$	10^{44}	10^{35}	10^{40}	10^{33}
$M/M_{\odot}$	10^{8}	1	10	1
$R(cm)$	10^{14}	10^{11}	10^{6}	10^{9}
$R_{coll}(cm)$	10^{17}	10^{16}	10^{11}	10^{11}
$B(Gauss)$	10^{4}	10^{3}	10^{9}	10^{6}

Table 1.1: Astrophysical jet parameters, with AGN=Active Galactic Nuclei, YSO=Young Stellar Objects, XRB=X-Ray Binaries, CV= Cataclysmic Variables, BH=Black Holes, NS=Neutron Stars, WD=White Dwarfs [135]

HH objects are a type of YSO that are associated with astrophysical jets. Astronomers have recorded excellent resolution images of the morphology of these HH jets. Bracciotti et al. [5] measured possible rotation in the base of the jet in the HH object DG Tau using spectroscopic measurements. Further analysis from Woitas et al. [151] of a similar jet emanating from RW Aur determined that this angular momentum could wrap up magnetic field lines from the accretion disk.

1.3.1 Theoretical Models of Astrophysical Jets

Astrophysicists have long relied on analytical models and hydrodynamic coding of simulations of astrophysical jets. The theories of astrophysical jet formation and collimation mainly fall into two categories [117]. The first category assumes that material is falling into the central object of a magnetized accretion disk. This material is ejected from the accretion disk and magnetic effects form and collimate the astrophysical jet. The second category assumes that the accretion disk is toroidal in shape. Material ejected from the central

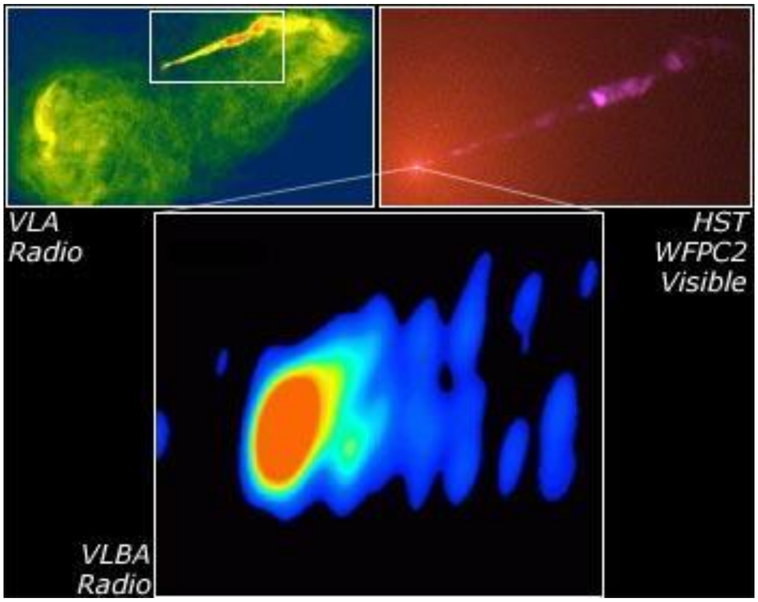

Figure 1.4: Images of the M87 in both visible and radio wavelengths. Image curtesy of NASA, National Radio Astronomy Observatory/National Science Foundation, John Biretta (STScI/JHU), and Associated Universities, Inc.

object expands spherically away from the central object. This ejected material is funneled out into space by the toroidal accretion disk. This funneling mechanism collimates the jet [68]. The jet can further collimate due to radiative cooling. Observation alone is inadequate to determine the collimation mechanisms of astrophysical jet, although a combination of these collimation mechanisms is certainly possible.

Magnetically formed jet production are modeled in three main ways which I will discuss [85]. Case 1 are steady magnetocentrifugal models where the jets are accelerated by a combination of centrifugal forces and magnetic pressure gradients. Case 2 relies on transient magnetic explosion models. Case 3 describes Poynting flux-dominated jets in which the flow remains pointing

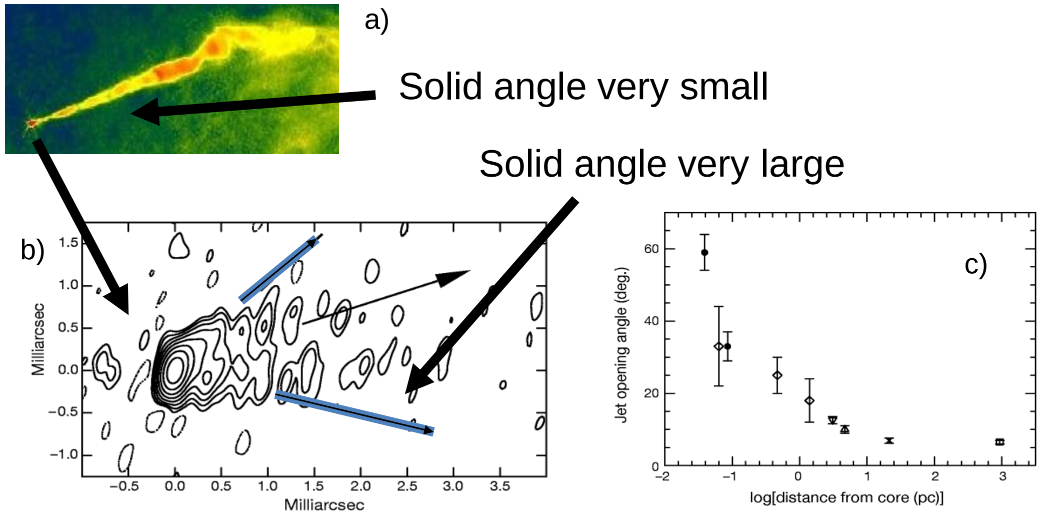

Figure 1.5: Radio telescope images have revealed that in the M87 jet collimation occurs thousands of light years away from the origin. a) is a radio image of the M87 jet as in figure 1.4 and b) is a topographic rendering of the close up image of the VLBA measurement of the jet origin. c) is the collimation angle of the M87 jet as a function of distance from its origin. Each individual figure reprinted by permission from Macmillan Publishers Ltd: Nature [73], copyright 1999.

flux dominated far from its origin.

Magnetocentrifugally driven jets are the most standard jet theory, and have their origin in accretion disks. Pelletier and Pudritz [110] describe the process of magnetocentrifugal jet formation as resulting from the accretion disk dragging the magnetic field toward the center of the accretion disk as in figure 1.6. The magnetic pressure in the accretion disk is much less than the thermal pressure. The magnetic pressure outside the accretion disk dominates the thermal pressure. With the magnetic field spiraling towards the center of the accretion disk the magnetic field outside the accretion disk becomes a spiral hour glass shaped field. As plasma leaves the accretion disk perpendicular to the accretion plane the plasma will be locked along the magnetic field lines. If these magnetic field lines are sufficiently inclined, the centrifugal force on the expelling plasma will be able to move the plasma along the magnetic field and overcome the gravitational force of the central object. This plasma is then free to flow along the magnetic fields into space.

As plasma flows away from the accretion disk the evolution is governed by the complicated Grad-Shafranov equation [110]. The Grad-Shafranov equation generally states that jet flow is required to be balanced by the generated magnetic field and this equation also describes the collimation of the flow [135]. The collimation will be dominated by the hoop stress of the toroidal (or azimuthal) magnetic field as in figure 1.6.

The magnetic explosion model includes a magnetized solid object in a plasma atmosphere. As the sphere rotates poloidal magnetic fields generate an azimuthal component that grows as the time evolves similar to figure 1.6, except that the rotating magnetic fields are not able to escape the system. This will cause the magnetic pressure force with $-\nabla B_\phi^2$ to point outward from the center of the system and explosively form a jet. Matt et al. [90] describes this process as two donut-shaped explosive charges detonating around the core. This forces magnetized plasma along the axis of rotation which forms an astrophysical jet. This was adapted from Wheeler's work describing the explosion of a supernova due to a jet produced in this manner in the stars core [146].

Poynting flux jets are an extreme regime of jet formation. Instead of the jet being driven by both kinetic and electromagnetic processes the evolution is dominated by the electromagnetic field in the Poynting flux case. Ustyugova

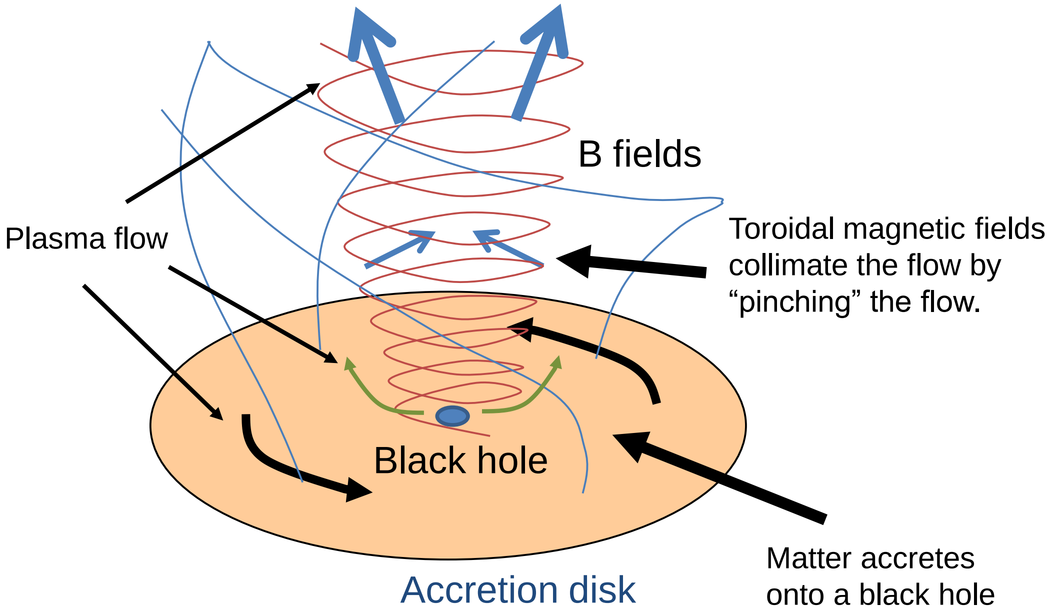

Figure 1.6: Description of the formation of magnetically dominated astrophysical jets [93][12].

et al. [142] states that if the magnetic field is aligned with angle less than 30° the matter flux will be dominated by the gravitational field. Then most of the energy will be carried away by the magnetic field. Poynting flux jets will therefore not have a high mass outflow.

1.4 Magnetospheres

The magnetosphere is an important part of our life and our way of life. The magnetosphere protects our biological life from the solar wind and it affect our communications systems, GPS, and power grids. Understanding the magnetosphere’s dynamics is of great importance.

The magnetosphere is the interaction of the magnetic field of a planet with the stellar wind coming from the star which it orbits. In the earth-sun system the solar wind is enhanced with Coronal mass ejections (CMEs) which are ejections of hot plasma along with magnetic fields frozen into that plasma from the solar corona.Earth directed CMEs can trigger geomagnetic storms, usually causing interplanetary shocks [91]. The solar wind is a flow of magnetized plasma with the following average parameters from CME events: the solar wind velocity $u_{\mathrm{SW}} \sim 450$ km/s, the solar wind density $n_{\mathrm{SW}} \sim 5$ cm^{-3}, the interplanetary magnetic field $B_{\mathrm{IMF}} \sim$ 5-7 nT, and the solar wind temperature $T_{\mathrm{SW}} \sim 1.2 - 1.4 \times 10^5$ K (10-12 eV) [18][77]. Some CME events can give solar wind parameters as high as $u_{\mathrm{SW}} \sim$ 650-800 km/s, $n_{\mathrm{SW}} \sim$ 40-60 cm^{-3}, $B_{\mathrm{IMF}} \sim$ 25-30 nT [18][77]. The boundary of the magnetosphere is called the magnetopause which forms when the solar wind pressure balances the planets magnetic field.

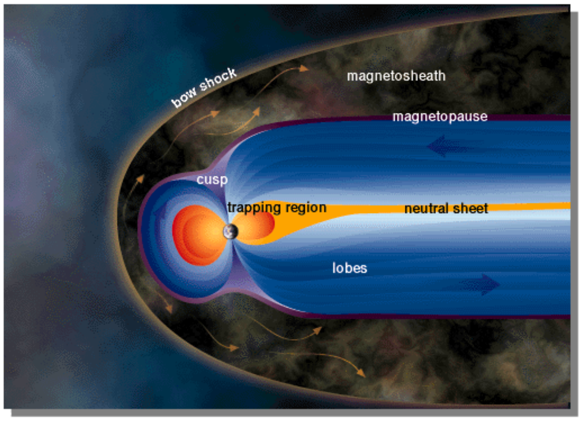

Figure 1.7: Diagram of different sections of the magnetosphere [95].

There are many different parts to the magnetosphere as depicted in figure 1.7. Except during fast dynamical events Pascal's law prevails giving

$P_{dyn} + P_{th} + P_B = constant$ throughout the system. Here $P_{dyn} = \rho v^2$ is the dynamical pressure, $P_{th} = p$ is the thermal pressure, and $P_B = B^2/2\mu_0$ is the magnetic pressure. The solar wind forms a bow shock in front of the magnetopause. In this shock region $P_{th} \gg P_B$ and in the magnetosphere $P_B \gg P_{th}$. The solar wind forms a large magnetosphere tail where the magnetic field extend for many earth radii [115]. In the cusp region plasma can accelerate toward the surface of the planet when certain conditions are met [129].

1.5 Goals of my Doctoral Work

The goal of my research was to perform novel laboratory astrophysical simulations of astrophysical jets and magnetospheres using laser-produced plasmas and discharges from capacitors. This thesis outlined the scientific underpinnings of the experiment, and details the processes and results obtained from the scientific inquiry. The most significant results of the thesis were the work done on laboratory simulations of astrophysical jets described in chapter 5. All other work in this thesis was geared to support this chapter or were side projects related to the experimental jet simulations.

My astrophysical jet simulations required a high energy YAG Oscillator Glass Amplifying (YOGA) laser system. In chapter 2, I discussed the creation of the YOGA laser system, including the predictions for the system and its measured performance specifications. A background of relevant theoretical ideas was given in chapter 3. MHD was the theoretical basis of jet formation and the expansion of laser-produced plasmas in magnetic fields. I briefly discussed z-pinches, as z pinches are a dominant function of our jet evolution. I also discussed MHD scaling and its relevance to our experiment. Basic laser-plasma interaction physics was described in order to discuss the diagnostics of the system.

Before generating plasma jets, it was necessary to understand the behavior of laser-produced plasmas with and without magnetic fields. Chapter 4 described precursor experiments using optical probes to observe laser-produced plasmas with and without magnetic fields. I obtained impressive comparison results between measurements of our laser produced plasmas and simulations from the hydrodynamic code HYADES.

Magnetized plasma jets were created in a novel experiment with a vacuum arc set up for the purpose of laboratory simulations of astrophysical jets as discussed in chapter 5. The scaling parameters of the jet were similar to the parameters in YSO astrophysical jets. Vacuum arc technology was used to construct plasma jets where a supersonic unmagnetized anode jet remnant served as the initial conditions for a magnetized cathode jet. The anode jet created a non-magnetized supersonic flow with a measurable barrel shock in an axial magnetic field. The barrel shock bounded a cone of higher densities and temperatures overlaid in a colder background gas. With this barrel shock cone embedded in an axial magnetic field, the currents upon reversing direction funneled down the cone due to the anisotropic conductivity in the magnetized plasma and the differences in plasma conductivity between the two regions. Maxwell SV software calculated the current distribution under similar conditions and showed that the axial current in the cone is quasi-uniform as outlined with the fluxtube. This created a fluxtube outlined by the barrel shock with quasi-constant current subject to Bellan's MHD based fluxtube model. Modeling of Bellan's MHD based fluxtube model showed a dynamical progression of a jet-throat pinch similar to the observed laboratory jet progression [6]. Bellan's model predicted the distribution of mass within the flux tube similar to the plasma emission distribution in the ICCD images. Bellan's equations predicted rotation occurring in the fluxtube. Evidence of this is shown in the distribution of plasma emission in the throat of the jet as a divot. Kinks in the plasma tube column were measured in the jets and were compared favorably with Kruskal-Shafranov theory.

In chapter 6 the application of techniques from chapters 4 and 5 were examined to study laboratory simulations of magnetospheres. Both laser-produced plasma and plasma jets served as the solar wind against a dipole target. The scaling between the two frames agreed favorably with the experimental parameters calculated with HYADES. I discussed the data and explain its relevance to magnetosphere physics.

Chapter 2

YOGA Laser Development

2.1 Introduction

The use of a laser for astrophysical laboratory simulations is particularly exciting because a laser can deliver a large amount of energy in a small area in a short amount of time. The laser can deliver the energy precisely timed to the rest of the system. The plasma produced by a laser target interaction is reproducible. High powered lasers are an integral tool of laboratory astrophysics.

I presented in this section the design and construction of a glass amplified YAG laser system called YOGA (YAG Oscillator Glass Amplifier). The YOGA laser had four main operating components as illustrated in the CAD drawing in figure 2.1. One, the GCR laser was the seed and initial part of the entire laser system. Two, the glass laser heads and pulse forming networks (PFNs) were the main part of the system for obtaining a high energy laser pulse. Three, the image relay system was very important for delivering the laser pulse to the various amplification optics and was also very important to the safety of the optical components and laser operators. Four, the timing components of the system were very important for making the whole laser work as specified and delivered to the experiment. For the engineering of the laser system, calculations were made for laser amplification using photon population equations. At the end of this chapter I compared the results of this laser modeling with the performance results of the YOGA laser. Other information about the construction of the YOGA laser is contained in appendix A and the laser S.O.P. is contained in appendix A.2.

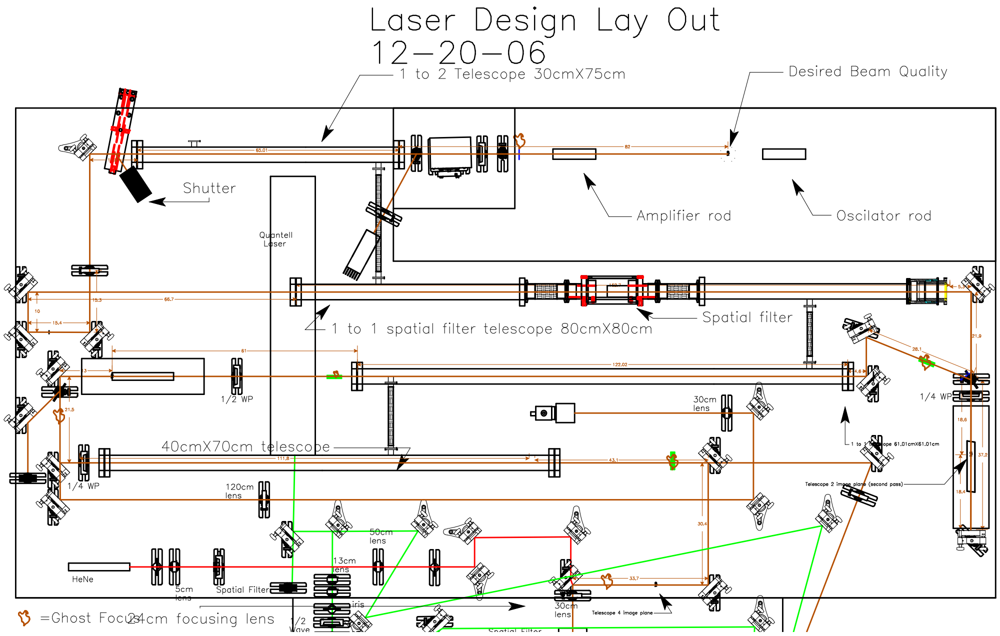

Figure 2.1: We design the layout of the laser using a CAD program.

2.2 Laser Physics and Modeling

Lasers work by the principle of amplified stimulated emission within an optical cavity with gain material where stimulated emission can cascade into a laser pulse [14]. I built a glass amplified system that was seeded with a YAG laser rod. The YAG laser was a Dot Cavity Resonator (DCR) that has been converted to a Gaussian Cavity Resonator (GCR) to achieve a more uniform beam profile to amplify though the glass rods. GCR-YAG lasers are unstable resonators that sacrifice beam quality for short pulse lengths and high energies.

Modeling of the laser system has its roots in population equations. The model to calculate the gain though the laser rods included a population of excited atoms in the gain medium with a cross-section corresponding to the interaction of an incoming photon with the excited atoms for stimulated emission. The geometry played an important role with the face area of the rod giving more available atoms for interactions and the length gave more time for the laser pulse to increase in energy due to stimulated emission.

In modeling the photon gain through a laser medium consider an initial population of incoming monochromatic photons given as the photon flux density. Let the gain medium have a density of excited atoms with a stimulated emission cross section for the incoming photon frequency. Let the probability of an atom emitting a photon from stimulated emission be $W_i = \phi(z)\sigma(\nu)$ where $\phi(z)$ is the photon flux density ($\sharp$ photons/sec$\cdot$Area) and $\sigma(\nu)$ is the stimulation cross section based on the frequency nu of the photons [46]. Then as a number of photon passes through the medium, the number of added photons from stimulated emission is $d\phi = n_0 W_i dz$ where n_0 is the density of atoms in the excited state. Thus

$$\frac{d\phi(z)}{dz} = n_0\sigma(\nu)\phi(z) \tag{2.1}$$

which is a standard exponential population equation. With the intensity of the laser beam being related to the photon flux by $I(z) = h\nu\phi(z)$ equation 2.1 can be integrated to get the intensity as a function of length or

$$I(z) = I(0)e^{n_0\sigma(\nu)z}. \tag{2.2}$$

Thus for a laser rod of length L the gain can be written as $G = e^{(n_0 * \sigma * L)}$.

Glass type	Q-88 Phosphate	Q-246 Silicate
Peek Wavelength (nm)	1054	1062
Cross Section ($\times 10^{-20}$ cm^2	4.0	2.9
Fluorescent Lifetime (μsec)	330	330
Linewidth (nm)	21.9	27.7
Index of Refraction at lasing wavelength	1.536	1.561
Nonlinear Index N2(10^{-13} esu)	1.1	1.4

Table 2.1: Specification of phosphate and silicate glass material from Kigre.

This model for laser interactions is dependent on the initial amount of stimulated Nd atoms in a glass medium. The laser rod was a cylindrical gain medium that absorbs energy from the surrounding laser flashlamps. These flash lamps were discharged though a large capacitor bank. The standard rule of thumb was that a glass laser rod will store 1% of the energy dissipated in the flash lamps to the quantum states in the active element. Or 1% of the flash lamp energy will be available for amplified stimulated emission.

There were many types of glasses that are used for glass laser systems. Two main types of glass were phosphate and silicate glass. For YOGA, Q-246 silicate was used because the peak wavelength was 1062 nm as compared with 1054 nm for phosphate. With the line widths being on the order of 25 nm FWHM the peak wavelength should be tuned to as close as possible to the wave length of the GCR or 1064 nm. These and other parameters were given by Kigre and are presented in table 2.1.

To calculate the gain, $G = e^{(n_0 * \sigma * L)}$, in the laser rods one needs to calculate the stimulation density n_0, by dividing the 1% energy deposition ($E_{deposited}$) from the flash lamps by the energy of the photons at the emission frequency ($\nu = c/(1064nm)$.) and divide by the volume of the rod ($\pi R_{rod}^2 L$):

$$n_0 = \frac{E_{deposited}}{\pi R_{rod}^2 L h\nu}. \tag{2.3}$$

As the laser pulse moves through the rods n_0 was depleted as the laser pulse was amplified. Thus the stimulation density was adjusted by

$$n = n_o - \frac{\Delta E}{\pi R_{beam}^2 L h\nu} \tag{2.4}$$

where ΔE is the difference of the seed pulse and the amplified pulse, and R_{beam} is now the radius of the beam and not the rod. I calculated the amplification of the laser pulse by splitting the laser pulse into 200 compartments, and sending these compartments in through the rod one at a time. The results of the calculations are in figure 2.2 and in tables 2.3 and 2.4. Using this measurement a temporal peak shift was calculated with a ratio of .88 of the shift lag (temporal shift of the peak + FWHM/2/temporal shift of the peak - FWHM/2) when compared with the FWHM. The energy calculated for the laser system using the amplification in the actual set up is in table 2.4. As will be discussed later on in this chapter there were two PFN systems that were termed red and black PFN. The laser rod associated with the black PFN was double passed. The total calculated energy of the system was 4.57 J. I used the parameters found in table 2.2 for the calculation.

I calculated the B integral of the system. The B integral is a measurement of the accumulation of nonlinear phase, and is given by the equation

$$B = \frac{2\pi}{\lambda} \int_0^l \gamma I(x) de \tag{2.5}$$

where γ is the nonlinear, intensity dependent index of refraction of the material and I is the intensity of the laser pulse through the medium [26]. This relation

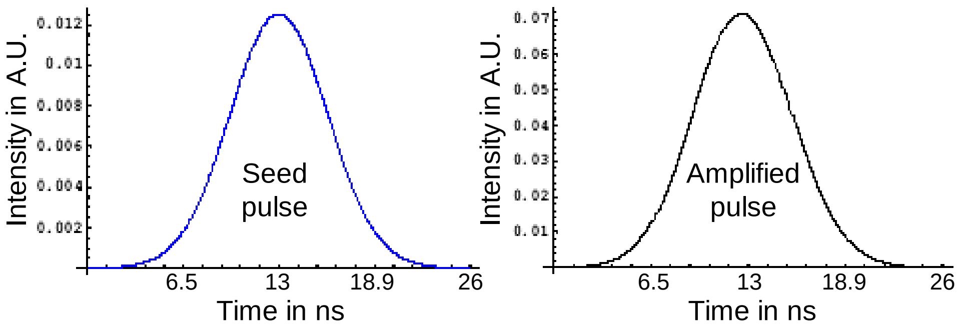

Figure 2.2: Results of the modeling of laser amplification. On the left is the initial seed of the modeling, and on the right is the full amplification through both laser rods. The peak has shifted .53 ns in the calculation.

was more important to investigate with high intensity lasers as it was an intensity effect. Keeping the B integral low was important for the safety of the optics in the system. The B integral needs to be less than one in the laser system to have the optical system behave linearly [46]. I found that the B-integral of the system was minimal at approximately 0.12 rad.

2.3 The Gaussian Cavity Resonator

The GCR was originally a DCR built in the early part of the 1980's. Greg Hays used a gaussian resonator mirror to convert the DCR to a GCR. He refurbished and cleaned the laser before I took over the responsibility of the laser maintenance. The laser had to be aligned after the conversion to a GCR, and the alignment was monitored using a Cohu CCD camera model 4812 which had good spectral recognition at 1064 nm. The highest energy output I measured coming directly from the GCR was 886 mJ at the beginning of operation.

Parameters:	
Seed input energy	800 mJ (unless otherwise noted)
Energy in Rod	12.14 J
σ, cross section	$2.9 \times 10^{-20} cm^2$
Length of laser rod	4.7”
$h\nu$ at 1064 nm	1.805×10^{-19} J
n_0	1.99×10^{18}(excited atoms)
Diameter of Beam	15 mm
$n_0 \sigma * L$	0.69
$e^{(n_0 * \sigma * L)}$	2.01

Table 2.2: General parameters used for photon gain population laser modeling.

Number of passes	Energy in Joules	Fluence J/cm^2
1	1.54	0.87
2	2.71	1.54
3	4.22	2.39
4	5.73	3.24
5	6.88	3.89

Table 2.3: Simulation of energy gain of multiple passes through the Nd laser glass rod.

	Energy in Joules	Fluence J/cm^2
Single pass calculation, Red PFN	1.43	0.81
Double pass calculation, Black PFN	2.71	1.54
Full pass calculation	4.57	2.59

Table 2.4: Calculations of gain energy and fluence in the Nd glass laser rods. The Red PFN powered the single pass laser rod in the laser system, and the Black PFN powered the double pass laser rod in the system.

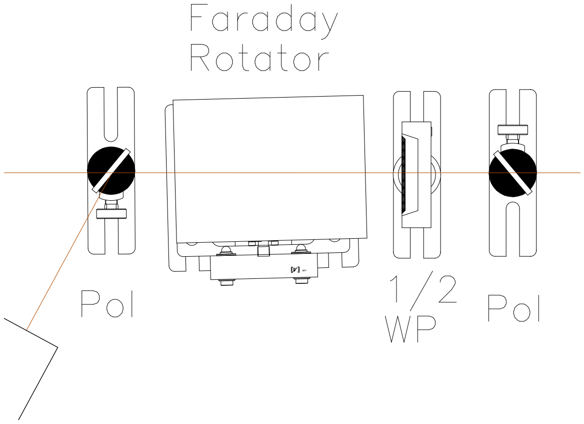

Figure 2.3: An optical isolator uses a polarizer-1/2 waveplate-Faraday rotator-polarizer combination to ensure that reflected beams do not propagate back into the laser. The 1/2 waveplate-polarizer combination also served as a beam energy modifier.

The GCR was capable of delivering an average of $\sim$ 800 mJ pulse with 8 ns pulse duration at 1064 nm. The beam exiting the laser was polarized. The GCR was equipped to use a SH doubling crystal, but for amplification purposes the fundamental mode of the laser was used. There were 1/4 waveplates throughout the system that can be adjusted to give maximal energy. The oscillator and amplifier had separate controls to control the energy. I operated the GCR always at full power to keep uniformity with the mode, with the system kept under a nitrogen purge. I constructed an optical isolator immediately outside the laser to protect the laser from any retroreflections in the system. The isolator, as illustrated in figure 2.3, was aligned using a 1064 nm diode laser. Amplification of laser beams can damage glass amplification rod if the beam profile is poor. High curvature regions in the spatial profile of the laser beam or "hot spots" can amplify nonlinearly, causing self focusing. Self focusing can damage the rod and other optics. The damage threshold of the glass was about 25 J/cm^2 for an 1 ns pulse and the damage threshold of the coatings were about 8 J/cm^2 for an 8 ns pulse. These damage thresholds were all greater than the expected greatest average fluence of 2.5 J/cm^2, but hot spots in the beam can increase greatly and locally the fluence of the beam. To reduce injury to the amplification rods the best spatial profile beam possible was used to propagate though the rods. The beam quality through the rods was controlled by image relaying the most adequate beam from the GCR laser though the rods. A z-scan of the GCR was taken to determine the best beam profile from which to image relay. The results are shown in figure 2.4.

The laser was a reliable device for the experiment, although since the laser was an old device and since there was no one left in the commercial industry willing to fix it, the problems encountered with the laser were worth mentioning in this thesis in appendix section A.5.

2.4 Glass Laser Heads and Pulse Forming Networks

Integral to the construction of YOGA were the Glass laser heads that contained the Nd-glass amplification rods. These heads were constructed at LLNL and have been in use for many years in various projects. They consisted of a stainless steel housing with a water inlet and outlet. They housed the 19 mm glass rod about 4.7" in length. They hold six flashlamps arrayed cylindrically and uniformly around the glass head. A macor reflector encompassed the flashlamp - glass rod assembly. The flashlamps and glass rods were sealed in the laser head with high temperature silicon o-rings. For more information on the assembly of the laser heads see appendix A.1.

The glass laser head had to be cooled with a deionized water system that

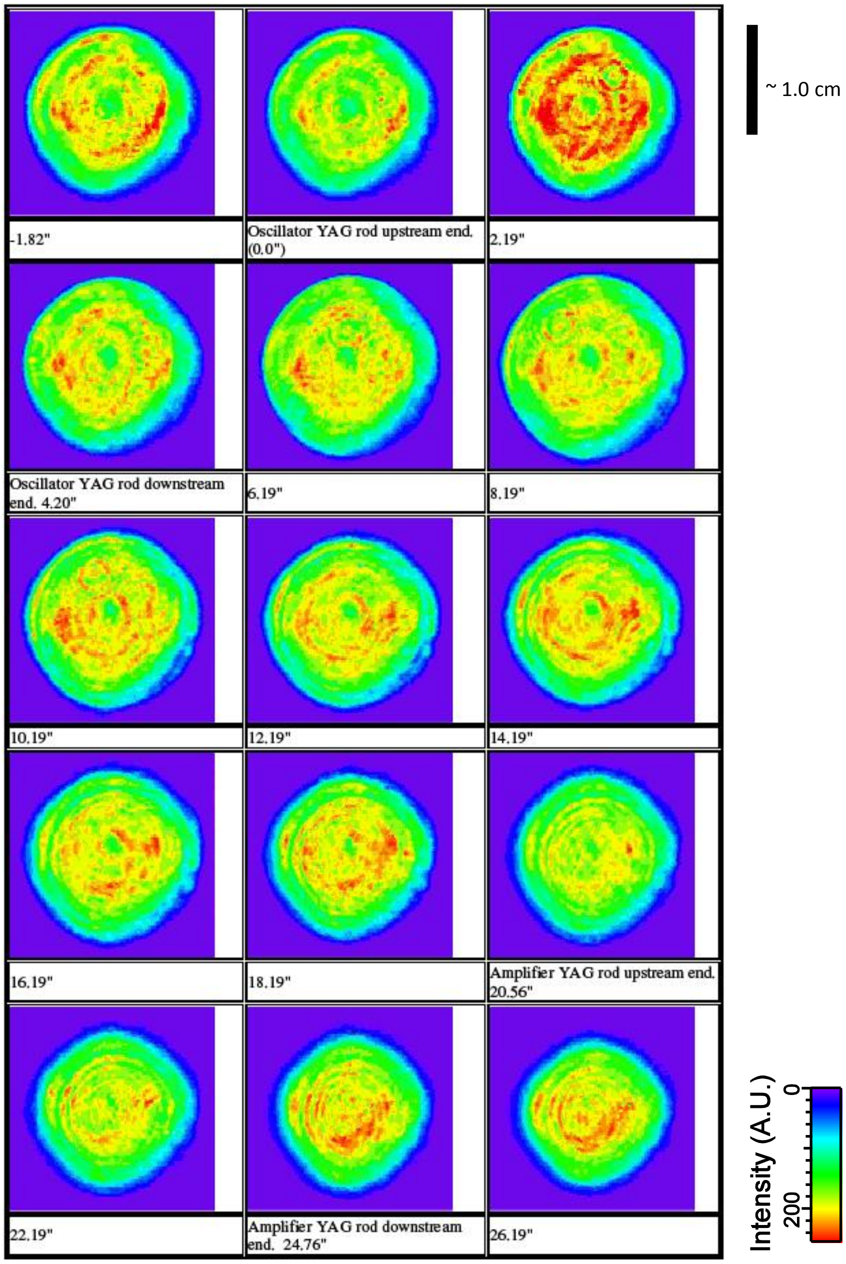
-1.82"
Oscillator YAG rod upstream end. (0.0")
2.19"
Oscillator YAG rod downstream end. 4.20"
6.19"
8.19"
10.19"
12.19"
14.19"
16.19"
18.19"
Amplifier YAG rod upstream end. 20.56"
22.19"
Amplifier YAG rod downstream end. 24.76"
26.19"

Figure 2.4: Beam image profiles of the GCR as a function of distance along the beam path.

was free from copper. Copper in the system could coat the flash lamps during operation. The cooling system needed to have enough heat capacity to take out the heat from the rods rapidly. I used an Affinity chiller in conjunction with the GHOST laser to cool the rods. The cooling in the rods must be constant, especially when using the beam to focus onto a small target.

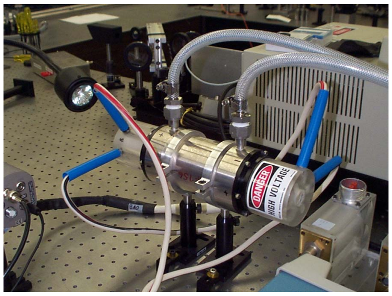

Figure 2.5: This is a picture of one of the Laser heads.

I purchased the Nd-glass laser rods from the Kigre laser glass company with 1.5 wt% neodymium doping. I chose Kigre over Schott, because they had a larger selection of neodymium dopings and advertised platinum free glass. The coatings received from Kigre had many visible imperfections on them, to which Kigre said they were within specifications. It was these imperfections on the coatings that failed near the end of my experiment. Kigre also suggested putting an 8° wedge on the laser rods to avoid back reflections. From an oversight on my part this 8° wedge made it impossible to pass an 18 mm beam through the laser head assembly. The University of Texas physics machine shop made new laser head insulator end caps that would allow the laser to pass through the laser head assembly with the greatest angle possible. This still did not allow the full 18 mm beam to pass through the laser head assembly. I settled on using a 15 mm beam and allowed for some soft diffraction.

The pulse forming network modules or PFNs came from Lawrence Livermore National Laboratories. There are two PFNs, one for each laser head which were referred to as the red PFN and the black PFN. Each PFN unit consisted of a high voltage power supply, a triggering circuit, a capacitor and inductor discharge circuit, and a trigger transformer. There were two capacitor and inductor circuits in each PFN. Each of these circuits was connected to three flash lamps in series. There were three 3500 volt rated 70 μF capacitors in each PFN connected in series with an 80 μH inductor. The trigger transformer created an initial ionizing pulse in the flashlamps from which the capacitors freely discharged through. For each glass laser head there were six flash lamps. Three flashlamps in series were connected to the capacitor through one of the 80 μH inductors. The total energy stored in the capacitor bank, when the capacitors were charged to 3500 V, was 1286.3 J. The rule of thumb for how much optical energy was stored in the laser rod was one percent of the capacitor discharge energy. So this gave a maximum of 13 J of available energy in the rods.

I experienced many triggering problems with PFNs which were fixed by Joe Narduzzi. Narduzzi built another triggering box for the black PFN after not being able to repair the black PFN triggering system. I have used Narduzzi's triggering box successfully throughout our experiment. The Black PFNs Power Supply could be charged 4 kV, but since the capacitors were specified for use under 3.5 kV the black PFN was charged only to 3.4 kV. The maximum charge for the Red PFN was 3.2 kV whereas the capacitors were rated at 3.5 kV.

There were several timing problems with the PFNs and I were able to fix them with electronics. The Red PFN needed a converter from 1000 Ω to

50 Ω which required amplification of the TTL pulse. This required building an electrical device containing a signal amplification device.

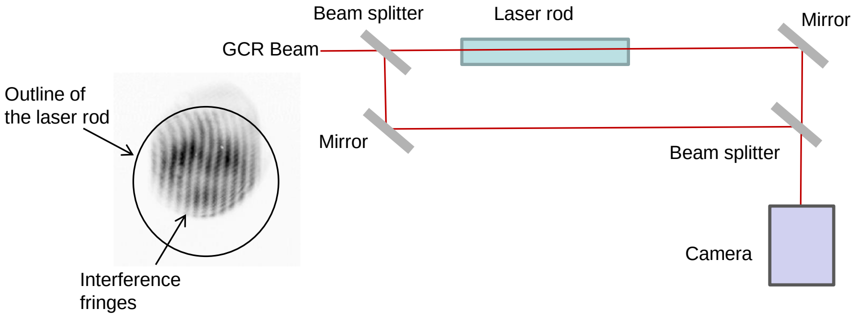

Figure 2.6: The heat load was measured in the rods using a Michelson interferometer of the right. The interferogram, on the left, clipped on the edge of the laser rod to view edge effects of the heat load.

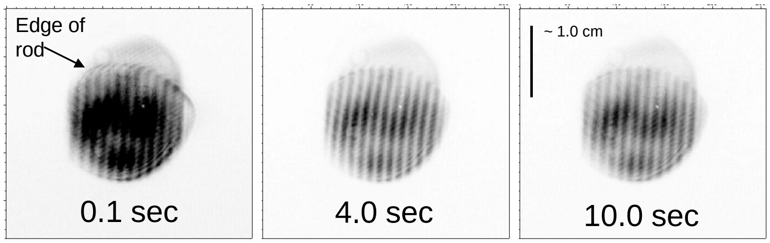

Figure 2.7: The heat load was measured in the rods using interferometry. I use 1 PFN shot for this measurement.

I measured the effect that the heat load induced by the PFNs had on the laser rods. This gave an indication about how often the PFNs could be fired. This was an important measurement because if the laser rod was over loaded with heat the rod could crack. Also, heat in the rod can significantly distort the wave front of the beam, which can cause serious problems for the stability of the laser system. I set up a Michelson interferometer to measure the index of refraction changes due to the heat load in the rods as in figure 2.6. A 1064 nm beam splitter was used to send part of the GCR beam through the laser rod and the other part around the laser rod. The GCR beam was used at low energy. I chose a view to include clipping on the laser rod to view edge effects.

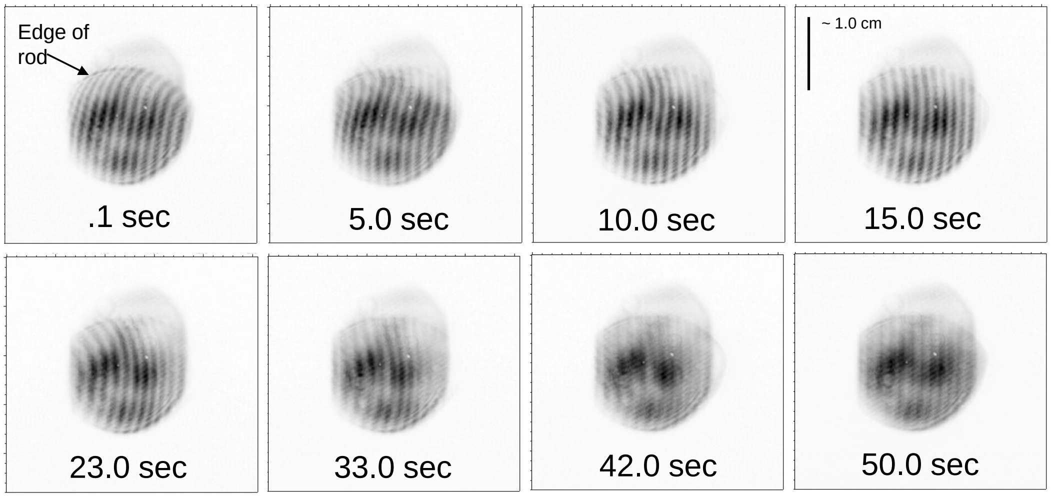

Figure 2.8: The heat load is measured in the rods using interferometry. I use 5 PFN shots at 2 Hz for this measurement.

There were distinct changes of fringe with the onset of the PFN pulse as in figure 2.7. The edge of the rod was on the top part of these interferograms. At the beginning of the PFN pulse noticeable fringes were seen at the edge of the rod. For a single PFN pulse the heat was distributed more in the rods at 4.0 sec, after the pulse, with the fringe lines having curvature throughout the rod. At 10 sec the fringe lines were effectively straight. I flashed the PFNs five times at 2 Hz to obtain a more noticeable effect on the fringe shift as in figure 2.8. This effect showed heat effects to 50 sec after the PFNs were fired five times. At 50 sec the fringe lines were nearly straight. This confirmed roughly that the heat load lasted five times as long with five times the input energy as compared with the example in figure 2.7 with only one PFN shot fired. Thus, one can assume that any major heat load from one PFN shot in the rods will be dissipated after about 10 sec. For extra safety measures I chose 30 seconds between shots to ensure the safety and stable optical operation of the laser rods.

Sufficient fluctuations of the temperature in the chilling cycle had a measurable effect on the fringe shift (see figure 2.9). The chiller fluctuated at 33 second intervals about 3°C. This led to an implementation of the chilling cycle fluctuations of the chiller to less than one second. That reduced significantly the fringe changes on the interferometer, although very slight effects were still noticeable in the focus of the laser.

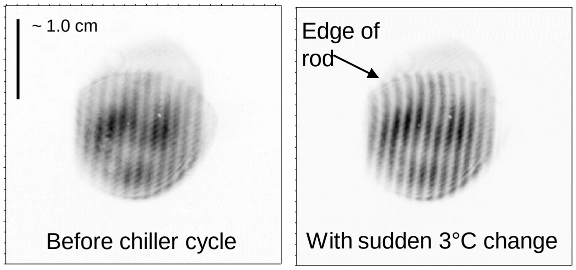

Figure 2.9: Interferometric effects of the chiller as it goes though a 33 sec cooling cycle differing by 3° C.

2.5 Image Relaying and Optical Components

A 4 foot by 8 foot optical table housed the YOGA laser system. This was then the space available for the GCR, the glass laser heads, and for the image relay system. All these different components were carefully arranged to accommodate for the small space provided for on this table. The image relay system relayed the optimal beam profile throughout the laser system, and accommodated for the sage treatment of ghost foci. The image relay system took up most of the space on the optical table. Some safety modifications protected one of the glass laser heads as it was on the very edge of the table.

I wanted to run the GCR in single shot mode for this laser. There were many ways to do this. The GCR had a single shot mode option available, but when a GCR changes modes of operation the thermal, optical and electrical properties also change. So if the laser was aligned in one mode of operation it will not be aligned in another mode of operation. It was much easier to align the YOGA laser in a 10 Hz setting than it is in single mode operation. Hence I decided to build a mechanical shutter to facilitate a single shot mode with 10 Hz GCR operation.

The mechanical shutter would allow the user to use the low energy setting (using a wave plate and a polarizer) to align the laser and then allow a high energy pulse from the GCR to be used in the laser system. The mechanical shutter consisted of a high energy reflecting mirror mounted on a brass slide as shown in figure 2.11. The slide connected to one end with springs and the other end with a solenoid. I calculated that the pull back from the springs should have a period with $T/4 = .09\ sec$ for the switch to be fast enough. The mirror holder and solenoid core had mass $\sim$ 112 g. This gave us spring constants of $k = 34.1\ kg/s^2$. I chose the springs accordingly. The shutter controller consisted of a self built 555 timing box and an optoisolator-triac system that allowed 120 volts AC to be supplied to the solenoid with a specified time pulse as illustrated in figure 2.10. The width of the pulse supplied by the 555 timing circuit was determined by an RC circuit, and the time width of the pulse was RC. The user could adjust the width of the timing pulse supplied to the shutter using an adjustable resistor in the circuit. The mechanical shutter, when closed, reflected the GCR laser pulse into a beam block, and, when open, let a GCR laser pulse through the system.

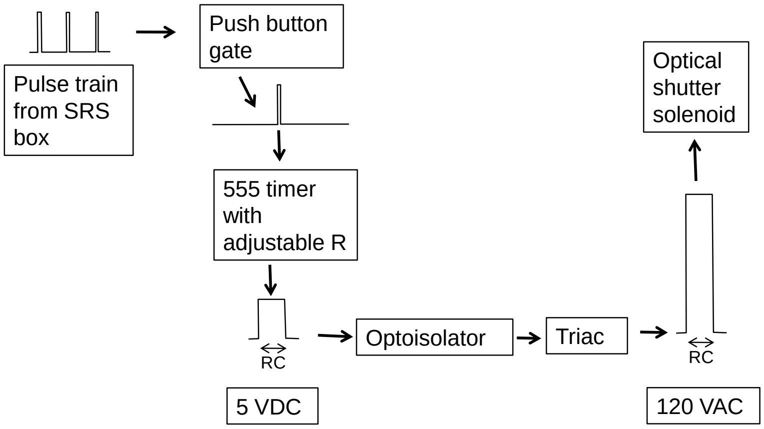

Figure 2.10:

The main problem of this mechanical shutter was the vibrations produced in the optical system. I fixed this by adding a lot of vibration dampening onto the shutter itself. The shutter was attached to the floor and not on the optical table by means of unistrut scaffolding. This eliminated the vibrational problems in the optical system. Other problems included timing problems of the shutter which were resolved by keeping the system clean and lubricated, and by making sure that there were no noise problems between the timing boxes and the shutter controller.

The GCR beam needed to be spatially filtered before amplification by the laser rods. The spatial fluctuations on a typical GCR laser pulse can be too much for amplification. Large spatial fluctuations in the laser pulse could

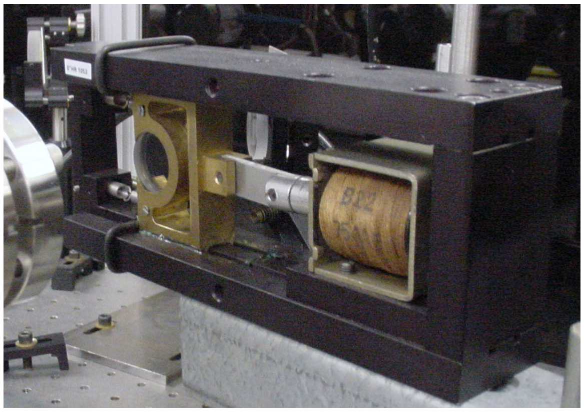

Figure 2.11: Shutter assembly designed to alow the switching of high energy beams.

lead to self focusing which could potentially damage the rod. For a Gaussian beam the pinhole diameter of $D_{opt} = F\lambda/a$, where F is the focal length, λ is the wavelength and a is the diameter of the beam, allows 99.3% of the beam through. This is generally recommended for spatial filters of Gaussian beams in industry [106]. This would give a diameter of 57 μm. The GCR beam was not Gaussian and because of the high energies involved about 10 times this diameter was used. I therefore used a spatial filter that was 500 μm in diameter because of its availability.

I built a spatial filter assembly with the purpose of being able to see where the laser focus was on the spatial filter block. This would enable the user to align the spatial filter with greater ease. The spatial filter assembly had a clear plastic cylinder surrounding the pinhole, as in figure 2.12, that allowed for the viewing of the laser focus during alignment. The effect of the spatial filter can be seen in figure 2.17.

I designed the laser layout around the occurrences of ghost foci. Ghost

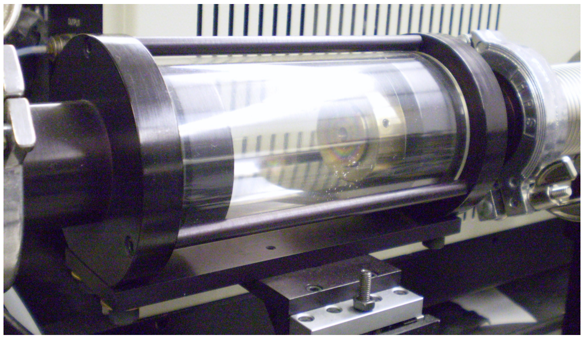

Figure 2.12: Spatial filter assembly designed to be able to see where the focus of the beam is located

foci are caused by partial stray reflections from lenses and other optics. They can come from a lens and focus upstream of the lens (1st order) or downstream of the lens (2nd order). I positioned optics with a large margin of error away from the ghost foci occurrences. I was especially careful that the laser rods were far away from any possible ghost foci. Optic coatings can degrade over time, especially in vacuum telescopes and this can cause reflections to occur that will put energy into these ghost foci and cause damage in the optics. Damage occurred once during the operation time from an uncalculated ghost foci from the chamber optics.

The ghost foci can be calculated using matrix lens equations [57]. For the 1st order ghost foci described in figure 2.13 the matrix formulation can be written as:

$$\begin{pmatrix} 1 & -D \\ 0 & 1 \end{pmatrix} \begin{pmatrix} 1 & 0 \\ \frac{2d}{n_{lens}} & 1 \end{pmatrix} \begin{pmatrix} 1 & -D \\ 0 & 1 \end{pmatrix} = \begin{pmatrix} 1 - \frac{2dD}{n_{lens}} & -2D + \frac{2dD^2}{n_{lens}} \\ \frac{2d}{n_{lens}} & 1 - \frac{2Dd}{n_{lens}} \end{pmatrix} \tag{2.6}$$

with the first and last matrix being the interaction with the curved surface of the lens and the middle matrix is the propagation of through the lens including the reflection of the planar surface of the lens as illustrated in figure 2.13.

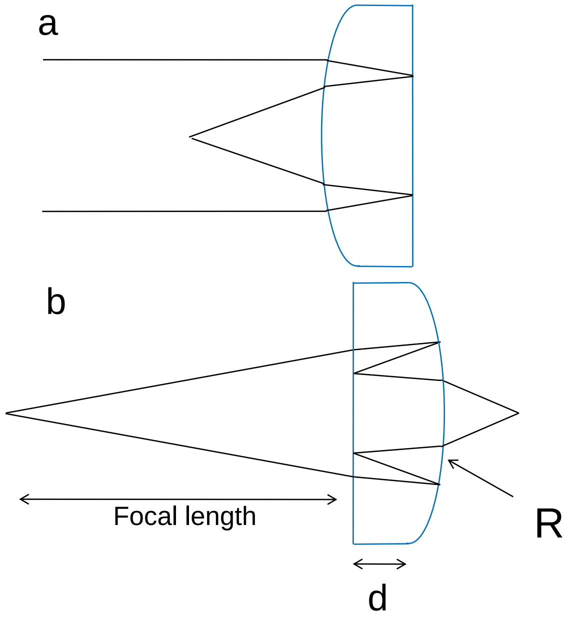

Figure 2.13: Ghost foci are caused by stray internal reflections in lenses. Here are two ghost foci common in laser systems, a) first order ghost focus, b) second order ghost focus.

Hence the propagation length in the propagation matrix will be $2d$ where d is the thickness of the lens. Also D is the dioptric power of the lens or the reciprocal of the focal length. The upper right entry of the combined matrix is $1/f$ where f is the focal length of the 1st order ghost focus. If, upon approximation, $d \rightarrow 0$ then

$$1/f = -2D = -\frac{2(n_{lens} - n_{air})}{R} \tag{2.7}$$

where R is the radius of curvature of the lens. This will then be $1/R$ if the approximation is taken to be $n \approx 1.5$. Thus $f = R$ or 1/2 the focal length of the lens, where f will be the focal length of the ghost focus.

The matrix configuration of the second order ghost foci is much more complicated and is of the form

$$\begin{pmatrix} 1 & -D \\ 0 & 1 \end{pmatrix} \begin{pmatrix} 1 & 0 \\ -\frac{2d}{n_{t_1}} & 1 \end{pmatrix} \begin{pmatrix} -1 & -\frac{2n}{R} \\ 0 & 1 \end{pmatrix} \begin{pmatrix} 1 & 0 \\ \frac{d}{n_{t_1}} & 1 \end{pmatrix}. \tag{2.8}$$

The first matrix on the right is the propagation through the lens. The second matrix is the internal reflection of the curved part of the lens which is treated the same as a curved mirror. The third matrix is the propagation through the lens twice upon internal reflection, and the last matrix is the refraction out of the curved part of the lens as illustrated in figure 2.13.

The calculation of this matrix with a generic R for the radius of curvature of the lens, $n_{t_1} = 1.54$, $d = 6.4mm$ (parameters of the lenses in the image relay optics), and the initial vector being the expanding beam of

$$\begin{pmatrix} R/2 \\ 1 \end{pmatrix} \tag{2.9}$$

is

$$\begin{pmatrix} -27.29/R^3 - 3.23/R^2 + 3/R \\ -54.61/R^2 - 19.203/R + 1 \end{pmatrix}. \tag{2.10}$$

With a relatively large R, this approximates to

$$\begin{pmatrix} 3/R \\ 1 \end{pmatrix} \tag{2.11}$$

which will give a focus of $f = R/3$ or a 1/6th of the initial focus of the lens. Both of these calculations give important results in determining the ghost foci in the system. In designing the YOGA laser system, all optics were then placed far from these predicted values in the telescopes used form the image relay system.

I took great care to align the double pass rod. This used a 1/4 wave plate polarizer system that allowed the laser beam to travel through the rod retroreflect from a 0° mirror at the end of the rod, then be diverted from the upstream path by a polarizer. I used a thin film polarizer that was aligned using the Brewster angle. This angle was critical with a 1° margin of error. To aid in this, I made special mounts to mount the rectangular thin film polarizers. They had angular edges machined into the holder that were at this Brewster angle. This helped place the polarizer in an approximate position before fine alignment. I measured the throughput of the system using a movable detector to scan over various angles. This was a challenge for this laser system because the wave plate - polarizer in the GCR isolator adjusts the energy of the beam. Thus, with low energy settings, the beam was very unpolarized. To circumvent this problem, I aligned the polarizer at higher energies than standard alignment procedure.

To aid in the alignment of the laser head I put the double pass glass head on a translation stage. The tilt on the glass laser head was produced manually with a magnetic base giving friction to the glass head. The translation stage acted perpendicularly to the laser beam. Great care needed to be taken to align through the laser heads, because the wedge in the rods created little room for error.

The actual telescope relay system relayed the best beam profile from the z-scan measurement throughout the system with the use of four telescopes. The telescope system imaged this profile through the rods so that the best profile would be imaged as the beam left the rod. With a double pass rod the best profile imaged on the end of the rod when it left the rod for the second time. The spatially filtered profile was relayed to the chamber to achieve best focus in the chamber. I expanded the beam before the rods to $\sim$15 mm and after the rods to $\sim$22 mm to decrease the fluence on the optics.

The system lost 10 % from the first isolator, about 5 % of the energy though the spatial filter and another 15 % though the double pass system. There was a loss of about 5 % going through the last head when the head was not flashed, and about 10 % from the last isolator. This gave a total of 45 % loss of energy through the system. The up stream pulse began with about 800 mJ from the laser and ended up with 500 mJ with no amplification.

2.6 Timing of the Laser System and Putting it all Together

The most important thing in constructing a laser with several precisely timed components was to have a good timing master control. In this case two timing boxes were used to control our experiment. I used an SRS timing box that was obtained from LLNL, and new Berkeley Nucleonics timing box. The timing logic diagram for the experiment that includes the YOGA laser is in figure 4.13.

I used a 10 Hz signal from another SRS box borrowed from the GHOST laser for the master clock. The internal 10 Hz trigger had too much noise shot to shot to be useful for the experiment. The internal trigger gave a standard deviation of 2.1 μs and the GHOST master clock gave a standard deviation of .28 μs. This was small enough not to effect the PFNs. The timing of the experiment usually went off the Quantel-GCR duo, and this could be made very accurate, but for triggering something like the ICCD camera with this jitter would be impossible. The SRS box sent signals to the lamps and q-switch for the GCR, and to the BNC box. I triggered the experiment from the previous pulse in the 10 Hz train. Thus all the important functions of the experimental system fired to be in synch with the next pulse of the GCR. This allowed the experiment to be a single shot experiment with the GCR stabilized at 10 Hz. The lead connecting the two boxes passed though a self constructed 555 timing gate circuit as illustrated in figure 2.10. This circuit had a button that when fired allowed one pulse from the 10 Hz train to go through. The BNC box controls the mechanical shutter, the camera, both PFNs and one other device if needed. An example of a timing chart can be found in table E.7.

2.7 YOGA Performance

I characterized the performance of YOGA mainly through energy measurements. Energy meters and photodiodes measured the amplification of a laser beam going to the laser heads. The GCR and a 1064 nm laser diode served as seed beams for the measurements. The small signal and saturated gain was measured from the glass laser head amplification. The small signal gain was in contrast with saturated gain where the laser pulse amplifies an amount comparable to the energy stored in the laser rod. I use low energy laser pulses (on the order on 10 mJ) to make small signal gain measurements. The maximal amount of GCR energy was used for the saturated signal gain measurements. These measurements were not fully saturated gain, but did show saturation in the gain. Finding the optimal gain while scanning the delay time was a crucial part of these measurements. This involved measuring the amplification vs. delay between the PFN timing trigger and the seed beam. The time for which the maximum amplification occurred was the time set for the PFN in the experiment (see figure 2.14). I monitored the profile of the flashlamp pulse in time with a photodiode. The maximum gain came about 100 μs before the maximum of the peak profile on the photodiode. This was most likely due to the mismatch of UV deposition into the rods that was beyond the sensitivity of the photodiode.

I performed spatial small signal gain experiments of the rod where a 1064 nm laser diode with small beam diameter passed through the laser rod. I varied the transverse position of this beam throughout the rod using a micrometer, with the beam parallel to the laser rod. The flash lamps were at high energy and the signal increase was measured with a photodiode. The results of this experiment are in figure 2.14, and show that the PFN energy was deposited more on the wings of the rod than in the center, which is typical in glass lasers with diffuse radial cavity optics [26].

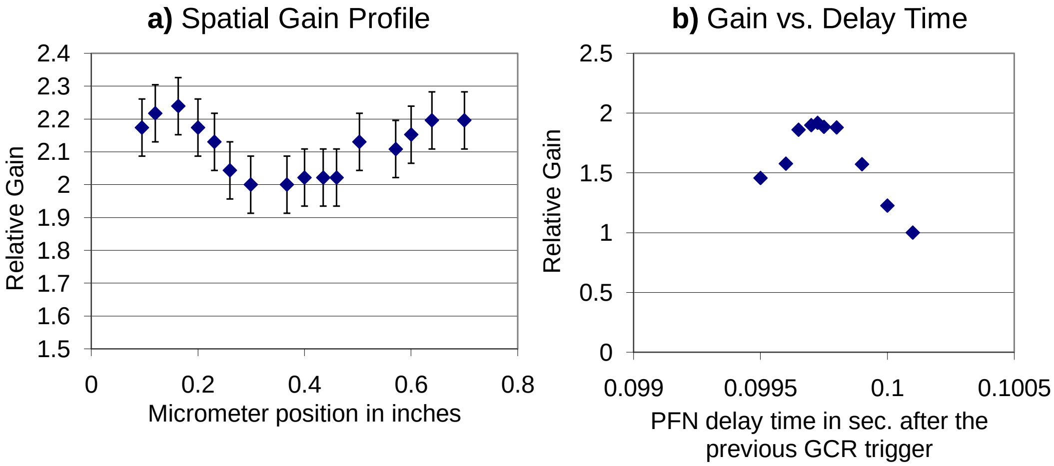

Figure 2.14: The spatial gain profile of the glass laser rods was measured in a). The gain vs. delay time was measured in b).

The small signal gain was defined by the amplified gain divided by the seed gain at small seed energies compared with the energies stored in the rod. I perform experiments by measuring the small signal gain vs. the input voltage on the PFNs. The small signal gain was measured separately for each laser head. The black PFN connected to the double pass rod which was the first laser rod in the laser chain. I connected the red PFN to the last glass laser rod in the system. The black PFN was set at 3400 V and therefore deposit more energy in a laser head. I therefore chose the black PFN to power the double pass rod. The energy of the laser pulses was measured using a Molectron and Ophir energy meter.

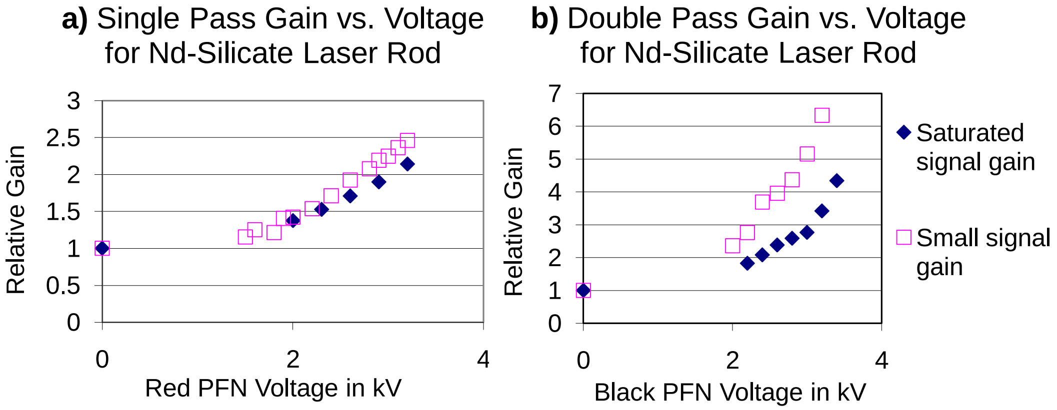

Figure 2.15: The single pass gain was measured of the single pass rod that was controlled by the red PFN in a). The Double pass gain was measured with the double pass rod that was controlled by the black PFN in b).

I fine tuned the alignment of the system before higher energies were measured. Close attention was paid to the laser rods and the soft diffraction caused by keeping the beam as large as possible through the laser rods. Small increments of energy were used with the PFNs to measure what effect the beam had on the laser system. A permanent observation beam was used through leakage of the one of the last stage mirrors onto a Cohu CCD camera. This aided in alignment and also allowed us to measure the beam profile at high energies. Images of the amplified beam at this location are in figure 2.17.

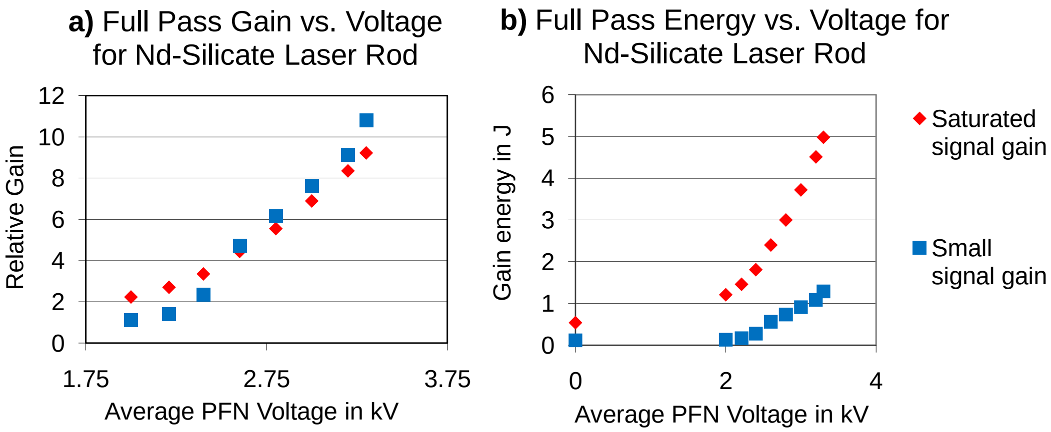

Figure 2.16: The gain (a) and energy (b) was measured of the full laser system.

I used an optical wedge to measure the high energies of the laser calibrated with an energy meter. This energy detection system was calibrated using low energy. The full amplification was measured separately with each laser head, and then a full system scan was performed. The laser energy was subsequently measured with a DET 210 photodiode, and was calibrated using the Ophir energy meter. The temporal scan of a YOGA pulse at full energy from this photodiode is in figure 2.19.

The results of the gain measurements are found in figures 2.15 and 2.16. The gain was measured for each rod system separately and then as a full system scan. The separate rod system measurements were made in accordance to the PFN set up. For the black PFN the gain, measurements were made with a double pass of the laser rod, and for the red PFN the laser rod was only single passed. In these figures both unsaturated gain (with a seed of 12 mJ) and the saturated gain (with a seed of 0.54 J, the maximum GCR energy) were presented together for comparison. The difference between the saturated

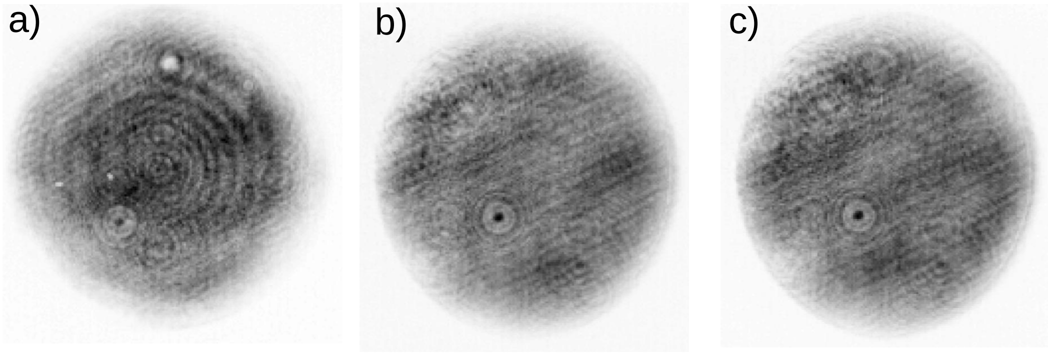

Figure 2.17: Beam profiles. a) without amplification or spatial filter, b) spatial filtered to 2.6 J, c) spatial filtered to 3.2 J.

and unsaturated gain was most apparent in the double passed rod, than in the single passed rod or the full system scan. The double pass of the rod should see more saturation because the rod was being doubly depleted. The saturated and unsaturated gain of the full system scan were nearly identical, which implies that the entire system was operating in the unsaturated regime even with the maximum seed energy from the GCR. This means then that more energy is available to the laser if the seed beam energy is increased or if the single pass rod is converted to a double pass rod. The energies of the full system amplification, as compared with the average PFN voltages, are in figure 2.16. The exponential character of the gain, as in equation 2.2, can be seen in this energy scan with the exponential variable based on the density. The density, n_0 was linearly dependent with deposition energy as in equation 2.3.

I measured the total laser energy as 4.98 J initially on the laser, which was more than the predicted energies. Other energy gain measurements were in table 2.5. The calculations matched the measured gains well. Discrepancies

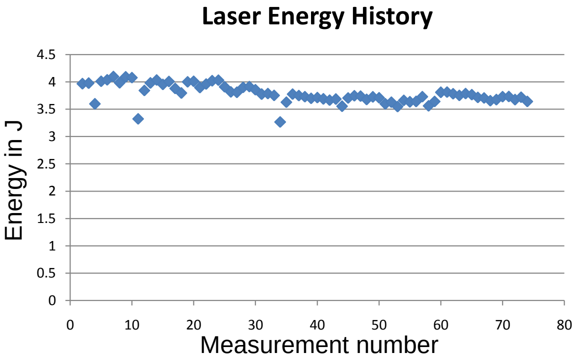

Figure 2.18: Energy history of measured full energy laser shots from 5/24/2006 to 2/7/2007. Average energy = 3.78 ± 0.17.

	Calculated Energy	Measured energy
Single pass calculation, Red PFN	1.43 J	1.14 J
Double pass calculation, Black PFN	2.71 J	2.47 J
Full pass calculation	4.57 J	4.98 J

Table 2.5: Calculations of gain energies in the laser rods compared with measured results.

can be blamed for various reasons including the 1% absorbtion rule and the leakage of laser light from the system. The effects of saturated signal gain were seen in the lower values of relative gain with the data obtained with a full GCR energy seed pulse. If the laser rods had less of a wedge more energy could be extracted from the rod. Since the energy was distributed toward the edges of the rods having a laser beam will result in a significant gain of energy.

The energy of the laser dropped to an average of 3.78 J as the experiment progressed and has kept at that constant rate for the duration of the experiment. The energy history over the course of the experiment is in figure 2.18. I have not found a definitive explanation of this drop. The energy measurement changed from wedge measurement to direct measurements, but this

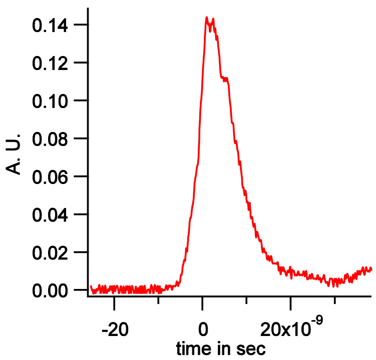

Figure 2.19: Temporal profile of a laser pulse amplified to 3.67 J with a FWHM of 9 ± 1 ns.

did not account for all of the energy loss, as the wedge measurement was carefully calibrated. The GCR energy dropped about ~ 40 mJ, after the initial gain measurements, due to a heat load problem that was not resolved (see appendix A.5). Also the laser flashlamps in the laser heads were about 10 years old at this time. Even though the lamps did not have a high accumulation of shots the lamps could still degrade over time. These reasons seemed like the most likely reason for the energy drop.

The laser system was contingent on the shutter part of the system, and this took a while to develop into a stable functioning part of the system. I had to isolate it from the table and get the noise out of the electronics, and keep the shutter lubricated. With the shutter working properly the YOGA laser system worked stably at an energy of 3.78 ± 0.17 J.

After three years of running the YOGA laser I found in routine checks of the system the development of several burn spots on the rods. Many of these burn spots were in the places where the coating looked damaged as obtained from Kigre. The burn spots made a significant divot in the center of the beam, and increased with further use at higher energies. The damage was on the surface of the glass laser rod and I decided to keep running with the damage spot at lower energies until the experiment was finished.

2.8 Conclusion

I have developed a laser using a Nd:YAG oscillator with a laser glass amplifier (YOGA) that is capable of delivering 1064 nm, 3.78 ± 0.17 J in an 8.0 ns pulse. The energy gain of the laser was modeled using photon population calculations, and the laser was found to be in good agreement with the simulation. The laser had a good beam profile and was stable in energy with a standard deviation of 0.17 J. The laser was timed precisely with experimental equipment to produce a functioning pump-probe laser experiment.

Chapter 3

Theoretical Discussion of Plasma Physics and Laser Plasma Interactions

3.1 Plasma Physics

Plasma is considered the fourth state of matter and is a major component of the universe. Only now in this century are physicists able to understand and control this state of matter. Plasma physics is a complex and rich study of dynamics. Plasmas promise great technological advances for the future including the hope of using fusion energy to power our energy needs.

3.1.1 Magnetohydrodynamics

Plasma physics is based on the principles of kinetic theory with the added complexity of charged particles [56]. From kinetic theory the dynamics of an ideal gas can be described using the moments of the kinetic equation

$$\frac{\partial f_s}{\partial t} + \nabla \cdot (v f_s) + \frac{\partial}{\partial v} \cdot (a_s f_s) = C_s(f) + I_s \tag{3.1}$$

where f_s is the distribution function, C_s is the collision operator and I_s is the source term for a particular species of particle "s". One can take the moments of the kinetic equation to obtain relations for the conservation of mass, momentum and energy. The results are as follows:

$$\frac{dn_s}{dt} + n_s \nabla \cdot \mathbf{V}_s = i_{s0}, \tag{3.2}$$

$$m_s n_s \frac{d\mathbf{V}_s}{dt} + \nabla p_s + \nabla \cdot \pi_s - e_s n_s(\mathbf{E} + \mathbf{V}_s \times \mathbf{B}) = \mathbf{F}_s + m_s \mathbf{i}_{s1} \tag{3.3}$$

$$\frac{3}{2}\frac{dp_s}{dt} + \frac{5}{2} p_s \nabla \cdot \mathbf{V}_s + \pi_s : \nabla \mathbf{V}_s + \nabla \cdot \mathbf{q}_s = W_s + \frac{1}{2} m_s i_{s2} \tag{3.4}$$

where i_s are source terms, π_s are generalized viscosity tensors, $\mathbf{F}_s$ are external forces acting on each species, W_s are the external heat sources acting on each species. Also n_s, $\mathbf{V}_s$, p_s, q_s, $\mathbf{E}$, and $\mathbf{B}$ are the density, velocity, pressure, heat flux, electric field, and magnetic field respectively. The time derivative is the convective derivative

$$\frac{d}{dt} = \frac{\partial}{\partial t} + \mathbf{V} \cdot \nabla. \tag{3.5}$$

These equations describe the dynamics of the plasma. Equation 3.2 is the continuity equation that keeps track of the flow of mass. The i_s term allows for particle to be removed or added to each species equation. Equation 3.3 describes the conservation of momentum by comparing the momentum of the mass flow with the gradient of the pressure and the electromagnetic terms. This equation also takes into account the friction in the flow with the viscosity tensor, and also momentum changes with particles exchanging species in the i_s term. Equation 3.4 is the conservation of energy equation that is similar in its physical description to equation 3.3.

The goal of magnetohydrodynamics is to describe the fluid behavior of a plasma in the limit that the ion gyroradius in the magnetic field is zero. When using laser-produced plasmas this limit is compromised because the ion energies are high [118] and the gyroradius is often comparable to the scale length of the plasma. The goal of describing any plasma system is to find an appropriate closure for the system. In basic MHD physics one assumes LTE and omits heat flow and anisotropic stress, which give $q = 0$ and $\pi = 0$. It is customary when describing idea MHD to omit the source terms. With $\rho = m_s n_s$ the MHD fluid equations reduce to

$$\frac{d\rho}{dt} + \rho\nabla \cdot \mathbf{V} = 0, \tag{3.6}$$

$$\rho\frac{d\mathbf{V}}{dt} + \nabla p - (\mathbf{J} \times \mathbf{B}) = 0 \tag{3.7}$$

$$\frac{dp}{dt} + \frac{5}{3}p\nabla \cdot \mathbf{V} = 0. \tag{3.8}$$

To close the system one must include

$$\mathbf{E} + \mathbf{V} \times \mathbf{B} = 0 \tag{3.9}$$

and Maxwell's equations

$$\nabla \times \mathbf{B} = \mu_0\mathbf{J}, \tag{3.10}$$

$$\nabla \times \mathbf{E} + \frac{\partial \mathbf{B}}{\partial t} = 0. \tag{3.11}$$

Equation 3.9 is referred to as the MHD ohms law. Performing a lorentz transformation on the plasma flow from the rest frame to the flow frame will change this relation to $\mathbf{E} + \mathbf{V} \times \mathbf{B} = \mathbf{E}'$ which gets rid of the $\mathbf{B}$ terms. This then states that in the flow frame the electric field is zero, which would be expected with the plasma resistivity being zero in the ideal case. Equations 3.10 and 3.11 are the only Maxwell equations that will contribute to the dynamics of the plasma.

These equations can be combined to give the relations:

$$\frac{d\rho}{dt} + \rho\nabla \cdot \mathbf{V} = 0, \tag{3.12}$$

$$\frac{dp}{dt} + \frac{5}{3}p\nabla \cdot \mathbf{V} = 0, \tag{3.13}$$

$$\rho\frac{d\mathbf{V}}{dt} + \nabla\Big(p + \frac{B^2}{2\mu_0}\Big) - \frac{1}{\mu_0}\mathbf{B} \cdot \nabla\mathbf{B} = 0, \tag{3.14}$$

$$\frac{d\mathbf{B}}{dt} - \nabla \times (\mathbf{V} \times \ \mathbf{B}) = 0. \tag{3.15}$$

These equations again describe mass, energy and momentum conservation with the addition of equation 3.15. MHD describes the interplay between magnetic fields locked into a plasma and dynamical fluid forces in the plasma. The magnetic field has tension like a stretched violin string. This tension (T) can be described by the equations

$$T_{\|} = p_{cm\|} - \frac{B^2}{2\mu_0}, \tag{3.16}$$

$$T_{\perp} = p_{cm\perp} + \frac{B^2}{2\mu_0}. \tag{3.17}$$

Thus increased magnetic field strength reduces the tension parallel to the magnetic field and increases the tension perpendicular to the magnetic field. The flow of the fluid can alter magnetic field as shown in the equation 3.15 With $\mathbf{V} \times \mathbf{B}$ being a quantity that changes when the plasma flow is perpendicular to the magnetic field. The curl of this quantity then alters the magnetic field strength. These forces are pictorially illustrated in figure 3.1. Along with this tension comes a velocity concerning wave propagation along the magnetic field lines using this tension. This is called the Alfven wave velocity, given by

$$V_A^2 = \frac{B^2}{\mu_0(m_i + m_e)n} \tag{3.18}$$

being highly dependant on the magnetic field and density. This velocity is similar to the sound speed in that it describes how fast magnetic information can be propagated through the plasma.

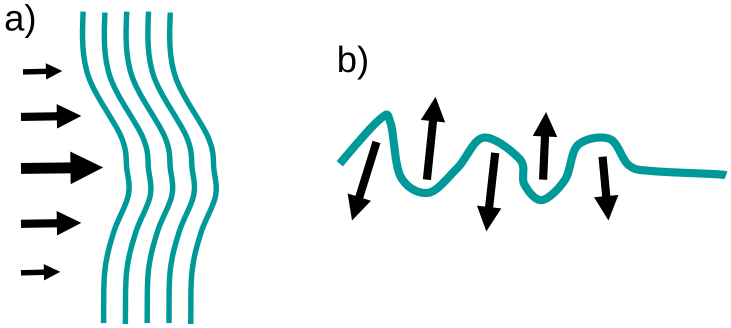

Figure 3.1: a) Plasma motion can affect the magnetic fields in a plasma, and b) magnetic tension can exert force on a plasma.

These MHD relations describe essential physics in the experiments used for jet dynamics. The principle of magnetic tension will be a dominating factor in describing the dynamics of jet evolution, laser-produced plasmas expanding in magnetic fields, and magnetosphere dynamics. The interplay between magnetic fields and fluid flow is one of the unique and fascinating components of plasma physics.

3.1.2 Brief Discussion on the Theory of Z-pinches

The z-pinch is a current fluxtube confined by self-induced magnetic fields where the current flows axially. To describe a z-pinch one uses cylindrical geometry and defines a current J_z flowing in a plasma. There will only be a B_θ magnetic component in the plasma. The following equations are reduced from the MHD equations for the symmetries described above:

$$\frac{1}{r}\frac{\partial B_\theta}{\partial \theta} = 0, \tag{3.19}$$

$$J_z = \frac{1}{\mu_0 r}\frac{d}{dr}(rB_\theta), \tag{3.20}$$

$$J_z B_\theta = -\frac{dp}{dr}. \tag{3.21}$$

These combine to give the equation

$$\frac{dp}{dr} + \frac{B_\theta}{\mu_0 r}\frac{d}{dr}(rB_\theta) = 0. \tag{3.22}$$

Equation 3.22 describes the pressure balance in the z-pinch were the thermal pressure balances the magnetic pressure caused by an axial current.

Z-pinch stability is formulated using the energy principle as outlined in Freidberg [39]. This is based on the principle that the most negative eigenvalue for the variation of the potential energy δW is a minimum for the potential energy of the plasma. Hence minimizing the potential energy can give information on the stability of the plasma. The energy principle, as calculated by Freidberg, gives the condition for stability as

$$2r\frac{dp}{dr} + \frac{m^2 B_\theta^2}{\mu_0} > 0 \tag{3.23}$$

where m is the mode number of the z-pinch fluctuation. This can be combined with the pressure balance equation 3.22 to get

$$\frac{r^2}{B_\theta}\frac{d\left(\frac{B_\theta}{r}\right)}{dr} < \frac{1}{2}(m^2 - 4), \tag{3.24}$$

$$\frac{1}{B_\theta^2}\frac{d(rB_\theta^2)}{dr} < m^2 - 1. \tag{3.25}$$

A z-pinch usually has the profile $d(B_\theta/r)/dr < 0$ which predicts stability for $m \geq 2$ from equation 3.24. If the current is small and the radius is large $B_\theta \sim 1/r$, which satisfies the relation 3.25. But near the origin we have $B_\theta \sim r$, as in the case inside a fluxtube, which will break the stability condition for the $m = 1$ mode because the left side of 3.25 will be positive. Thus a z-pinch with no external magnetic field will always be unstable to the m=1 mode. One can visualize the $m = 1$ mode by imagining a deformation in a fluxtube as in figure 5.11. The magnetic pressure will be much greater in the inner radius of curvature than it will be in the outer radius of curvature thus making the deformation grow.

This brief overview of the z-pinch illustrates one important aspect of fluxtube physics. A special instability related to the instability described here is the Kruckskal-Shafrav kink instability. I will discuss this in more detail in chapter 5, as it relates to the evolution of the laser triggered jets.

3.2 Scaling Laws Between Laboratory and Space

Ryutov et al. [122][123] presented two papers where they state that if two systems are both described by MHD they will evolve similarly if the initial conditions are geometrically similar and if the scaling relations hold. Ryutov states conditions that are needed to be satisfied for similarity. The first condition is that dissipative effects such as viscosity, thermal conductivity, and radiative cooling are unimportant in the system. The second condition is that the internal energy should be proportional to the pressure. The third is that the magnetic Reynolds number in both frames should be above one.

Ryutov states that the scaling conditions

$$\mathbf{r} = a\mathbf{r}_1, \rho = b\rho_1, p = cp_1, t = a\sqrt{\frac{b}{c}}t_1, \tag{3.26}$$

$$\mathbf{v} = \sqrt{\frac{c}{b}}\mathbf{v}_1, \mathbf{B} = \sqrt{c}\mathbf{B}_1 \tag{3.27}$$

will prove to be invariant in the ideal MHD equations 3.12 through 3.15. Another similar benchmark for scaling is equating the dimensionless Euler

	Galactic Jet	Experiment
h(cm)	10^{14}	10^{-2}
t(s)	10^5	10^{-7}
P(dyne/cm^2)	10^{-10}	10^{-4}
$n(cm^{-3})$	10^{-7}	10^{-1}
T(eV)	10^4	10^4
B(G)	10^{-8}	10^3
v(cm/s)	10^{10}	10^{10}
Euler	4	4

Table 3.1: These are the scaling relations between a galactic jet and an experimental setting. The scaling parameters are $a = 10^{16}$ (length scale parameter),$b = 10^{-6}$ (ρ scale parameter), and $c = 10^{-6}$ (Pressure scale parameter). [38]

number between the plasmas:

$$Euler = v_1\sqrt{\frac{\rho_1}{p_1}} = \nu_2\sqrt{\frac{\rho_2}{p_2}}. \tag{3.28}$$

The two frames are said to be similar if the Euler numbers are similar. The scalability of this relation follows from the above relations.

For examples of this type of scaling for astrophysical jets and laboratory experiment see tables 3.1 and 3.2. These tables take the parameters measured for galactic and YSO jets and relates them to the length and time scale parameters that can be measured in the laboratory. The Euler numbers are also set so they are within a factor of five with each other. The rest of the parameters are calculated from the scaling. The experimental conditions for simulating a galactic jet are quite unreasonable, but the experimental conditions for the YSO scaled case are obtainable. Thus there is incentive to create experimental conditions similar to the scaled YSO parameters, and, if achieved, the scaling will be meaningful of physical phenomena between the two frames.

This is one of the benchmark foundations for this research. In other

	Young Stellar Objects	Experiment
h(cm)	10^{11}	10^{-1}
t(s)	10^{4}	10^{-8}
P(dyne/cm^2)	10^{-8}	10^{6}
$n(cm^{-3})$	10^{3}	10^{16}
T(eV)	1	0.1
B(G)	10^{-4}	10^{3}
v(cm/s)	10^{7}	10^{7}
Euler	40	13

Table 3.2: These are the scaling relations between the YSO and an experimental setting. The scaling parameters are $a = 10^{12}$ (length scale parameter),$b = 10^{-13}$ (ρ scale parameter),and $c = 10^{-14}$ (pressure scale parameter). [4][135]

laboratory astrophysical research insuring scaling is always taken seriously. The end goal of the astrophysical comparisons made in this thesis will be to justify the laboratory astrophysical simulations with scaled results and show that the scaling is meaningful.

3.3 Laser Plasma Physics

3.3.1 Laser-Plasma Interactions for the use of Optically Probing Plasmas

Lasers can be used to optically probe plasmas. The way laser radiation interacts with plasma depends on the dispersion relation of the plasma. I briefly relate the formulation discussed in [87] to state the physics behind laser plasma interactions. The dispersion relation can be calculated by performing the necessary formulations of the electromagnetic wave equation through the plasma. This includes discussions of an electromagnetic wave,

$$\mathbf{E}(z,t) = \mathbf{E}_0 e^{i(kz-\omega t)} \tag{3.29}$$

propagating though an infinite uniform plasma. The goal of this discussion if deriving the dispersion relation or the relation between k and ω through this plasma.

Maxwell's equations, propagating through the plasma, can yield a wave equation that can give the dispersion relation between k and ω. Maxwell's equations useful to this process are:

$$\nabla \cdot \mathbf{E} = 4\pi\sigma, \tag{3.30}$$

$$\nabla \times \mathbf{E} = -\frac{1}{c}\frac{\partial \mathbf{B}}{\partial t}, \tag{3.31}$$

$$\nabla \times \mathbf{B} = \frac{1}{c}(4\pi\mathbf{j} + \frac{\partial \mathbf{B}}{\partial t}). \tag{3.32}$$

These Maxwell equations are in gaussian units, σ is the total charge density, and $\mathbf{j}$ is the current density. In this formulation $\mathbf{k} \cdot \mathbf{E} = 0$ which is the case of purely transverse waves and since $\nabla \cdot \mathbf{E} = i\mathbf{k} \cdot \mathbf{E}$ the plasma will be neutral with $\sigma = 0$. The generalized wave equation obtained by Maxwell's equations is:

$$\nabla^2\mathbf{E} - \frac{4\pi}{c^2}\frac{\partial \mathbf{j}}{\partial t} + \frac{1}{c^2}\frac{\partial^2 \mathbf{E}}{\partial t^2} = 0 \tag{3.33}$$

which is similar to the wave propagation in vacuum except with the added current density term.

The method for obtaining solutions to this equation is to find relations for the current density $\mathbf{j}$ in different situations. For an example of derivation I chose a case with no static fields and no collisions. The conditions for the densities and velocities of the various charged particles in the plasma give the relation $\mathbf{j} = en_i\mathbf{v}_i - en_e\mathbf{v}_e$. The forces on these particle are the following, assuming that the ions have charge state Z:

$$m_e\frac{d\mathbf{v}_e}{dt} = -e\mathbf{E}, \tag{3.34}$$

$$m_i \frac{d\mathbf{v}_i}{dt} = Ze\mathbf{E}. \tag{3.35}$$

Hence

$$\frac{\partial \mathbf{j}}{\partial t} = e(n_i \frac{\partial \mathbf{v}_i}{\partial t} - n_e \frac{\partial \mathbf{v}_e}{\partial t}), \tag{3.36}$$

$$= e^2(\frac{n_i Z}{m_i} + \frac{n_e}{m_e})\mathbf{E}, \tag{3.37}$$

but since $m_i \gg m_e$ these relations become

$$\approx \frac{n_e e^2}{m_e}\mathbf{E}. \tag{3.38}$$

Substituting this back into the wave equation gives the dispersion relation

$$-k_2 - \frac{\omega_p^2}{c^2} + \frac{\omega^2}{c^2} = 0, \tag{3.39}$$

where ω_p is the plasma frequency

$$\omega_p = \sqrt{\frac{4\pi n_e e^2}{m_e}}. \tag{3.40}$$

With the refractive index being the ratio of the phase velocity in vacuum to the phase velocity in the medium, or

$$\mu = \frac{c}{\omega/k}, \tag{3.41}$$

the refractive index from this dispersion relation will be

$$\mu = \sqrt{1 - \frac{\omega_p^2}{\omega^2}}. \tag{3.42}$$

This illustrates one peculiar property of plasma, that the refractive index through the plasma will be less than one for $\omega > \omega_p$.

Through other derivations the contributions of collisions and magnetic fields can be combined to the "no external field" case and obtain the dispersion relation

$$k^2 = \frac{\omega^2}{c^2}\Big[1 - \frac{\omega_p^2}{\omega^2(1 \pm \omega_e/\omega)(1 + i(\nu/\omega))}\Big], \tag{3.43}$$

where ν is the collision frequency and $\omega_e = eB_0/m_e c$ is the electron gyrofrequency. This gives a refractive index of

$$\mu = \sqrt{1 - \frac{\omega_p^2}{\omega^2(1 \pm \omega_e/\omega)(1 + i(\nu/\omega))}} \tag{3.44}$$

The index of refraction can be expanded if the related frequencies are small compared to ω as

$$\mu = 1 - \frac{1}{2}\frac{\omega_p^2}{\omega^2}(1 \mp \frac{\omega_e}{\omega})(1 - i\frac{\nu}{\omega}). \tag{3.45}$$

Looking at this relation for the simple plasma case (where $\nu = \omega_e = 0$) reduces back to the previous result, now expanded to $\mu = 1 - \frac{1}{2}\frac{\omega_p^2}{\omega^2}$. This again highlights the fact that light propagating through plasma will travel faster than the speed of light in vacuum. Now, with collisions, the negative imaginary term will cause an exponential decay of the propagating wave through the plasma. This would be expected as collisions will take away the energy from the propagating wave and give it to the thermal energy of the plasma. This is what is referred to as inverse bremsstrahlung which is the way a focused laser beam deposits its energy into its target. This will be discussed later on in this chapter.

The magnetic part of this dispersion relation has reference to Faraday rotation. The magnetic field in this formulation is aligned with **k**. The electrons are rotating around the magnetic field lines and this will enhance or retard the propagating fields depending on the helicity of the cyclotron rotation. This can be seen in the fact that linear polarized light can be separated into right and left circularly polarized light components. The light propagating with the same helicity as the cyclotron motion will be enhanced (or μ will decrease) and if it has the opposite frequency the light will be retarded (or μ will increase). This information is then important for Faraday rotation where a laser probe beam propagating through a magnetized plasma will give an experimental signature based on the magnetic fields in the plasma.

There can be nonelectronic refractivity contributions to the laser beam propagating through a plasma. If the laser beam wavelength is close to an emission resonance the refraction will be greatly reacted

$$\mu = 1 + \frac{2\pi e^2 n_e}{m_e} \sum_k \frac{f_k}{\omega_k^2 - \omega^2}. \tag{3.46}$$

where f_k is a characteristic oscillator strength at a emission frequency of ω_k. This is an could be an important contribution to the index of refraction to plasma if the laser frequency is close to an emission resonance, but f_k is difficult to calculate in plasma conditions. Precautions thus need to be made to choose a plasma that does not have any strong emission lines near the laser probe frequency.

Knowing the index of refraction for a plasma can then give useful information for laser probing of plasmas. Interferometry and Schlieren both require the information given by the index of refraction to extract meaningful physical measurements of the plasma. Interferometry through a plasma requires the interference of two coherent wave fronts, that are usually paired by a split beam that has gone though a medium such as a plasma and a reference beam. In a plasma we can usually neglect the effects of the neutral gas. If this is the case the fringe shift, N, will be given by the equation

$$N = \int [(\mu - 1)/\lambda] dl = \frac{-1}{2\pi} \frac{e^2 \lambda}{mc^2} \int n_e dl \tag{3.47}$$

where λ is the wavelength of the propagating light, μ is given by equation 3.45 and l is the distance the light travels through the plasma with density n_e. Thus symmetry and geometry are important for calculating the density of the plasma. The process of extracting the density information from an interferogram is call Abel inversion.

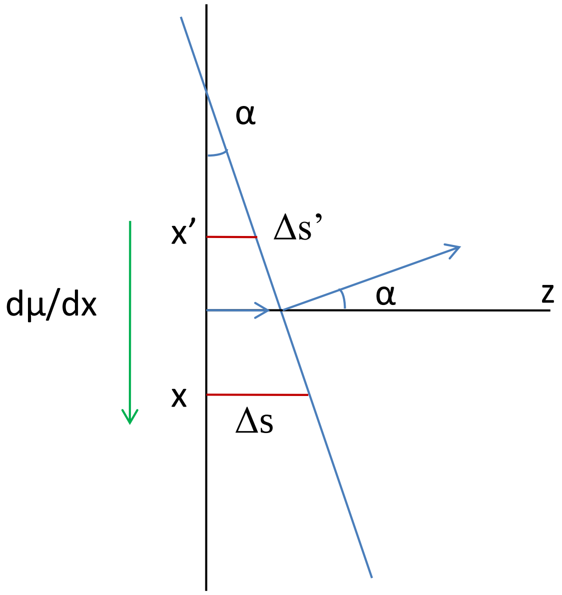

Figure 3.2: Diagram for angular displacement of a propagating electromagnetic wavefront resulting from index of refraction gradients involved with Schlieren imaging.

Schlieren can detect gradients of index of refraction in a plasma. Index of refraction gradients are related to density gradients in plasmas due to the fact that the plasma frequency is dependant on the density, and as discussed above, the index of refraction is depended on the plasma frequency. Schlieren imaging is a method of plasma probing that eliminates the fundamental modes in an optical image, thus measuring the amount of light deflection due to the gradients in the plasma. One can calculate the amount of deflection in the propagating beam based on the plasma gradient. If one has a gradient in the index of refraction $d\mu/dx$ one can calculate the deflected angle α as illustrated in figure 3.2 from the equation

$$\Delta\alpha = (1/\mu')(\partial\mu/\partial x)\Delta s \tag{3.48}$$

where $\Delta s = c\Delta t/\mu(x)$, and the propagation is in $\approx z$ direction. Taking the limiting process for a non constant gradient with the angular deflection small then $\Delta s \approx z$ and

$$\alpha_x = \int_0^z (1/\mu)(\partial\mu/\partial x)dz, \tag{3.49}$$

and

$$\alpha_y = \int_0^z (1/\mu)(\partial\mu/\partial y)dz. \tag{3.50}$$

We can take the value for μ to be one for a plasma as a good approximation and take $\mu = 1 - \frac{\omega_p^2}{\omega^2}$ with $\omega_p = \sqrt{\frac{4\pi n_e e^2}{m_e}}$. The result will be

$$\alpha = -(\lambda^2/2\pi)(e^2/m_e c^2)\int(dn_e/dx)dz. \tag{3.51}$$

Thus the angular deflection α can be compared with the density gradient as integrated of the propagation length. With careful geometrical calculations this can be related to Schlieren imaging. Schlieren imaging is usually more concerned with high gradient spatial outlines of plasma, and not the actual density numbers. More about Schlieren will be discussed in chapter 4.

Intense laser interactions are often used to create plasmas. The method for which laser plasmas deposit energy into the target material is with inverse bremsstrahlung [80]. Bremsstrahlung is the process whereby accelerated charged particles emit electromagnetic radiation. As in the laser interaction process described above, the electromagnetic field propagating through a plasma will cause the particles to accelerate, hence inverse bremsstrahlung.

Energy will not be deposited in the plasma unless there are collisions in the plasma to dissipate the heat. An intense laser-target interaction is a very collisional process. Using the formulation above with the collisional velocity term will be

$$\frac{d\mathbf{v}_e}{dt} = -\frac{e\mathbf{E}}{m_e} - \nu\mathbf{v}_e, \tag{3.52}$$

where ν is the number of electron-ion collisions per second. This will give a dispersion relation of

$$k^2 = \frac{\omega^2}{c^2}\Big(1 - \frac{\omega_p^2}{\omega^2(1 + i\nu/\omega)}\Big). \tag{3.53}$$

The imaginary part of this dispersion corresponds to a damping term in the electric field, which will attenuate the laser beam intensity. This is the method of how the laser deposits energy into the plasma. The electron ion collision term can estimated [87] using the relaxation time t_{ei} for electron reflections of 90° with singly charged ions at constant temperature as

$$\nu = \frac{1}{t_{ei}} = \frac{4\pi e^4 n_i ln\Lambda}{(2m_e)^{1/2}(\frac{3}{2}kT)^{3/2}}. \tag{3.54}$$

This shows that the laser energy is absorbed when the ion density is high and will decrease with high temperatures. We see also in the dispersion relations above that there can be a condition where μ becomes imaginary, in which case the plasma will reflect the laser light. Without collisions and magnetic fields this happens when $\omega < \omega_p$. Care must then be taken when estimating the amount of energy deposited into a laser-plasma and also that reflected laser light would not damage the laser.

As shown in this section laser interactions in plasma can be modeled in various circumstances. The index of refraction can be calculated for conditions involving collisions, magnetic fields, and basic plasma interaction. This can lead to the understanding of how interferometry and Schlieren probing techniques can give important physical measurements of a plasma.

3.3.2 Plasma Emission

Plasma emission is a function of temperature, density and line strength. Line emission will radiate strongly at an atomic or ionic resonance in the plasma. This results in a discrete spectra and calculating this spectra over a range of wavelengths for a heavy ion is very difficult. In addition to line spectra there are also continuous spectra resulting from bremsstrahlung radiation.

Zeldovich [156] describes the radiation from bremsstrahlung in the following way. For a unit volume of plasma let N_+ be the number of positive ions with charge Ze, and let N_e be the number of electrons. The electrons have a normalized Maxwellian velocity distribution of

$$f(v)dv = 4\pi\Big(\frac{m}{2\pi kT}\Big)^{3/2} e^{(-mv^2/2kT)v^2} dv \tag{3.55}$$

with T being the electron temperature. Zeldovich integrates the energy emitted from electrons per unit volume per unit time using the Maxwellian velocity distribution from the minimum velocity required to emit a photon ($1/2mv_{min}^2 = h\nu$) to ∞. The result is

$$J_\nu d\nu = \frac{32\pi}{3}\Big(\frac{2\pi}{3kTm}\Big)^{1/2}\frac{Z^2e^6}{mc^3}N_+N_e e^{-h\nu/kT}d\nu \tag{3.56}$$

where ν is the frequency of the radiated light, and J_ν is the spectral emission coefficient. The integrated spectral emission coefficient over all frequencies is therefore

$$J = \int_0^\infty J_\nu d\nu = \frac{32\pi}{3}\Big(\frac{2\pi kT}{3m}\Big)^{1/2}\frac{Z^2e^6}{mc^3h}N_+N_e. \tag{3.57}$$

The plasma emission is therefore strongly dependant on the density and weakly dependant on the temperature. On a typical detection system all the frequencies are not detected. For a range of frequencies from ν_1 to ν_2 this will give an integration of

$$J = \int_0^\infty J_\nu d\nu = \frac{32\pi}{3}\left(\frac{2\pi kT}{3m}\right)^{1/2}\frac{Z^2e^6}{mc^3h}N_+N_e(e^{h\nu_2/kT} - e^{h\nu_1/kT}). \tag{3.58}$$

This is slightly more dependent on temperature with the temperature being involved in the exponents. This still has the majority of dependence on the density.

Radiation from plasmas due to inverse bremsstrahlung can therefore be calculated using plasma parameters. A continuous spectrum detector such as an ICCD camera can detect a plasma snapshot over a small time interval and gain plasma radiation spatial profiles. This will be referred to in subsequent analysis in this thesis.

3.4 Conclusion

Theoretical formulations for MHD and plasma laser interactions give a basis whereupon physical processes can be described in these reactions. This is especially important when studying laser plasma laboratory astrophysics. This material will be used for analysis in subsequent chapters of this thesis and more theoretical formulations will be added upon when needed.

Chapter 4

Optical Probing of Laser-Produced Plasmas with and without Magnetic Fields and Comparison with Hydrodynamic Simulations from HYADES

4.1 Introduction

Laser-produced plasmas are a rich source of plasma physics. The use of laser-produced plasmas in these projects has been structured for the use of jet formation for laboratory astrophysics studied. The laser-produced plasmas were studied for their use as a plasma substrate with embedded currents and magnetic fields designed for jet production. The laser-produced plasmas were characterized over a wide range of parameters, using different thicknesses of aluminum and copper target wire, different laser energies, with and without magnetic fields, and probed with Schlieren, interferometry and ICCD photography. The axial radii of the plasma was measured and compared with self-similar plasma expansion models. A lagrangian hydrodynamic code, HYADES, was used to calculate plasma parameters, which, where possible, were compared with measured data. The results of this chapter are a characterization of plasma parameters from laser-produced plasmas that serve as a template for jet and magnetosphere physics in chapters 5 and 6.

Laser-produced plasmas have been studied since the dawn of the laser age; nevertheless, the study of laser-produced plasmas is far from exhausted.

Laser-produced plasmas have been studied for their own sake in plasma physics. Physicists have studied plasma physics processes in laser-produced plasmas due to their unique physical features. Physicists have studied laser produce plasmas for applications in fusion and tokamak studies, for applications in thin film processing, and for possible roles in laboratory astrophysics.

Tuckfield et al. [140] took high speed framing photographs of laser-produced plasmas in magnetic fields, and observed that the laser-produced plasma stopped expanding at a certain radius in the magnetic field. He observed a slight "bounce" of the laser-produced plasma as the plasma retracted from this radius. Several physicists have measured the density of laser produce plasmas early in their evolution using interferometry [3][7][34][149]. Rumsby et al. [121] measured the plasma characteristics of laser-produced plasmas using ion-collecting probes and microwave probes. Koopman [79] measured plasma characteristics of a laser-produced plasma expanding into magnetic field using the magnetic coil probes, Langmuir probes, and microwave diagnostics. Decoste et al. [22] stated that a two-temperature model was needed to study the plasma expansion of a laser-produced plasma. Sudo et al. [133] made observations of the laser-produced plasma as it stagnated in the magnetic field and found that the plasma temperature increased on the boundary of the plasma. Sudo termed this phenomenon as re-thermalization of the plasma. Dimonte et al. [24][23] also made measurements of a laser-produced plasma expanding in a magnetic field. He used a gated imager to take pictures of the plasma profile and observed instabilities forming, and also observed the laser-produced plasma bouncing back from the magnetic field. He also made measurements of the magnetic field in the plasma using FR5 glass and Faraday rotation.

Ripin et al. [118][119] studied laser-produced plasmas as sub-Alfvenic expansions into magnetic fields. He used a variety of plasma probes and the fast-gated microchannel-plate optical camera. Ripin was able to observe the laser-produced plasma expansion in a magnetic field along the axis of the magnetic field. He observed flute-like instabilities developing across the magnetic field faster than conventional theories expected. Ripin also discusses the large Larmor limit of MHD, and described that in laser-produced plasmas in magnetic fields the ion Larmor radius is much larger than the electron Larmor radius which alters the dynamics of standard MHD theory. Peyser et al. [111] irradiated hollow glass cylinders in the presence of the background magnetic field and observed that instabilities grow in the plasma related to the magnetic field strength. Peyser concluded that the electron-ion hybrid instability, which is a modified form of the Kelvin-Helmholtz instability, was consistent with their results.

Kasperczuk et al. [75][152] made three-frame interferometric measurements of laser-produced plasmas expanding into the magnetic field. The three-frame interferometer could make three measurements in time of the same plasma expansion. Kasperczuk used a strong pulsed magnetic field ranging from 5-15 T, and he used a laser pulse with energy E=5 J. Kasperczuk measured the density of the expanding plasma and found that the plasma expanded along the boundary of the expanding diamagnetic cavity forming a horseshoe shape. Dyakin et al. [143] measured laser-produced plasma expanding in a strong magnetic field at the same facility using x-ray emission spectra. Kasperczuk et al. [74] recently made interferometric measurements of laser-produced plasmas without magnetic fields and made comparisons between the density profile and the crater shape in the target material.

Magnetic fields are naturally created in laser-produced plasmas. McLean et al. [92] measured the spontaneous magnetic fields in a laser-produced plasma using the Zeeman effect. Briand et al. [16] measured megagauss magnetic fields in laser-produced plasmas by Faraday rotation. Matoba et al. [89] measured the plasma properties of colliding laser-produced plasmas. Jellison et al. [70] measured the laser plasma expansion in a magnetic field using resonant optical probing. The resonant optical probing gave the measurements much more sensitivity and the plasma dynamics could then be measured farther out in time using Schlieren and shadowgraphy. Suckewer et al. [132] investigated the possibility of using laser-produced plasmas in magnetic fields as an amplification medium for x-ray lasers. Mason et al. [88] measured the effects of laser-produced plasmas in magnetic fields in atmospheric pressures. Zakharov et al. [155] investigated the possibility of extracting electricity from expanding laser-produced plasmas in magnetic fields.

VanZeeland et al. [144][145] have studied the effects of the laser-produced plasma expanding into a magnetized plasma. These experiments were done on the LAPD machine and were measured by many diagnostics. The purpose of the experiments was to measure Alfven wave and currents produced in the magnetized plasma. Gekelman et al. [42] has recently published an exhaustive set of data in this same machine measuring the collision of two expanding laser-produced plasmas. Gekelman has measured three-dimensional evolution of currents and magnetic fields generated by this collision. Gekelman claims to have measured recombination associated with the produced currents and magnetic fields. Pribyl et al. [113] is working on the development of micro Langmuir and B-dot probes to study the small-scale dynamics of the laser plasma expansion in the LAPD experiment.

Harilal et al. [52] has studied laser-produced plasmas for their applications in engineering. Harilal has measured the effects of ambient gas on laser-produced plasmas; because laser-produced plasmas are useful in the development of extreme ultraviolet lithographic light sources. One problem with the use of laser-produced plasmas in this way is the production of unwanted debris. He found that the ambient gas could effectively mitigate this debris and still propagate the extreme ultraviolet source. Laser-produced plasmas are also useful for the deposition of material for thin film surfaces. The same problem of debris exists for these applications. Harilal et al. [54][53] has made several studies of laser-produced plasmas and magnetic fields that the purpose of this knowledge serves the community trying to mitigate this debris. Many engineers have used curved magnetic fields to guide laser-produced plasma onto a thin film device. The curved magnetic fields successfully guided the plasma on to the substrate away from the debris produced by the laser target interaction [138][137][72]. Kokai et al. [78] uses magnetic fields and laser-produced plasmas to enhance the growth of carbon cluster ions. Other physicists have used laser-produced plasmas to investigate their possible use in superconducting thin film layers [44][40]. Others have used spectroscopy to measure laser-produced plasmas for producing thin film layers [48][50]. And others have studied spectroscopy of laser-produced plasmas for the use of laser induced breakdown spectroscopy, which is a useful tool for studying the elemental composition of targets [126][114].

There have been many theoretical treatments of laser-produced plasmas in magnetic fields. Huba and Hassam [65][55] have developed the formation of magnetohydrodynamics in different limits related to laser-produced plasmas in magnetic fields. These limits are when the ion Larmor radius is large and the use of hall magnetohydrodynamics where the plasma dynamics occur on length scales of less that the ion inertial length and time scale smaller than the ion cyclotron frequency. They have simulated the Rayleigh-Taylor instability, and have found that it evolves much faster than the limit of the small ion Larmor radius [67]. Brecht et al. [15] has made similar calculations specifically looking at the structure of the plasma expanding at sub-Alfvenic speeds. Bhadra [10] and Ditmire [25] have made calculations describing plasma expanding in a magnetic field showing that the plasma stagnates against magnetic field, and under certain conditions can bounce back. Bernstein et al. [9] discusses the theoretical aspects of a resistive plasma expanding in a uniform magnetic field where the magnetic field does not perturb the plasma.

I propose to expand upon this wealth of knowledge concerning this subject through my experimentation and analysis of laser-produced plasmas using optical probing and ICCD imaging. The experiments performed used laser optical probing with laser-produced plasmas with various types and sizes of wire as targets. The most productive diagnostic was obtained with ICCD photography. There are many quantifiable features from this data. This data was analyzed using various theoretical formulations lined out in the theory section of this section and comparing the features found in the ICCD camera with the numbers predicted by these theoretical formulations. The most successful methods of analysis were from using the hydrodynamic program HYADES. This gave very accurate results of the position of the high temperature front of the laser-produced plasma. This gave new results in laser-plasma analysis that can expand upon the afore mentioned papers dealing with the subject. This chapter is developed with a detailed overview of the experimental procedures of this experiment and the experiments outlined in chapters 5 and 6. The results of the HYADES simulations are compared to the data obtained with ICCD photography.

4.2 Theory

Extremely high temperatures and intense pressures from laser deposition initiate laser-produced plasmas. The laser deposits energy into the target material in a very short amount of time. This allows the material to heat up to high temperatures and pressures without significant expansion. After the laser has deposited the energy in the bulk material the dense plasma will expand adiabatically into a vacuum. Many models have been derived to calculate and describe this plasma expanding into a vacuum. The goal for this theory section is to state basic models of laser-produced plasma expansion into a vacuum with and without magnetic fields. Various other magnetic effects relevant to this study will be explored.

One model of a laser-produced plasma expansion is the self-similar expansion model [59][156] where the governing equations are simplified by describing the dynamics by x/t instead of having x and t as independent variables. As the plasma flow progresses the variables describing the flow will remain similar to themselves based on their dependence of x/t. This predicts that only the scale of these parameters changes with time. Thus use of the self-similar model is dependant the plasma not having any characteristic length of time scales. One must also not have any dissipative effects in the plasma such as viscosity or heat conduction. All plasmas do have characteristic length and time scales, such as mean free path and collision frequencies, but if these are insignificant to the macroscopic flow dynamics and dissipative processes they will not effect the self-similar nature of the plasma dynamics. Plasmas generally do have the sound speed as a characteristic dimensional parameter, but this parameter has the same dimensions as the x/t combination and therefore is an important characteristic of the self-similar expansion. The self-similar formulation cuts down on the number of variable in the dynamical calculation. The characteristic expansion velocity of a spherical expansion is then of the form $V(r,t) = V_0(t)r/R$ where R is a maximal radius of the plasma expansion, r is the subradius of the expansion, and $V_0(t)$ is the velocity of the maximal radius of the expansion [59][156].

The self-similar expansion of the laser-produced plasma in a magnetic field can be modeled by self-similar MHD equations as given by Sudo et al. [133]:

$$\frac{3}{2}N\frac{dT}{dt} = -p\Big(\frac{dV}{dt}\Big) + \int \eta j^2 dV + W_L \tag{4.1}$$

$$p\Big(\frac{dV}{dt}\Big) = \frac{M}{2}\frac{d}{dt}\Big(\frac{dR}{dt}\Big)^2 + \frac{B^2}{2\mu_0}\frac{dV}{dt}. \tag{4.2}$$

In these equations N is the total number of particle in the expanding plasma, T is the ion and electron temperature, assuming they are the same, V is the volume of the plasma, $p = 3NT/4\pi R^3$ is the pressure, W_L is the power imputed into the plasma by the laser, M is the total mass of the plasma, R is the maximal radius of the plasma as prescribed by the self-similar formulation, B is the magnetic field, η is the resistivity of the plasma and j is the current density. These equations are modifying the MHD formulas given in section 3.1.1 and by using the adiabatic relationships between temperature and pressure. The use of the self-similar term in the velocity reduces the number of variables significantly in the system. For simplicity I ignore the resistivity of the plasma in the calculations. From these equations comes the equation:

$$(3/2)NT + (M/2)(dR/dt)^2 + (B^2/2\mu_0)V = E_0. \tag{4.3}$$

In this equation $N = n(Z+1)$ and $V = \frac{4}{3}\pi R^3$. For an adiabatic process $TV^{\gamma-1} = constant$ with implies that $NT = NT_i V_i^{\gamma-1}/V^{\gamma-1}$ which for simplicity $\gamma = 5/3$ for a monatomic gas. Then $NT = NT_i R_i^2/R^2$ where R is the radius of the expanding plasma sphere. Thus equation 4.3 becomes

$$(M/2)(dR/dt)^2 = E_0 - (B^2/2\mu_0)\frac{4}{3}\pi R^3 - 3/2NT_i R_i^2/R^2 \tag{4.4}$$

or

$$dR/dt = \sqrt{(2/M)(E_0 - (B^2/2\mu_0)\frac{4}{3}\pi R^3 - 3/2NT_i R_i^2/R^2)}. \tag{4.5}$$

This equation describes the expansion of the plasma with initial energy E_0. This initial energy competes with the magnetic energy and the thermal energy in the expansion giving the total kinetic energy of the plasma expansion.

In the case of modeling these experiments a base number of atoms are assumed for N. A 25 μm wire is used often in my experiments and is useful for determining the initial ion count. For a 25 μm copper wire the mass per unit length is M=4.4×10^{-6}kg/m and the number of copper atoms per unit length in this wire is n=1.5×10^{19} atoms/m. For an aluminum wire of the same size the mass per unit length is M=1.3×10^{-6}kg/m and the number of copper atoms in this wire per unit length is n=2.9×10^{19} atoms/m. For modeling purposes I used a 41 micron length portion of the wire, as the laser intensity is high in this diameter as measured with a CCD camera and in more direct ways including figure 4.18. The initial R_i was the radius of a sphere that contains the volume of the ablated material used. For the initial temperature I used the average energy deposited by the laser pulse throughout the medium. The initial magnetic energy was added to E_0 to avoid numeric inconsistencies in the simulation resulting in equation 4.5 becoming negative. An example of this calculation is in figure 4.1.

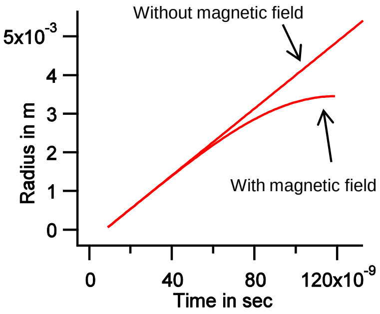

Figure 4.1: Self similar expansion with and without a magnetic field for an ablated 25 μm Al wire with a 200 mJ laser pulse.

A laser-produced plasma expanding into a magnetic field is an electrically conducting material expanding into a magnetic field. This conducting plasma will expel the magnetic field as it expands by producing currents as illustrated in figure 4.2. The expanding plasma will eventually stop expanding because of the energy required to produce the currents. One way to estimate the radius of expansion in a magnetic field is to consider the balance of energies in the expansion similar to the above self similar formulation. The expanding plasma will expel the amount of field with energy density equaling the initial energy in the plasma supplied by the laser pulse. Or as stated in the equation:

$$E_{lp} = \frac{B^2}{2\mu_0}\frac{4\pi R_{max}^3}{3}$$

were E_{lp} is the energy deposited into the plasma by the laser pulse, and R_{max} is the maximum expansion radius of the plasma in the magnetic field. This is the condition where the plasma β is one, or when $\beta = \frac{P_{fluid}}{B^2/2\mu_0} = 1$. E_{lp} is not the energy in the laser pulse but it is the energy that the plasma absorbs from the laser pulse. The laser pulse will begin to be reflected from the laser-target interaction when the plasma reaches the critical density. The laser pulse usually deposits about half its energy into the plasma as reported in literature [42] with similar conditions related to this experiment.

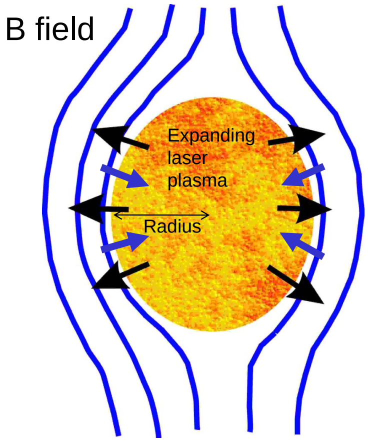

Figure 4.2: An expanding laser-produced plasma will expel magnetic fields. There will be a point in time where the energy of the expanding plasma will balance the energy of the expelled field.

The magnetic field will begin to diffuse back into the plasma as the plasma expands as illustrated in figure 4.3. The time this diffusion will occur can be estimated by using the magnetic fusion equation taken from ideal electromagnetism or:

$$\nabla^2 A = \mu_0 \sigma \frac{\partial A}{\partial t}. \tag{4.6}$$

From this an order of magnitude magnetic diffusion time can be calculated as

$$\tau = O(\mu_0 \sigma L^2), \tag{4.7}$$

where σ is the conductivity of the plasma. The diffusion time for a 1.0 eV laser-produced plasma on a length scale of 1.0 cm is $\sim 10^{-8}$ sec which is on the time scale of the experiment.

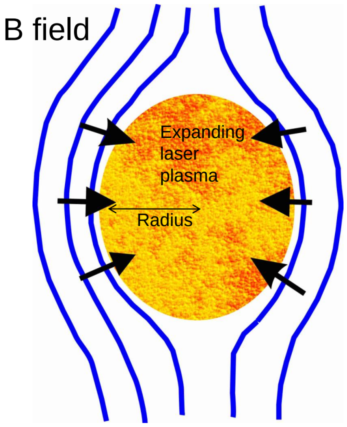

Figure 4.3: Because the laser-produced plasma is resistive the magnetic field will diffuse back into the plasma.

In laser-produced plasmas the ion larmor radius is usually much larger than the electron larmor radius and is comparable to the scale length of the plasma. This then encroaches on the assumptions in MHD where the larmor radius is essentially zero. With the ion larmor radius comparable to the length scale of the plasma the ions will be unmagnetized, while the electrons will be magnetized. For example, a 50 eV plasma will have an ion larmor radius of .36 cm for a singely charged aluminum ion in a 1.0 T magnetic field. The electrons of this same plasma will be .002 cm. The ion larmor radius will generally be much larger than this because the Temperature of the laser-produced plasma is initially very high, and the ions will carry the momentum gained by the initial expansion into the vacuum. It is estimated that ions carry 90% of the total plasma energy in directional kinetic energy [118]. In a strong plasma flow with these conditions through a magnetic field the electrons will be held by the magnetic field and the ions will progress uninhibited. This will cause a charge separation that will induce $\mathbf{E} \times \mathbf{B}$ drifts in the plasma and will bind the ions to the magnetic field through the electrostatic forces of the electrons.

4.3 Experimental Materials and Methods for Measuring Laser-Produced Plasmas in Magnetic fields

The experimental design for all mature experiments in this thesis revolve around the YOGA laser and the accompanying target chamber setup. The YOGA laser served as the drive beam with energies up to 4.0 J. The vacuum chamber was equipped to be optically probed with Schlieren, interferometry, and ICCD photography. The vacuum chamber also allowed for the delivery of currents to the targets and the targets to be spatially manipulated. A magnet, that was integral to the experiment, was specially designed for the vacuum chamber. These components combined with timing instruments and other details created the conditions for the study of laser-produced plasmas, laboratory simulations of astrophysical jets and magnetospheres. These components are described in detail in this section.

4.3.1 Vacuum Chamber and Related Hardware

The laser-produced plasma experiment, and all other current experiments discussed in this dissertation, were built with the YOGA laser as the drive beam. These experiments are built around an 8” 6-way-cross converted into a vacuum chamber, with the YOGA laser depositing energy into the vacuum chamber and the diagnostics measuring the interactions in the chamber.

The 8” stainless steel 6-way-cross was purchased from MDC. All sides of the 6-way-cross were closed with modified 8” stainless steel conflat flanges as in figure 4.5. The bottom conflat flange was modified to have a hole in the center that had a custom made stainless steel elbow welded to the flange.

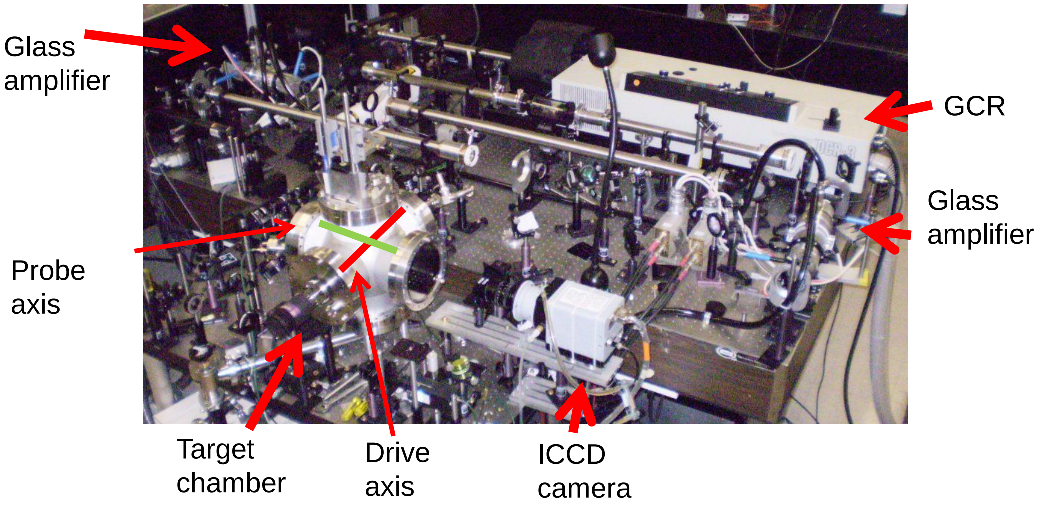

Figure 4.4: Representative picture of the lay out of the YOGA laser system.

Two opposing flanges on the lateral side of the cross have a single optical port for a 2” optic to be held in place with a modified 2 3/4” conflat flange. There are two ports on these flanges that are made for 1 1/3” conflat flanges. Through this flange I delivered the YOGA laser to the target and allowed for the unabsorbed portion of the YOGA beam to exit the flange. I attached to a flange a Granville-Phillips 275 convectron vacuum gauge and a vacuum valve to vent the chamber to air. The other two ports on the lateral plane have one 2” optical window port and two extended 2” optical window ports. This set of flanges with their accompanying ports allow probe beams to pass through the chamber. On the top of the chamber is a xyz-stage designed by Brendan Murphy.

The vacuum chamber stood on a 2’ by 4’ breadboard table, with 1” posts aiding as a nut for the CF flange and attaching to the table as illustrated in figure 4.10. I attached the 2’ by 4’ table solidly to the YOGA laser

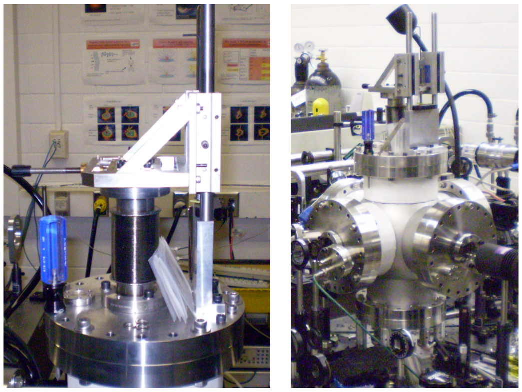

Figure 4.5: An 8” 6-way-cross converted to the target chamber with a custom designed xyz-stage.

breadboard table. The height of the 2’ by 4’ table was set to accommodate the height of the YOGA laser beam and to allow the vacuum line to enter into the bottom of the chamber.

The xyz-stage on the top of the chamber (see figure 4.5) was custom built in the machine shop, which significantly cut costs of the experiment. The xyz-stage does not have bearings but consists of two metal plates that are able to slide in each other. Finely threaded screws move these plates in the x and the y direction, with springs attached to these plates to counterbalance the force from the screws. The center plate attaches to a 2 3/4 CF flange that is welded to a flexible bellows. A shaft is screwed into the vacuum side of the CF flange and continues down into the chamber to connect to the target holder. A third screw controls the z direction of the xyz-stage with gravity and the pressure from the chamber providing the counter weight. With the weight of the atmosphere on the bellows the springs on the xyz-stage are often unable to compensate, requiring the operator to manually push the xyz-stage onto the screws.

A Leybold roughing pump with pumping speed of about 65 cubic feet/min pumped the vacuum chamber. The vacuum pump was close to the vacuum chamber to minimize the pump down time. There was a five-foot hose connecting them together. I put a KTX-150-2 oil trap from MDC between this hose and the vacuum pump to protect the vacuum chamber from the vacuum pump oil.

The Leybold pump pumped through a supplemental small Edwards EO 40/55 diffusion pump, with pumping speed of 60 lps, but with a chamber protecting bevel the speed was 27 lps. Collaborators worried that the diffusion pump would spoil the optics in the vacuum chamber. I found no oily residue during the operation of the diffusion pump using the protective bevel. The optics in the chamber did become spoiled, but this damage was from the target interactions in the experiment as evidenced by metallic spots on the optics.

The small diffusion pump required that the chamber be evacuated first to a level below 500 mTorr. I had the roughing pump connected directly through the diffusion pump, instead of having a separate evacuation line to cut costs. After the chamber was initially evacuated the diffusion pump required four minutes to warm up before it would properly pump the chamber. I sealed off the chamber from the diffusion pump during this time. The total pumping time used to reach the working pressure of 1.0 mTorr was about 30 minutes. The chamber could be pumped down to below 0.1 mTorr but it took much longer. I determined, however, that 1.0 mTorr was sufficient for our experiment as determined through reasoning discussed in section 4.4.3. The diffusion pump needed 20 minutes to cool down before it could be brought to atmosphere.

4.3.2 Custom Built Permanent Magnet

The possibility of using a permanent magnet was desirable due to the complications of using electromagnets. Electromagnets required another power source, and a pulsed magnetic field would produce electrical noise. Electromagnets can produce stronger fields and allow for probing plasmas along the magnetic field lines, but since I was interested in relatively modest magnetic fields (on the order of a tesla) for our experiment I chose to use a permanent magnet.

Rare earth metal permanent magnets can give strong fields, dependant on the amount of material used and the way the magnetic field lines are "conducted" around the magnets in a similar phenomenological way as electricity is conducted trough a simple circuit. This experiment had a size constraint on the amount of material that could be used. The magnet had to safely fit inside an 8" six-way-cross, allowing for removal of the magnet and for experimental probing to take place.

Constructing a large magnetic field over a certain volume is more complicated than just putting two magnets together in close proximity around said volume. Placing two magnets close together around a certain volume with opposite poles facing each other will produce a larger field than if one magnet was used. Magnetic permeable material conducts magnetic fields like a metal conducts electric currents. In order to construct the strongest magnetic field out of a permanent magnet I needed to have two strong magnets encompassing a volume with the opposite poles of the magnet facing each other with an iron yoke encompassing the two magnets conducting the magnetic field lines from one magnet to the other.

I modeled the design of the magnet on a program called Maxwell SV.

Maxwell SV is a 2D electromagnetic simulation program developed by Ansoft. Maxwell SV uses 2D Finite Element Method (FEM), tangential vector finite elements, and automatic adaptive meshing procedures to calculate electrical and electromagnetic properties of physical configurations at low frequencies. Users can input various physical parameters on a 2D model for use in the calculation. The simulation design for the magnet includes constructing a 2D figure of the magnet along with the iron yoke and the program will calculate the magnetic field throughout the whole structure. I worked with the constraints that I had, which were fitting the entire magnet and yoke into the vacuum chamber, getting the largest volume between the two magnets and having the largest magnetic field in that volume, and minimizing the size of the magnetic material. The highest quality material MCE had was used to construct the magnet, which was a N5563 NdFeB rare earth magnet. MCE listed the parameters for recoil permeability as 1.05 and the magnetic retentivity as 1.5 T. Maxwell SV calculated the following numbers from these two numbers: magnetic coercivity= -1.14×10^6 Ampere/m and Magnetization $=1.19 \times 10^6$ Ampere/m. Using these numbers and a BH-curve from MCE Maxwell SV calculated the magnetic field of my design. I had the physics machine shop construct the iron yoke out of 1018 steel. 1008 steel gave better numbers, but was more difficult to purchase. I calculated that the center between the magnets would be $.97 \pm .01$ T with the geometry I chose and with 1018 steel as illustrated in figure 4.6.

I was concerned about the two magnets coming together accidentally in the process of the experiment. An aluminum scaffolding was made to prevent the magnets from coming together as seen in figure 4.7, if they came loose from the steel yoke. This would be unlikely, however, because the force that

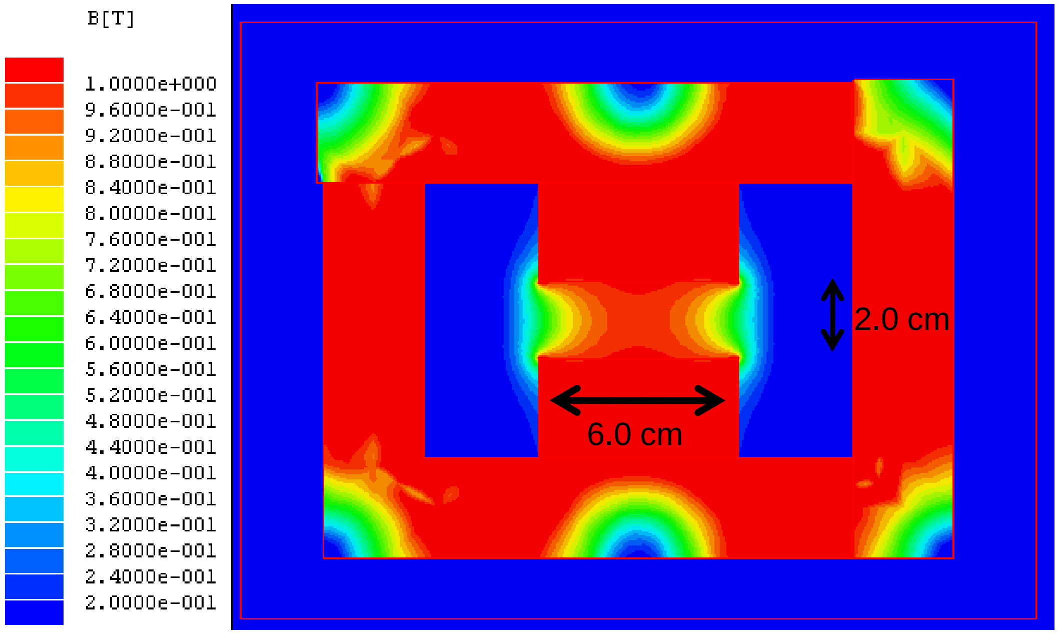

Figure 4.6: Calculation of the magnet system using Maxwell SV. Steel 1018 was used as the iron yoke and N5563 NdFeB for the magnet.

the magnet would attach to the steel yoke with is on the order of 200 lb. The magnets would not come together unless they came significantly off of the yoke. However, since such a catastrophe would break the magnets and possibly break an operators finger the scaffolding was used. This scaffolding cut down on the field of view for observing the laser-produced plasma, and made it more difficult to fit the target between the magnet.

I commissioned the UT physics machine shop to build all the nonmagnetic parts and sent these parts to MCE, and they assembled the entire magnet system. The magnetic field was measured with a hall probe on an xyz-stage. The actual measurement was .87±.02 T in the middle of the magnet (see figure 4.8), compared with the prediction of .97±.01 T. The discrepancy is most

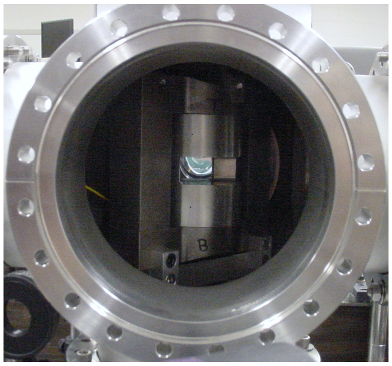

Figure 4.7: The custom designed magnet in the target chamber.

likely due to the difference between the 2 dimensional calculation and the actual 3 dimensional structure, and also slight differences in the amount and shape of the material used.

4.3.3 Targets and Alignment Techniques

Targets and target fabrication are an important part in any laser-target experiment. Parameters for the construction of targets have to include availability, ease of target fabrication, and ability to repeatably align and interact with the laser. I used copper and aluminum wire for targets for their availability and difference in mass and atomic number. I used two sizes of wire, a 50 gauge or $25\mu m.$ wire, where the diameter of the wire is smaller than the focus of the laser, and the other size is an 18 gauge or $1.0mm$ where the diameter is much larger than the laser focus. For the copper wires I used magnet wire, stripping the insulation off with paint thinner.

I attached the wires to the xyz-stage through a shaft that connected to the top of the chamber. I constructed numerous ways to connect the wires with the xyz-stage shaft. I positioned the wires so the target area of the wire

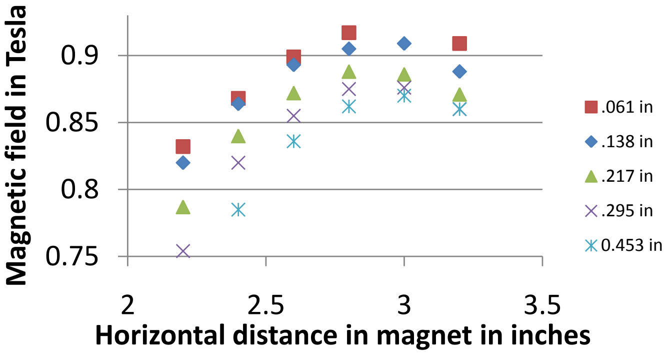

Figure 4.8: Z-component of the magnetic field measured with a hall probe. The values of each data series are in different distances from the top of the magnet with 0.453" being close to the center of the magnet.

was above the mount. The shaft angled from the top of the inside of the chamber, allowing an adjustable shaft to hold onto the wire. I constructed one particular wire holder to hold the wire target with electrical contact to an electrical discharge system discussed in the appendix B. Another holder was a small hollow ceramic tube that clamped on the shaft and held the wire with a plug.

Alignment happened with two different frames. One would involve the use of a HeNe laser and the other would involve the probe imaging system. I set up a HeNe laser on our experiment as a permanent alignment system. I spatially filtered the HeNe beam and expanded the beam to give a shorter focal region. I sent the HeNe beam though the dielectric mirror that directed the YOGA laser into the target chamber. I used crosshairs on the input and output drive ports of the vacuum chamber to get the HeNe beam as collinear as possible to the YOGA beam. I aligned the focus of the HeNe beam with the YOGA focus using a 20X microscope objective. See appendix section E.4 for alignment details.

The probe imaging system offered a straightforward way to align the target in the z (up down) and y (along the axis of the drive beam) directions. With the shadow of the target on the camera image clearly visible the target can be precisely placed. The position of the laser focus can be directly measured on the probe image by using either Schlieren or backlighting. With the target in position from the probe image direction the target can be aligned in the x (along the axis of the probe beam) using the diffraction of the HeNe beam from the target being in the HeNe beams focus. For precise alignment procedures see appendix section E.4.

4.3.4 Diagnostics

I used mainly optical diagnostics for measuring the laser-produced plasma expansion as illustrated in figure 4.9. This included Schlieren, interferometry, and ICCD camera images. I tried other diagnostics including shadowography, Faraday rotation and Langmuir probes, but either I did not get any significant information out of these measurements or I was not able to pursue the full development of these diagnostics. Out of the Schlieren, interferometry and ICCD camera images the ICCD camera images gave the most spatial information. The plasmas were not dense enough at later times in the expansion to efficiently probe with laser diagnostics. I present in the following sections the set-up for these three diagnostics.

4.3.5 Laser Probing of Small Laboratory-Produced Plasmas

I had a Quantel Brilliant YAG-laser available for the experiment. The Quantel was a convenient, easy-to-use laser. The Quantel used standard 110 Volt power and was air/water cooled. This laser was frequency doubled to

532 nm. The higher the frequency of the probe the lower the resolution of the Schlieren or interferometry as described in equations 3.47 and 3.51. Although the fundamental beam, in theory, would have given better results, I chose not to use the fundamental frequency of the Quantel (1064 nm) because the drive beam in the experiment is the YOGA beam which is also 1064 nm. This drive beam is so bright that I had to filter the scattered laser light from the probe diagnostics to protect the camera and to prevent the YOGA laser from distorting the image. Hence I used the 532 nm frequency doubled laser beam.

The Quantel laser had adjustable energy, and could give up to 120 mJ per pulse in the 532 nm beam. The energy was adjusted internally by adjusting the q-switching time. The Quantel, at its maximum energy, has a 2.0 ns FWHM spreadin its temporal duration. The line width is $1.4c/m = 4.2 \times 10^8 Hz$. When using lower energy settings the temporal profile broadened and became less desirable and noisy. The best and shortest temporal profile for probing the laser-produced plasma was desired to get the best temporal resolution for the measurement. I therefore had to run the Quantel with full energy and pick off a fraction of the energy with an optical wedge.

As with the YOGA laser I mapped out the beam path of target chamber laser systems with the GRAPHITE program. Figure 4.10 shows the layout for the Quantel optics. The Quantel path meanders thought the 2' by 4' table. There were several reasons for having the path length so long. One, the beam needed to be conditioned so that it was adequate for optical probing, and, two, enough space was needed after the laser plasma interaction to image the beam properly.

YAG laser beams are notorious for having very nonuniform spatial profile beams. YAG beams are designed for their energy and not their spatial

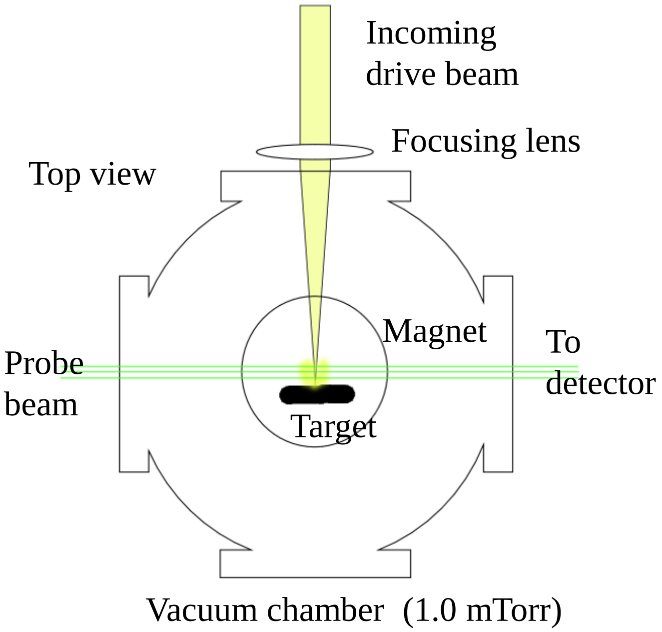

Figure 4.9: View of the experimental interaction region from the top looking down.

profile. Good spatial profiles in the beam are essential for interferometry and Schlieren. Therefore I took special measures to improve the spatial profile of the Quantel laser.

There were two things done to improve the beam quality. One was choosing a small and good part of the YAG beam with an iris. The other was to spatial filter the beam. For the first method, I took the beam that was split off from the main Quantel beam, from the wedge, enlarged the beam with a negative 13.0 cm focal length lens, and used an iris to cut out the part of the beam that looked the cleanest to spatial filter. This iris needed the freedom to adjust to different parts of the beam. Also the iris could be adjusted in size to

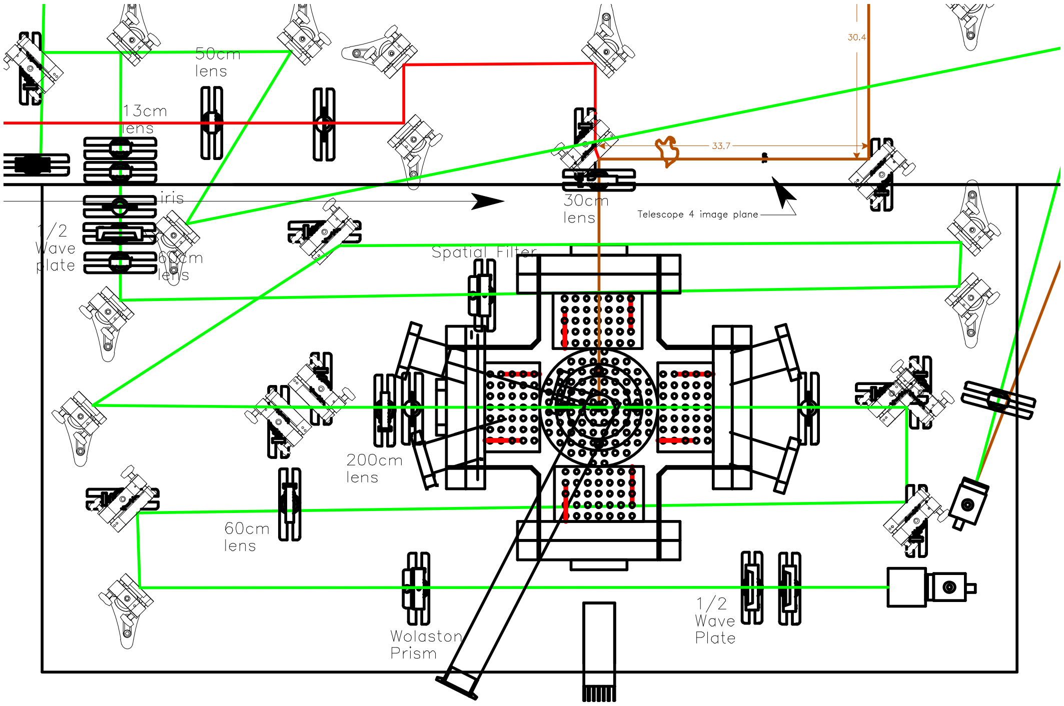

Figure 4.10: This is a line drawing of the laser experimental region of the experiment. A YAG laser was used to probe the laser plasma interaction.

adjust the amount of the beam we wanted to pass through. The iris produces strong diffraction, but this diffraction was eliminated by the spatial filter.

A spatial filter is a hole placed in the waist of a focusing telescope that removes high-frequency parts of the spatial profile of the beam. The focus of a laser beam through a spherical lens is the Fourier transform of the beam profile at the plane a focal length upstream from the lens [57]. For a gaussian beam the fraction of power transmitted through a hole at the waist of the focus is

$$\frac{P(D)}{TP} = 1 - e^{-\frac{1}{2}\left(\frac{\pi a D}{\lambda F}\right)^2} \tag{4.8}$$

where D is the diameter of the spatial filter hole, a is the e^{-2} radius of the gaussian beam upstream from the lens, F is the focal length of the lens, TP is the total power in the laser beam, and λ is the wave length of light. Industry recommends the use of a pinhole the diameters of $D_{opt} = F\lambda/a$ [106]. This will pass 99.3% of the energy of a gaussian beam. The beam of a YAG laser has a flat top profile and not a gaussian profile. Thus much more of the beam energy will be blocked by the pinhole.

For the use of the probe beam the spatial filter came after the beam-selecting iris and was a part of the imaging telescope that expanded the laser beam to be large enough for the experiments. If the spatial filter hole was too small the laser would disintegrate the hole, and distort the beam in the process. The recommended diameter above was on the order of $27\mu m$ in diameter. A pinhole on the order of $50\mu m$ was used and significant distortion of the beam was measured due to the denigration of the hole. Hence I used a spatial filter that was $400\mu m$ in diameter, which was the smallest pinhole the physics machine shop could make. This filters out a significant amount of the laser beam spatial noise to give an adequate profile for imaging.

The expanding telescope was a 60 cm - 200 cm telescope. I was unconcerned with the exact beam profile imaging of this telescope because it passes through a spatial filter. The second telescope images the laser-produced plasma onto the camera. This is a single lens telescope with a 60 cm lens. The distance of the interaction to this lens was on the order of 140 cm and the distance from lens to the camera was on the order of 105 cm. This gave a magnification of .75 for the telescope. I had to use a single lens telescope to use a Wollaston prism interferometer. The beam block was placed for the Schlieren in the focus of this telescope.

I used a CCD camera connected to a control card on a computer to measure the spatial profile of a laser beam. I used both Sony and Kohu cameras in working with the laser system, but for the purposes of taking the data I used the Sony camera XC-57 because the Sony that I had was a better camera.

I used the Spiricon imaging system in the early part of the experiment because I had access to the program. Spiricon is an imaging system geared for diagnosing laser systems. The Spiricon set up is expensive, and the Spiricon functionality was not needed in the experiment. A National Instruments I-MAQ 1405 card was used to control the camera. This was a low cost single channel color or monochrome image acquisition card with 16 MB memory. The National Instruments card had an external trigger input for precise timing of the camera. This card used Labview and Vision Assistant to operate.

One problem with externally triggering these cameras is that the camera's internal trigger is not a multiple of $10Hz$, which is the timing frequency the experiment was based upon. Hence there are times when the camera is not in sync with the camera grabber card and the desired image will not be recorded. Also with the nature of these cameras is the fact that they overlace images. The camera has two frames that it uses, each involving half the lines available to the camera. The camera alternates between which of these frames it sends to the card. I was able to time the camera so that the camera card would pick up on both overlaces for a total of 30 seconds, then it would switch to the half laced view for thirty seconds. I worked with this problem by manually timing when I would run the experiment so that the camera would measure the full field view.

In working with camera imaging systems, I was confronted with a problem of marking the location of a particular reference point of an image on the screen. I was concerned with this in terms of alignment etc. Marking the screen with a physical marker gave poor quality results because of parallax. The distance and curvature of the glass screen to the image of the monitor made it difficult to get accurate results in alignment.

Sean Keely wrote a Windows program for me called grid.exe to make markers and grids that were permanently on the foreground of the computer monitor. Hence, even while accessing the program that had the image of the CCD camera the marker would still be visible on the computer screen. The position of the markers could be saved so that the alignment is not destroyed if the computer crashes.

The program has a main window that acts as a grid that has adjustable spacing and thickness of the grid lines. This grid and window are always at the forefront of the screen. This is very convenient for alignment of crosshairs, etc in the YOGA alignment. The program also has circular markers that have a cross in the middle for precise alignment. They have adjustable colors and sizes, and are always in the foreground of the computer screen. Both these markers and grids can have their transparency adjusted to see the images behind them. These markers are really convenient for alignment procedures as marking where the focus is of the YOGA laser breakdown in air and then moving the target onto the position of the marker. The position and size of the imaging program window is also saved by the program incase the window gets moved or the computer crashes. This program has been a valuable part of the experiment, along with other experiments other researchers have performed in the Thor lab.

4.3.6 Schlieren Images of Small Laboratory-Produced Plasmas

Schlieren or dark field imaging techniques are ideal for measuring strong density gradients. I chose this as our main diagnostic for the beginning part of our investigation because there are significant density gradients in laser-produced plasmas and because of the ease of using this diagnostic. The Schlieren technique images a laser beam that has passed through the laser-plasma interaction, where in the imaging process the fundamental modes of the image are blocked by placing a beam block in the focus of the imaged laser beam as illustrated in figure 4.11. With the fundamental modes blocked, only the part of the beam that has been significantly deflected by the plasma will pass to the detector. I have made various beam paths for Schlieren imaging over the course of the experiment, that consist of either a two lens telescope of a single lens telescope.

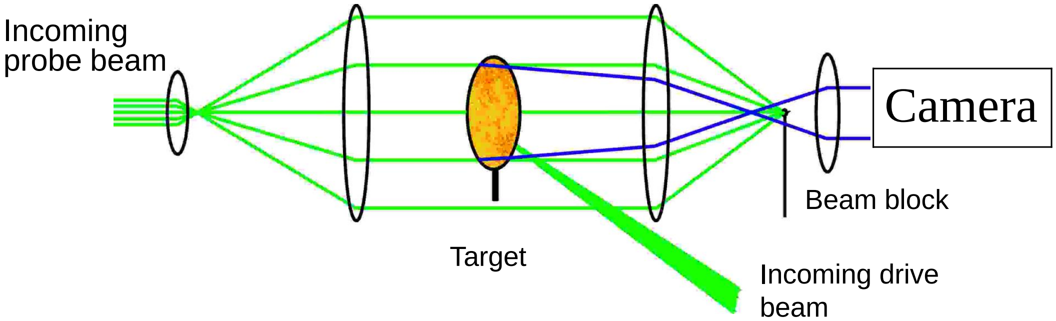

Figure 4.11: A Schlieren imaging system works by blocking out the fundamental parts of the image.

The beam block I used for the experiment was a wire that is connected to a xyz-stage. I used three sizes of wire for the Schlieren beam block, 0.02", 0.015", and 0.013". The majority of the shots used the 0.013" wire. Positioning the beam block was an important factor in the Schlieren data that was being taken. If I had the column of the wire blocking the beam, then parts of the image would be missing along the wire direction. Using the top of the wire as a beam block gave us more spatial information from the plasma. The thinner the beam block the more sensitivity of gradients could be detected from the plasma, but the probe laser was then more likely to burn through the wire. The thicker the wire the crisper the image would be, but only the most intense gradients would be detected.

The energy of the probe beam had to be large enough to be detected by the camera, but weak enough that the beam block and other focal points of the beam path will not degrade the performance of the probe beam. I had to block the camera with about 3.5 worth of ND's and one BG-39 colored glass filter designed to absorb 1064 nm light so that the YOGA laser scatter and the plasma emission would be sufficiently attenuated. The camera had a 532 nm interference filter to further block out the YOGA light. The probe laser energy could not be too high because the energy in the probe beam would ablate the Schlieren beam block. I could increase the length of the telescope to further attenuate the YOGA beam, since the YOGA scatter intensity would drop off more with $1/R^2$ and the probe beam would be collimated. Having a long telescope with comparatively small lenses decreases the resolution of the Schlieren. I used trial and error to find the optimum values for these parameters. The time delay between the probe beam and the YOGA laser gave the temporal measurement of the Schlieren image, and the camera card would take the spatial information of the Schlieren image.

4.3.7 Interferometry of Small Laboratory-Produced Plasmas

Interferometry is based on interfering two coherent laser beams where one beam has passed through an object such as a plasma, and the other beam has not. One technique operate interferometry is to split off two beams with a beam splitter and pass one beam through the plasma and send the other through a path of equal length then rejoin them with a beam splitter for the two beams to interfere. This can be a cumbersome process and is very difficult to do, and can be influenced by available space and the coherence length of the probe laser. There are other ways of making interferometers that include interfering one part of the beam with another part of the beam that can circumvent these problems.

One such method uses a Wollaston prism. I adapt the Wollaston prism interferometry formulation as outlined by Benattar et al. [8]. A Wollaston prism splits the beam into two beams of opposing polarizations with a divergence angle specified by the kind of Wollaston prism (see figure 4.12). If a laser beam comes out of a focus from a telescope with the polarization at 45° to the Wollaston prism axis, the two beams will come out of the Wollaston prism with opposing polarizations. If the Wollaston prism's angle is on the order of 1° the divergence will be small enough that the beams will overlap. Then passing the split beams trough a polarizer will interfere the two beams with each other. I used a Wollaston prism with a .75° angle.

Knowing the parameters of the Wollaston prism set up allow for the calculation of the distance between two fringes. Knowing the distance between two fringes is important because this determines the sensitivity of the interferometer. Interferometry sensitivity derives from the fringe shift of the interferogram. Having larger fringe spacings will therefore give more spatial

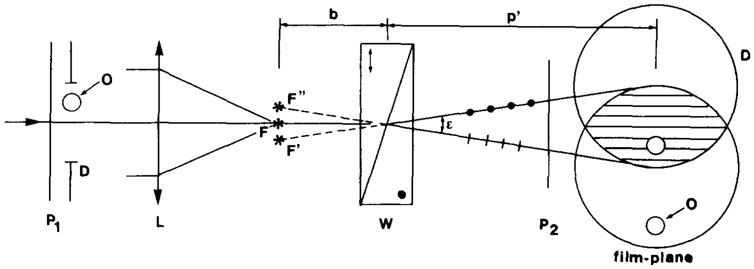

Figure 4.12: A Wollaston prism separates the beam into two polarizations. Sending these two beams through a polarizer will cause one side of the beam to interfere with the other [8] (Copyright (1980) by The American Physical Society).

information of the fringe shift. The down side of this is the larger the fringe spacing the more noise will be introduced in the data. The system must be adjusted to obtain the best fringe sensitivity vs. noise level introduced into the system. The fringe spacing can be determined by the equation

$$i = (\lambda/\epsilon)(p'/b) \tag{4.9}$$

where p' and b are given in figure 4.12, λ is the laser wavelength and ϵ is the Wollaston prism separation angle [8]. This equation can be modified to put the prism upstream of the focal spot. I found from manipulating the analysis that the equation is the same as equation 4.9 but b is the distance between the prism and the focal spot and p' is the full distance of the prism to the detector plane. The Wollaston prism was generally held at 8.0 cm upstream from the telescope focal point. This gave fringes with 5.33 lines per mm at the camera which corresponded to 4 lines per mm of the actual interaction accounting for the magnification.

For this interferometer to work the coherence length of the probe beam bust be larger than the phase separation induced by the interferometer. From

Hecht [57] we learn that the wave nature of light requires for a cosinusoidal wave with the amplitude modulated by a gaussian envelope that the product of the width of its Fourier space (Δk) with the width of its spatial scale must be $\Delta k \Delta x = 4\pi$. This is equivalent to $\Delta\omega\Delta t = 4\pi$. With $\Delta\omega = 2\pi\Delta\nu$ the above relation becomes with a generalized wave packet

$$\Delta\nu \approx 1/\Delta t. \tag{4.10}$$

This Δt is called the coherence time and the coherence length is $\Delta l_c = c\Delta t_c$ where c is the speed of light. The frequency line width is related to the mean frequency and wavelength by $\Delta\nu/\Delta\lambda = \overline{\nu}/\overline{\lambda}$. This combined with $\nu = c/\lambda$ gives the coherence length as

$$\Delta l_c = \overline{\lambda}^2/\Delta\lambda. \tag{4.11}$$

With the spectral line with of the Quantel laser $4.2 \times 10^8 Hz$ and the mean wavelength 532 nm the coherence length will be $\Delta l_c = 0.71m$. This is typical for a YAG laser and is more than sufficient for Wollaston interferometry where the difference in the interfering path length is less than 5.0 mm.

Because polarization is an important issue for this interferometer, I employed the use of two half wave plates in the beam path. One wave plate adjusted the polarization of the probe beam before the laser plasma interaction, and the other adjusted the polarization of the beam before it entered the Wollaston prism. The polarization was adjusted before the probe laser enters the laser-produced plasma in order to account for the plasma in a magnetic field being birefringent and can alter the interference effects of the interferometer. The half wave plate before the Wollaston prism is important because the polarization can change through the beam path optics before the probe gets to the Wollaston prism, and because I wanted the flexibility to choose the angle of the Wollaston prism to satisfy imaging requirements.

There were several problems encountered with the set up. I assumed from miscalculation that the laser-produced plasma would be much smaller than it was, so I found that the .75° was a too small to get good results over the field of view desired. With the larger field of view I was hard pressed to get a larger beam through the spacing I had for the magnet, and still have space in the beam that would not be affected by the laser-produced plasma. The beam quality I had, even after the improvements made for it, was not good enough to get perfectly straight fringes. They were adequate for the experiment, but this induced a lot of noise into the data. Vibrations were also a big problem especially when taking a background shot. The interference fringes would vibrate at times over a fringe shift in the set up. This noise was subtracted out in the analysis with moderate success.

4.3.8 ICCD Images of Small Laboratory-Produced Plasmas

An Intensified CCD (ICCD) camera is a CCD camera with an intensifier placed in front of the CCD camera. The intensifier is a multichannel plate that amplifies the light signal when a high voltage source is sent to the plate. The ICCD camera not only intensifies the image, but due to its operation has a gate pulse which sets the exposure time. This exposure time can be very small. In our case the minimum exposure time was 4.0 ns, but other models can have electronic gates much smaller than this.

Professor Bengtson had a spectrometer that had as part of its set up a Princeton Instruments ICCD camera. This ICCD camera was modified to image plasma emissions. I purchased a part from Princeton Instruments that enabled us to attach an imaging camera lens to the ICCD camera housing. The part needed to be modified to be attached to the camera housing.

The ICCD model number was Princeton Instruments ICCD-576G/RBE, and had several components associated with its operation. A function-timing generator was able to adjust the delay and width of the gate pulse to the camera, and a power supply amplified this pulse to 200 V. The power supply also supplied the voltage on the multi-channel plate in the camera. A gain adjustment controlled this voltage with adjustments available from 0-100 A.U.. The camera had two settings; the gate setting from the external timing box and a internal trigger controlled by the camera imaging software.

The ICCD camera had to be cooled to obtain low noise counts and good image quality. The camera was cooled with an ice bath or a Neslab Coolflow CFT-33 refrigerated recirculator chiller. This chiller did not keep the camera as cool as the ice bath, but the temperature was much more stable. Because of the cooling involved the camera was susceptible to condensation on the multi-channel plate. Condensation combined with the voltages involved with the multi-channel plate will destroy the camera. Thus dry nitrogen flushing was essential to the camera's operation.

The camera had a frame grabber and controlling card/program that controlled the camera called WinSpec. The internal trigger could be specified on this program to allow untriggered snapshots from the camera for alignment. WinSpec enabled the camera to be triggered by an external trigger, before a shot was taken. The image could be manipulated and saved from the program.

I did not use the triggering source from the BNC box to trigger the ICCD camera because noise on the order of 1 microsecond would not be sufficient for studying the laser-produced plasmas. I instead used a photodiode that picked off a part of the YOGA beam through a dielectric mirror early in the YOGA beam's evolution. This produced a 16±1 ns delay between the triggering of the ICCD camera and when the picture was actually taken after the Laser target interaction. This delay was sufficient, because no measurement of the laser-produced plasma earlier than 16 ns would be made due to the intense YOGA laser light and plasma light existing at that time. Also the physics of the plasma evolution at that time was not important to the experiment.

ICCD cameras are very sensitive to laser light and intense light sources in general. Great caution was taken to not burn out the camera. The camera can become permanently damaged if it is exposed to twice the saturation intensity. I put three BG-39 and BG-18 filters before the camera to block out the YOGA laser light. The Camera is not very sensitive to 1 micron light anyway, but I wanted to take all the precautions necessary to protect the camera.

When measuring an unfamiliar plasma state, special incremental attenuation measures were used to determine the proper exposure. The attenuation tools used were the camera lens iris, and the camera gain to measure the interaction with high attenuation and slowly lessening the attenuation until the interaction was observed with low intensity levels. The intensity approximately doubled with every gain setting change of 5 A.U.. The intensity increased by approximately 1.3 times with every f number stetting increase with the camera lens iris.

The ICCD camera had a rectangular chip that could be oriented to the experiment by choosing the side of the camera to mount. The lens on the ICCD camera could be focused like a standard camera. I placed an extender between the camera and the lens to change the magnification of the image.

I focused the camera by putting the camera into shutter mode where the WinSpec program controlled the shutter. The standard imaging exposure was 1 ms, iris setting f22 and a gain of 10. I used background light or flashlight light. The 60 Hz lighting in the room may have made the illumination on the camera unreliable.

The ICCD camera was the most descriptive data measuring device in the experiment. As will be shown, the ICCD camera gave valuable spatial information of the expanding plasma. The camera was able to give fine details that are too faint to be seen with interferometry, and they gave adequate timing resolution. The ICCD camera measured plasma emission over a broad range of frequencies from 350 nm to 575 nm due to the filters placed before the camera. As discussed in section 3.3.2 the plasma emission gives some information of the density distribution of the plasma, which is a useful tool in characterizing the laser-produced plasma.

4.3.9 Other Diagnostics

I used a DET 210 photodiode to measure the timing between the laser pulse and the probe pulse. The DET 210 photodiode has modest spectral capabilities at 1064 nm, but has a fast 1.0 ns rise time. I picked off beams from both lasers through mirrors to direct onto the photodiode. I used an appropriate amount of ND filters to adjust the intensity of both beams so that they could both be detectable. The calculated timing difference from geometrical calculations between the interaction of the beams at the photodiode and the interaction of the beams in the chamber was -7.0×10^{-10} sec, which is small enough to be ignored.

I used this photodiode to measure the energy of the YOGA laser for each high energy YOGA shot used in the experiment. The beam from the YOGA laser was adjusted using ND filters to be less than 50 mV so the photo diodes response would be linear. This required that the cable to the oscilloscope be shielded. The probe pulse was less intense than the YOGA laser pulse so the YOGA pulse could be used as a trigger on the oscilloscope. For the calibration techniques see appendix E.1.

I optically measured the laser-produced plasma with shadowography, which is an unmodified image of the laser pulse going through the plasma (see figure 4.17). This gave information of the opacity of the plasma at the laser wavelength. I also measured the laser-produced plasma with Faraday rotation by sending a polarized beam through the plasma and having a crossed polarizer blocking out the light as it comes out of the plasma onto the camera. If the laser plasma altered the polarization of the probe beam the altered beam would pass through the polarizer onto the camera. I measured no signal from the plasmas measured this way. The angle change for Faraday rotation is $\theta = 2.63 \times 10^{-17} \lambda^2 n_e B \ell$ rad in cgs [87]. For parameters best hoped for in this experiment $n_e = 10^{18}\ cm^{-3}$, $B = 10^4$ G, and $\ell = 1.0$ cm then $\theta = 7.4 \times 10^{-4}$ rad which is very small. These numbers are also best estimates because B must be parallel to the probe beam propagation, and the plasma at high densities expels the magnetic field early in the expansion.

4.3.10 Timing the Experiment

I used the same set up for timing as in section 2.6 except that I controlled the lamps and the q-switch of the Quantel laser with the SRS box. The timing logic diagram for the experiment is illustrated in figure 4.13. To make timing scans with the probe beam I adjusted the Quantel lamp channel on the

SRS box. Calibration of this adjustment was facilitated by the photodiode. To see a typical timing chart refer to appendix E.7.

4.4 Data from the Laser-Produced Plasma Experiment

An exhaustive amount of data was taken of laser-produced plasmas with Schlieren, interferometry, and ICCD photography. A range of parameters were used to give a template of laser-produced plasma possibilities. This section describes the data taken of laser-produced plasma in detail.

4.4.1 Schlieren Data

Schlieren imaging was used from the beginning of the experiment, and the literature discussing Schlieren imaging with laser-produced plasmas always viewed images of laser-produced plasma early in time. The first Schlieren images on both the Thor experiment (see figure B.4 in appendix B) and the YOGA experiment consisted of irradiating relatively thick wires. I used 25 μm thick wire in the YOGA experiment with the same magnetic field. There were slight differences with and without magnetic fields which I later discovered were due to differences of background pressure (see figure B.8 in appendix B). For these first experiments the magnet from a Faraday rotator was used. This magnet outgassed and had many virtual leaks. This caused the background pressure to be about 50 mTorr greater than the nonmagnetic field case. The amount of mass that the background pressure would have at 20 mTorr was comparable to the mass of the expanded laser-produced plasma under these conditions. I calculated that the mass of a background pressure of 1 mTorr would be sufficiently less than the laser-produced plasma. This calculation is detailed later in section 4.4.3. The rest of the experiments to used a diffusion

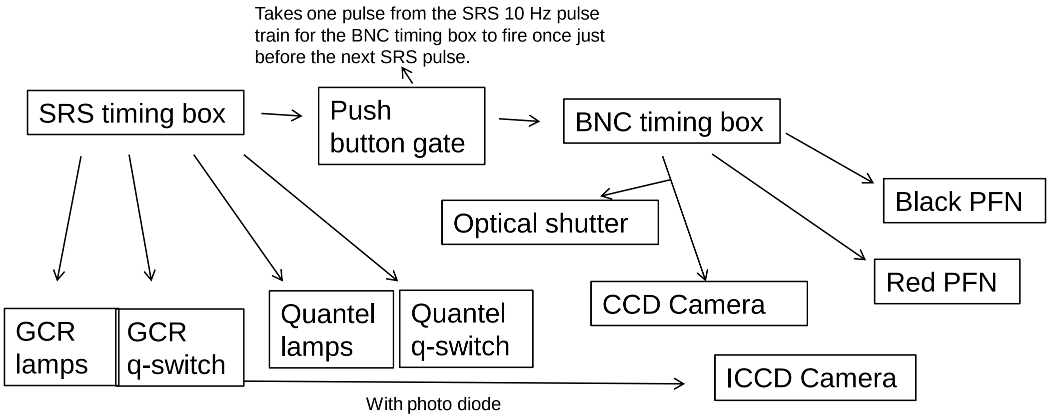

Figure 4.13: Timing logic diagram of the experiment.

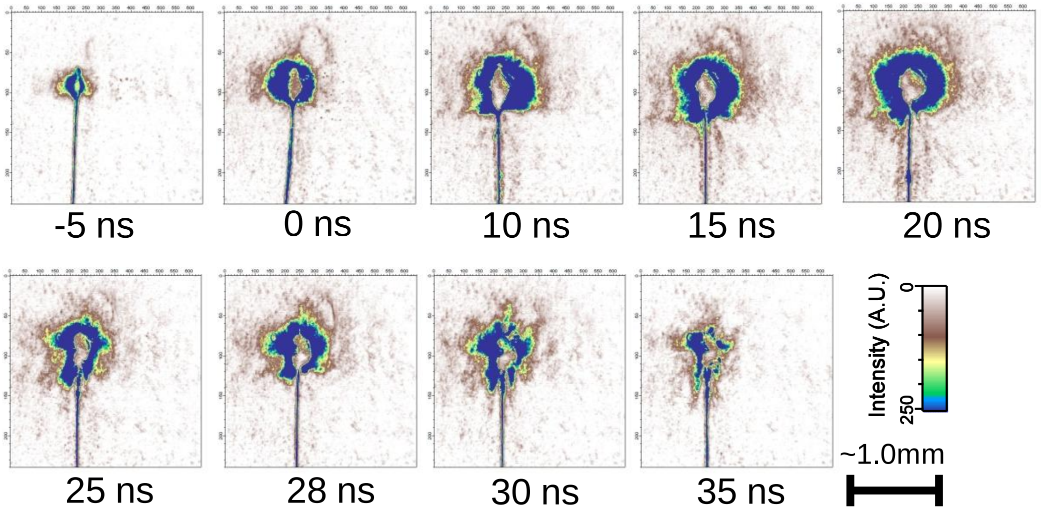

Figure 4.14: Schlieren run at early times using a 3.7 J pulse and 25 μm copper wire with no magnetic field. The laser is coming in from the left.

pump. This allowed the use of a consistent 1.0 mTorr pressure setting for both the magnetic field and the nonmagnetic field case.

I took an exhaustive amount of data with the new magnet and consistent 1.0 mTorr background pressure looking for quantitative differences with and without magnetic fields. A sample of these data are in figures 4.14,4.15 and 4.16. I used a 25 micron copper wire and 4 Joules of laser energy to produce the laser-produced plasma. A 0.012" copper wire was used as the Schlieren beam block.

There are many distinct spatial patterns that form in these images. In the first 40 ns there is a uniform spherical expansion that expands to a certain radius. In most of these images including these earlier times there was a central area of opacity. These opacity areas are confirmed to be opaque by using shadowography (see figure 4.17). There are several possible reasons for this opacity. First the plasma could reach a critical density where the plasma frequency is the laser probe frequency. For a 532 nm probe beam the critical density is $3.94 \times 10^{21}\ cm^{-3}$. This is a reasonable density to achieve at the early stages of expansion. This is unlikely for all cases because this opaque region exists for a very long duration. Another possible source is that the copper had a resonance at the probe laser's frequency of 532 nm. For longer times when the plasma is not very hot and could in fact be just copper gas, the light could be too highly deflected if the gas was acting as a spherical lens. The angular deflection of a spherical lens can be derived to give $\alpha = -2sin^{-1}(\frac{y}{R}) + 2sin^{-1}(\frac{n_0 y}{n_i R})$ where R is the radius of the sphere, n_i is the index of refraction of the gas and y is the axial distance of the beam away from the central part of the sphere. If R=1.0 mm, y=0.5 mm and n_i=1.01 then α=-.01 rad. For a 2" lens and a 1 m beam path the maximal angular

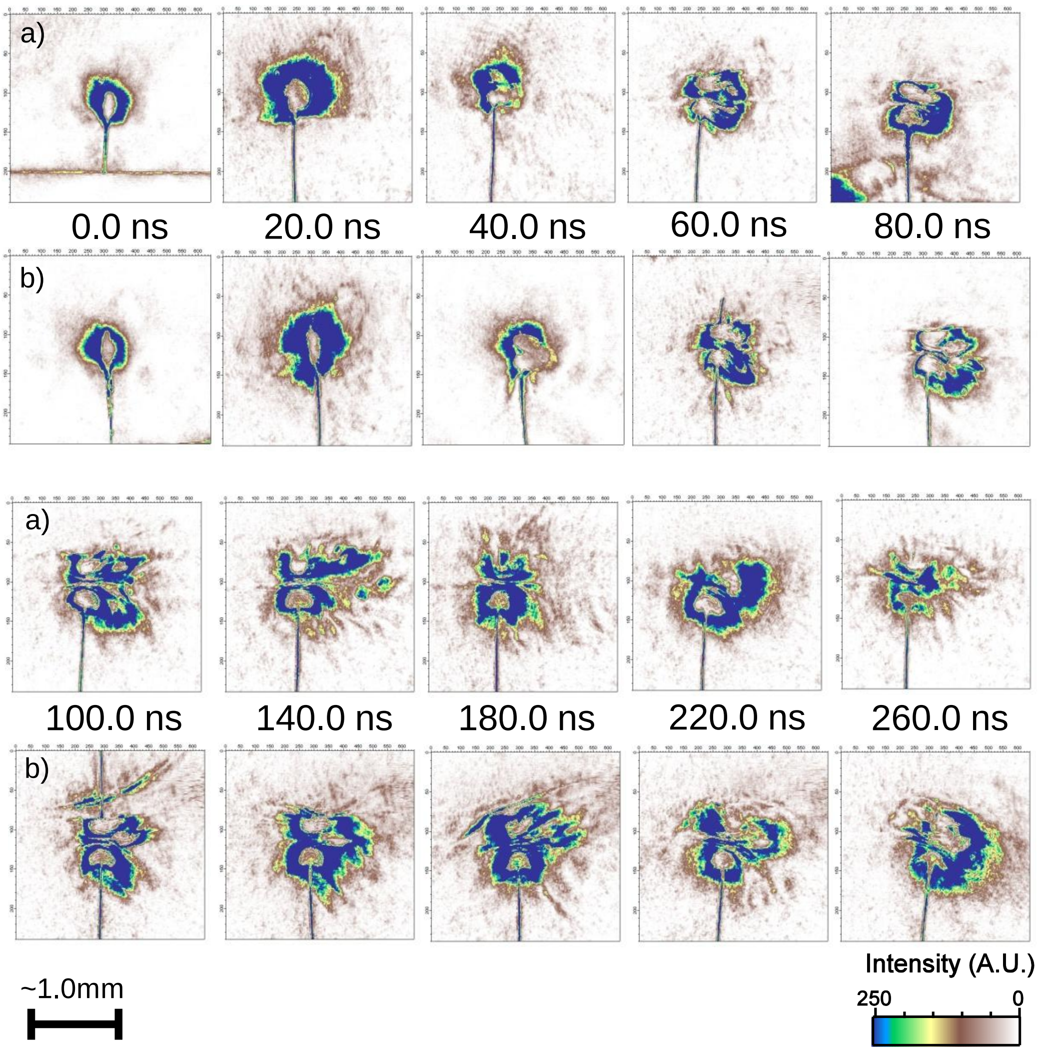

Figure 4.15: Schlieren images of laser produced plasma progression where the input laser energy is ~3.7 J and the target is ~25 μm thick Cu wire. a) is without B fields and without an enclosure and b) is with ~.85 T enclosed B fields.

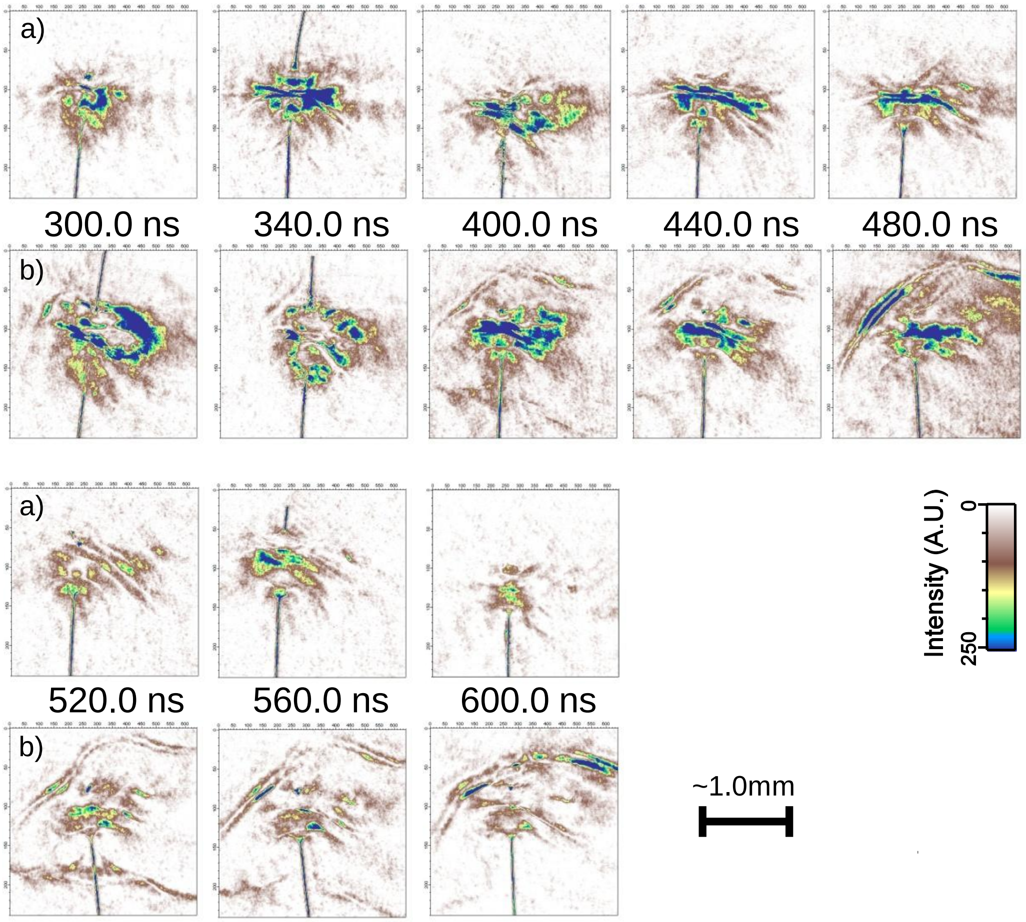

Figure 4.16: Schlieren images of laser produced plasma progression where the input laser energy is ∼3.7 J and the target is ∼25 μm thick Cu wire. a) is without B fields and without an enclosure and b) is with ∼.85 T enclosed B fields.

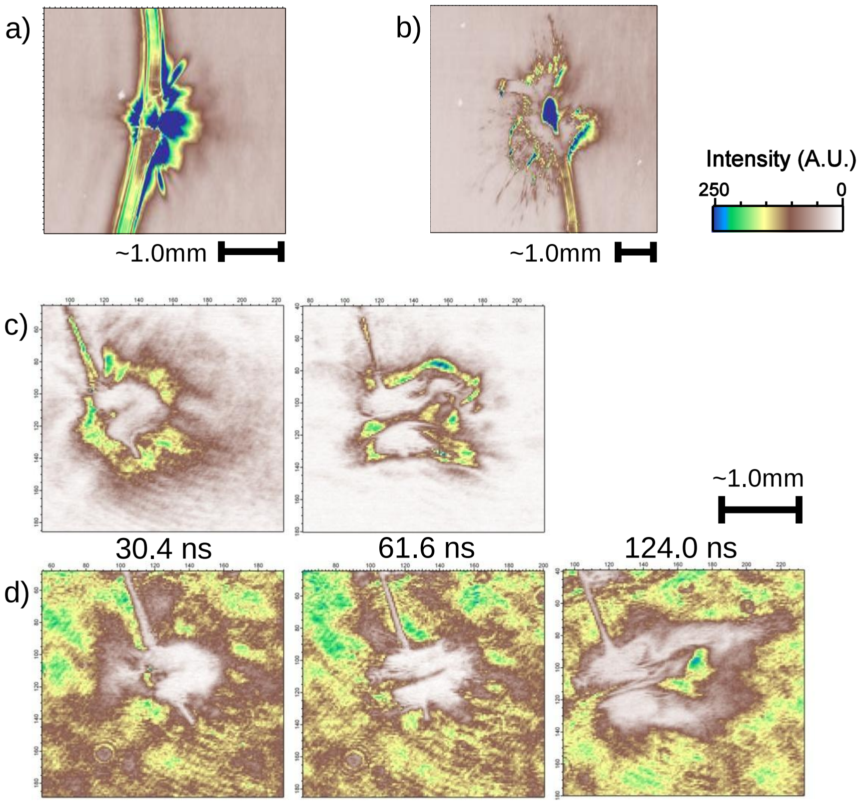

Figure 4.17: Schlieren images from the Thor experiment a) in a week $\sim$0.1 T magnetic field, 40 ns, and laser energy is .69 J, b) without fields, 200 ns and laser energy is .69 J. Schlieren images c) and shadowography images d) of laser produced plasma with energy $\sim$4.0 J.

deflection allowed is $\theta = \frac{2.54}{100} = .025$ rad. This is certainly comparable if the gas can have a index of refraction of 1.01.

Other features include a expanding ball that lasts for 40 ns shrinks back down to a small size and after 40 nanoseconds expands slowly again for the remainder the shots as in figure 4.14. A double spherical expansion seems to be forming above and below the point where the laser ablated the wire. This is most likely due to the fact that the laser focus has a hot spot in the middle and a low intensity halo around the hot spot about 330 μm wide as in figure 4.18. Thus the laser would ablate the center of its target on the wire with high intensities. This would cause this portion of the wire to expand at high velocities. The portions in the halo will be irradiated at low intensities, and will expand slowly with a much lower temperature expansion. This would explain the two lobes observed above and below the laser-target interaction. The rest the expanding plasma was therefore a very low temperature plasma. This is confirmed by the interferometry that will be discussed later. There was a positive fringe shift during these times. This indicated that the expansion was not due to a highly ionized plasma.

To quantify the differences with and without the magnetic field I measured the thickness of the Schlieren feature in the images at a specified intensity threshold at the point where the laser ablated the wire. The results of this measurement are in figure 4.19. I measured both the vertical expansion and the horizontal expansion. There was no significant quantitative differences with or without magnetic fields with these Schlieren measurements. The reason that significant differences with or without magnetic fields were not observed in these images is most likely due to the fact that the plasma measured in not a high temperature plasma beyond 40 ns in the images. It would be the high

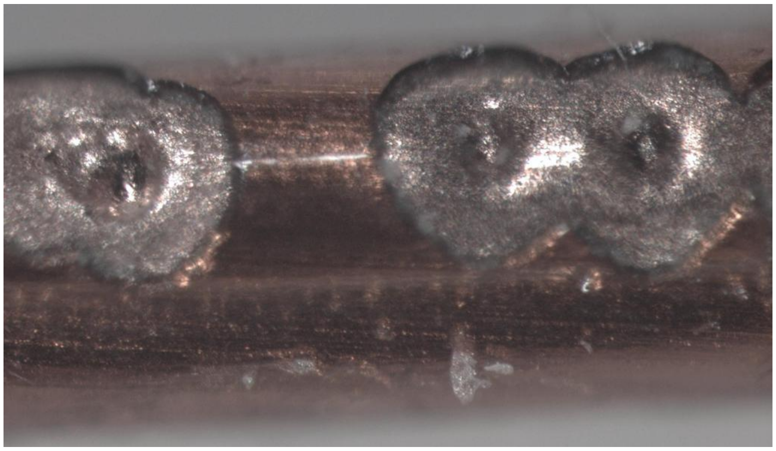

Figure 4.18: Image of 200 mJ laser focused shots on an insulated Cu wire. The focus exhibits a halo around the the intense region of the focus. The wire diameter is .066 cm and the halo is ∼330 μm.

temperature plasma that would interact with the magnetic field. Before 40 ns, where there is high temperature plasma measured, the pressures in the plasma are much greater than the magnetic field pressure. Thus it is unexpected to measure the difference with or without the magnetic field before 40 ns, and the observed plasma is too low in temperature after 40 ns to measure any difference with and without a magnetic field.

4.4.2 Interferometry Data

I took the majority of the Interferometric data of laser-produced plasmas from 25 μm Cu wire ablated with 3.7 J laser pulses. The interferometric data was much more sensitive than the Schlieren data. Interferometry also gave information about the fringe shift in the plasma. For instance the plasma would give a negative fringe shift and a nonionized dense gas would give a positive fringe shift (see figure 4.20).

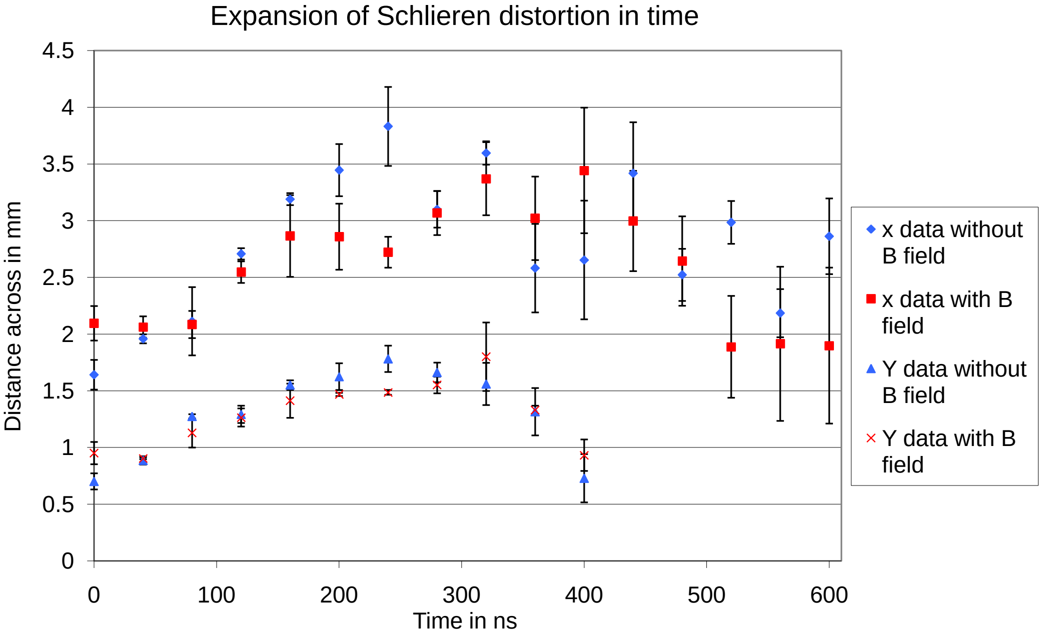

Figure 4.19: I measured the width of the laser-produced plasma in both the x and the y directions as detected using Schlieren imaging.

I performed several experiments using interferometry looking at laser-produced plasmas with and without magnetic fields. The temporal limits of these measurements from 0.0 to ∼500.0 ns for these plasmas. The laser-plasma was measured along with the laser-plasma interaction with the surrounding enclosures of the experiment. The widest field of view possible was used and with this view different areas of the interaction were measured.

Dr. Will Grigsby and Dr. Gilliss Dyer created a program to use in Igor that unwrapped the interferometry data we obtained [47][29]. When one obtains Interferometric data one must unwrap the interferogram to get fringe information from the image. This process included performing a fourier transform filter to create an idealized version of the interferogram. This eliminated

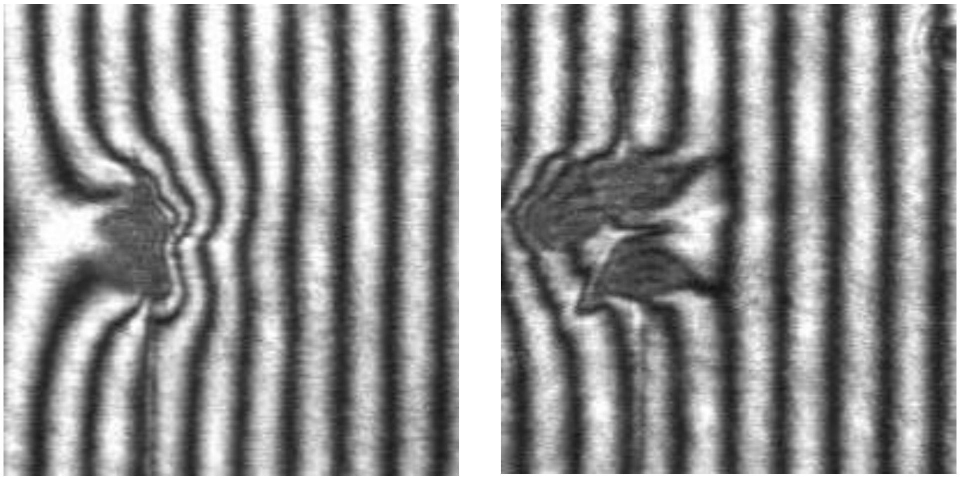

20 ns

140 ns

Figure 4.20: Raw interferograms showing negative (left) fringe shift at early times and positive (right) fringe shift at later times.

much of the noise in the system. According to this program the specifications of this filtering could be chosen. Once the image was filtered the phase could be unwrapped using algorithms involving fourier transforms. The program had six different unwrapping algorithms to choose from. I found that the Flynn unwrapping algorithm worked the best for our measurements. This algorithm was able to circumvent poles created by missing fringe shift information. From this process I obtained an image of fringe shift over the spatial area of the interferogram.

With the fringe shift information I could obtain useful information from the data. If the basic geometry of the plasma was assumed the densities can be calculated using the formulation in section 3.3.1. For probing frequencies

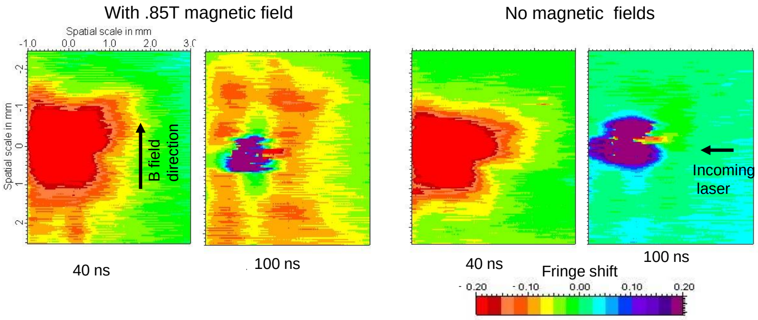

Figure 4.21: When measure the fringe shift of an interferogram of laser-produced plasma. I compare the fringe shift of a laser-produced plasma with and without magnetic fields.

of $\lambda = 532nm$ equation 3.47 becomes

$$N = -2.38 \times 10^{-18}\ cm^2 \int n_e dl \tag{4.12}$$

where N is the fringe shift, n_e is the electron density, and the integral is a line integral along the probe axis. If the plasma is assumed to be spherical with radius R and having a constant density the density will be given by

$$n_e = \frac{N}{-4.76 \times 10^{-18} R} \tag{4.13}$$

where N is the fringe shift observed in the center of the sphere. In the processed data I could measure fringe shifts reliably down to 1/20th of a fringe shift as in figure 4.21. With the above equation densities down to $10^{16}\ cm^{-3}$ can be measured for the most sensitive measurements.

The presence of sufficiently dense plasma gives a negative fringe shift, as shown by the interferograms in figure 4.21, taken 40 ns and 100 ns after the laser-plasma interaction. The magnetic field confines the plasma to a measurable density at 100 ns. No measurable plasma is detected without a

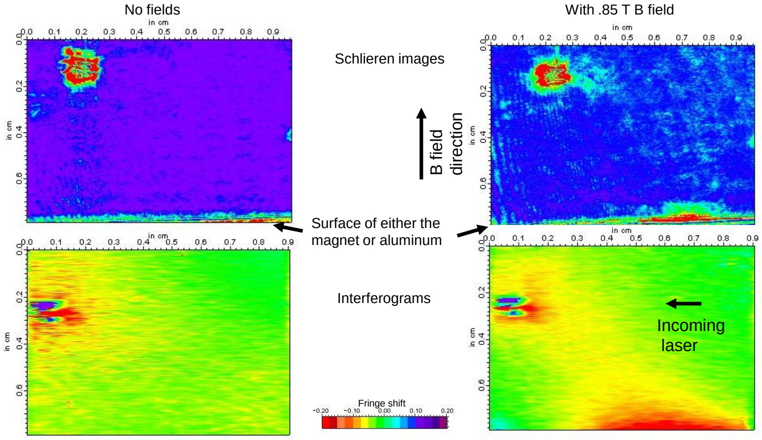

Figure 4.22: Interferograms and Schlieren images of irradiated copper wire show differences with and without magnetic fields at 100ns.

magnetic field. I calculate that the plasma density at 100 ns is on the order of $10^{16} - 10^{17}$ part/cm^3 when a magnetic field is applied. The laser-produced plasma also experienced axial lengthening in the direction along the magnetic field, which would be expected in magnetic field confinement.

I found differences between with and without magnetic fields, but these differences were very slight as in figures 4.21, 4.24,and 4.22. I found that the plasma was more visible with the magnetic field at 100 ns than without a magnetic field as in figure 4.21. The majority of the differences observed were in the interaction of the laser-produced plasma with the magnetic enclosure as in figures 4.22, 4.25, and 4.26. This interaction was comparable to the ICCD camera images in section 4.4.3. To view what the magnetic field values are in these interactions I have overlayed the measured magnetic field values over the fringe shift image in figure 4.23

I was not able to see significant differences between these two cases

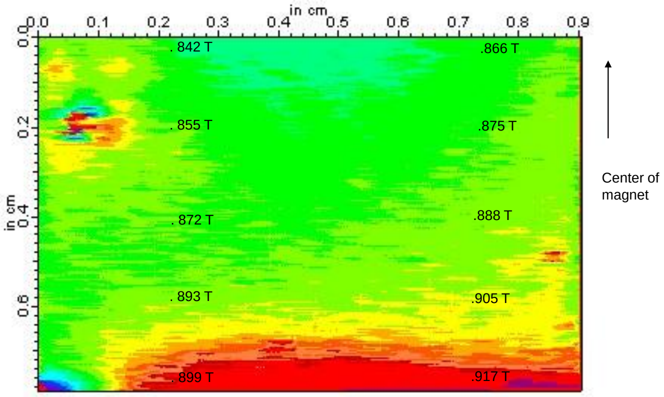

Figure 4.23: I measure the magnetic field of the magnet using a hall probe. In this figure we overlay the magnetic field with the interferometric data from figure 4.22.

enough to gain any understanding of the physics of magnetic fields acting on plasmas. But these data do give information about the densities of the plasma of the early stages of the evolution. It also showed that the fringe shifts from negative to positive as the plasma increases. This positive fringe shift can be caused by several factors. One, the entire field of view could be filled with a uniform hot plasma that upon subtraction will cause this colder plasma to have a positive fringe shift. This is unlikely out to the times the data was taken of 400 ns and beyond. From the ICCD camera data the plasma dissipates quickly at these times, especially without a magnetic field. If the copper has a resonance absorption at 532nm the index can also shift positive. If the expanding copper is a hot, but unionized gas the amount of index of refraction change to induce one fringe shift at a 532 nm probing frequency through 0.1 cm of material is $n - 1 = 5.32 \times 10^{-4}$. This is not an unreasonable number for a hot dense copper gas expanding from the wire. This helps explain the data taken with the Schlieren imaging system. In the Schlieren images the plasma

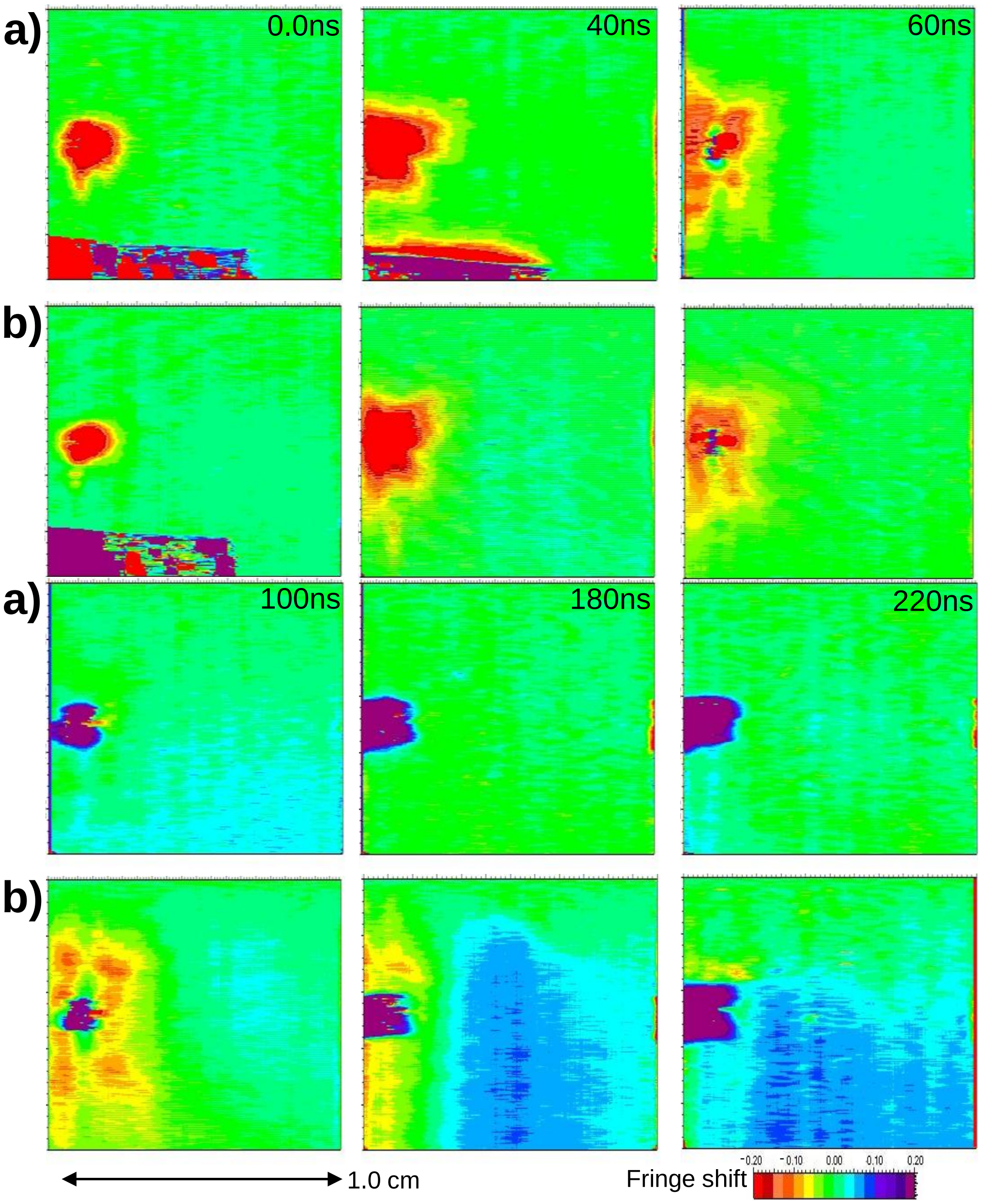

Figure 4.24: Interferometry fringe shift of laser produced plasma progression (Laser energy is ∼3.7 J) from a ∼25 μm Cu wire. The nonmagnetic field case was not enclosed and the wire holder had a wide and thick base. a) without B fields and b) with ∼.85 T enclosed B fields.

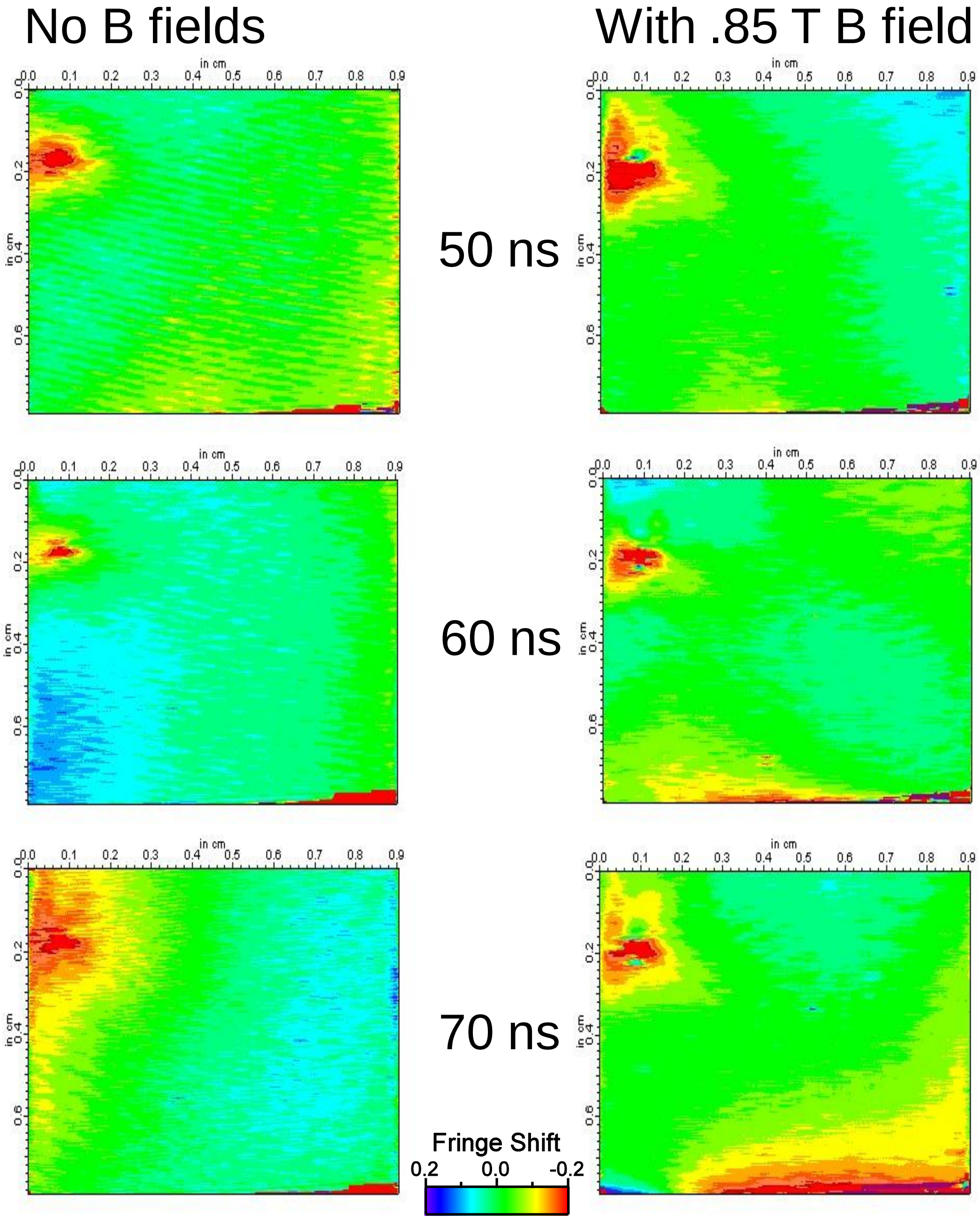

Figure 4.25: Interferometry fringe shift of laser produced plasma progression (Laser energy is ~3.7 J) with ~25 μm Cu wire. The wire holder is thin and the both cases have the same geometry in figure 4.22.

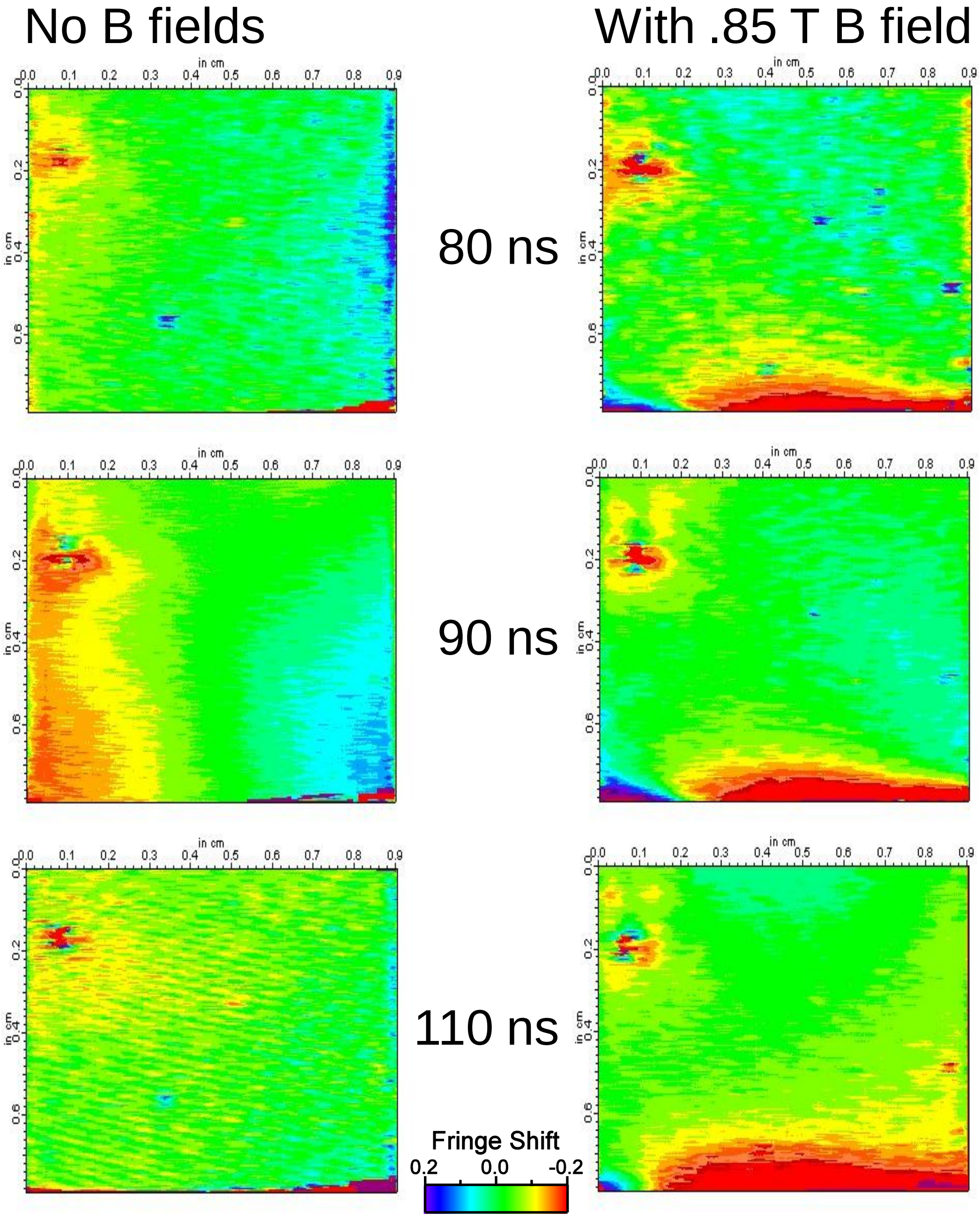

Figure 4.26: Interferometry fringe shift image of laser produced plasma progression where the input laser energy is ~3.7 J and the target is ~25 μm thick Cu wire.

increased in size quickly in the beginning of the expansion and then quickly decreased after about 40 ns. The interferometry then shows that there was a hot plasma expansion to begin with and then hot copper gas began to expand away from the interaction. So the majority of the shots taken of the copper with the Schlieren imaging were most likely hot copper gas.

Unfortunately I did not take any interferometric measurements with aluminum as a target. There are sharp features in the ICCD camera when the aluminum target was used in the magnetic fields. I did have Schlieren images of aluminum plasma in a magnetic field which showed telltale signs of a plasma boundary stopped by the magnetic field as in figure 4.27. There are many lines indicative of a plasma boundary in these Schlieren images. They are about the same size of the plasma expansion measured with the ICCD camera, although the energies are too different to give a good comparison. This would be an interesting subject of study for future investigators.

4.4.3 ICCD Camera Data

The ICCD camera gave much more detailed images as to how the laser-produced plasma was reacting to the magnetic field. The plasma emission from the laser-produced plasma produced enough information to show that the magnetic field was stopping the plasma in the perpendicular direction to the magnetic field. I took several ICCD camera images of laser-produced plasma evolution over various conditions, many more conditions than the Schlieren or interferometry case. In table 4.1 I list all the laser-produced plasma evolutions that were taken with their various conditions.

The first ICCD images of laser-produced plasma were from a run testing out the ICCD camera, with a thick Al wire as a target in a magnetic field. If

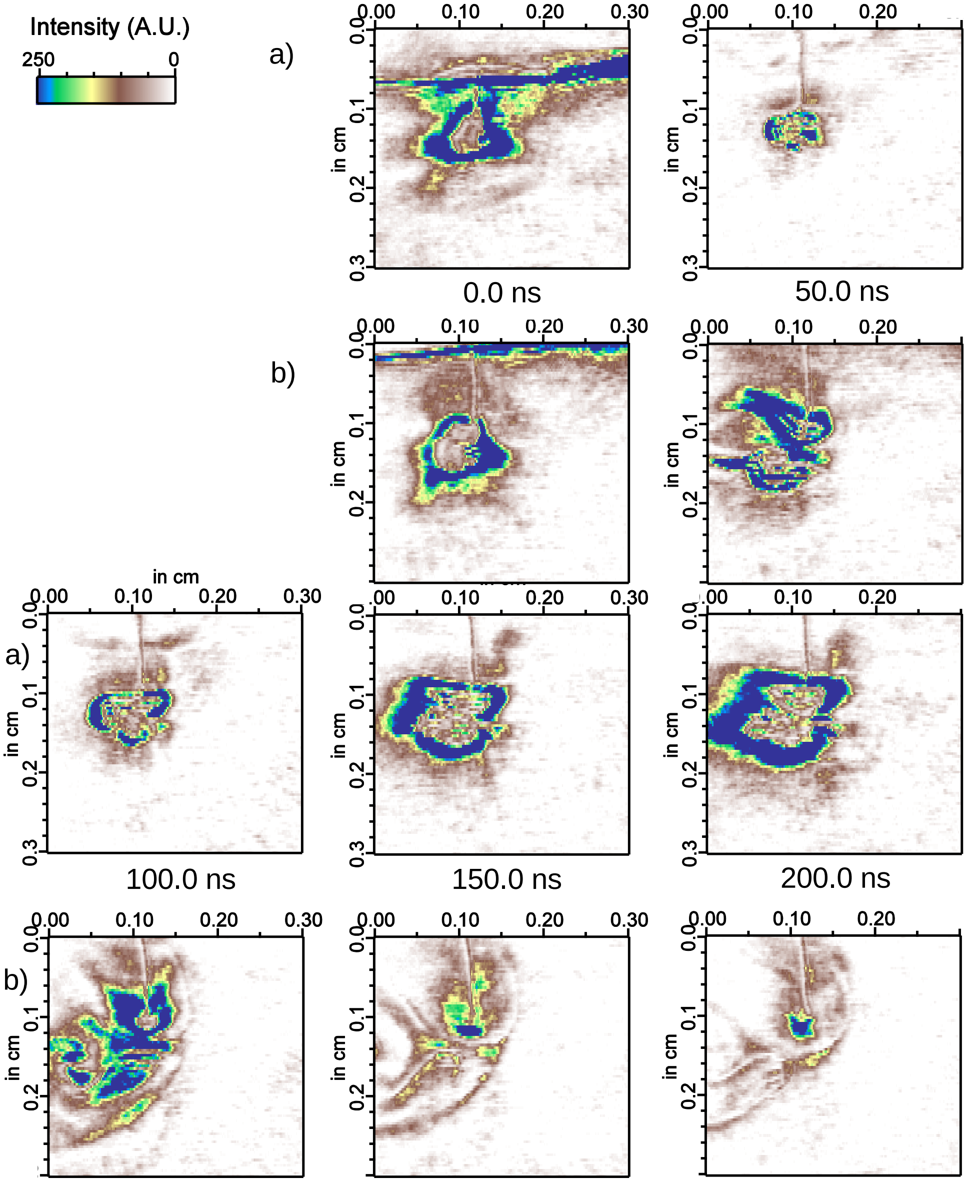

Figure 4.27: Schlieren images of laser produced plasma progression where the input laser energy is ∼3.7 J comparing copper (a) and aluminum (b) in the presence of a .85 T magnetic field. Due to an experimental error the copper times need 20 ns added to them.

Wire Diam.	Wire Material	B Field	physical condition
~1.0 mm	Al	0.85 T	encl.
~1.0 mm	Al	0.0 T	encl.
~1.0 mm	Cu	0.85 T	encl.
25μm	Al	0.85 T	encl.
~1.0 mm	Cu	0.0 T	encl.
25μm	Al	0.0 T	encl.
25μm	Cu	0.85 T	encl.
25μm	Cu	0.0 T	encl.
25μm	Cu	0.85 T	encl.

Table 4.1: Table of all ICCD measured lpp evolutions and the physical conditions in which they were produced.

the same spot was irradiated on the wire multiple times the spatial profile of the laser-produced plasma changed after each shot. The profile was extremely constant if a new spot on the target was used. I chose the policy of using a clean spot every time a shot was made. From this exercise ICCD gain settings were obtained that were appropriate for image taking.

Subsequent scans showed incredibly repeatable spatial images of the laser-produced plasma. Thus multiple measurements for each condition were not made. I took measurements of the available parameter space to learn about the effects of energy, target size, target material, and magnetic field strength. The reason for the large parameter space was to understand what would be the best material and conditions to use in the jet experiment.

I used four different targets to conduct our general ICCD exploration of laser-produced plasmas. These four targets were copper and aluminum wires with thicknesses 25μm and ~1 mm. I used roughly four different laser pulse energies to create our Laser-produced plasmas. These energies were 20 mJ, 200 mJ, 500 mJ, and 2 J. The use the 2 J setting was used sparingly because of the damage of the glass laser rods. An ablated target is shown in figure 4.28.

Figure 4.28: 1 mm thick Al wire target showing 200 mJ shots on the left, 20 mJ shot in the center and 500 mJ shots on the right.

The ICCD images show various spatial features of the laser-produced plasmas, which were analyzed using imaging software. In analyzing this data the logarithm of the intensity of the images was taken. This enabled the analysis of faint features of the laser-produced plasma as compared with the more intense features. These pictures showed two regions of the laser-produced plasma as shown in figure 4.29. The first region was a faint yet highly energetic spheroid that emanated from the laser-plasma interaction. This spheroid expanded with speeds on the order of 10^7 cm/s. When the spheroid interacted with other objects such as the casing surrounding the target region luminescent ablation occurred. To show that this front is not a shock wave I present images with the intensity greatly enhanced to see faint parts of the evolution in figure 4.31. There is actually a shock front visible in both frames at the same position with and without a magnetic field. A shock wave will be largely unaffected by the magnetic field, but as shown in the figure the plasma front is greatly distorted with a magnetic field present.

The evolution of the spheroid was greatly influenced by the magnetic field as illustrated in figure 4.30. Although its evolution speed did not completely stop from the magnetic field action, it does slow down considerably.

This spheroid in the presence of a magnetic field expanded much more quickly along the direction of the magnetic field lines than it did without the magnetic field. I found this peculiar because the plasma motion in the magnetic field should not accelerate along the field lines, but should flow along the magnetic field lines unimpeded. There are several conditions that might cause this phenomena to occur. In a laser-plasma the electron Larmor is much shorter that the ion Larmor as discussed in section 4.2. This will cause charge separation in the plasma. Because the aluminum surfaces of the magnets are conducting mirror charges up will develop on these surfaces causing the plasma to accelerate toward the surfaces of the magnet.

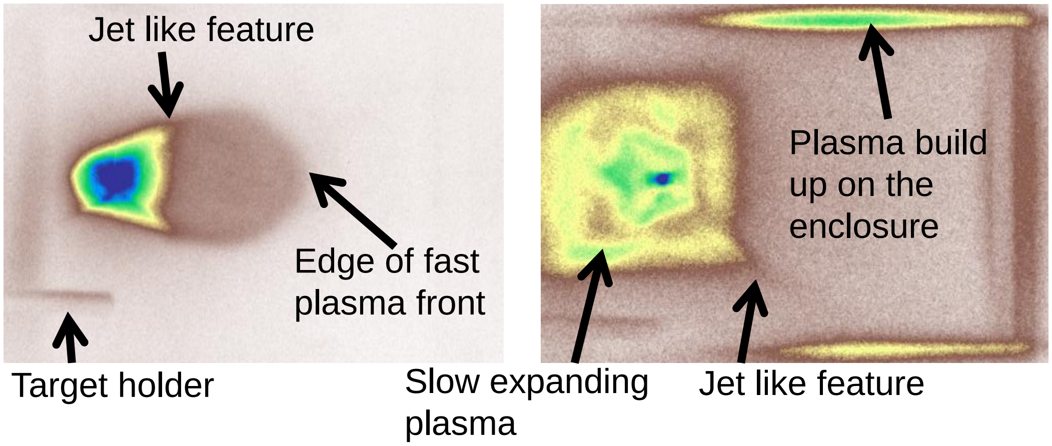

Figure 4.29: General features of a ICCD image of a laser-produced plasma without a magnetic field early in time on the left and last in time on the right.

The second part of the laser-produced plasma is a much more luminescent plasma that progressed with slower speeds. This plasma remained visible for longer durations of time. This part of the plasma also was affected by the magnetic field. This plasma builds up at certain distances from the target. This boundary did not stop completely in time, but the boundary

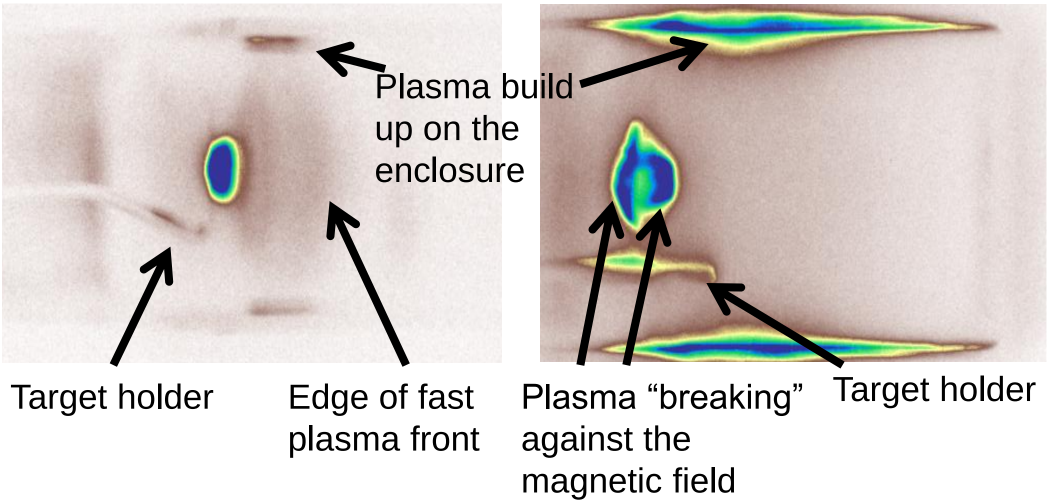

Figure 4.30: General features of a ICCD image of a laser-produced plasma with a .85 T enclosed magnetic field early in time on the left and later in time on the right.

was very sharp and became brighter than the plasma around the target interaction as in figure 4.30. This could be due to what authors have called the re-thermalization of laser-produced plasmas [133]. Sudo et al. has measured the temperature of the plasma increases at the stopping boundary of the magnetic field. This could be happening in our case with the increased temperature showing as increased luminosity. I do not have more sufficient measurements to back this up.

Significant differences were found among all the various conditions measured. In the comparison between aluminum and copper the aluminum showed more buildup against the magnetic field than did copper. The aluminum developed a bright boundary where as the copper developed a less intense boundary as in figures 4.33, 4.35, and 4.37. The high energy spheroid expansion of the copper expanded at roughly the same speeds as the aluminum except the lobe

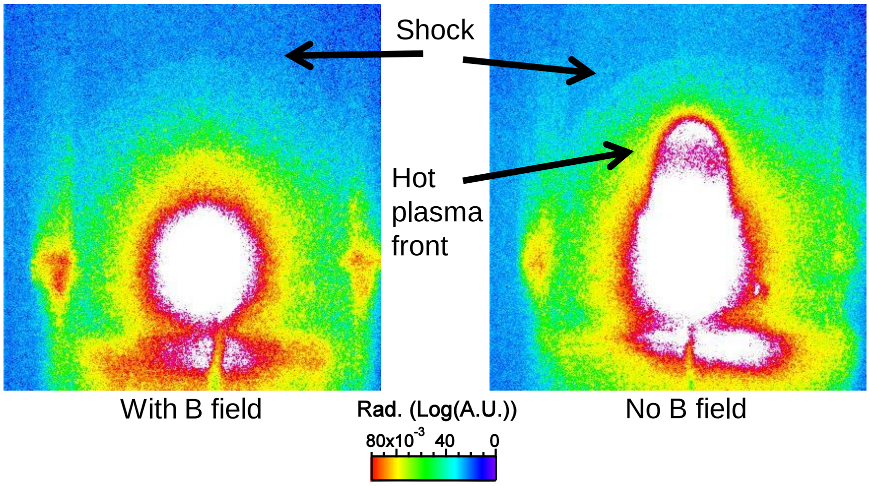

Figure 4.31: The formation of a shock wave with and without magnetic fields as compared with the energetic plasma front.

expansion perpendicular to the laser direction expanded much slower than the aluminum as in figures 4.34,4.39 and 4.36. So the expansion appeared much more cylindrical.

Plasma protrusions formed out of the more dense region along the boundary of the spheroid. This is reminiscent of features seen by Xu et al. [153], and by previously performed Schlieren measurements. Xu describes these features as jets and suggest that they form because they are on the boundary of a hot and cold plasma region. Data from my experiment on the Thor lab demonstrates these features very clearly with Schlieren imaging as in figure 4.17.

I measured differences in the expansion with a 25 μm wire compared with a 1 mm wire. In the 1 mm wire case the plasma flow was unidirectional, and the 25 μm wire case was bi-directional as in figures 4.33, 4.34, and 4.39.

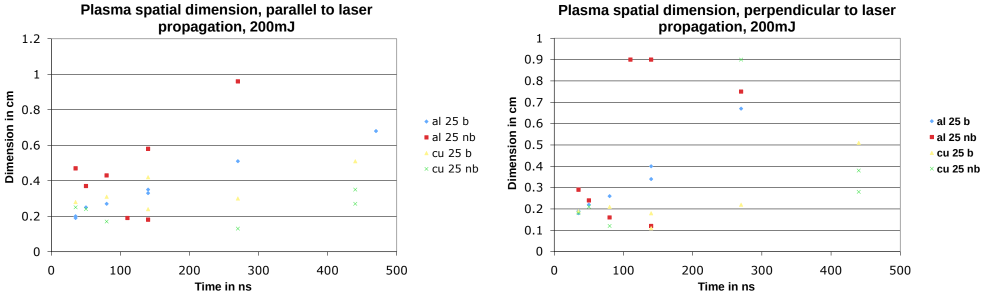

Figure 4.32: The spatial dimension of the laser-produced plasma with and without magnetic field at 200 mJ, using Cu and Al 25 μm wire. Symbols on the graph “al 25 b” mean 25 μm Aluminum wire with B field etc. “nb” means no B field.

The hot plasma also expanded behind the wire. The colder plasma broke against the magnetic field in both directions, both upstream of the drive pulse and downstream of the pulse. This plasma boundary had a downstream radius much larger than the upstream radius when in the presence of the magnetic field. I measured the expansion with and without magnetic fields both along the magnetic field lines and across the magnetic field lines. The expansion was slowed in the magnetic field case as compared with the nonmagnetic field case.

Experiments were performed to look at the effect of the background pressure on the progression of the laser-produced plasma. I performed experiments using a thick copper wire in 10 mTorr , 1.0 mTorr, 0.1 mTorr, and a ∼200 mJ pulse. The ICCD images are shown in figures 4.41 and 4.35. In the 10 mTorr regime there was a luminescence build up along the axis of propagation and in front of the denser portion of the laser-produced plasma with and without magnetic field. This feature is not in the 1.0 mTorr case or the 0.1 mTorr case. In fact there are no measurable differences between the 1.0

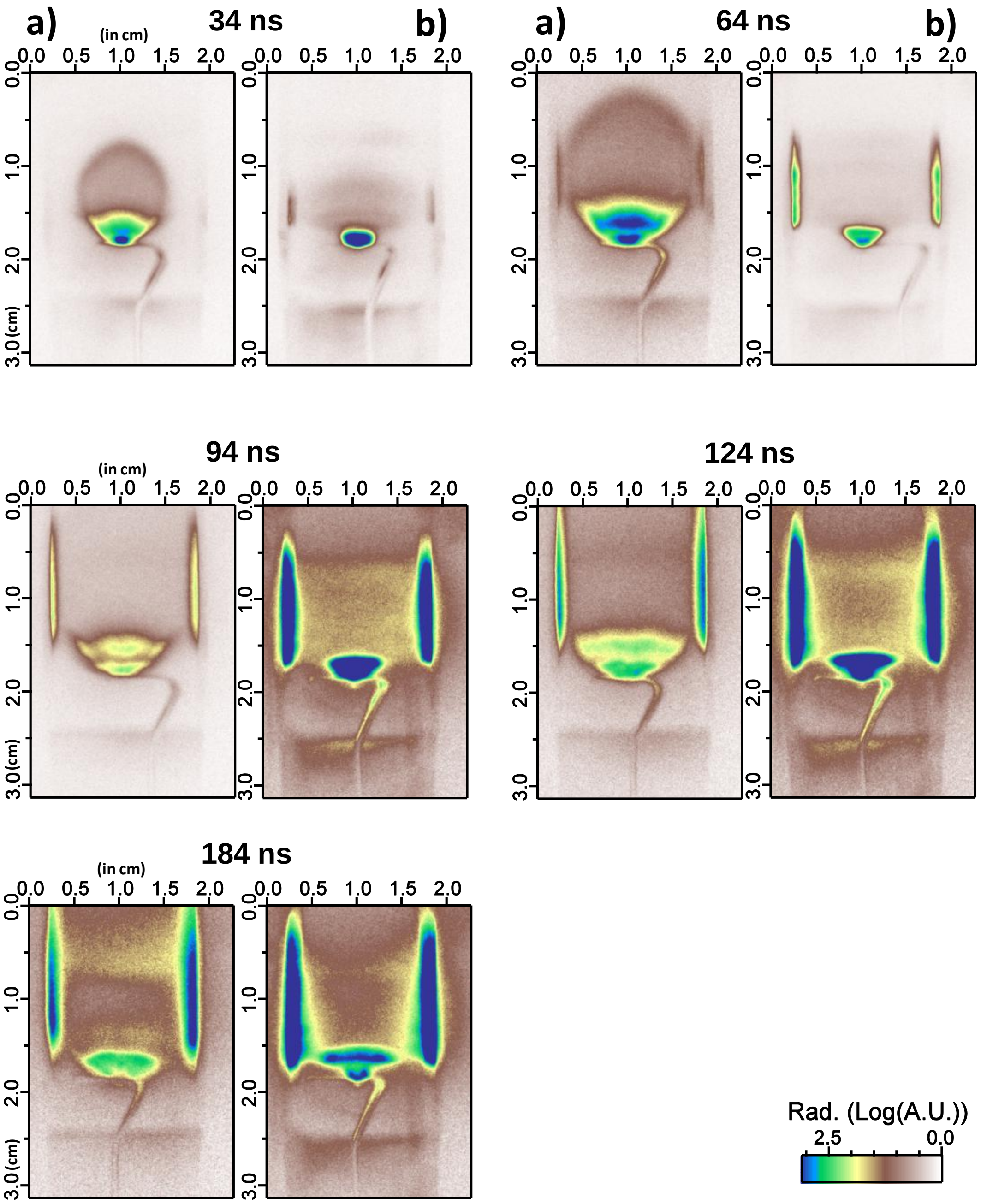

Figure 4.33: ICCD image of laser produced plasma progression where the input laser energy is ∼ 200 mJ and the target is ∼ 1.0 mm thick Al wire. a) is without B fields and b) is with ∼ .85 T enclosed B fields.

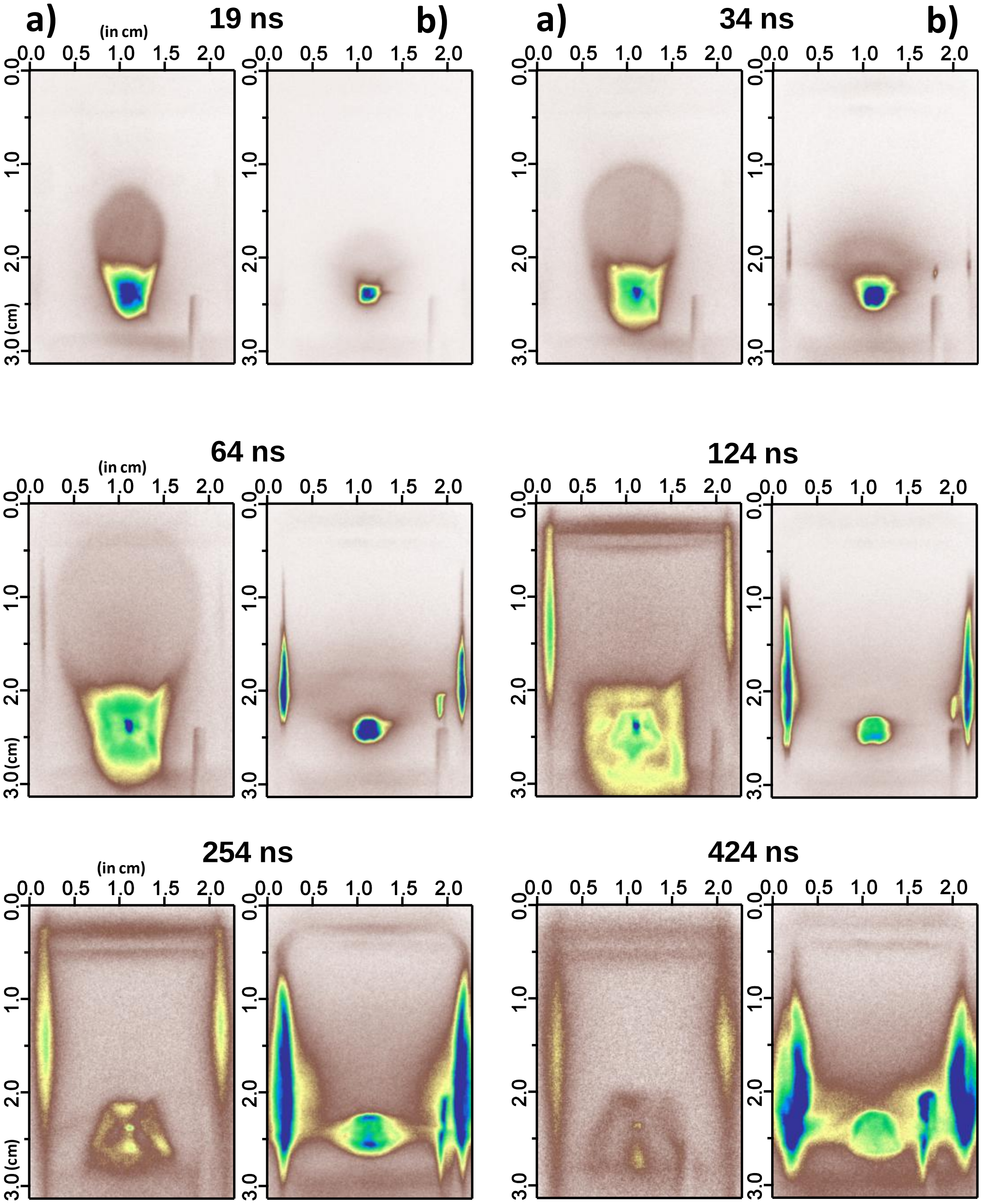

Figure 4.34: ICCD image of laser produced plasma progression where the input laser energy is ∼200 mJ and the target is ∼25 μm thick Al wire. a) is without B fields and b) is with ∼.85 T enclosed B fields.

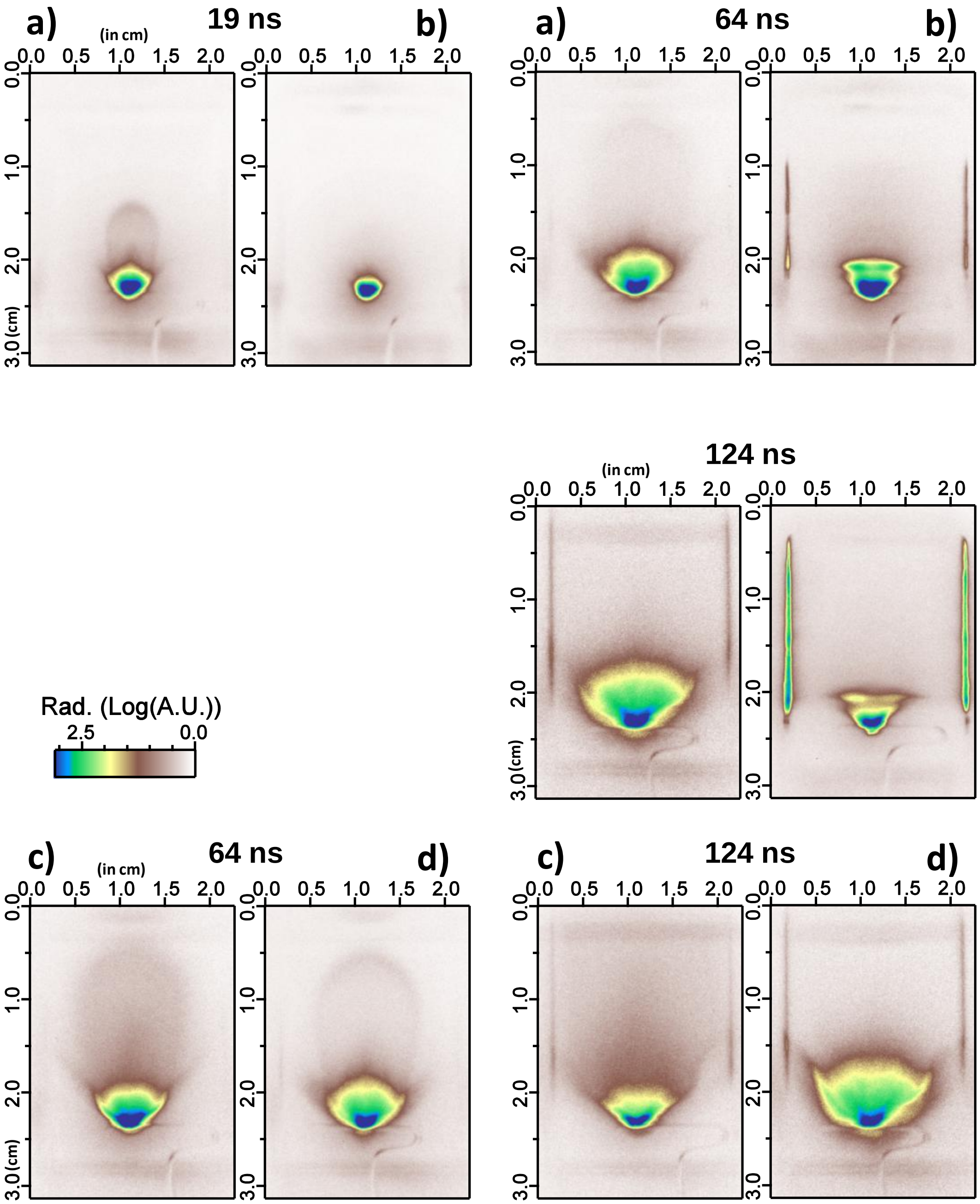

Figure 4.35: ICCD images: Laser energy∼200 mJ, target∼1.0 mm Cu wire. a) without B fields and b) with ∼.85 T enclosed B fields. c) $P_{background} =$ 10 mTorr and d) $P_{background} = 0.1$ mTorr both without B fields).

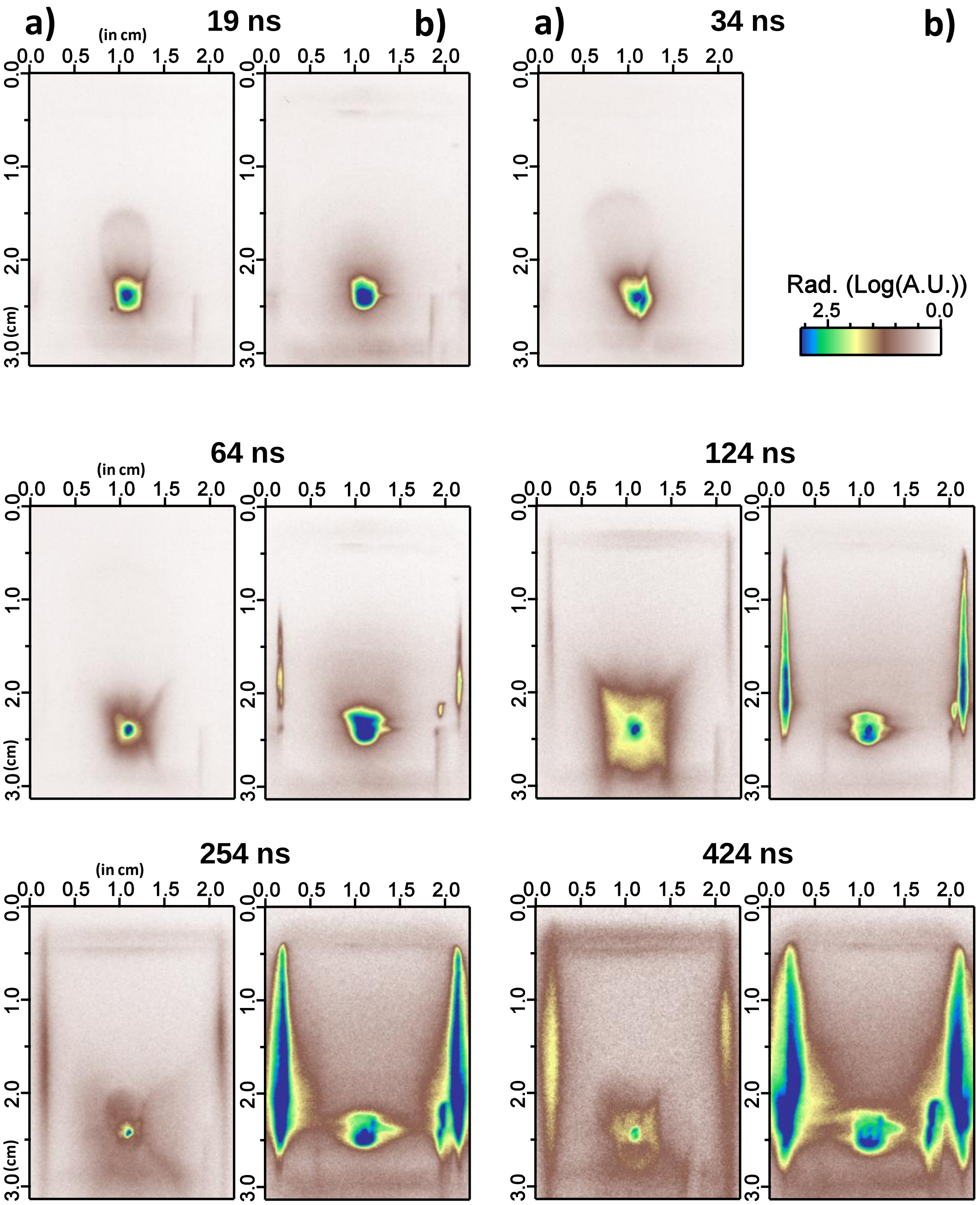

Figure 4.36: ICCD image of laser produced plasma progression where the input laser energy is ∼200 mJ and the target is ∼25 μm thick Cu wire. a) is without B fields and b) is with ∼.85 T enclosed B fields.

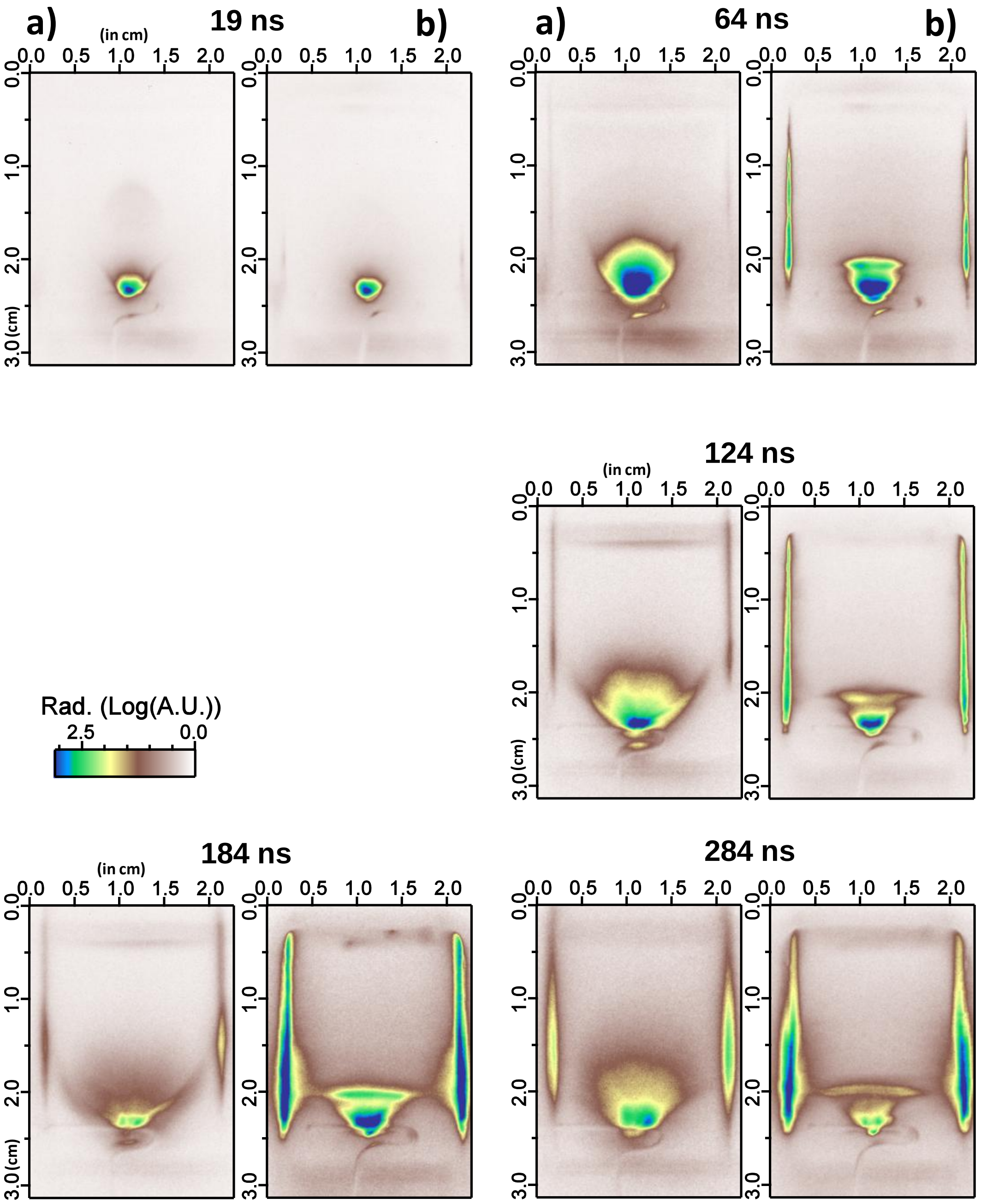

Figure 4.37: ICCD image of laser produced plasma progression where the input laser energy is ∼500 mJ and the target is ∼1.0 mm thick Cu wire. a) is without B fields and b) is with ∼.85 T enclosed B field.

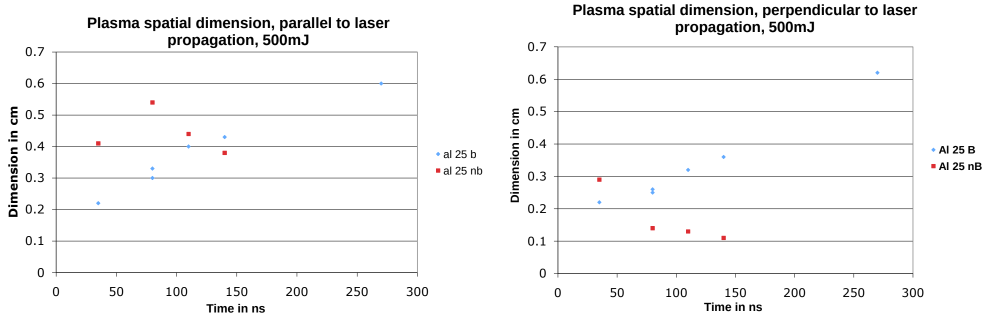

Figure 4.38: The spatial dimension of the laser-produced plasma with and without magnetic field at 500 mJ, using Cu and Al 25 μm wire. Symbols on the graph "al 25 b" mean 25 μm Aluminum wire with B field etc. "nb" means no B field.

mTorr case and the 0.1 mTorr case. This confirms the calculations made that the expanded laser-produced plasma would be comparable to the background gas at pressures above 10.0 mTorr and that at 1.0 mTorr and below the laser-produced plasma would not be at comparable densities with the background gas.

The calculation for determining the minimum background pressure involved the comparing the weight of the background gas with the weight of the metallic plasma. The difference should be more than 10%. Typical measurements from literature of laser-produced plasmas where interesting phenomena occurs between magnetic fields and non magnetic fields was 10^{15} cm^{-3} [133]. Copper has 63.53 amu weight, and aluminum has 26.9 amu whereas N_2 has weight 28.0 amu. Thus copper is the limiting factor and the density will have to be less than 5×10^{13} cm^{-3} to be under 10% mass difference. The density at 1.0 mTorr at STP is 3.2×10^{13} cm^{-3}, which is in the allowable range. At 3.2×10^{14} at 10.0 mTorr there will be more than 10% and may be what caused the differences seen in the ICCD camera images. This is justification for using

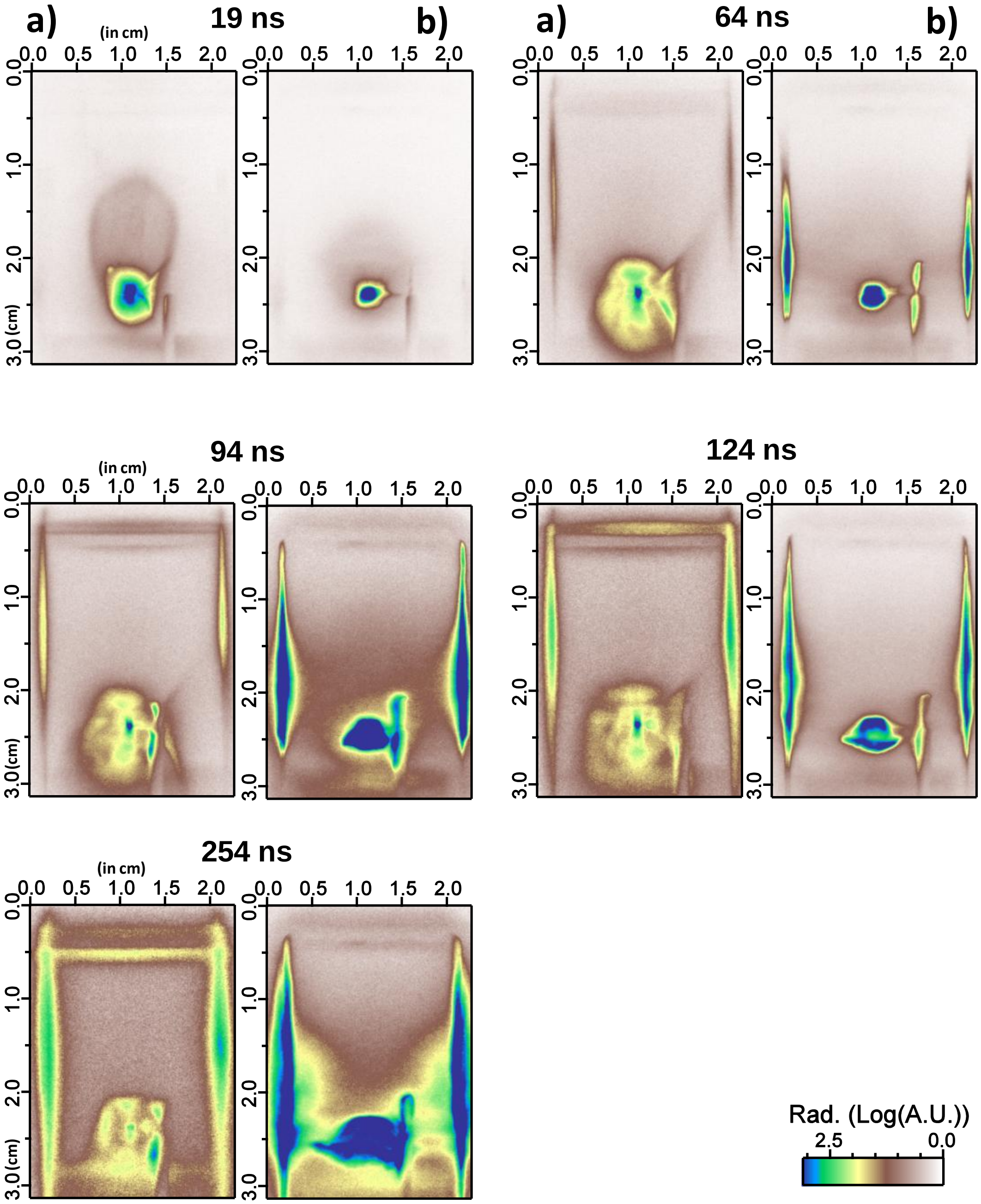

Figure 4.39: ICCD image of laser produced plasma progression where the input laser energy is ∼500 mJ and the target is ∼25 μm thick Al wire. a) is without B fields and b) is with ∼.85 T enclosed B fields.

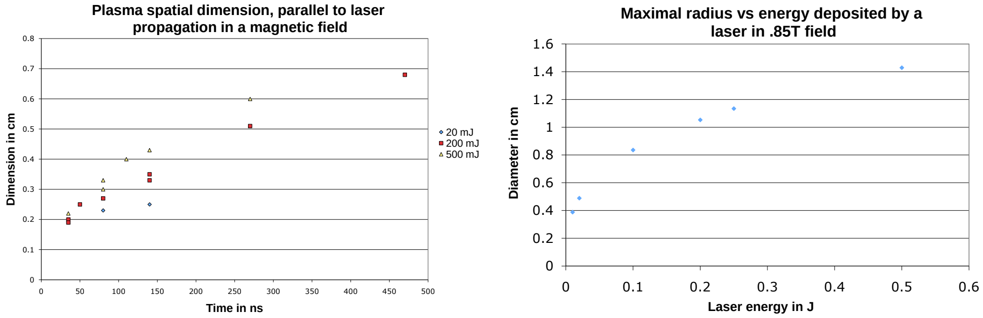

Figure 4.40: The spatial dimension of the laser-produced plasma in a magnetic field and an Al 25 μm wire target compared with the theoretical maximal expansion of a laser produced plasma in a magnetic field.

1.0 mTorr for our laser-produced plasma experiments.

The ICCD data taken are not exactly comparable with the Schlieren and interferometer data that was taken previously because the full energy of the laser was not used. At the time of this data collection the YOGA laser had damage spots on the beam so I used the high-energy mode sparingly. I did take data with 2 J of energy with a 25 μm copper wire to compare with previous results (see figure 4.43). The alignment procedure may not be very accurate for the full energy YOGA beam on this small target. I had very reproducible data for laser energies that did not involve the PFN's, but when the PFN's were used the data became much less defined and less reproducible. This may be because the focus changed positions and shape with the YOGA beam on such a small focus point. The focus may also be variable because of heating fluctuations in the cooling system. This may explain why the Schlieren data had many fluctuations and was not as consistent as the ICCD data taken at low energies. I did not measure the PFN amplified focus directly because of the energies involved.

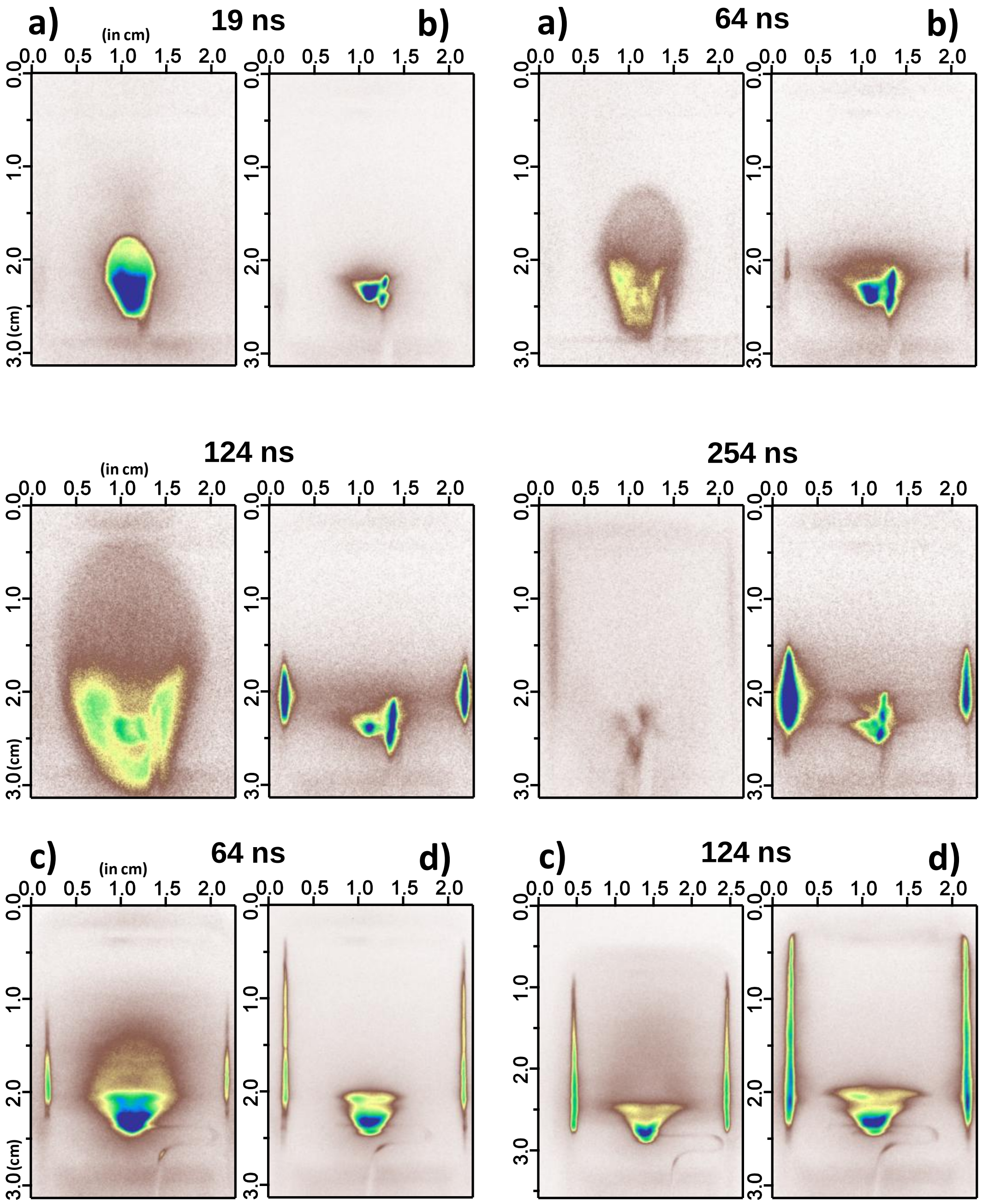

Figure 4.41: ICCD images: Laser energy∼20 mJ, target∼25 μm Al wire for a) without B fields and b) ∼.85 T enclosed B field. c)-d) 200 mJ, ∼1.0 mm Cu wire target and ∼.85 T enclosed B fields with c) 10 mTorr, d) 0.1 mTorr.

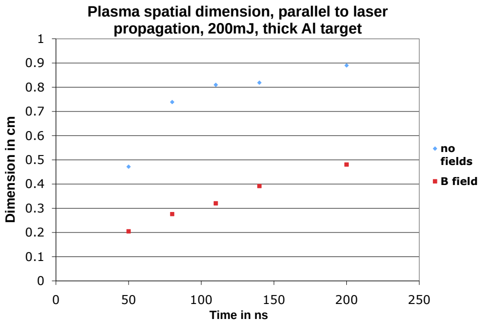

Figure 4.42: The spatial dimension of the laser-produced plasma with and without a magnetic field and an Al 1.0mm wire target.

4.4.4 Comparison of Spatial Dimensions of Laser-Produced Plasma with Self-Similar Hydrodynamic Expansion Models.

I measured the spatial dimensions of several of the expanding plasmas. The denser and more radiant part of the expansion was measured and the measurements of the plasma front are studied in the next section. With a magnetic field, this part of the plasma is marked with well define boundaries that are straightforward to quantify. Without a magnetic field this part of the plasma expands uniformly into the vacuum and makes a good quantitative measurements of this plasma difficult. I made line-outs of the various plasmas and took a relative threshold to measure the radius of the plasma. This only gave meaningful results for very early times without a magnetic field because of the difficulty of quantification and the reported measurement in the graphs should be ignored for longer time scales in the non-magnetic field case. I pay particular attention to the 25 μm wire target cases because the symmetry of the expansion allows for a more spherical approximation. Both the parallel and perpendicular dimensions of the plasma were measured with respect to the drive laser propagation for copper and aluminum wires as in figures 4.32

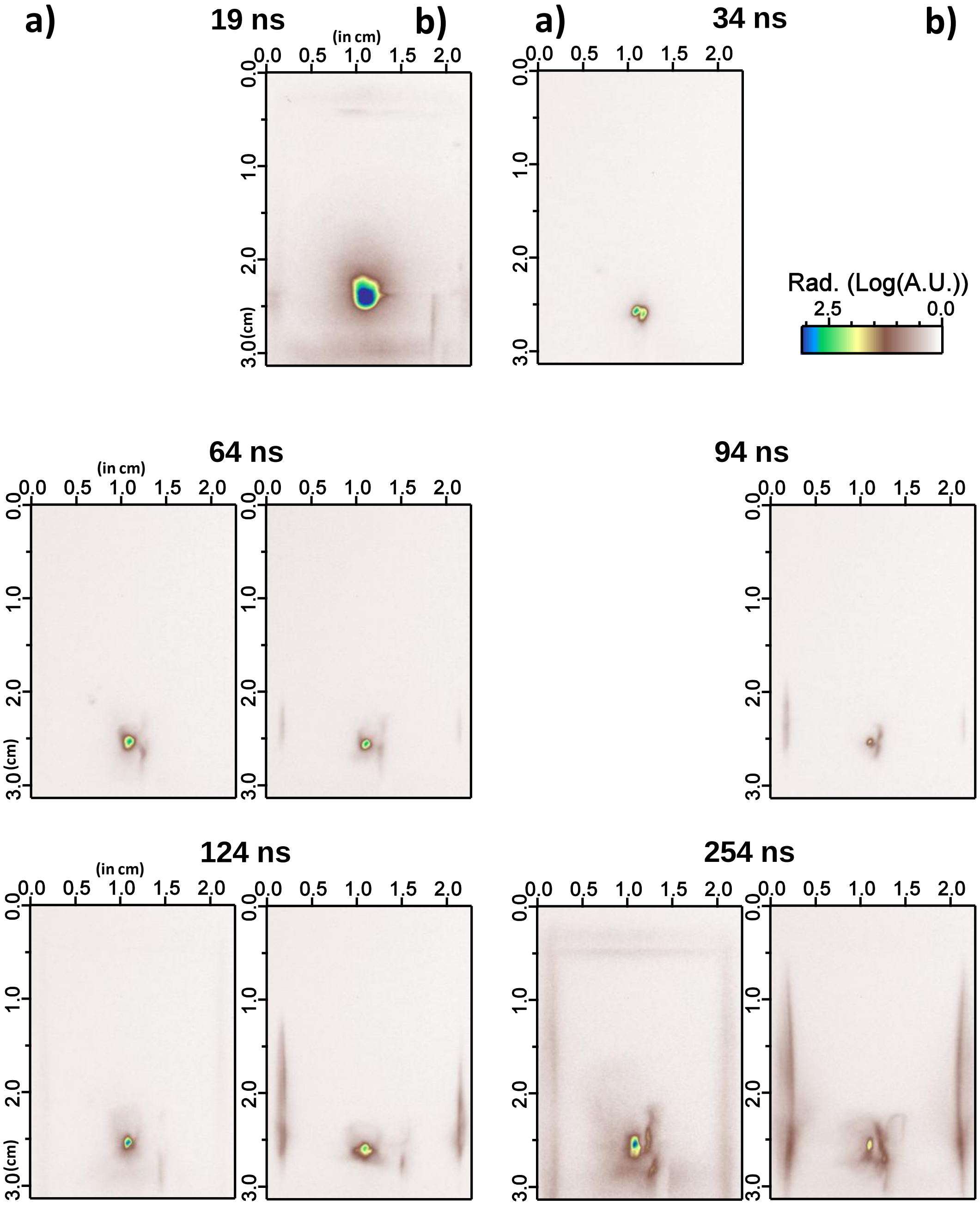

Figure 4.43: ICCD image of laser produced plasma progression where the input laser energy is ~2.0 J and the target is ~25 μm thick Cu wire. a) is without B fields and b) is with ~.85 T enclosed B fields.

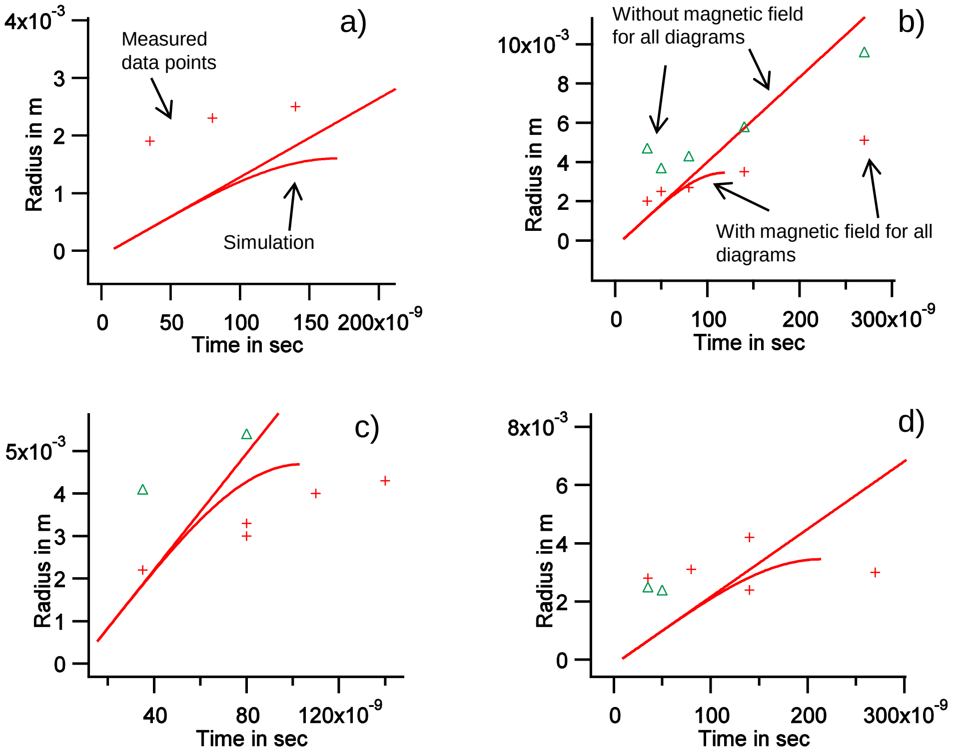

Figure 4.44: Self-similar expansions with and without magnetic fields compared to actual measurement. For each energy example the energy from the laser pulse was assumed to be 1/4 of the laser pulse, because of reflections due to critical densities and because the target is smaller than the focus. a) is with 25 μm Al wire ablated with a 20 mJ pulse, b) is with 25 μm Al wire ablated with a 200 mJ pulse, c) is with 25 μm Al wire ablated with a 500 mJ pulse, and d)is with 25 μm Cu wire ablated with a 200 mJ pulse

and 4.38. Generally the data showed slower plasma propagation in the magnetic field except for larger times where the nonmagnetic field measurements are meaningless. The expansion along the magnetic field lines was similar to the same expansion without a magnetic field as predicted by MHD theory. Examples of measurements from a thick aluminum wire are in figure 4.42.

The formulation for measuring the maximal radius using the volume of the expelled magnetic field can be compared with these results as in figure 4.40. The maximum radii correspond better to energies lower than the input laser energy by more than half. The plasma does not stop at this boundary but continues to progress marginally past this boundary. This is also reported in literature [54]. Reasons for this are most likely due to the resistive nature of the colder plasma.

I simulated the expansion with and without magnetic fields using the formulation outline in section 4.2 for the 25 μm wire targets as illustrated in figure 4.44. I used a quarter of the energy of the laser to match with the data. More sophisticated techniques could estimate the best initial energy for this formulation, but may not give more important results. The energy of the laser is reflected away from the target by the plasma. Also the 25 μm target is smaller than the focus of the beam. As the laser irradiates this target, the material will expand and begin to absorb more of the area of the laser focus [133]. Nevertheless the laser will not deliver all of the energy to the target. There is some agreement between the measured data and the simulation. The data would be best represented if it's initial radius were larger. In the simulation the laser pulse is instantaneous, which is not the case in reality. I artificially put an 8 ns delay in the expansion to account for the width of the pulse in the simulation. This does not significantly effect the measurement.

The data obtained from the ICCD camera has given much information to the laser plasma distribution in the experiment. This information helped in learning about the conditions needed for the jet and magnetosphere experiments in this thesis and to understand the data taken with Schlieren and interferometry. There is a wealth of parameter space from these measurement available for future experiments.

4.5 Modeling and Analysis of Laser-Produced Plasmas Using HYADES

HYADES is an one-dimensional lagrangian hydrodynamic code developed for such uses as laser-target interactions. The code was developed by Jon Larsen [82] as a program for experimentalist to use with little training in computation. The code is able to handle many hydrodynamic situations but is not intended to be exhaustive. The calculations are meant to be more pedagogical in nature and not for the use of serious engineering.

To use the HYADES program a researcher inputs an information source file that lists the various parameters for input and output of the program. The physical set up is a mesh formulation and physical parameters such as type and density of material are added as needed. HYADES can use various energy inputs into the system such as a laser source. HYADES returns the mesh parameters in time slices that are specified by the user.

Care must be taken in setting up the problem to avoid situations that give incorrect results or make the computation process take too long. The health of the calculation can be monitored by monitoring the process where

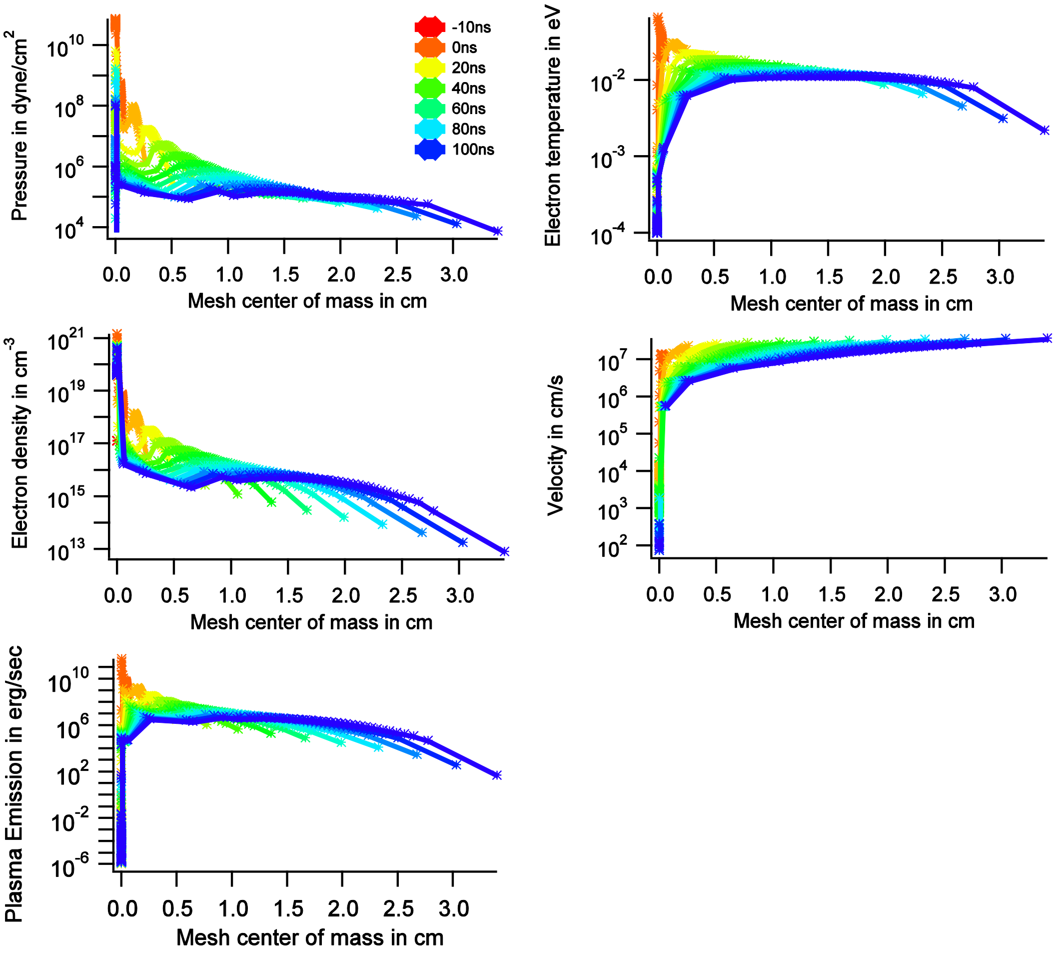

Figure 4.45: Plasma parameters for a 200 mJ laser pulse impinging on a 25 μm aluminum wire in cylindrical geometry.

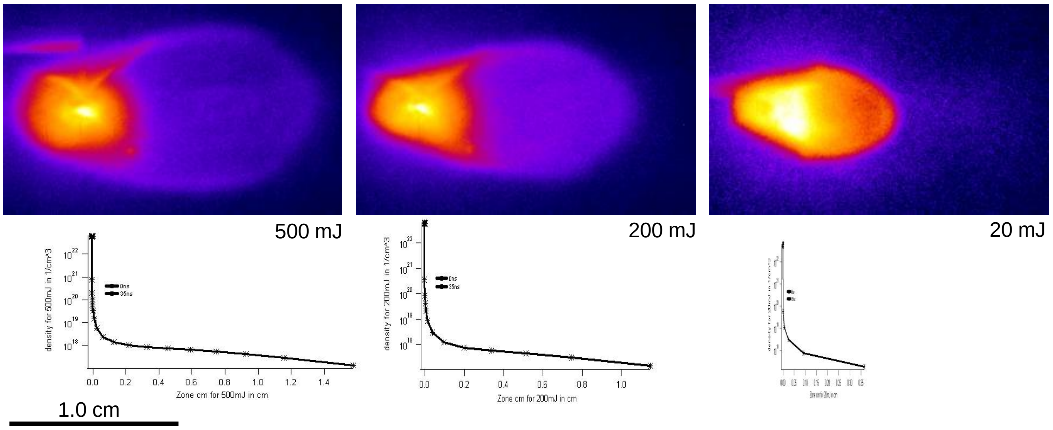

Figure 4.46: Comparison of HYADES expansion with ICCD expansion at 35 ns. The HYADES graphs have been adjusted to match the same spatial scale as the images.

the minimum time step is determined. Problems occur when this process stalls on a particular time step determining process. This is an indication that the physics of the problem is being stymied by a particular part of the problem set up, such as a large mass mismatch between mesh points. Mass of adjacent mesh points should not vary more than 5%. This becomes difficult in vacuum boundaries. Appropriate feathering of mesh points were used to get as small of a mesh point that was practical on a vacuum boundary. The time determining process should change position and type often in the problem calculation.

The simulations investigated with HYADES were laser-produced plasmas similar to our experiment without magnetic fields. A 25 μm Al wire was used as a target. I performed the calculation in planar, cylindrical, and spherical coordinates. A ball was used 25 μm in diameter in the spherical case and a slab 12.5 μm thick in the planar case. I used this thickness in the planar case as a type of radius average the actual wire experiences in the experiment. 5%

feathering was used in the entire bulk of the material. The planar case used double feathering starting in the center of the material. I used the QEOS for aluminum in the experiment. The results from the cylindrical calculation are in figure 4.45.

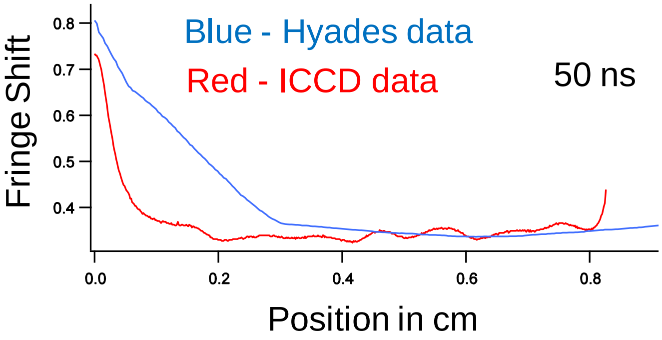

Figure 4.47: The fringe shift is compared with the line integral of the electron density from a cylindrical calculation from HYADES. The initial laser energy was 3.7 J on a copper 25 μm wire.

In comparing the calculation with the experimental results I looked at the plasma front in both cases, and compared the distances traveled. The front in the experimental case was measured by quantifying the faint spheroid that expanded away from the target with high velocities. In the calculation I measured the distance of the last mesh point in the “r” output of HYADES. There is excellent correlation in the data points as in table 4.2. Pictorially this is demonstrated in figure 4.46 with the HYADES output lined up with the same spatial dimension as the ICCD images of the plasma front.

This agreement between the laser-produced plasma measurement and HYADES is significant and gives weight to the relevance of the output of HYADES in describing corresponding data. This calculation deals with the

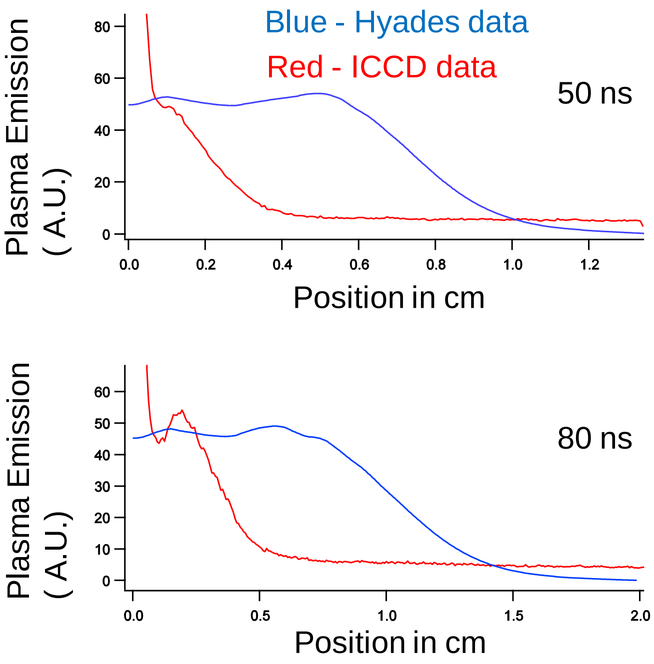

Figure 4.48: The line integral of the plasma emission is compared with the corresponding ICCD data. The initial laser energy was 200 mJ impinging on a 25 μm aluminum wire in cylindrical geometry.

hot part of the plasma expanding away from the interaction point at high speeds. This gives an indication for the validity of the parameters in the laser-produced plasma useful in other parts of this experiment, such as sending currents through the plasma, knowing its conductivity, etc. This calculation is useful for calculating the magnetosphere parameters in the experiments outlined in chapter 6.

There are several things in this calculation to mention when testing for the actual physics of the calculation. First of all the HYADES code is one dimensional. Thus this experiment has to be compared to 1D, cylindrical, or spherical coordinates. Investigating the geometry of the set up implies that

Time (ns)	Energy (mJ)	Measured Length (cm)	Planar (cm)	Cylindrical (cm)	Spherical (cm)
35	20	0.64 ± 0.10	0.27	.37	.16
80	20	1.23 ± 0.10	0.68	0.88	0.32
35	200	1.18 ± 0.10	1.00	0.98	0.64
50	200	1.48 ± 0.10	1.48	1.47	0.87
80	200	2.36 ± 0.10	2.48	2.61	1.37
35	500	1.33 ± 0.10	1.51	1.33	1.02

Table 4.2: Comparison between the measured plasma front distance from the interaction as compared with HYADES calculations in planar, cylindrical, and spherical coordinates.

neither of these possibilities fully gave a complete picture of the physics in the experiment. There is a one-dimensional component to the interaction of the laser on the target and the material expanding along the stream of the laser. This front has a 1D expansion in this direction but then has a cylindrical expansion on the axis of this propagation. Of the three situation when a t-test is compared between the three samples the results give a Pearson correlation of .96, .99, .89 for planar, cylindrical, and spherical respectively. This would give cylindrical geometry the best correlation between the two. This holds for the front only. The question remains about the validity of the other parameters. Density will be greatly effected by the geometry.

Inverse bremsstrahlung plasma emission can be calculated using plasma parameters from the HYADES simulations. The plasma emission formula given in section 3.3.2 can be integrated over the frequencies measured from the ICCD camera - filter combination which are 350 nm to 575 nm. This gave, as a formula,

$$J = \int_0^\infty J_\nu d\nu = \frac{32\pi}{3}\Big(\frac{2\pi kT}{3m}\Big)^{1/2}\frac{Z^2e^6}{mc^3h}N_+N_e(e^{h\nu_2/kT} - e^{h\nu_1/kT}). \qquad (4.14)$$

with $\nu 1 = 5.21 \times 10^{14} Hz$ and $\nu 2 = 8.57 \times 10^{14} Hz$. An example of this calculation for a particular simulation is given in figure 4.45. The plasma emission calculated from the HYADES cylindrical coordinate calculation can be line integrated along the view-axis of the ICCD camera to give the emission in terms of the detection signature of the ICCD camera. This calculation is reported in figure 4.48, as it is compared with the line-outs of corresponding ICCD camera images from the center of the interaction along the axis of symmetry with a 200 mJ laser pulse on a 25 μm aluminum wire. The relative intensities of the two curves have been adjusted for comparison. This calculation showed an correlation between the measured emission of the plasma with the HYADES calculation. There is a peek in the wings of both profiles. The peek in the HYADES emission line is shifted about twice that of the ICCD line and is a result of the density distribution calculated with HYADES. The cause of this shift is unknown, apart from standard error sources of differing geometries, etc. This peek in the wings is often observed in the laser produced plasma ICCD images and can then be explained, from HYADES, as an artifact of the hydrodynamic expansion of a laser-produced plasma from a thin aluminum wire.

The fringe shift can also be calculated as a line integral of the electron densities derived from the HYADES simulation. This is compared with the corresponding interferometric data in figure 4.47 of a 3.7 J laser pulse impinging on a 25 μm copper wire. This shows a very similar range of fringe shifts as measured with the interferometry over the corresponding spatial scale. The values for the interferometer have an arbitrary additive constant given by the background subtraction process. The relative values were additively matched. This then states that the average values of the expanding plasma of 10^{17} cm^{-3}

as calculated by HYADES match well with observations.

HYADES is capable of approximately modeling the physical situations related to the measured laser-produced plasmas in this thesis. The total width of the laser-produced plasma has been compared with the width calculated from HYADES under various input energy conditions with high accuracy giving a Pearson correlation constant of .99 for the cylindrical case. The plasma emission can also be calculated and compared with ICCD giving similar morphologies in intensity. The calculated fringe shift for interferometry gave similar range of numbers as compared with the measured interferometry fringe shift.

4.6 Conclusion

Experiments have been performed studying the effect of a laser-produced plasma with and without a magnetic field using optical probing. I measured the most striking differences between the two cases using an ICCD camera. Differences between these conditions measured with schlieren imaging could not be detected, but with interferometry some differences could be quantified. The results of the ICCD camera measurements were compared, with and without magnetic fields, to self similar calculations of the expansion of a laser-produced plasma with reasonable success. The ICCD images and interferometry, without magnetic fields, where compared to HYADES simulations. The results gave good agreement with calculations.

Chapter 5

Novel Laboratory Simulations of Astrophysical Jets

5.1 Introduction

Jets are ubiquitous in nature and in industry, created by natural causes and designed for application. As discussed in the introduction of this thesis there is a growing field of physics interested in simulating astrophysical jets in the laboratory. The goal of this research is to help understand the proposed mechanisms of jet formation from astrophysicists. These proposed mechanisms are whether or not astrophysical jet formation is magnetically driven or hydrodynamically driven, and what role radiation has in collimation.

The pursuit of laboratory simulations of astrophysical jets has been a subject of research for may years after Ryutov et. al. published their work on laboratory frame to astrophysical frame scaling [122]. There have been two major areas in relation to laboratory simulations of astrophysical jets. Astrophysical jets radiate energy due to plasma emission. If this radiation process is strong enough collimation may occur. Many groups have been working on laboratory jets where radiative cooling collimates the jets. Many laboratory astrophysical experiments have measured jet formation with the purpose of exploring the role of radiative cooling in jet formation. Foster el al. [36][37] conducted many experiments involving intense lasers backlighting targets that collimates ablated material. Foster measured the jet as it interacted with different materials, and compared the experimental data with hydrodynamical simulations. Other experimenters use laser ablated hohlraums to drive jets through different materials [86]. Farley et al. [33] used lasers to ablate a conical target to form jets. The jet formed because the ablated material coalesced on the axis of the conical target. Mizuta et al [97]and Stone et al. [131] compared simulations with these experiments and found that radiation played an important role in the collimation of these jets.

Lebedev et al. [83] conducted radiatively cooled plasma jet experiments using tilted conical z-pinch arrays. The ablated material from these conical arrays coalesced along the axis of the conical array. Lebedev induced angular momentum into the jet by using a poloidally twisted and tilted conical array [84]. Although radiation most likely is not important to the collimation of the jets in this thesis, the research mentioned above show other similar laboratory to astrophysics comparison techniques.

The other area of jet research is where magnetic fields control the collimation of the jets. There are two major groups of experimenters, that of Lebedev and Bellan, working on laboratory astrophysical simulations of jets with significance to magnetic collimation of astrophysical jets. Lebedev has been studying magnetic jet formation using radial z-pinch arrays and Bellan has been studying magnetic jet formation using a coaxial gun device. Lebedev et al. [85] performed his experiments on the MAGPIE pulsed power Machine. Lebedev used a radial wire array made with 16 tungsten wires 13 μm in diameter. Lebedev's pulsed power system delivered a 1-MA current pulse with a 240 ns rise time to the radial wire array. The current ablated the wires and the plasma created expanded away from the array due to $\mathbf{J} \times \mathbf{B}$ forces with a poloidal magnetic field created by the current flowing through the center electrode. The current formed a magnetic bubble by expelling all the conducting material away from the array plane. The current formed a magnetic tower in the center of this bubble by pinching the material magnetically. This magnetic tower evolved over time as a magnetized jet.

Lebedev measured the evolving jet using interferometry, Schlieren, time resolved XUV and soft x-ray imaging. The jet had an expansion velocity of about 200 km/s, a density of $10^{18} - 10^{19}\ cm^{-3}$ and had a temperature of 120 eV. Lebedev made these following conclusions about astrophysical jet physics from his experiments. Magnetic fields can create outflows and hoop stress can collimate jet flows. There are possibly two mechanisms of collimation. While magnetic fields collimate the jet during its formation the jet can remain collimated without magnetic fields once the jet becomes supersonic if there is sufficient cooling. The return current was carried by the magnetic bubble, which can help explain where the return current would be in an astrophysical jet if astrophysical jets were collimated by magnetic fields. MHD instabilities do not always destroy the jet flow.

Bellan [62][63][64][154] used a large coaxial gun device with axial and poloidal magnetic fields emanating from an annular electrode configuration. The annular electrode was connected to a large capacitor bank. Breakdown happened when a puff of gas was induced across the electrodes. The jet formed as a group of "spider legs" coalesced. The spider legs were the discharge of the capacitors through the puffed gas along the magnetic field lines. Typical parameters of the plasma gun were $V_{gun} = 4 - 6kV$ with $I_{gun} = 70 - 120kA$ and $B \approx 0.1 - 1.0kG$. Bellan categorized these jets into three categories which depend on the value $\lambda_{gun} = \mu_0 I_{gun}/\Psi_{gun}$ where Ψ_{gun} was the magnetic flux of the coaxial plasma gun. These three categories are a stable column, a kinked column, and a detached plasma column as seen in figure 5.1. Bellan compared the kink instability with his data using the equation $q(R) = 2\pi RB_Z/LB_\phi = 1$. Bellan's theoretical premise for these experiments was that the collimation of any initially flared current carrying fluxtube, including astrophysical jets, is due to magnetohydrodynamic forces from the flared current profile which I will describe in detail in section 5.2.3. After the fluxtube has evolved collimation will increase due to the pinch effect.

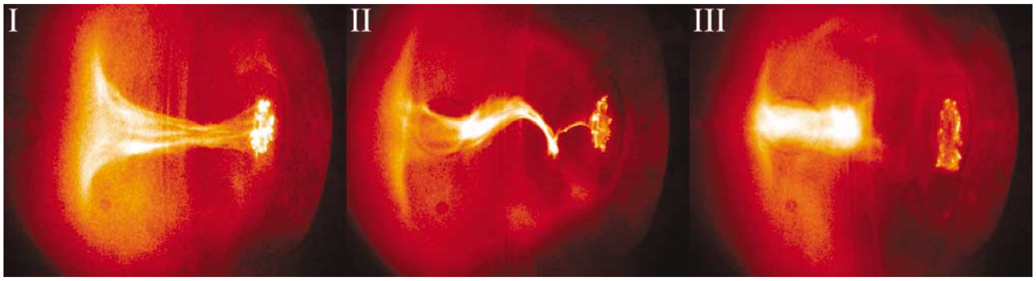

Figure 5.1: Bellan forms jets using a gas injected coaxial device with three different morphologies for the jets he created I stable, II Kinked, and III detached [63] (Copyright (2003) by The American Physical Society).

In this chapter I discuss how magnetized plasma jets were created in a novel experiment with a vacuum arc set up for the purpose of laboratory simulations of astrophysical jets. The scaling parameters of the jet were similar to the parameters in YSO astrophysical jets. Vacuum arc technology was used to construct plasma jets where a supersonic unmagnetized anode jet remnant served as the initial conditions for a magnetized cathode jet. The anode jet created a non-magnetized supersonic flow with a measurable barrel shock in an axial magnetic field. The barrel shock bounded a cone of higher densities and temperatures overlaid in a colder background gas. With this barrel shock cone embedded in an axial magnetic field, the currents upon reversing direction funneled down the cone due to the anisotropic conductivity in the magnetized plasma and the differences in plasma conductivity between the two regions. Maxwell SV software calculated the current distribution under similar conditions and showed that the axial current in the cone is quasi-uniform as outlined with the fluxtube. This created a fluxtube outlined by the barrel shock with quasi-constant current subject to Bellan's MHD based fluxtube model [6]. Modeling of Bellan's MHD based fluxtube model showed a dynamical progression of a jet-throat pinch similar to the observed laboratory jet progression. Bellan's model predicted the distribution of mass within the flux tube similar to the plasma emission distribution in the ICCD images. Bellan's equations predicted rotation occurring in the fluxtube. Evidence of this is shown in the distribution of plasma emission in the throat of the jet as a divot. Kinks in the plasma tube column were measured in the jets and were compared favorably with Kruskal-Shafranov theory.

5.2 Theoretical Ideas of Importance to the Jet Experiments

The novel idea for investigating astrophysical jets that was different from both Bellan's and Lebedev's work was the idea of having a supersonic uncollimated plasma jet in a magnetic field where then the currents were switched on and the evolution of the jet boundary could be measured. The added novelty in this set up is that this idea could be created with a rather mundane and inexpensive vacuum arc setup, whereas the experiments performed by both Bellan an Lebedev were in large and intricate plasma facilities. This idea was postulated from simulations of astrophysical jets in the literature where the initial conditions are an accretion disk with thermally and centrifugally driven winds emanating from the disk as an uncollimated jet or wind. The rotation of the disk and central objects interaction with the magnetic field is turned on which created a toroidal magnetic field that collimates and accelerates the jet [109][142][35][141]. For our experiment the introduction of the toroidal magnetic field is not created by gravitational induced rotation, but by the current from a capacitor in an axisymmetric setup with magnetic fields providing symmetry for the current to follow.

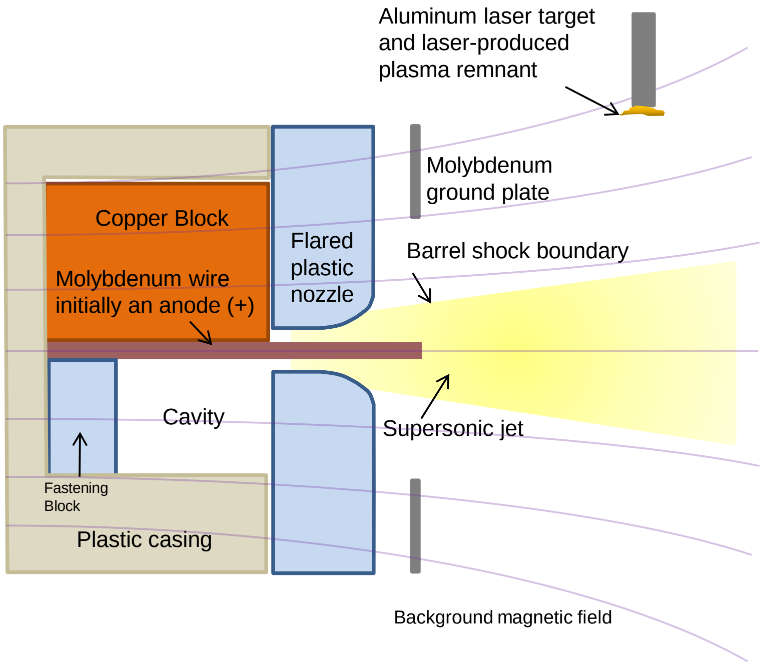

Figure 5.2: A flared nozzle creates a supersonic flow from the cavity containing the molybdenum electrode where the cavity fills with vaporized molybdenum from the heated wire.

I wanted to make the flow supersonic because under the right conditions supersonic flows form barrel shocks (see section 5.2.2 for definition). This, if detected, will form a sharp boundary that will bound two different regions of plasma conductivities. Also, barrel shocks from nozzles typically have an opening solid angle on the order of 60° [125] which is the same angle as the measured opening of the jet in M87 [93] and of what is predicted in magneto-centrifugal theory [109]. Supersonic jets are formed under certain conditions when a pressurized chamber opens into a vacuum through a nozzle. For this set up the chamber is filled with plasma from a superheated electrode as in figure 5.2. With this supersonic jet embedded in a magnetic field currents will flow anisotropically through the jet as in figure 5.3. With the current then flowing through this cone $\mathbf{J} \times \mathbf{B}$ forces will pinch the cone and accelerate the plasma as in figure 5.4. This will then show the dynamics of a progressing magnetic jet. Different background magnetic field strengths were used in the experiment, but only the stronger background magnetic fields gave the experiment the required symmetry to make assumptions about the current density, etc. Thus the majority of the analysis focused on jets measured with strong background magnetic fields. Similar phenomena occurred without the background magnetic field, but because of the lack of symmetry the jets were very difficult to quantify.

This is then different from Bellan's and Lebedev's work in that in this experiment there would be already a supersonic flow emanating from the electrode configuration, and then the current that pinches the jet is turned on. In their work the gas flow and the pinching begin at the same time. This proposed set up could give information on the development of the astrophysical jet as it is already emanating thermally driven winds, then as the magnetic field develop from magnetic dynamo, the jets will form. So with this general overview the theory section will contain three main points. One, basic facts about vacuum arc technology will be reviewed. Two, supersonic flows through

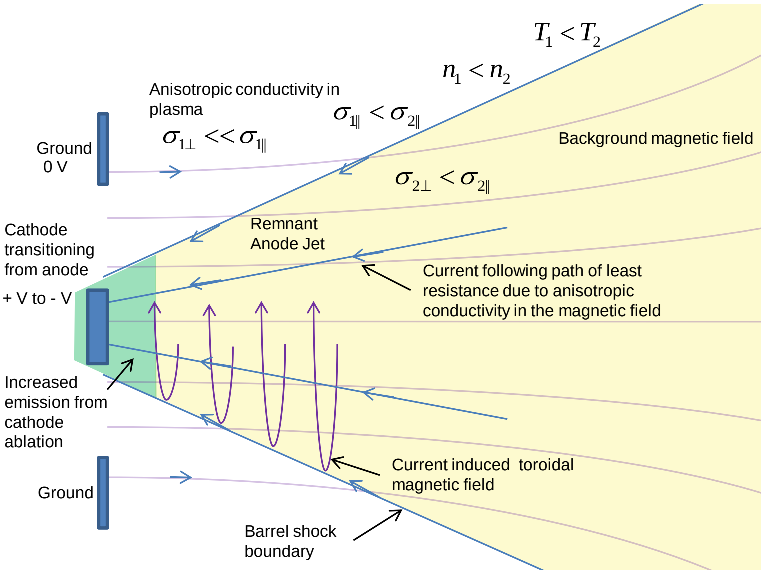

Figure 5.3: With a remnant jet flowing from the plasma contained in the cavity, the current upon reversing direction will flow through an anisotropic conductivity field, that will form a quasi-uniform current distribution throughout the cone bounded by the barrel shock.

flared nozzles will be discussed, and three, the dynamics will be discussed concerning currents through flared fluxtubes. The scaling physics between laboratory frames was discussed in section 3.2, and a more detail description of astrophysical jets was discussed in section 1.3.

5.2.1 Discussion of Vacuum Arcs

This experiment is intimately connected with vacuum arc physics and uses many of the unique features of vacuum arcs to its advantage. This intimate connection involved supplying a current to a cylindrically symmetric electrode configuration in vacuum. Vacuum arcs have been used in numerous applications such as welding, vacuum switch gear, etc [45]. Vacuum arcs

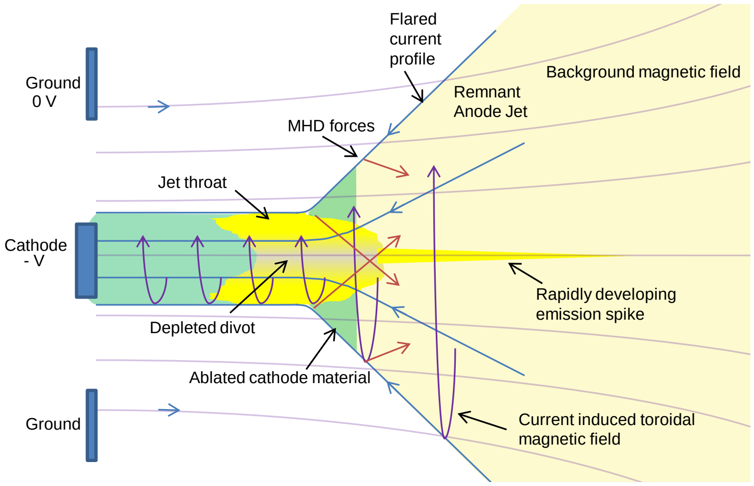

Figure 5.4: $\mathbf{J} \times \mathbf{B}$ forces will pinch the cone and accelerate the plasma axially. The non constant current will cause the plasma jet to rotate and force material away from the center causing a divot in the jet throat.

have been studied quite thoroughly this century but there are many things related to vacuum arcs that are still unexplained [81]. A vacuum arc consists of a biased anode and cathode in a vacuum system, which conducts electricity though ionization of the inter-electrode gas. The breakdown of the vacuum arc is dependent on many factors. One very important factor is the Paschen effect [13], which is a relation between the breakdown voltage of a vacuum gap and the length of the gap and the background pressure. Once breakdown occurs electrons will be emitted from the cathode and ions will bombard the cathode.

The cathode and the anode react differently to the vacuum arc, a fact that is exploited in this experiment. Concerning the cathode, the incoming current enters the cathode in high current density localized areas called cathode spots (see figure 5.5). Each cathode spot has a set current value depending on the material used [81]. For example each cathode spot on a molybdenum electrode has about 150 A flowing through it. The exact current density for a cathode spot is a matter of controversy, but the general consensus states the density range on the order of 10^5 to 10^8 A/cm^2 [81]. The cathode spots have many mysterious properties that have not yet been resolved. One of these properties is that in a magnetic field the cathode spots move in the opposite direction prescribed by $\mathbf{J} \times \mathbf{B}$. Cathode spots vaporize the cathode and form vaporized metallic jets [94].

Current flowing out of the anode behaves much differently than the cathode. The anode does not get as hot as the cathode unless the anode is thermally isolated from its surroundings. If the anode is thermally isolated it will get hot enough to vaporize the anode material. This is called a Hot Anode Vacuum Arc or HAVA. The anode will form a single anode spot from which vaporized metal will expand in the form of an anode jet [13] (see figure 5.5). In this experiment particular use was made in creating an HAVA during the positive part of the cycle. Then, as the cycle became negative and the center electrode became a cathode, particular use was made of the electrode being locally ablated at the tip instead of the global ablation found in the HAVA.

Engineers, for applications such as vacuum switchgear, have studied the parameters of inter-electrode plasmas. Measurements of ablated material expanding away from cathodes have been made using luminosity measurements as reported by Mesyatz [94]. They have found in their investigations that the expansion velocity is on the order of 10^6 cm/s for various metal cathodes studied. They found that the velocity remained unchanged in their experiments when the current and the voltage are changed within an order of magnitude. The expansion velocities for both Mo and Al were measured to be

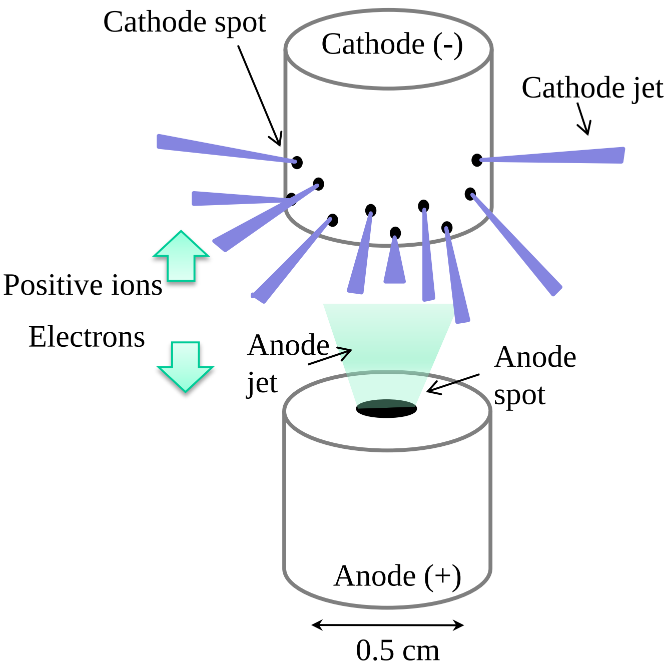

Figure 5.5: Cathode jets originate from cathode spots which have a high current density but move erratically. Anode jets form uniform outflows. [81].

1.8×10^6 cm/s where the voltage was on the order of 20 kV. Measurements of the inter-electrode density and temperature have been compiled from numerous experiments in Boxman's book [13]. Boxman stated that the electron density was found empirically to be proportional to the current density. Studies have shown that copper inter-electrode plasma is on the order of 10^{15} cm^{-3} with a J value of 10 MAm^{-2}. Various inter-electrode temperatures have been measured to the order of 5 eV. A molybdenum experiment gave 6 eV when the current was 1200 A according to Boxman [13].

The work done on vacuum arc engineering gives approximate benchmarks for the conditions in the current experiment. The difference between anode and cathode behavior is very apparent in this study and will be used extensively in the jet analysis. The use of a temperature of 6.0 eV for the inter-electrode plasma will be used throughout the analysis, plasma densities will be compared with $10^{15}\ cm^{-3}$, and the unmagnetized velocity of the expanding plasma will be taken to be about 1.8×10^{6} cm/s.

5.2.2 Supersonic Jets

The expansion of a supersonic flow into a vacuum has been well studied for scientific applications. The flow through various nozzles can create a supersonic flow. In this experiment a supersonic jet of anode plasma is created as an initial condition for the magnetically controlled jets. This allows for a higher temperature cone bounded by a barrel shock and produced by the supersonic jet to be embedded into a lower temperature gas. This will create a unique situation for magnetic jets to form. This is the motivation behind the theoretical discussion of supersonic jets.

The gas dynamics of the flow through a constricted converging-diverging nozzle can be derived using several assumptions about the flow [136]. The assumptions are that the gas is perfect and invicid, that the flow is stationary, isoentropic and one-dimensional, and that the nozzle has varying dimensions and has frictionless walls. The duct is also connected to a chamber with constant pressure and density and no velocity on one side of the duct and the other is connected to the discharge chamber with much lower pressure and density. The duct area can be characterized by a one-dimensional function $A = A(x)$ where x is the dimension along the duct and the duct is axisymmetric, and that there is one value of x in the duct where $A = A(x)$ is at a minimum.

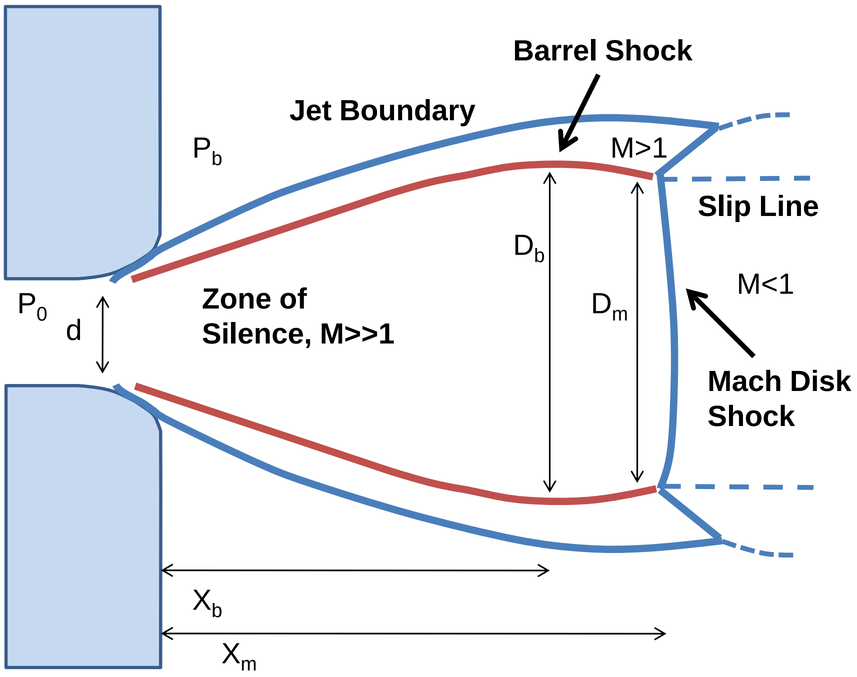

Figure 5.6: Diagram of a supersonic jet expansion into a background gas [136][125].

The continuity equation will give

$$\nabla \cdot (\rho \mathbf{u}) = 0 \tag{5.1}$$

with u being the flow velocity assuming $(\partial \rho / \partial t) = 0$. Integrating this equation gives

$$\int_V \nabla \cdot (\rho \mathbf{u}) dV = \int_S \rho \mathbf{u} \cdot \mathbf{n} dS = \rho_2 A_2 u_2 - \rho_1 A_1 u_1 = 0. \tag{5.2}$$

This shows that the flow rate

$$Q = \frac{dm}{dt} = \rho A u = constant \tag{5.3}$$

throughout the nozzle. Using this equation and other relations we can derive an equation describing the basic dynamics of the flow through the nozzle. The derivative of the flow rate divided by the flow rate gives

$$\frac{d\rho}{\rho} + \frac{dA}{A} + \frac{du}{u} = 0 \tag{5.4}$$

with the sound speed being $a = \sqrt{dp/d\rho}$ equation 5.4 will take the form

$$\frac{dp}{a^2\rho} + \frac{dA}{A} + \frac{du}{u} = 0. \tag{5.5}$$

A variation of the Bernoulli equation gives

$$\frac{dp}{\rho} = -u^2\frac{du}{u}. \tag{5.6}$$

putting this into equation 5.5 will give

$$\frac{du}{u} = \frac{1}{M^2 - 1}\frac{dA}{A} \tag{5.7}$$

where $M = u/a$ is the Mach number. This equation states that in a converging-diverging nozzle the velocity will increase if M is greater than one in the nozzle throat, and will decrease if M is less than one in the nozzle throat. In the current experimental set up a flared profile has been made to create a supersonic flow with the same conditions required for this formula. These calculations will be compared with the experiment in section 5.6.1.

As the jet expands into the chamber the pressure, temperature and density will decrease due to hydrodynamic expansion. This will be important in determining the plasma parameters where the $\mathbf{J} \times \mathbf{B}$ forces will be acting on the jet material. Hagena [49] gives the pressure, temperature, and density as a function of distance from the cavity due to an adiabatic expansion into the vacuum, with

$$\frac{n}{n_0} = 0.150\big(\frac{x}{d}\big)^{-2} \tag{5.8}$$

$$\frac{T}{T_0} = 0.282\big(\frac{x}{d}\big)^{-4/3} \tag{5.9}$$

$$\frac{p}{p_0} = 0.042\Big(\frac{x}{d}\Big)^{-10/3} \tag{5.10}$$

where d is the diameter of the nozzle.

Supersonic gas jets expanding into a vacuum have several spatial properties that are observed in this experiment as illustrated in figure 5.6 [136][125]. The most prominent parts of the jets are the Mach disk and the Barrel shock. The Mach disk in a supersonic flow is the point where the flow velocity of the jet reaches the sound speed of the background gas in the direct line of the jet motion. This shock is motionless in the steady state. The barrel shock is the same idea as the Mach disk shock except it occurs on the periphery or " barrel" of the shock. The dimensions of these quantities can be calculated in an approximate empirical manner to give

$$(x_m/d) = 0.67(P_0/P_b)^{1/2} \tag{5.11}$$

where x_m is the distance from the nozzle to the Mach disk, d is the diameter of the nozzle, P_0 is the pressure in the enclosed chamber, and P_b is the background pressure. With a 25% margin of error the other dimensions are $x_b = 0.63x_m$, $D_m = 0.5x_m$, and $D_b = 0.75x_m$ where x_b is the distance from the nozzle to the maximum diameter of the barrel shock, D_m is the diameter of the mach disk, and D_b is the maximal diameter of the barrel shock. These relations give the solid angle of the barrel shock as $60°$. These dimensions are observed in the anode jets measured and are used to calculate the ratio of pressures involved in the jet expansion in section 5.6.1.

For a basic review of shock physics recall that a hydrodynamic shock is a wave propagating through a fluid that is characterized by a sharp, nearly discontinuous increase in temperature, density, and pressure. The fluid parameters (mass, momentum, and energy) are conserved across the shock as described in the hydrodynamic equations [156][30]

$$\rho_1 v_1 = \rho_0 v_0 \tag{5.12}$$

$$p_1 + \rho_1 v_1^2 = p_0 + \rho_0 v_0^2 \tag{5.13}$$

$$h_1 + \frac{p_1}{\rho_1} + \frac{v_1^2}{2} = h_0 + \frac{p_0}{\rho_0} + \frac{v_0^2}{2} \tag{5.14}$$

where $v_0 = -D$ and $v_1 = -(D - v)$. D is the velocity of the shockwave in the rest frame of the unperturbed fluid, v is the velocity of the penetrating fluid also in the rest frame of the unperturbed fluid. v_1 and v_0 are therefore the velocities of the fluid upstream and downstream of the shock in the frame of the shock front.

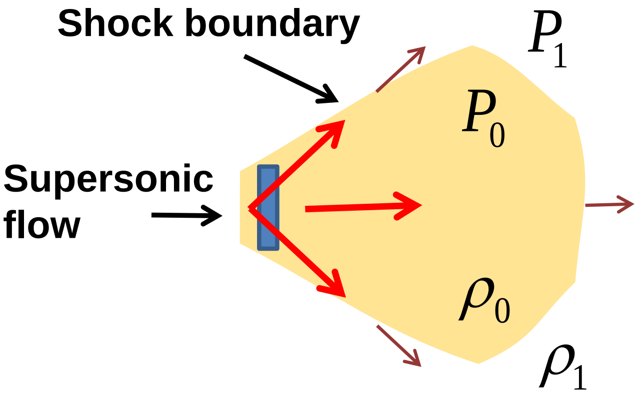

Figure 5.7: Diagram of a supersonic jet shock structure.

These conservation relations lead to the Rankine-Hugoniot equation that describes the pressure and density across the shock wave. This equation can have the form

$$\frac{p_1}{p_0} = \frac{(\gamma+1) - (\gamma-1)\frac{\rho_0}{\rho_1}}{(\gamma+1)\frac{\rho_0}{\rho_1} - (\gamma-1)} \tag{5.15}$$

where subscript 1 represents the upstream parameters, subscript 0 represents the downstream parameters as in figure 5.7 and γ is the adiabatic index. For a monatomic gas the density ratio can have a maximum of 4 across the shock. From Huba [66] the relations of density and temperature in hydrodynamic shocks can be related by the Mach number M as

$$\frac{\rho_1}{\rho_2} = (\gamma+1)M^2/((\gamma-1)M^2+2) \tag{5.16}$$

and

$$\frac{T_1}{T_2} = ((\gamma-1)M^2+2)(2\gamma M^2-\gamma+1)/(\gamma+1)^2M^2 \tag{5.17}$$

This will be useful in the analysis section 5.6.1.

5.2.3 Magnetic Jets

Bellan [6] has formulated a theory for the collimation and dynamics of fluxtubes in magnetic fields. A fluxtube is a volume of space with a tube-like shape defined by the presence of axial magnetic fields and currents. Magnetic fluxtubes are tubes that are defined by the magnetic flux. Current fluxtubes are defined by the current distribution. In this chapter the term fluxtube will refer to a current fluxtube. Bellan sets the evolution of the fluxtube in three stages. The fluxtube takes place in a bowed magnetic field as in figure 5.8. Bellan defines the terms toroidal as the azimuthal direction and poloidal as the r and z direction. Bellan assumes ideal MHD in his set up and assumes that the currents are bounded uniformly in the fluxtube. Axial symmetry is also assumed in his formulation. The first stage of the evolution involves the ramping up of the current and the development of a toroidal plasma velocity. This is derived from the magnetic induction equation assuming $I = 0$. The second stage includes the current in steady state, a radial pressure balance. For a flared current profile this resulted in a net force along the axis of the fluxtube pointing toward the flare. The third stage includes as Bellan says “convection of toroidal flux, fluid stagnation, heating, and compression.” These three stages do not happen separately in reality, in fact in most cases they are all happening at once. But to describe them theoretically the equations greatly simplify for each of the three stages, allowing for the calculation of basic parameters. When analyzing the jet data using these techniques no attempt will be made to combine the theories, as in our case both I and dI/dt are nonzero. They will be handled separately and compared in the spirit of approximation. In this theory section I will focus on the first two stages outlined by Bellan.

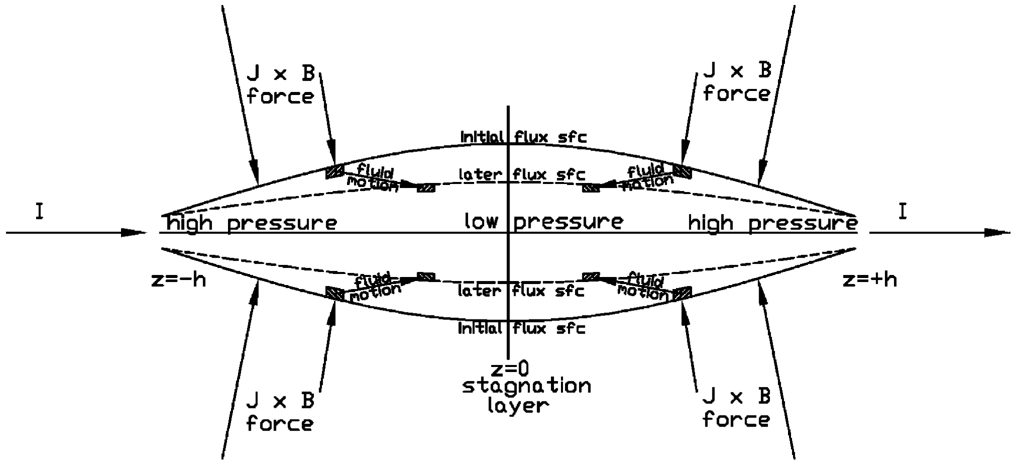

Figure 5.8: The evolution of a fluxtube according to Bellan’s gobble model. The flared fluxtube profile causes material to be accelerated along the z direction and onto the fluxtube axis. Reprinted with permission from [6]. Copyright 2003, American Institute of Physics.

Bellan’s conditions for a fluxtube when addressing the $I \neq 0$ case require only a current fluxtube. The current must be axisymmetric in his case but the calculations only refer to a pressure balance between the $(J \times B)_r$ force and the $\partial p/\partial r$ force. Thus as long as the equations can be integrated one can obtain a result for the resulting forces. For simplicity Bellan chooses a constant current density bounded by the fluxtube resulting in a constant integrated current throughout the fluxtube. By the transparency of his formulation it can be seen that relatively large variations in initial current density will give roughly the same behavior. In the dynamical calculations in this thesis done in section 5.6.3 Bellan's constant current density was used. I will show through anisotropic conductivity calculations that the fluxtubes bounded by the barrel shock will have roughly this type of current distribution.

Before exploring Bellan's theory further I will discuss the plasma parameters that relevant to this experiment and how the experiment will relate to the assumptions made using MHD theory. Then I will discuss the type of fluxtube used in this experiment by discussing anisotropic conductivities and currents calculated from these anisotropic conductivities using a program called Maxwell SV. Then the derivation of important results from Bellan's theory will be presented along with a discussion of the kink instability.

Bellan's equation and all other discussions relating to magnetically confined plasma jets are based on the assumption that the plasma is magnetized. A plasma is magnetized, according to Hazeltine [56], when the characteristic scale L is large compared with the thermal gyroradius $\rho_t = v_t/\Omega$ where Ω is the gyrofrequency. The characteristic length scale of the jets would be the effective diameter or about .4 cm. The thermal gyroradius for the case of $B = .45\ T$, $T = 6\ eV$ (from Lafferty [81]) and for singly charged molybdenum ions and electrons will be .5 cm and .001 cm respectively. Thus the electrons will be magnetized and the ions will not be. This will lead to the condition that the ions will be bound to the magnetized dynamics of the plasma by the electrostatic pull of the electrons. The collision frequency of the electrons off the ions will be according to the equation 5.20, with the electron density of 10^{16}, temperature of 6 eV, and with singly ionized Mo ions will be $2.9 \times 10^{10} Hz$ the cyclotron frequency for the conditions above will be $1.3 \times 10^{10} Hz$. So the frequencies are roughly comparable, which means that the magnetization will be affected by the collisionality of the plasma. The cyclotron frequency was roughly fixed in this experiment and the collision frequency was highly variable among the parameters of the experiment and will likely be less than the number calculated. Other related plasma parameters are, for the conditions above, the electron-electron collision rate is 2.0×10^{10} Hz which is also comparable to the gyrofrequency, and the ion-ion collision rate is 3.3×10^{7} Hz. The ion gyrofrequency is 4.5×10^{5} Hz so that the ion-ion collision is much greater than the ion gyrofrequency again suggesting that the ions are not magnetized. The Alfven speed is 1.0×10^{6} cm/s which is comparable to the dynamical processes measured in the jets as stated in section 5.4. The magnetic Reynolds number is important in determining how frozen the plasma is to the magnetic field lines. This quantity is given by $MR = \mu_0 L V \sigma$ where L is the characteristic length, V is the characterization velocity, and σ is the conductivity of the plasma. This number for our parameters with $L = .002$ m, $V = 4 \times 10^{4}$ m/s, and $\sigma = 1.9 \times 10^{4}$ siemens/m for a 7 eV plasma is 1.9. The diffusion time for magnetic field to permeate for the same plasma is $\tau = \mu_0 * L^2 \sigma = 1.0 \times 10^{-7}$ *sec*. This suggests that the current plasma conditions are on the limit for having frozen in magnetic fields. A good magnetically frozen plasma will have a Reynolds number much greater than one. The diffusion time is comparable to the times duration of the jets, being 500ns. These parameters as a whole state that MHD will be approximately respected in describing behavior from these conditions in this experiment.

The fluxtubes in the case of this experiment will be caused by the anisotropic conductivities created by the magnetic fields and by the differences in regional conductivities bounded by the barrel shock. The current density distribution can be calculated in a demonstrational sense to back up general claims of how the current was distributed in the Remnant Anode Jet (or RAJ) profile. The RAJ is the uncollimated remnant of the anode jet mode. This claim is that due to the higher conductivity in the RAJ cone and because of the anisotropic conductivity of the plasma in a magnetic field the current must be "funneled" down the cone into the electrode. Maxwell SV is a 2D electro-magnetic simulation program, as described in section 4.3.2, that can calculate the current density of an anisotropic medium. Several cases will be considered that will be reported in section 5.6.2. This will use information from the supersonic anode jet section 5.6.1 as a comparison, and will provide information in modeling dynamical processes in the jets in section 5.6.3.

Maxwell SV, as described in section 4.3.2, can calculate the AC current distribution in materials with anisotropic conductance. The anisotropic conductances must be manually given to the program. Plasma in a magnetic field has anisotropic conductance according to the direction of the magnetic field. The electrical conductivity through a plasma can be formulated using the typical current equation as $J = \sigma_{el} E$ where the current is related by the movement of the electrons through the plasma by $J = e n_e v_d$ where n_e is the electron density and v_d is the drift velocity of the electrons. In an electric field an electron will gain a velocity of $v_f = -eE\tau_c/m_e$ before the electron suffers a collision. $\tau_c = 1/\nu_c$ is the mean time between collisions. The average v_f will be the drift velocity or $v_d = 1/2v_f = -eE/(2\nu_c m_e)$. Thus the current will be

$$J = en_e v_d = \Big(\frac{e^2 n_e}{2\nu_c m_e}\Big)E. \tag{5.18}$$

Thus

$$\sigma_{el} = \Big(\frac{e^2 n_e}{2\nu_c m_e}\Big). \tag{5.19}$$

There are many ways to calculate the collision frequency ν_c. One such method for electron reflections of 90° with singely charged ions at constant temperature as

$$\nu = \frac{1}{t_{ei}} = \frac{4\pi e^4 n_i ln\Lambda}{(2m_e)^{1/2}(\frac{3}{2}kT)^{3/2}} \tag{5.20}$$

as discussed in chapter 3. For simplicity I use the Spitzer conductivity formula in Huba [66] which is $1/\sigma = 1.03 Z ln\Lambda T^{-3/2}\Omega m$ with Z=1 and $ln\Lambda = 10$.

For conductivity through partially ionized gases, as discharge plasmas typically are, the plasma will begin to behave like a fully ionized plasma once ionization reaches about 10% [13]. The ablated material coming off of the center electrode will be much more conductive than the RAJ material, and from the previous subsection 5.6.1 the RAJ cone will be more conductive than the background gas due to the decrease of temperature across the shock. Because of this conductivity difference I postulate as stated before that for early stages of the expansion the current will funnel through the expanding ablated material back onto the electrode. Then because of the geometry of the setup and the anisotropic conductivity the current will distribute itself throughout the RAJ material, as in figure 5.48, and avoid coalescing along the axis of the jet, until it reaches the cathode ablated material. A cartoon drawing of this process is also in figure 5.9. I input this information into Maxwell SV to calculate the current distribution. The calculation in Maxwell SV then has the following purposes. The Maxwell SV calculation will give a distribution of current to demonstrate the funneling idea in the RAJ presented above. These calculations will show what happens when a pointed feature develops in the center. These calculations will also provide the density calculated from the formulation given by Bellan [6], which can be compared to the ICCD images.

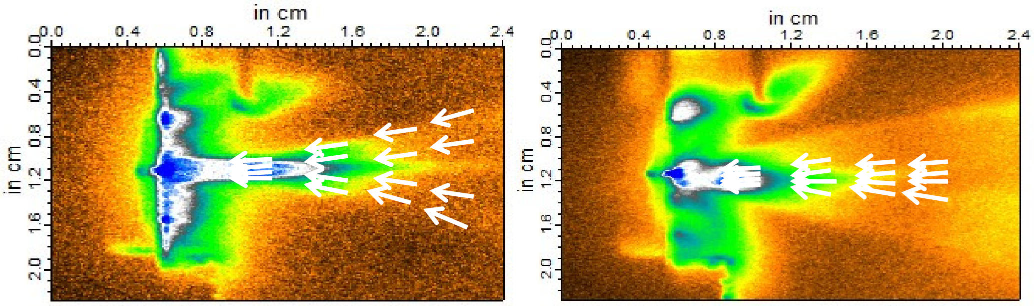

Figure 5.9: This is a cartoon of the possible current distribution of the jet with a magnetic field (on the left) and without a magnetic field (on the right). The white arrow signify the currents.

The derivation of the conductivity of the plasma perpendicular to a magnetic field is as follows [13]. Assuming an electric field $\mathbf{E} = E_x\hat{\mathbf{i}}$ and a magnetic field $\mathbf{B} = B_0\hat{\mathbf{k}}$ we investigate the force equation in this field set up with a velocity term $\mathbf{u}$ and a uniform density, with no net acceleration of the flow. The force equation is thus

$$0 = qm(\mathbf{E} + \mathbf{u} \times \mathbf{B}) - mn\nu\mathbf{u} \tag{5.21}$$

where ν is the collision frequency. This reduces to the following set of equations

$$mn\nu u_x = qnE_x + qnu_yB_0 \tag{5.22}$$

and

$$mn\nu u_y = -qnu_yB_0. \tag{5.23}$$

This reduces to an equation of u_x to be

$$mn\nu u_x = qnE_x + (qnB_0)^2 u_x/mn\nu \tag{5.24}$$

or

$$u_x = \frac{qn}{(mn\nu)(1 + \left(\frac{(qnB_0)}{mn\nu}\right)^2)} E_x. \tag{5.25}$$

The current is related to the flow (for $Z = 1$) by $J = qn_e u/2$ as from the above discussion. Hence the current is

$$J = \frac{q^2 n}{(2mn\nu)(1 + \left(\frac{(qnB_0)}{mn\nu}\right)^2)} E_x. \tag{5.26}$$

The quantity $\frac{q^2 n}{(2m\nu_{ei})}$ is the Spitzer conductivity discussed above. Hence the actual conductivity across the magnetic field is

$$\sigma_\perp = \frac{q^2 n}{(2m\nu)(1 + \left(\frac{(qnB_0)}{mn\nu}\right)^2)} = \frac{\sigma}{(1 + \left(\frac{(qnB_0)}{mn\nu}\right)^2)}. \tag{5.27}$$

Having defined how the fluxtube will be formed and characterized in this experiment I return to Bellan's MHD derivations of specific fluxtube conditions. In Bellan's formulation the first stage of the expansion, where the dynamics of the fluxtube when the current is $I \sim 0$ and when $\partial I/\partial t \neq 0$, is illustrated by the toroidal part of the induction equation,

$$\frac{\partial B_\phi}{\partial t} = r\mathbf{B}_{pol} \cdot \nabla\left(\frac{U_\phi}{r}\right) - r\mathbf{U}_{pol} \cdot \nabla\left(\frac{B_\phi}{r}\right) - B_\phi \nabla \cdot \mathbf{U}_{pol} \tag{5.28}$$

where U is velocity, B is the magnetic field an r is the radius in cylindrical coordinates. The poloidal and azimuthal directions are defined above. When $t \sim 0$ $\mathbf{U}_{pol}$ has not had time to develop and is therefore negligible at the initial time. The induction equation then reduces to

$$\frac{\partial B_\phi}{\partial t} = r\mathbf{B}_{pol} \cdot \nabla\left(\frac{U_\phi}{r}\right). \tag{5.29}$$

A change of variables of $r, z \rightarrow s$ where s is the distance along the poloidal field can give an approximation of this induction equation to be

$$\frac{\partial B_\phi}{\partial t} \cong B_{pol} \frac{\partial U_\phi}{\partial s}. \tag{5.30}$$

This equation can be integrated to give

$$U_\phi \cong \frac{s}{B_{pol}} \frac{\partial B_\phi}{\partial t} = \frac{\mu_0 s}{2\pi B_{pol} r} \frac{\partial I}{\partial t}. \tag{5.31}$$

This states that there is an azimuthal velocity developed by the changing current. This is essentially the rotation of plasma frozen into the magnetic field as the magnetic field twists due to the developing azimuthal magnetic field as illustrated in figure 5.10. Since this is a rotation of magnetized plasma this implies that there needs to be a radial (or perpendicular to the poloidal direction) current to cause $\mathbf{J} \times \mathbf{B}$ rotation. This can be stated in the equation

$$\rho \frac{\partial U_\phi}{\partial t} \cong -J_\psi B_{pol} \tag{5.32}$$

where ψ is the direction perpendicular to the poloidal direction. This leads to a

$$J_\psi = -\frac{\rho}{B_{pol}} \frac{\partial U_\phi}{\partial t} = -\frac{\rho}{B_{pol}^2} \frac{\mu_0 s}{2\pi r} \frac{\partial^2 I}{\partial t^2}. \tag{5.33}$$

J_ψ is called the polarization current, because it is due to the $\mathbf{v} \times \mathbf{B}$ separation of the ions and electrons moving in the magnetic field. It is apparent in this formulation that both U_ϕ and J_ψ vanish when I has reached a steady state. I will show rough evidence of this rotation in section 5.6.3.

For the second stage of fluxtube evolution in Bellan's analysis, when I is constant, he evaluates the z-component force on the fluxtube material Bellan's formulation of flared fluxtube analysis assumes a radial pressure balance when

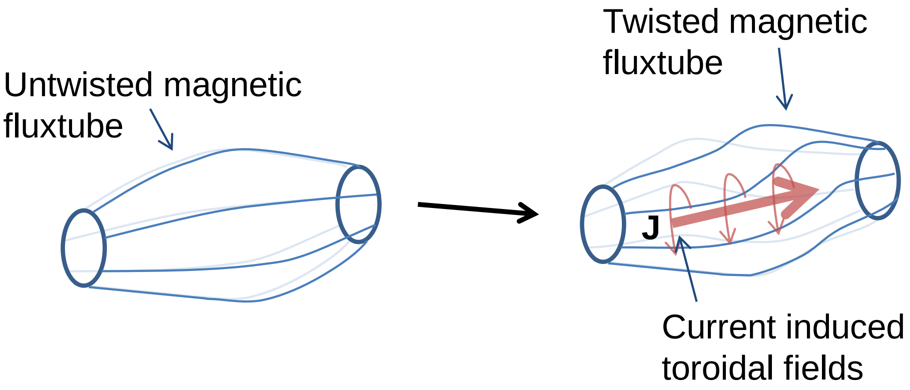

Figure 5.10: The magnetic fields in a fluxtube will twist with an increasing axial current.

modeling a cylindrically symmetric current fluxtube [6]. This sets the velocity terms in the MHD equation,

$$\rho \frac{d\mathbf{V}}{dt} = \mathbf{J} \times \mathbf{B} - \nabla P \tag{5.34}$$

to zero. Bellan's formulation [6] gives

$$\mathbf{J} \times \mathbf{B} = -\frac{\mu_0}{8\pi^2 r^2} \nabla I^2 \tag{5.35}$$

where I is the constant fluxtube current of the form

$$I(r, z, t) = \int_0^r J_z(r', z, t) 2\pi r' dr'. \tag{5.36}$$

This $\mathbf{J} \times \mathbf{B}$ is obtained by using the standard formulation of B from an axial current or $B_{phi} = \mu_0 I / 2\pi r$ and by calculating J with the gradient of I. A pressure balance in the radial direction will then give

$$\frac{\partial P}{\partial r} = -J_z B_\phi = -\frac{\mu_0}{8\pi^2 r^2} \frac{\partial I^2}{\partial r} \tag{5.37}$$

This equation can be integrated for a known I to find the pressure in the fluxtube. This pressure can then be related to the density by $P = nkT$. For a radially constant current density the current, I, will be integrated to $I(r,z) = (r/a(z))^2 I_0$, where $a(z)$ is the fluxtube radius and I_0 is the total fluxtube current. Using this current the pressure can be integrated to get

$$P(r,z) = \frac{\mu_0 I_0^2}{4\pi^2 a^2}\Big(1 - \frac{r^2}{a^2}\Big) \tag{5.38}$$

and thus if T is chosen, for simplicity, to be constant

$$n = \frac{1}{kT}\frac{\mu_0 I_0^2}{4\pi^2 a^2}\Big(1 - \frac{r^2}{a^2}\Big). \tag{5.39}$$

Using this pressure the total axial magnetohydrodynamical force on the flux tube can be calculated by taking the derivative of the pressure as in

$$F_z = (\mathbf{J} \times \mathbf{B})_z - \frac{\partial P}{\partial z} = \frac{\mu_0 I_0^2}{2\pi^2 a^3}\Big(1 - \frac{r^2}{a^2}\Big)\frac{\partial a}{\partial z}. \tag{5.40}$$

This shows that the greatest force occurs for the smallest a and the greatest flare $\frac{\partial a}{\partial z}$. These two formulations reduce the number of variables in the description of flux tube dynamics. They can therefore be modeled without large codes. This will be a subject of analysis in section 5.6.3.

We can also compare this to the unmagnitized inter-electrode plasma discussed in the vacuum arc section 5.2.1 that states that the density is empirically proportional to the current density. If the density equation above is rewritten for $r = 0$ and $J = I_0/\pi a^2$ the result is

$$n = \frac{1}{kT}\frac{\mu_0 a^2 J_0^2}{4}. \tag{5.41}$$

This shows a proportionality to J^2 and not to J, which is most likely a result of the pressure balance confining density. Thus the densities from the vacuum arc engineering were not magnetically confined.

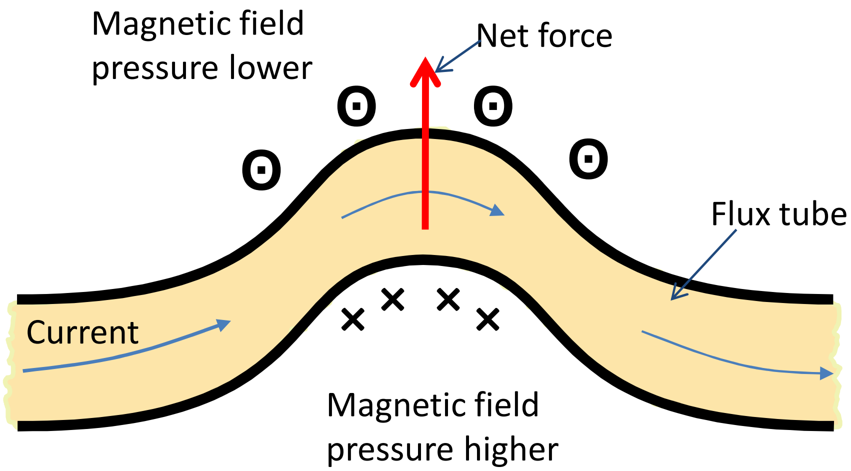

Figure 5.11: This is an illustration of the kink instability, where a perturbation in the side of a fluxtube will cause the magnetic pressure to increase, causing an instability.

This plasma column is a current fluxtube which is subject to Kruskal - Shafranov theory that describes the kink instabilities [64]. The kink instability condition is dependent on the magnetic flux, the fluxtube length, the fluxtube radius, and current. The kinking parameter, or the condition for the development of the kink instability, is given by the equation

$$q_{edge} = \frac{4\pi^2 B_Z}{\mu_0}\frac{a^2}{\ell I} = \frac{4\pi}{\lambda\ell} \tag{5.42}$$

where a is the jet radius, ℓ is the jet length, I is the current and B_z is the background magnetic field [62]. We can define q_{edge} using the parameter $\lambda_{gun} = \mu_0 I_{gun}/\Psi_{gun}$. λ comes from integrating the relation $\nabla \times \mathbf{B} \cong \lambda\, \mathbf{B}$ around the flux tube. This relation holds when the currents are aligned with the magnetic fields and a force free setting [62]. The relation for λ can be obtained by integrating this relation around the electrode. According to the Kruskal - Shafranov theory the kink instability begins to grow when q_{edge} is less than one. The kink instability appears as helical mode vibrations off the jet axis. An illustration of the origin of the kink instability is shown in figure 5.11 and a more in depth look at these types of instabilities is given in section 3.1.2.

5.3 Experimental Setup

Putting a current in a laser-produced plasma to create jet formation has gone through several evolutionary stages. I recite the history of the evolution of this experiment in appendix B to explain the reasons for the experimental setup, and to show important conclusions about this experiment from experiments that did not meet their objectives.

The general experimental set up is the same as it is in chapter 4 with the exception of supplying the potential to the targets. I measured the jet formation in the same way as in the laser produce plasma case, with an ICCD camera, Schlieren, and interferometry. Refer to chapter 4 for the general details of the experiment not included in this chapter.

5.3.1 Experimental Details for the Experiments that Produced Magnetic Jets

The engineering goal for this experiment was to create an unmagnetized supersonic jet embedded in a magnetic field that would serve as the initial conditions for a magnetically controlled jet. The supersonic jet initial conditions are similar to astrophysical jets computer models [109][141] that are uncollimated and unmagnetized in their initial state. Then, in these models, when the magnetic fields form in the central object and the accretion disk the magnetic fields will begin to collimate the jet. Hence experimentally one would like an unmagnetized jet, without from significant currents, that could then have axial currents “turn on” after the unmagnetized jet is established. The magnetic field would serve as a medium to create anisotropic conductivities in the plasma to create a uniform current fluxtube, or a fluxtube defined by the currents and not magnetic fields.

This was accomplished using anode and cathode technology. The electrode was connected to a capacitor that will naturally ring with a characteristic frequency depending on the inductance of the system. Thus the biased electrode will alternate between anode and cathode behavior. This was used to our advantage in a mundane way that produces novel results. As stated in section 5.2.1 an anode that was thermally isolated will heat up very quickly to high temperatures. I chose a small .5 mm diameter Mo wire press held to a copper lug with a plastic cylinder as the electrode. The wire did not deform while pressed against the lug and was hence significantly thermally isolated from its surroundings. A chamber was constructed in which this wire, upon ablation, would fill with molybdenum plasma. A simple flared nozzle created a supersonic flow into the vacuum chamber as in figure 5.2. The amount of material that will be evaporated from this anode will be high, and with the proximity of the ground to the boiling part of the wire, no significant dynamics of the flow through the plasma will be seen. The electrode cathode behavior will not cause the entire wire to heat up globally, but will locally heat up the electrode through the use of cathode spots [13]. In choosing the electrode so small the cathode spots are force to be close to each other thereby increasing the ablation at the tip of the wire.

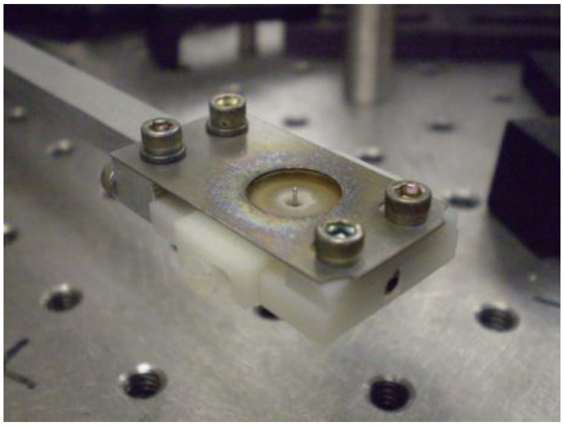

Figure 5.12: Picture of the electrode configuration. The center electrode can be removed. Notice the ablation on the grounded plane.

The entire electrode configuration consisted of a thin molybdenum plate with a 1.0 cm diameter hole with a wire aligned perpendicularly to the plate in the center of the hole as in figure 5.12. The wire was replaceable. The tip of the wire was coplanar with the molybdenum plate. I used 0.5 mm molybdenum wire in the experiment. The electrode was fastened to a small copper lug using a set screw and plastic rod. This lug was connected to a wire that was coaxially enclosed to the feed-through of the chamber. The molybdenum plate was held at ground while the wire held the bias voltage from the capacitor. I designed the electrode holder to be as thin as possible to be able to perform this experiment in close proximity to a permanent magnetic field. With the gap of the electrode being about 0.4 mm, the Paschen curve will ensure that at 1.0 mTorr the voltage will not break down under 5000 V. The molybdenum plate was not in direct contact with the plastic covering that connected to the center electrode. This ensured that carbonization (which is the degrading of the insulation to carbon, a conductor) would not occur in the plastic fixed between the two electrodes.

The capacitor was a 2.4 μF 30,000 V rated capacitor with a .02 μH measured inductance. The high voltage limit ensured that the ringing discharge would not hurt the capacitor. The bias on the capacitor was supplied with a SRS PS300 series 25 W, ±5000 V power supply. The power supply was current limited to ensure no damage would be induced by the discharge. The magnetic field was supplied by the same magnetic field discussed in section 4.3.2 except the magnet was no longer enclosed with another magnet. The magnetic field was measured and reported in figure 5.13 as compared with Maxwell SV calculations of the magnet in figure 5.14.

The YOGA laser was used to trigger the vacuum arc gap. An aluminum target was situated above the electrode system. A pulse of 20 or 200 mJ was used to ablate the aluminum target. Before the ablation the current did not flow in the system because of the Paschen effect. With the introduction of the laser-produced plasma and the subsequent ablated material created in the discharge, current began to flow. As seen in chapter 4 laser-produced plasma created repeatable, well temporally controlled plasma injection sources. This was important to the repeatability and measurement of the jets.

5.3.2 Diagnostics

The main diagnostic for the electrical discharge data was the ICCD camera described in section 4.3.8 and a 411 Pearson transformer. A high voltage probe was used in conjunction with the Pearson transformer to measure the voltage of the capacitor. Schlieren and interferometry were used to laser probe the interaction as described in sections 4.3.6 and 4.3.7. When I implemented the laser probing of the electrical discharge there was no enclo-

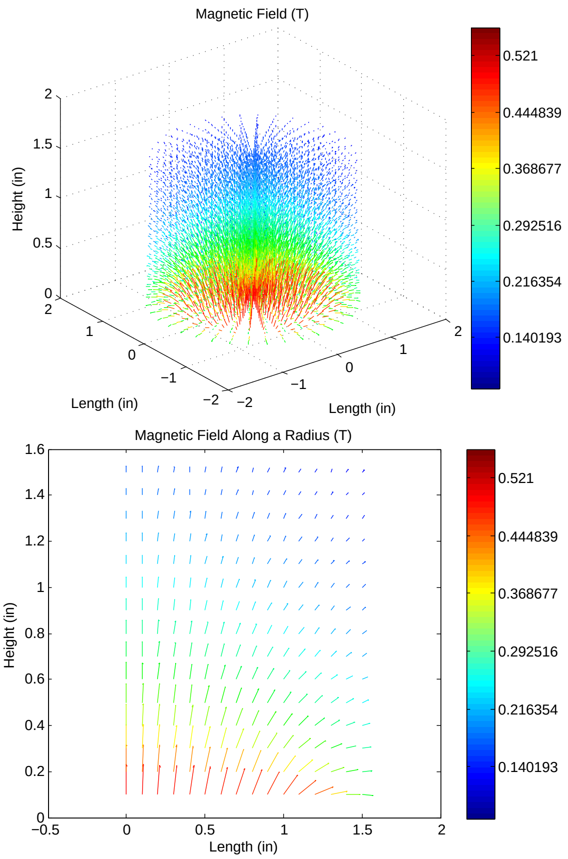

Figure 5.13: Measured values of the magnetic field

sure at the laser plasma interaction to limit the viewing field as was in the laser-produced plasma sections 4.3.6 and 4.3.7.

5.4 Jets Produced using the YOGA Laser

Data taken using ICCD photography revealed varied repeatable spatial features in the images investigated that are related to plasma-jet phenomena. The ICCD camera measured the integrated plasma emission from the

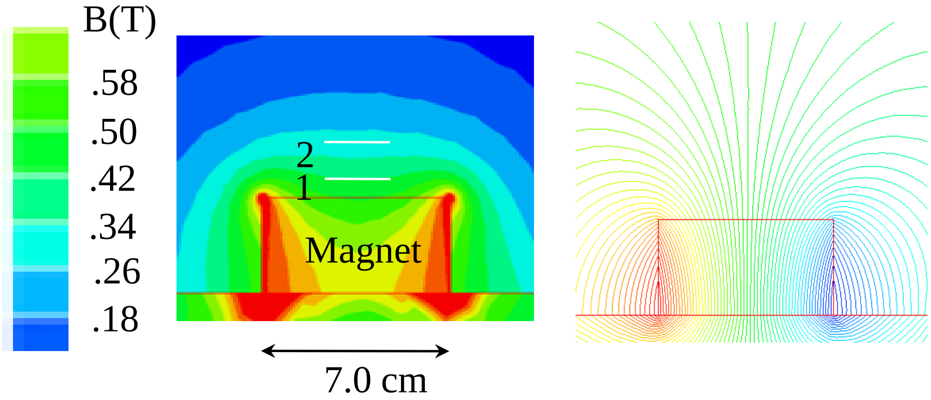

Figure 5.14: Magnetic field calculations of the magnet we use in our experiment using Maxwell SV.

jet area over a range of spectra from 350 nm to 575 nm. The emission is from line radiation and bremsstrahlung radiation. The ICCD camera can not give information about line radiation in this set up, but can give approximate bremsstrahlung measurements. This is related to mostly the density and partially to the temperature as discussed in section 3.3.2. To see these various features together on the same image I used the logarithm of intensity and multi-leveled color maps as in figure 5.15. These features were temporally synchronized to the laser trigger and current discharges were temporally measured. Supersonic nonmagnetic jet dimensions were measured at certain temporal regions of the discharge. Rough estimates of the jet density profile can be obtained using radiance as referred to in section 3.3.2. The barrel shock was measured as a faint cone emanating from the electrode at specific times. Magnetic jet velocities, lengths, and morphologies were measured by quantifying specific features in time. The evolution of a spike formed when the jet was in a sufficiently high magnetic field was measured. The evolution of a divot was measured when in a high magnetic field. With this the current and the morphology of the jet, whether the jet was kinked or straight, were measured.

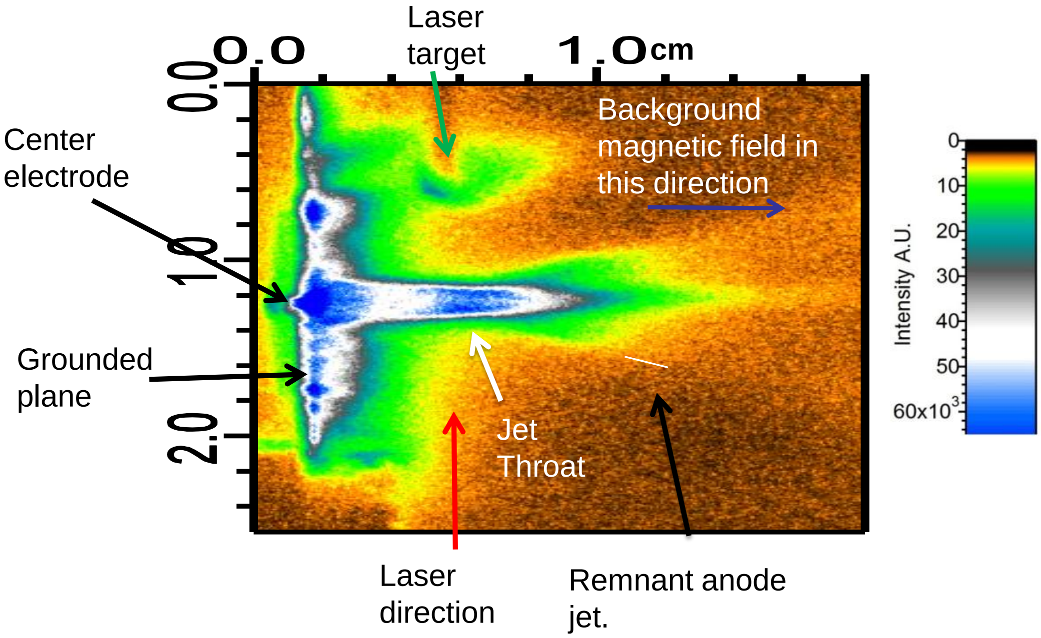

Figure 5.15: Shown are various features found in the ICCD images.

The discharge through the electrode was subject to the alternating current produced by the capacitor and the inductance in the system. The discharge cycle period is about 8.8 μs. I call the time when the current first reverses direction during the discharge “the jet forming region” or the region where a fluxtube developed out of the electrode. This was the temporal region where a remnant supersonic flow was still emanating from the wire cavity. This period is illustrated in figure 5.16. This is the time when the center electrode turns from being an anode to a cathode if the initial bias is positive. Because of the different behaviors electrodes display between anodes and cathodes one would expect that the morphology of this fluxtube varies depending on the initial charge on the capacitor. This is in fact what is observed as in figure 5.17.

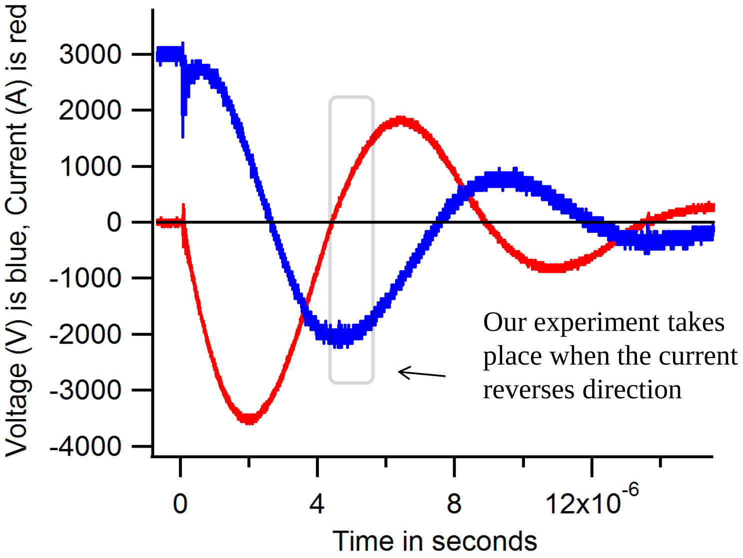

Figure 5.16: Voltage and current measurement of the discharge when the center electrode is biased at 3000 V.

The electrical discharge before the temporal jet-forming region has the center electrode as an anode. As discussed earlier in section 5.2.1, if an anode does not have a sufficient thermal sync the anode will become extremely hot and will boil off metal as a vapor, which is happening right before the jet-forming time. The intensity is high right at the electrode and material coming from the supersonic jet of the electrode setup emanated in a cone with an angle of about 65°. The angle of this cone does not change when placed in a tilted magnetic field. By the time jets form there is a faint, but visible, remnant anode jet or RAJ that is seen just above the noise level of the ICCD camera image as a cone with angle 65°. The boundary of this cone is a barrel

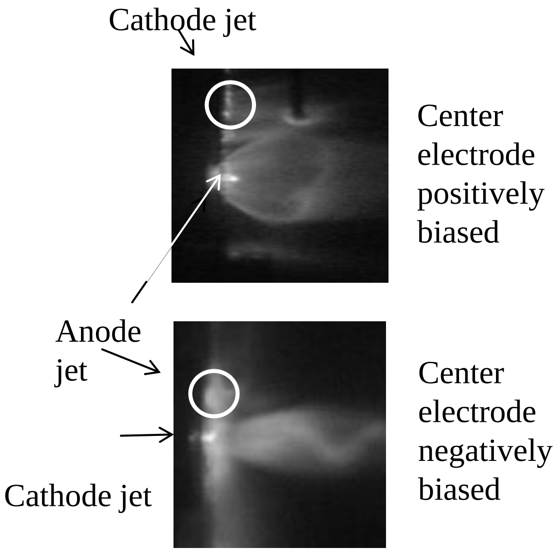

Figure 5.17: In this figure the difference when the center electrode is biased differently can be seen. Notice the cathode spots on the top picture.

shock related to the supersonic flow from the initial anode jet. This will be discussed in the analysis section 5.6.1.

To measure the effects of the anode jet the bias on the center electrode is reversed so it is initially negative. This will then form the supersonic flows and barrel shock during the jet forming region. With and without a background magnetic field a semi spherical shell evolves out of the center electrode as in figure 5.18. This spherical shell has filamentary features that outline the curve on the outer boundary of the expanding plasma indicative of supersonic gas jet formations which will be discussed in section 5.6.1.

Measurements were made for these particular jets using biased voltages of 3000, 4000, and 4900 V, with magnetic field strength of 0.0 T, 0.1 T, 0.23

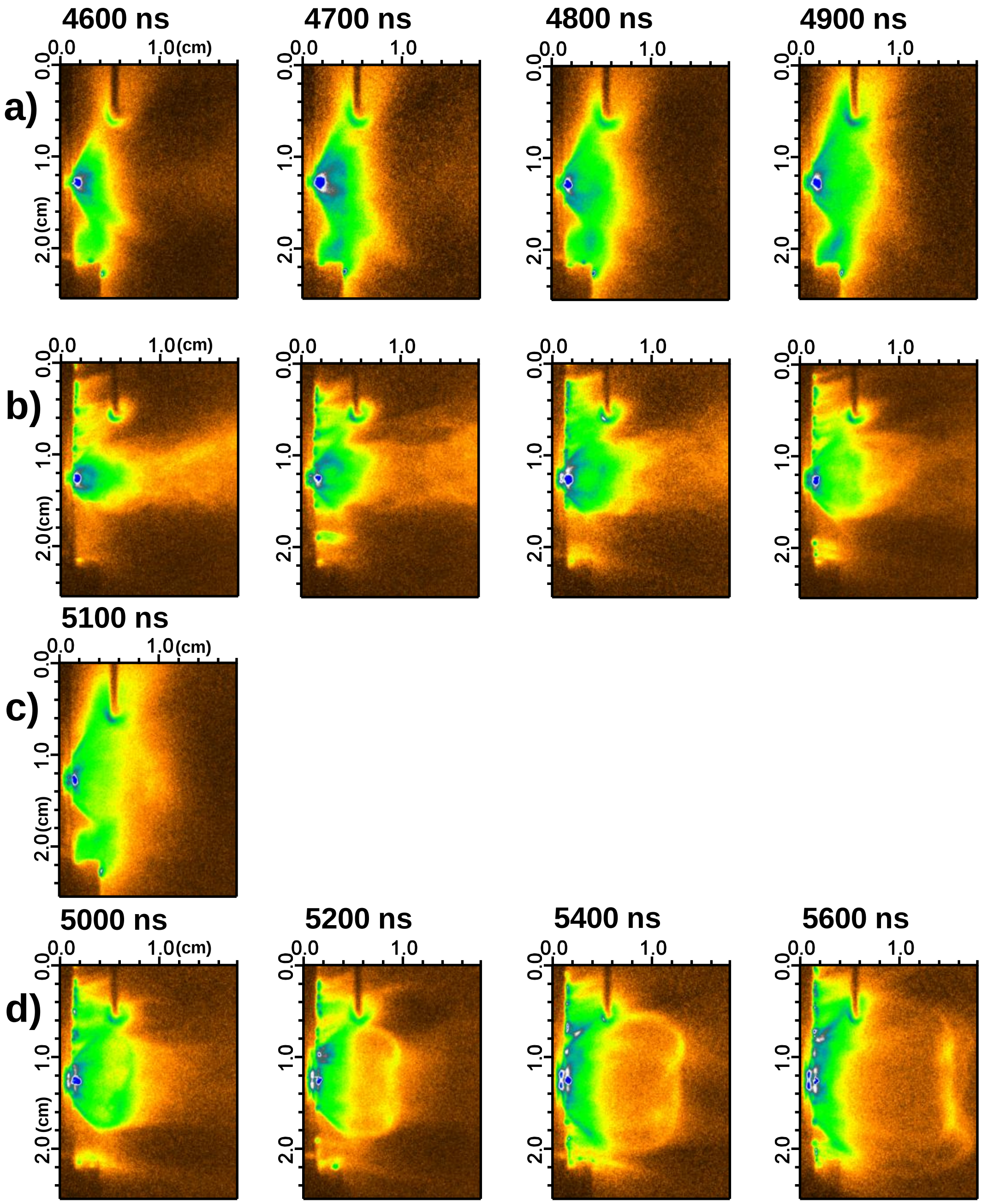

Figure 5.18: Jets with Mo center electrode biased to -3000 V with a) ∼0.0 T and b) ∼.45 T. For figure details see figure 5.15.

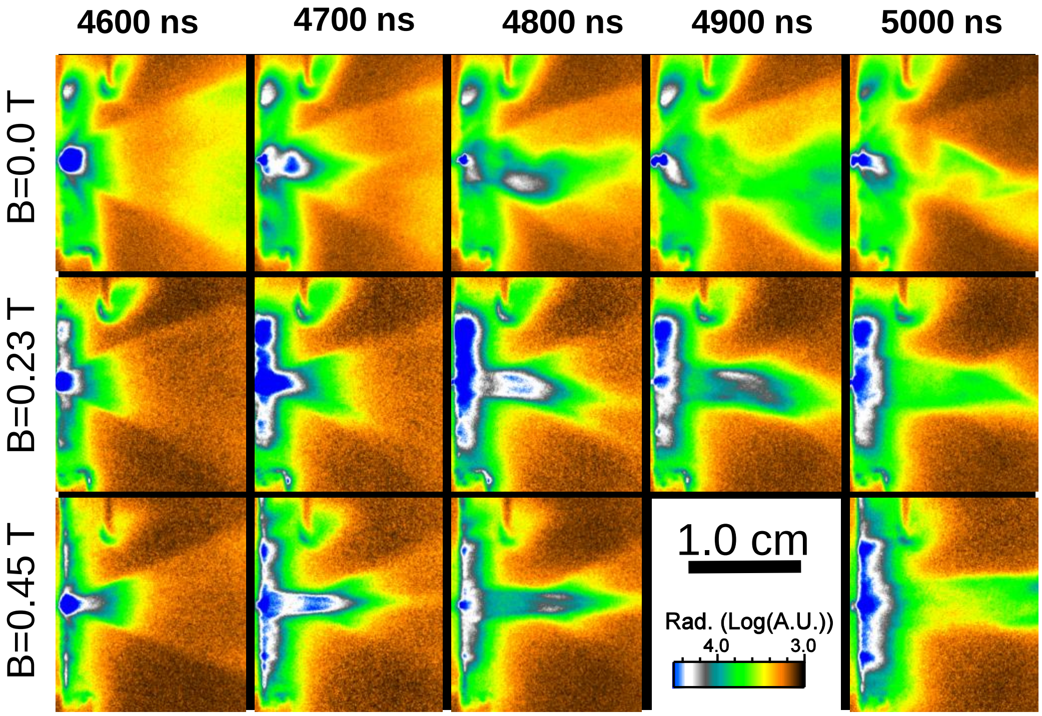

Figure 5.19: Jets with Mo center electrode biased to 4000 V with the early evolution of the RAJ shown. When the current reverses directions (around 4500 ns) the RAJ showed no significant differences with differing background magnetic field strengths.

T, and 0.45 T at the tip of the electrode. The magnetic field strengths were adjusted by elevating the electrode above the magnet. The majority of the emphases was placed on the 0.45 T case and the other magnetic field strengths were for comparison. When investigating the Mo jets in a strong magnetic field of 0.45 T there are many features that differ between different initial voltages (see figures 5.20, 5.21, and 5.22). All of the jets measured in a 0.45 T magnetic field are stable (i.e. no kinks) in the early to mid-late stages of the jet formation. The RAJ formed in all cases with the initial voltage being above

3000 V. The RAJ was very faint in the 3000 V case yet was still measurable. The RAJ was not significantly affected by the magnetic field in the initial phases as seen in the early part of figure 5.19. I took detailed data of the progression of the 4900 V jet in a 0.45 T magnetic field which is reported in figures 5.23 and 5.24. I took images of the 4900 V jet in a 0.45 T magnetic field with a greater field of view as in figures 5.25 to 5.26. These features do extend to longer distances and there are more detailed interactions with the RAJ. There was further evidence of kinking in the magnetic field in these greater field of view measurements. The dark circle around the jet in these images is due to an artifact in the chamber and not to a circular return current.

I performed this experiment also with the electrode arm tilted in the magnetic field. I gave the electrode the maximum tilt possible in the constraints of viewing the interaction in the chamber. The filament expanded in the same general direction without the magnetic field. It seemed to be slightly more kinked in this case. With the magnetic field the filament aligned with the magnetic field. The remnant anode jet seemed to be unaffected by the magnetic field. In the magnetic field case with a 4900 V jet there was a violent kinking detachment of the filament from the electrode region (see figure 5.28). This shows that the magnetic field was definitely important in the formation of jets.

There are distinct differences of plasma emission that are most likely due to the current in the system, with and without magnetic fields. Without the magnetic fields long filamentary features formed in the middle of the RAJ (see figure 5.30). This filamentary feature in the 0.0 T magnetic field case is kinked. There is a different feature with a strong magnetic field. Instead of a kinked filamentary feature a roughly flat profile cone radiated in the remnant

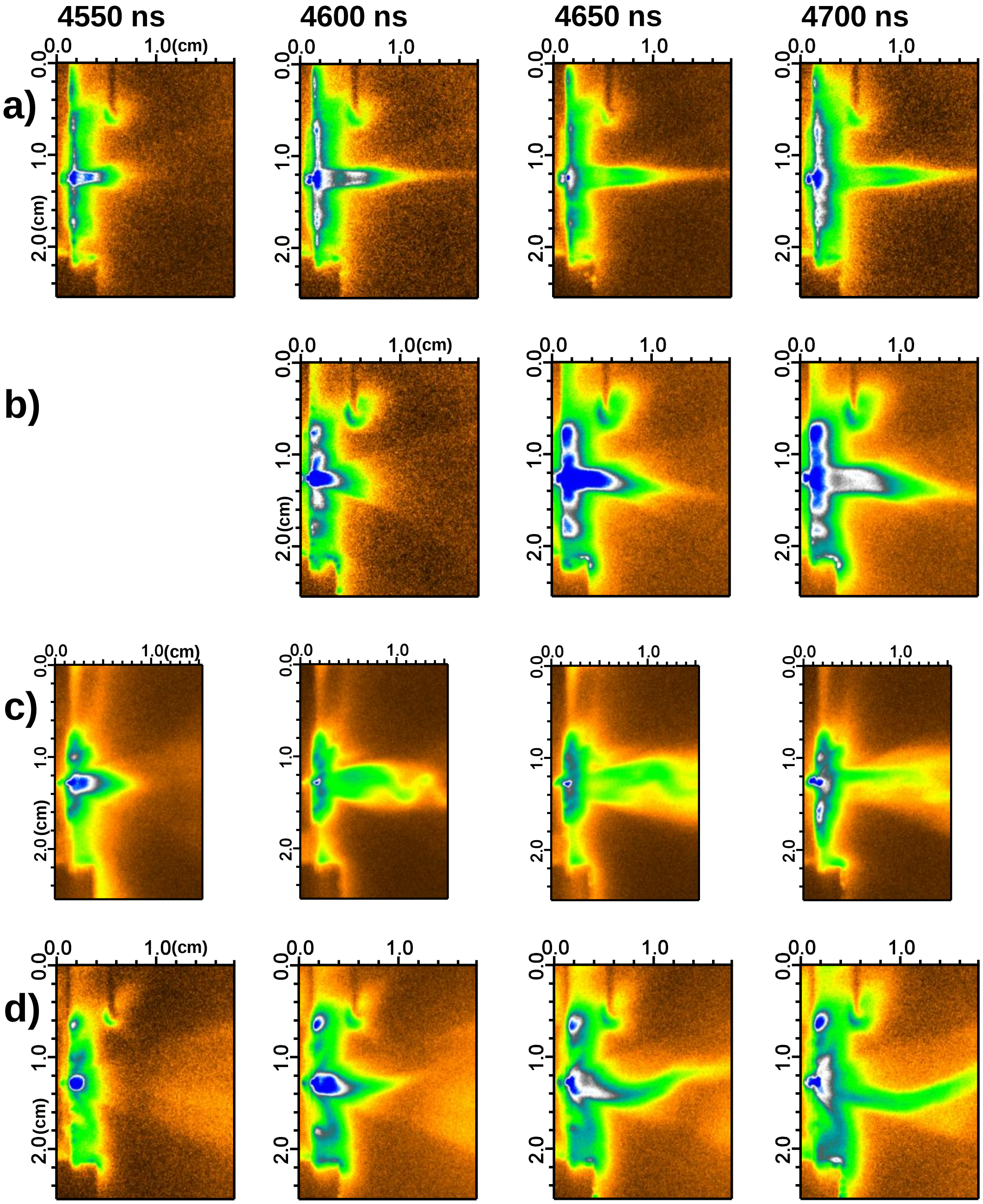

Figure 5.20: Jets with Mo center electrode biased to 3000 V. The varying magnetic field strengths are a) ∼.45 T, b) ∼.23 T, c) ∼.1 T, and d) ∼0.0 T. For figure details see figure 5.15.

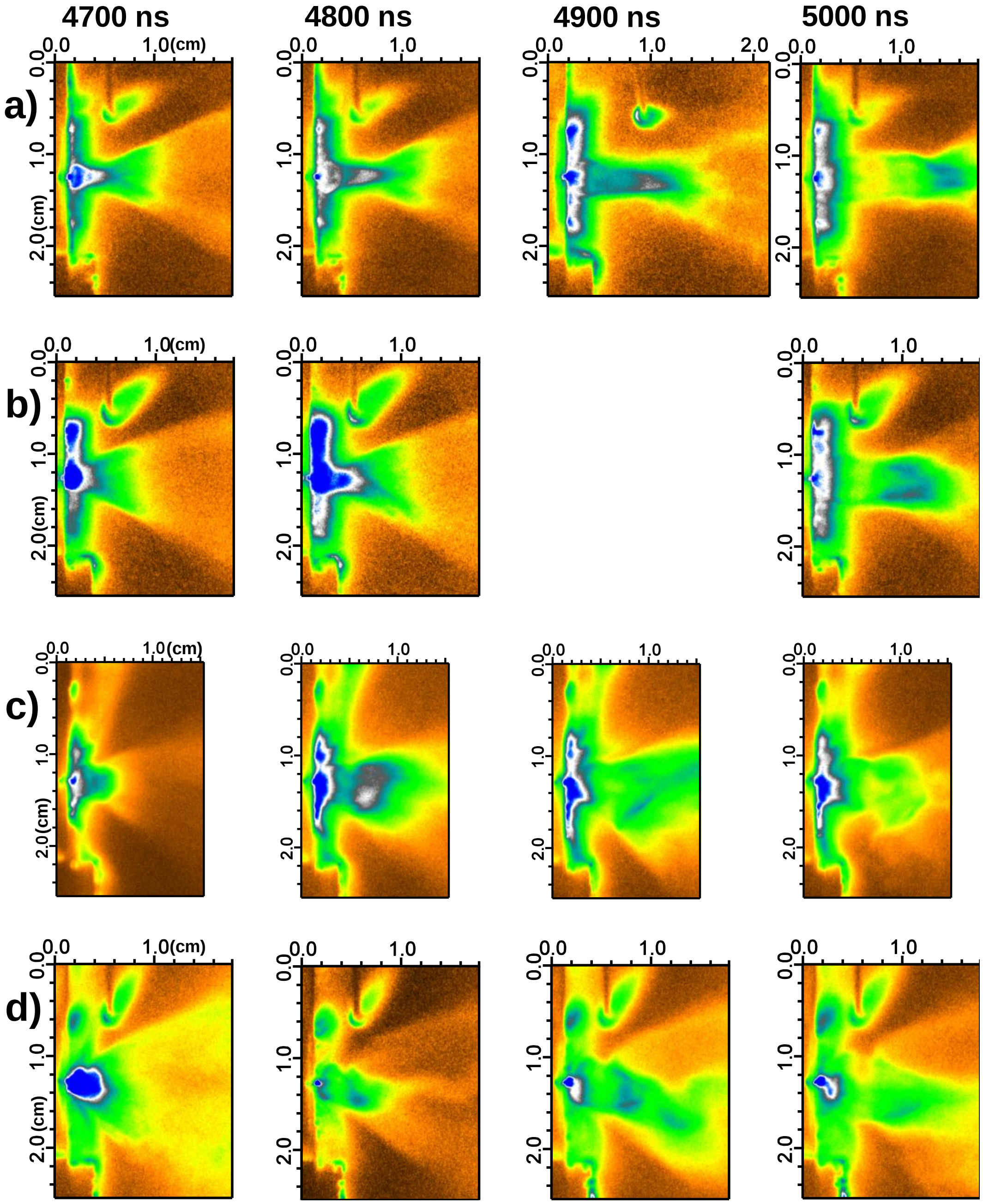

Figure 5.21: Jets with Mo center electrode biased to 4900 V. The varying magnetic field strengths are a) ∼.45 T, b) ∼.23 T, c) ∼.1 T, and d) ∼0.0 T. For figure details see figure 5.15.

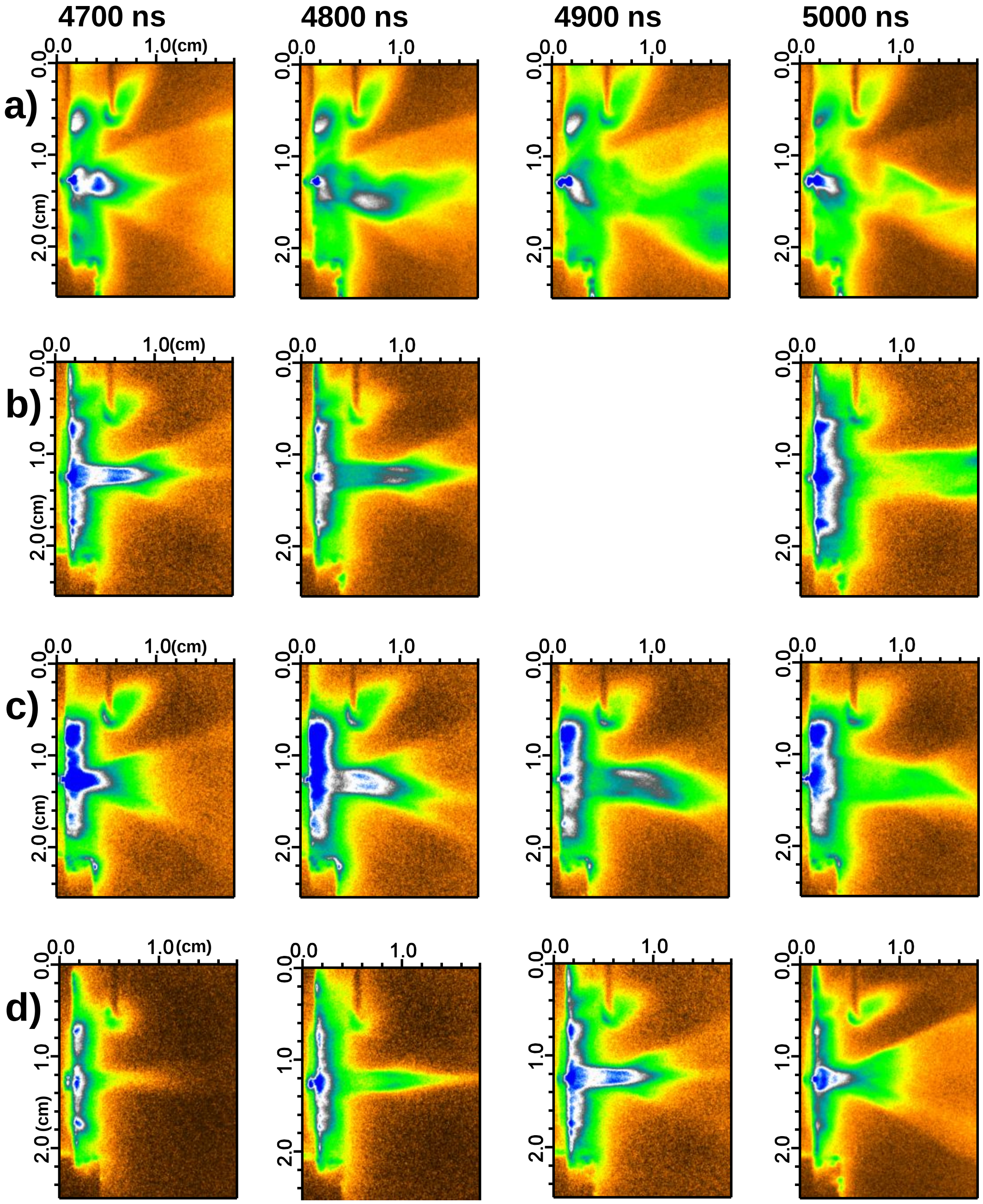

Figure 5.22: a)-c) Mo center electrode biased to 4000 V. a) no B field, b) ∼.45 T B field, and c) ∼.23 T B field. d)progression of Mo jet in ∼.45 T B field at 4700 ns with 2000 V (on the left), 3000 V, 4000 V, and 4900 V.

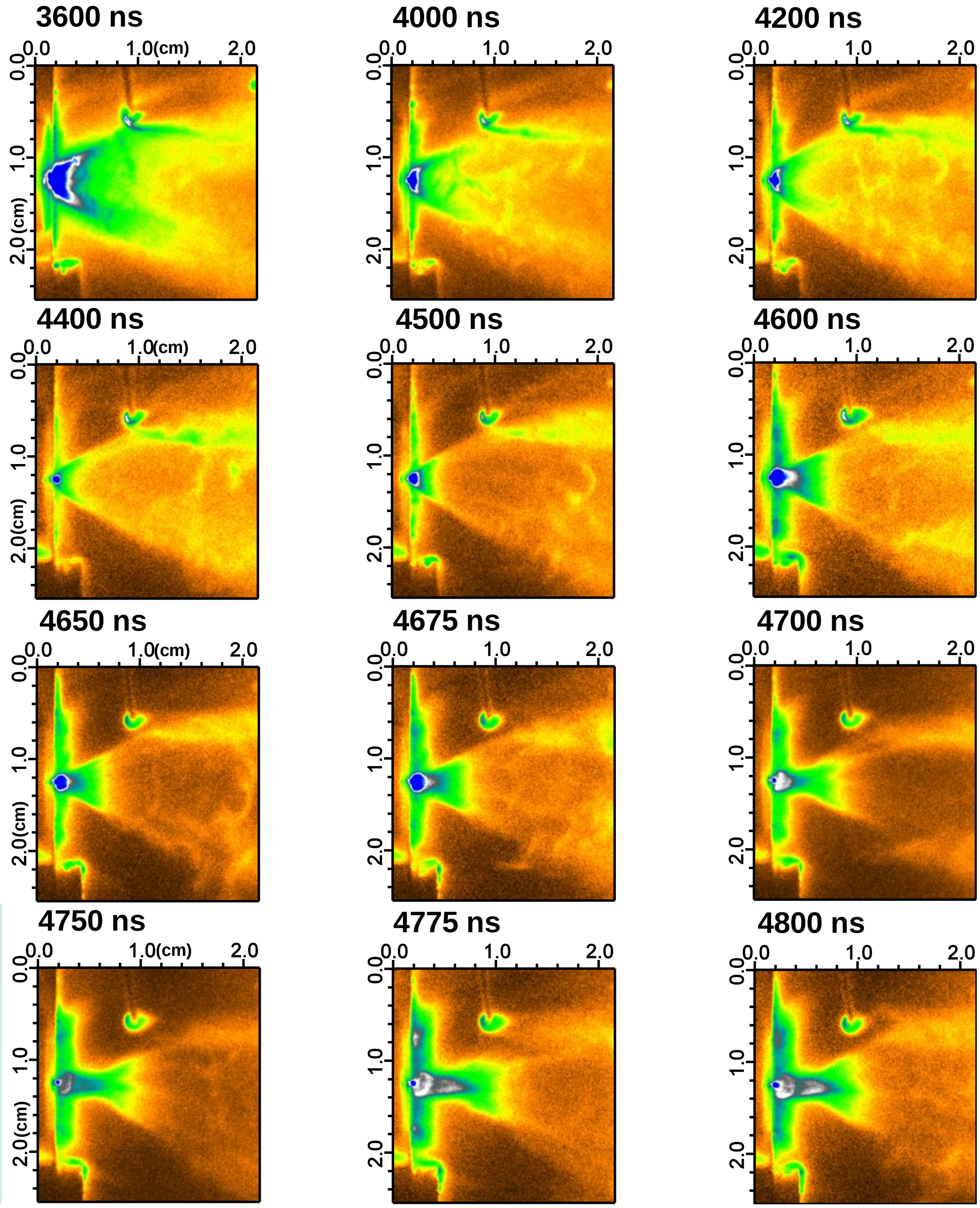

Figure 5.23: Jet sequence with Mo electrode biased to 4900 V in a ∼.45 T open magnetic field. For figure details see figure 5.15.

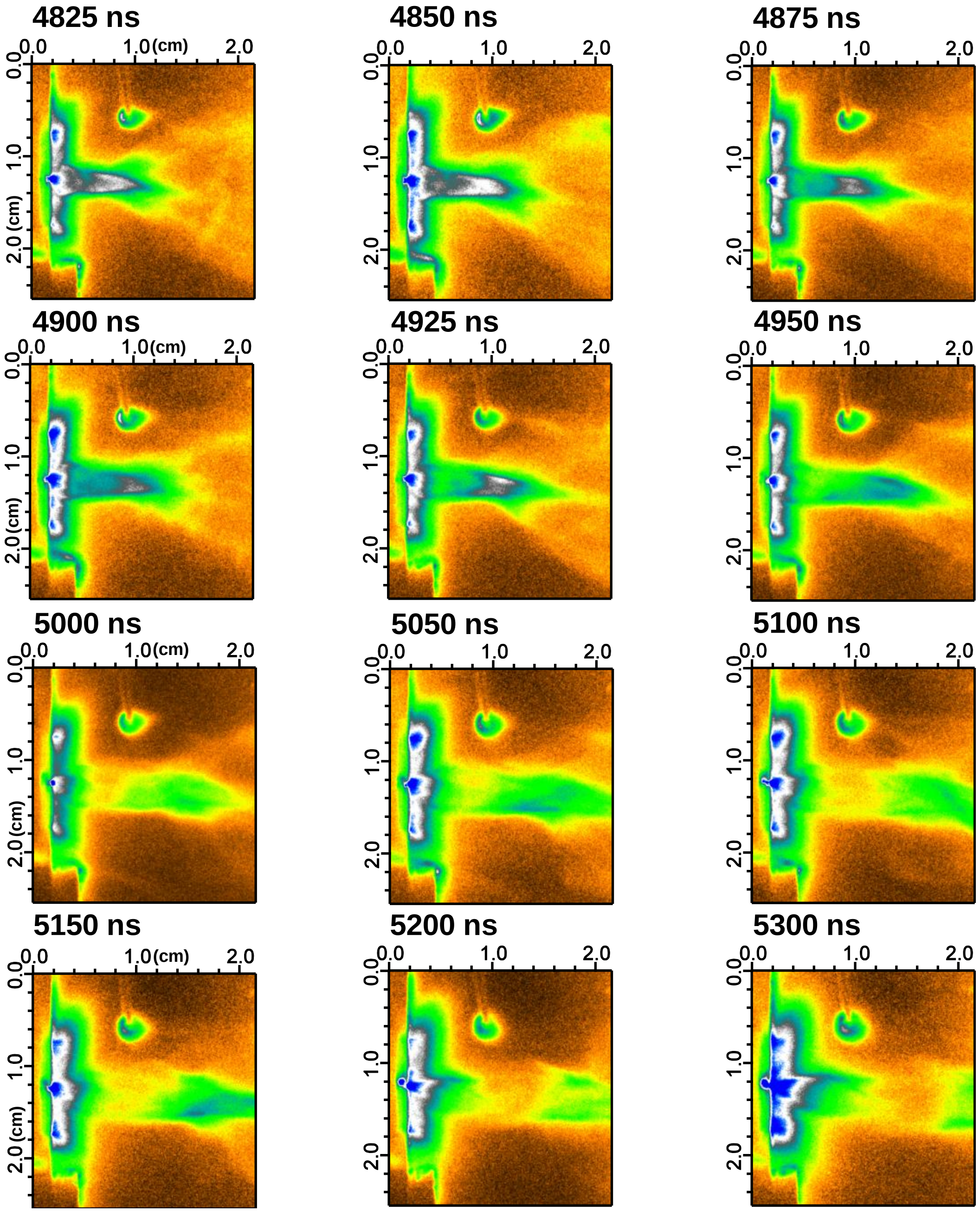

Figure 5.24: Jet sequence with Mo electrode biased to 4900 V in a ∼.45 T open magnetic field. For figure details see figure 5.15.

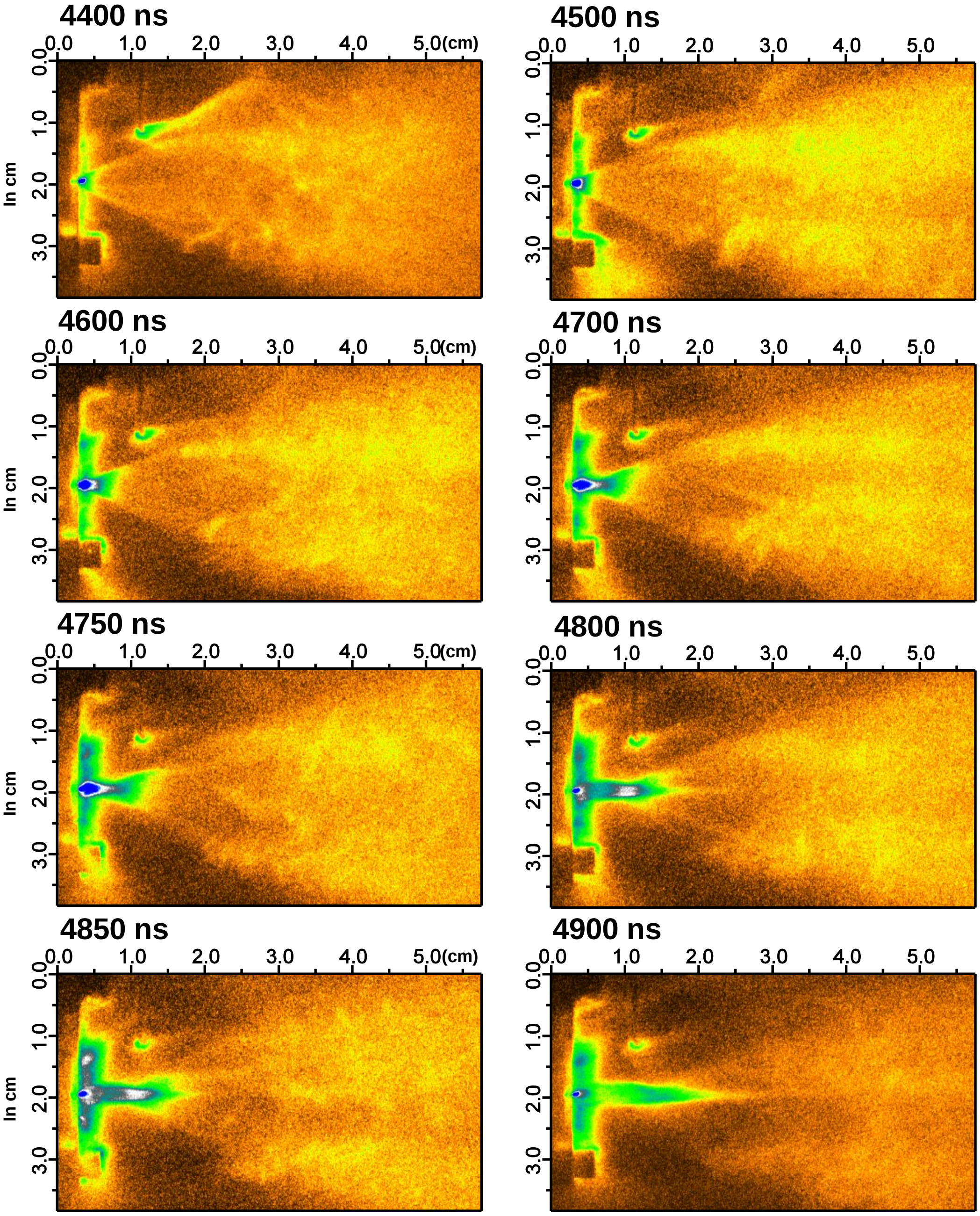

Figure 5.25: Jet sequence with Mo electrode biased to 4900 V in a ∼.45 T open magnetic field. The field of view has been extended. For figure details see figure 5.15.

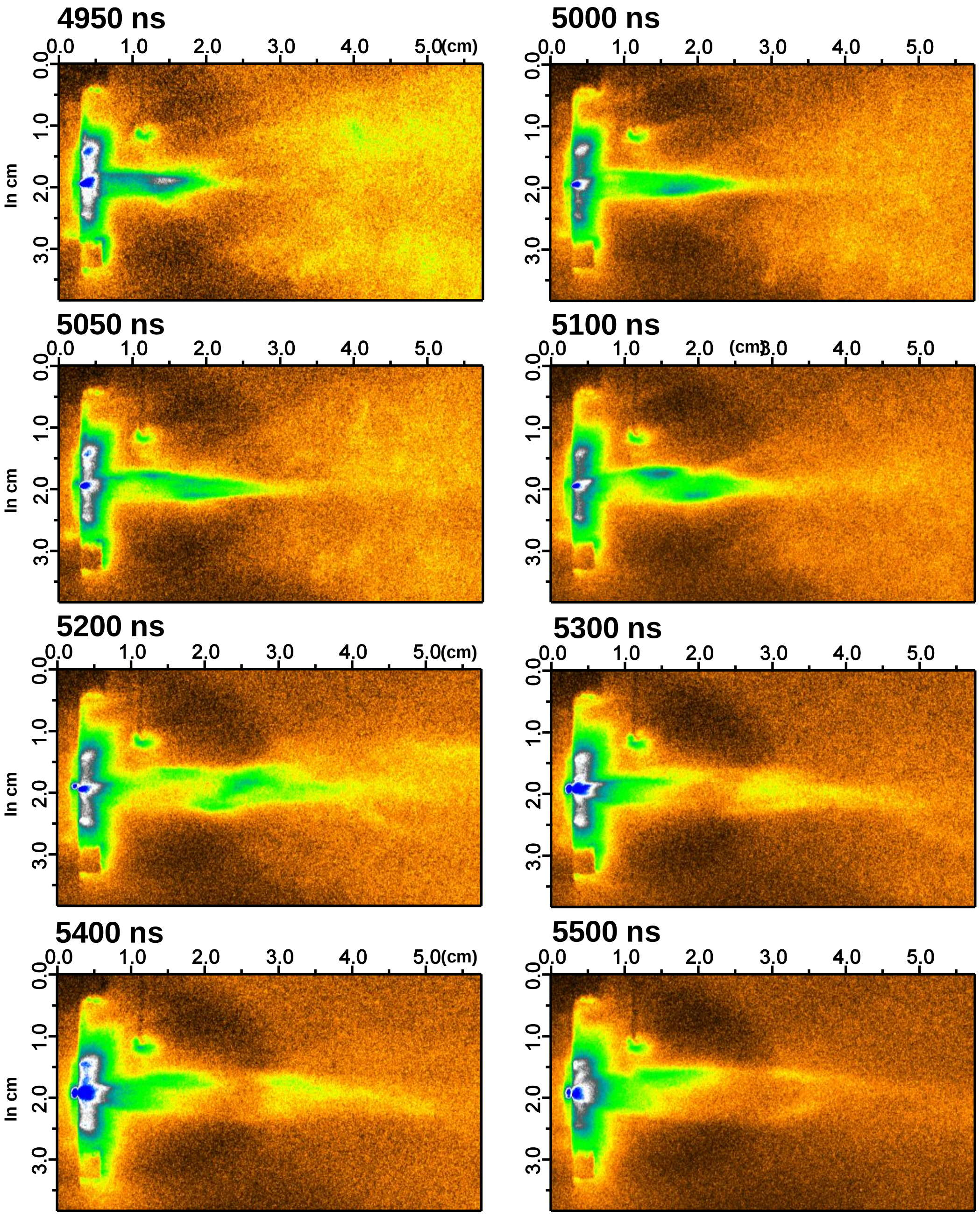

Figure 5.26: Jet sequence with Mo electrode biased to 4900 V in a ~.45 T open magnetic field. The field of view has been extended. For figure details see figure 5.15.

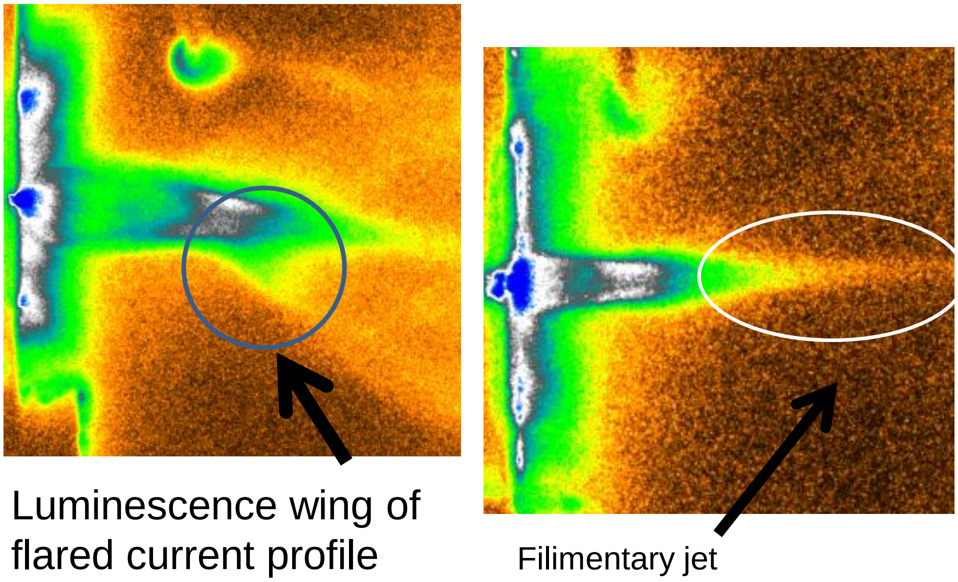

Figure 5.27: With the magnetic field, an emission spike formed out of the jet (on the right) which I call the filamentary jet or jet tip. The effects of the flared current profile can still be seen when this feature is present (on the left).

anode jet (see figure 5.29). This flat profile develops a protrusion in the center as time progressed but in the higher voltage cases you can still see part of this flat profile adjacent to this protrusion as in figure 5.27. A long straight filamentary feature developed in the center of the remnant anode, that could clearly be seen to have grown in modest initial voltages as in figure 5.27. This feature grows extraordinarily fast as compared with the jet throat, and is reproducible. This feature is distinctly visible in the cases 3000 V to 4900 V with magnetic fields .23 T and .45 T. I call this the jet tip and report its velocity in table 5.3.

The luminosity of the jet throat decreased uniformly over time, and a divot, or dip-like depletion, in the luminosity increased over time to about 50%

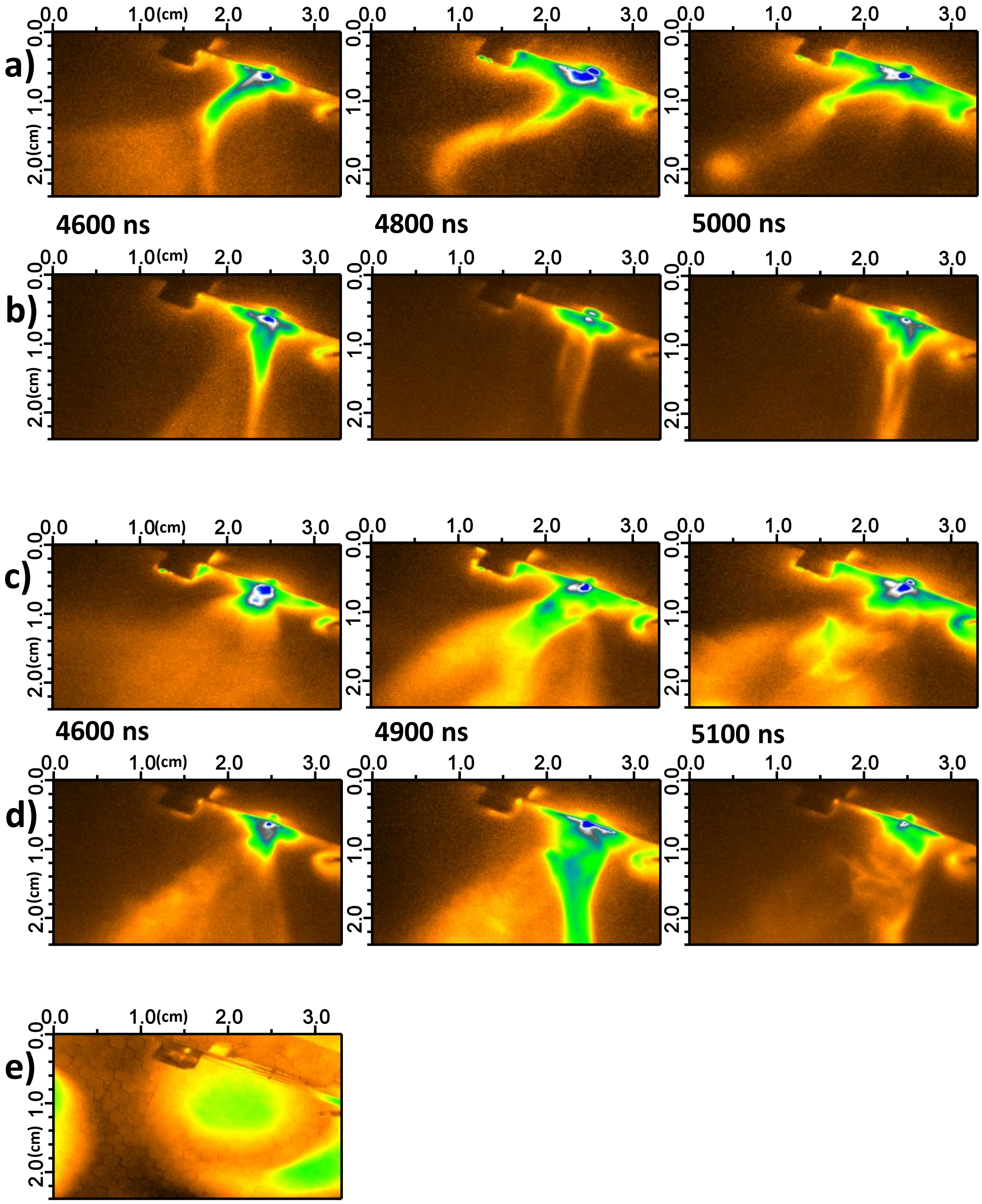

Figure 5.28: Mo jet progression in tilted B fields with a) 3000 V and ∼0.0 T B field, b) 3000 V and ∼0.4 T B field, c) 4900 V and ∼0.0 T B field, d) 4900 V and ∼0.4 T B fields. The B fields align with vertical axis.

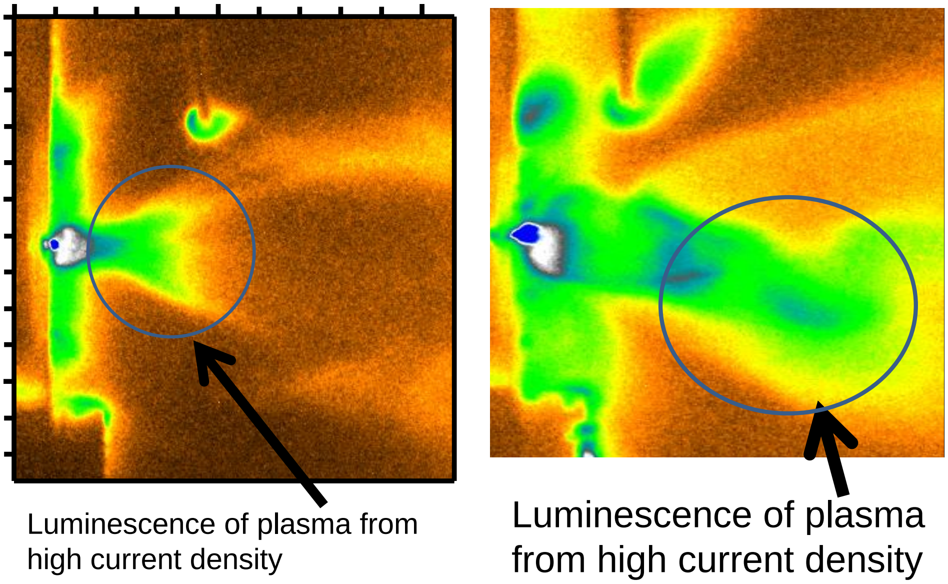

Figure 5.29: When the fluxtube decreased in diameter, the pressure balance predicts that the current density and the plasma density increased, and hence the plasma emission increased. This was manifest differently with magnetic fields (on the left) and without magnetic fields (on the right). With the magnetic fields the current forms a flat cone shaped profile and without the magnetic field the current forms a more narrow non symmetric fluxtube.

in the log scale as in figures 5.31 and C.6. This divot formed in all of the Mo cases in a magnetic field above and including 3000 V. This divot formed also in cases where the magnetic field is less and even zero, but it is more distinct in the higher magnetic field case.

The repeatability of the data is an important issue to address. The images look similar between different shots of the same time. Most of the features seem to evolve similarly in a time evolution. Multiple shots of the same time were not often taken, because of the importance of taking many varied shots and the time it takes to make one shot. But of the shots that

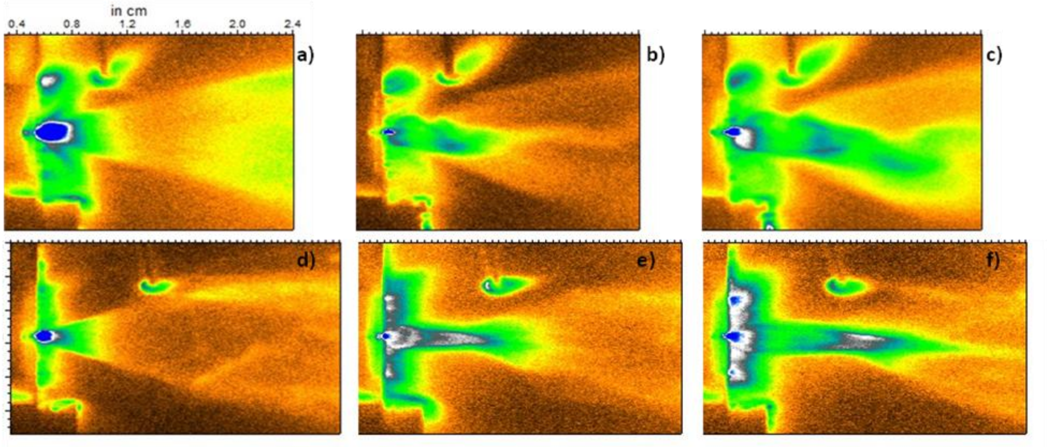

Figure 5.30: Jets with and without B field with the capacitor charged initially to 4900 V. False color ICCD images with a logarithmic scale. a) - c) are without a magnetic field and d) - f) are in the presence of a .45 T magnetic field aligned horizontally on the images. a) and d) are at 166ns , b) and e) are at 366ns , and c) is at 466ns and f) is at 491ns after the $I = 0$ point.

were taken with the same times and circumstances were very visually similar. This was also seen in the similarity of the evolution of the various features in the jets. Data from the Pearson transformer also showed repeatability.

The Pearson transformer data shows a typical damped RLC oscillator circuit discharge as in figure 5.16. I used a 10X probe to measure the output of the Pearson transformer. Often the oscilloscope does not measure the complete dynamic range of the Pearson transformer, but there was enough information from the discharge to fit an appropriate damped oscillator equation to the data. Because of the repeatability of the data only about three data shots per experimental parameter were taken. Obtaining the timing information between the Pearson data with the images was problematic. I measured the timing delay of the Pearson transformer as measured with the experiment

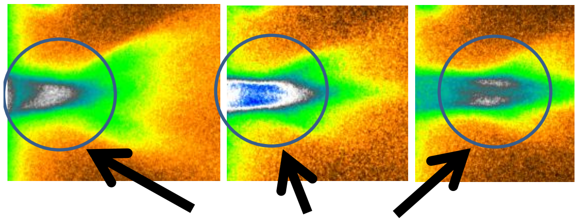

Progression of divot feature in the ablated plasma

Figure 5.31: A divot in the luminosity profile of the jet throat forms as the jet progresses.

	0.0 T	0.23 T	0.45 T
3000 V	$6.2 \pm 0.5 \times 10^4 \mathrm{m/s}$	$3.6 \pm 0.3 \times 10^4 \mathrm{m/s}$	$4.1 \pm 0.4 \times 10^4 \mathrm{m/s}$
4000 V	$5.1 \pm 0.3 \times 10^4 \mathrm{m/s}$	$3.2 \pm 0.5 \times 10^4 \mathrm{m/s}$	$5.9 \pm 0.4 \times 10^4 \mathrm{m/s}$
4900 V No.1	$3.9 \pm 0.2 \times 10^4 \mathrm{m/s}$	$4.1 \pm 0.4 \times 10^4 \mathrm{m/s}$	$4.4 \pm 0.9 \times 10^4 \mathrm{m/s}$
4900 V No.2			$4.8 \pm 0.4 \times 10^4 \mathrm{m/s}$

Table 5.1: Jet throat velocity as fit with a linear regression from measurements obtained from ICCD data. 4900 V No.1 is of the jet measured with the standard field of view as in figure 5.23, and 4900 V No.2 is of the jet measured with the larger field of view as in figure 5.25.

during one data set. I measured an uncertainty of the timing from this measurement that was used for the analysis.

In the presence of a background magnetic field the material in the jet throat is confined along the axis of the electrode. Without the magnetic field this plasma has a more or less hemispherical expansion. I measure the velocity of the expanding jet throat material by fitting the jet throat region with a Gaussian function and recording the peak. This collection of data then gave the velocities of the jet throat progression. The data measured is in figure

	0.0 T	0.23 T	0.45 T
3000 V	$-1.3 \pm 1.8 \times 10^{4}\mathrm{m/s}$	$4.1 \pm 5.8 \times 10^{4}\mathrm{m/s}$	$1.5 \pm 3.3 \times 10^{4}\mathrm{m/s}$
4000 V	$-0.1 \pm 4.7 \times 10^{3}\mathrm{m/s}$	$3.0 \pm 2.2 \times 10^{4}\mathrm{m/s}$	$3.4 \pm 2.4 \times 10^{4}\mathrm{m/s}$
4900 V No.1	$6.9 \pm 4.6 \times 10^{3}\mathrm{m/s}$	$1.9 \pm 1.5 \times 10^{4}\mathrm{m/s}$	$3.3 \pm 1.2 \times 10^{4}\mathrm{m/s}$
4900 V No.2			$2.6 \pm 0.2 \times 10^{4}\mathrm{m/s}$

Table 5.2: RAJ intercept velocity as fit with a linear regression from measurements obtained from ICCD data. 4900 V No.1 is of the jet measured with the standard field of view as in figure 5.23, and 4900 V No.2 is of the jet measured with the larger field of view as in figure 5.25.

	0.0 T	0.23 T	0.45 T
3000 V	$1.4 \pm 0.3 \times 10^{5}\mathrm{m/s}$	$1.7 \pm 0.3 \times 10^{5}\mathrm{m/s}$	$1.5 \pm 0.3 \times 10^{5}\mathrm{m/s}$
4000 V	$7.1 \pm 1.2 \times 10^{4}\mathrm{m/s}$	$7.9 \pm 1.4 \times 10^{4}\mathrm{m/s}$	$9.2 \pm 1.4 \times 10^{4}\mathrm{m/s}$
4900 V No.1		$5.4 \pm 1.4 \times 10^{4}\mathrm{m/s}$	
4900 V No.2			$7.7 \pm 0.4 \times 10^{4}\mathrm{m/s}$

Table 5.3: Jet tip velocity as fit with a linear regression from measurements obtained from ICCD data. 4900 V No.1 is of the jet measured with the standard field of view as in figure 5.23, and 4900 V No.2 is of the jet measured with the larger field of view as in figure 5.25.

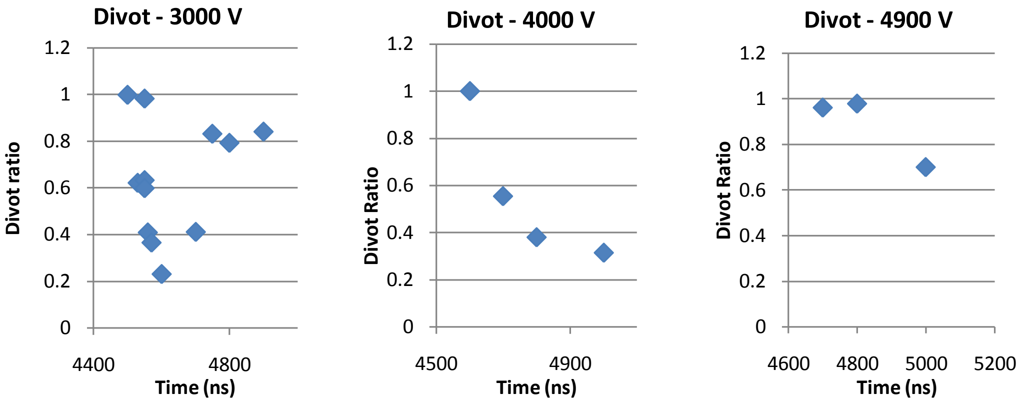

Figure 5.32: Progression of the divot formed in the throat of the jet. The line profile was fit to two opposing gaussian profiles, with the divot given a negative number for the gaussian amplitude. The reported number in the graph is the percent of the subtracted gaussian area from the positive gaussian area.

5.33, and the velocities calculated are in table 5.1. I quantify the evolution of the RAJ by fitting two boundary lines enclosing the cone that emanates from the approximate position of the electrode. I record the slope of both RAJ lines and the intercepts of these two lines as the RAJ intercept as in figure 5.38. The angle of the RAJ is reported in figure 5.35, and the position of the RAJ intercept is reported in figure 5.36, with the velocities in table 5.2. Other points were recorded, such as the jet tip of the filamentary feature that expands away from the jet as reported in figure 5.34. A comparative study that will be discussed in chapter 6 and appendix D deals with jet produced that emanated onto a magnetic dipole. In one instance this created something akin to a plasma flare as in figure D.4 and 6.10. The position of this flare is reported in figure 5.37 and the initial velocity is $1.12 \pm .12 \times 10^7$ cm/s. Also the divot was quantized by fitting the intensity profile of the divot with a double

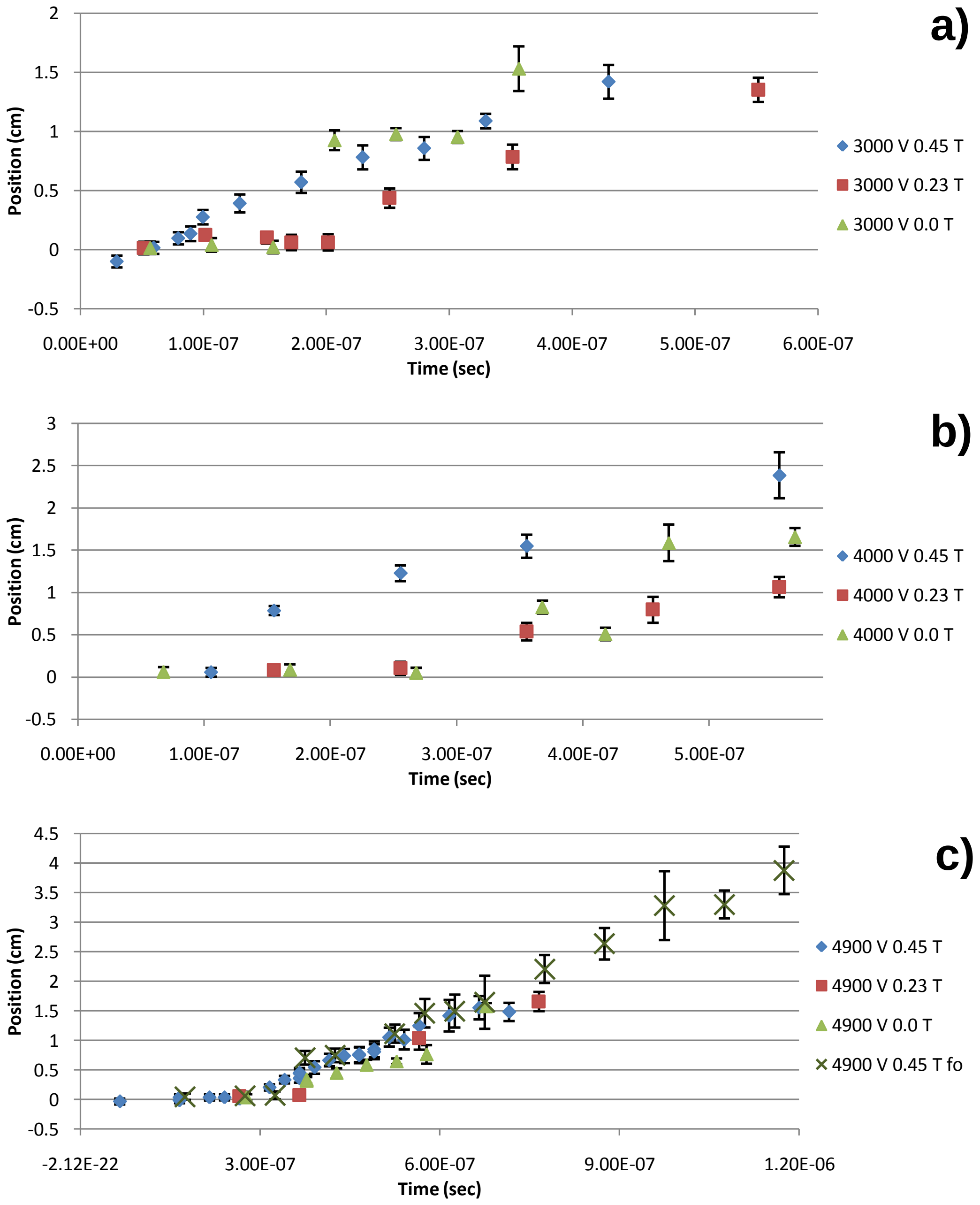

Figure 5.33: Dense jet throat region progressing with time, a) 3000 V, b) 4000 V, and c) 4900 V

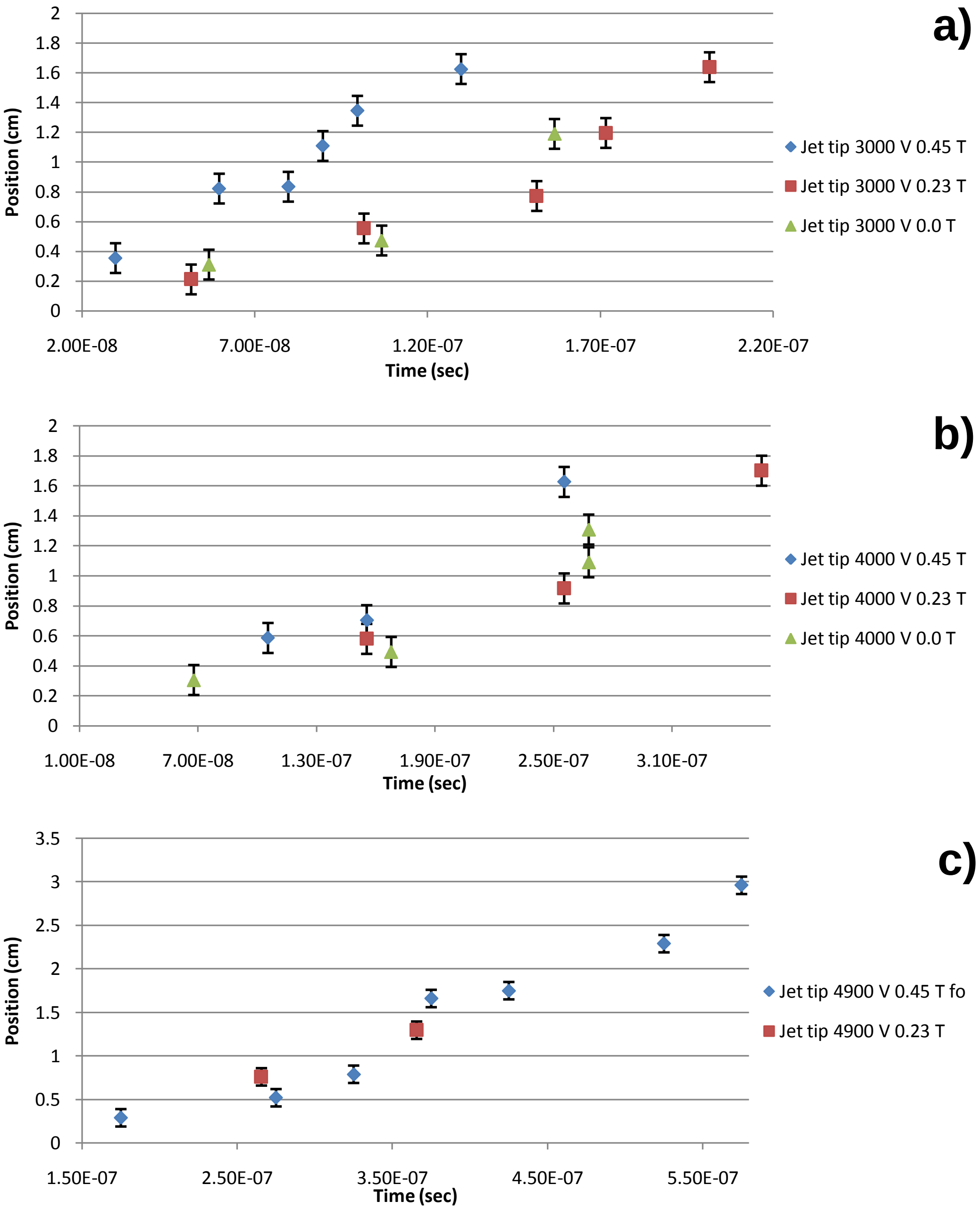

Figure 5.34: Tip of the jet progressing with time, a) 3000 V, b) 4000 V, and c) 4900 V

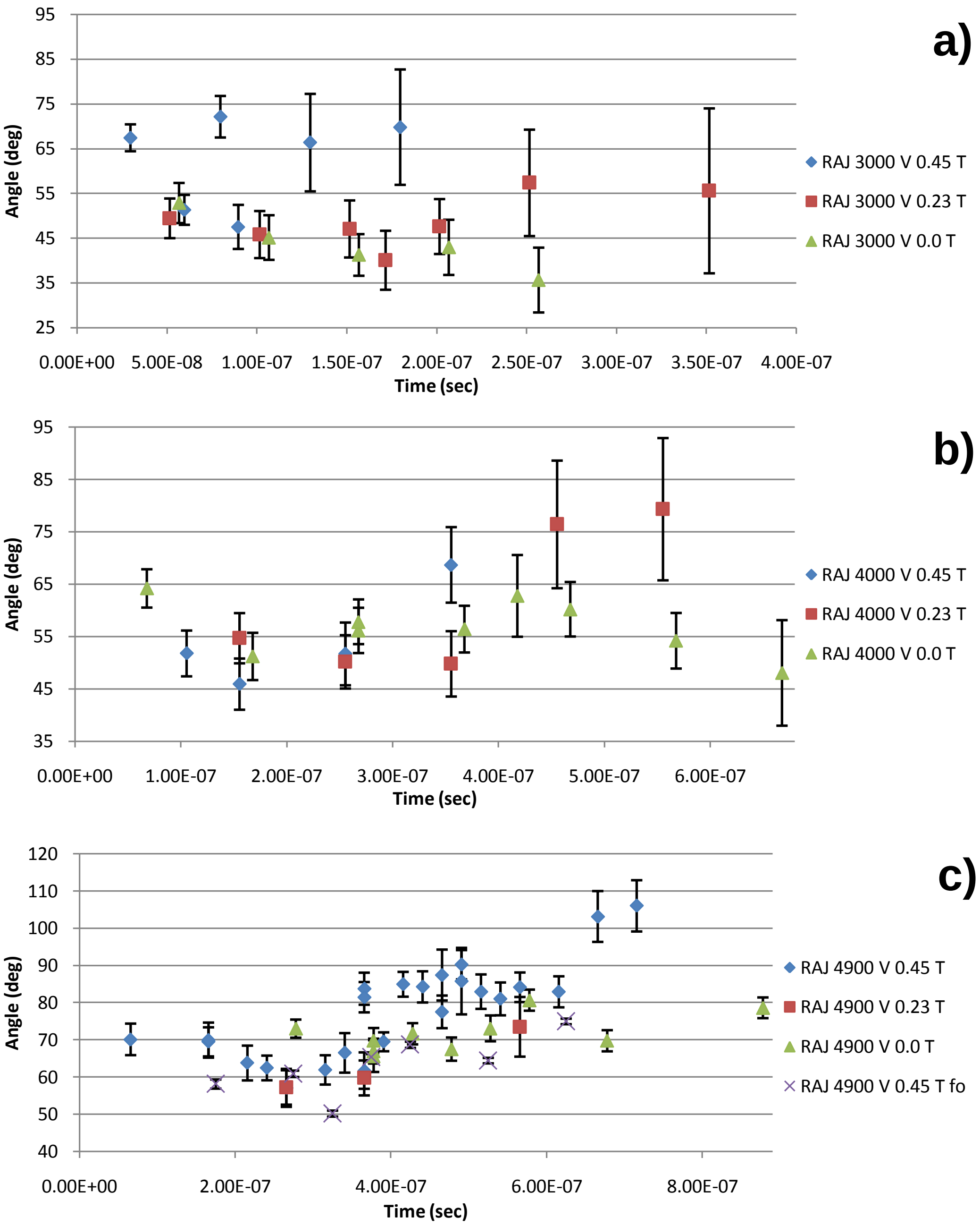

Figure 5.35: RAJ angle progressing with time, a) 3000 V, b) 4000 V, and c) 4900 V

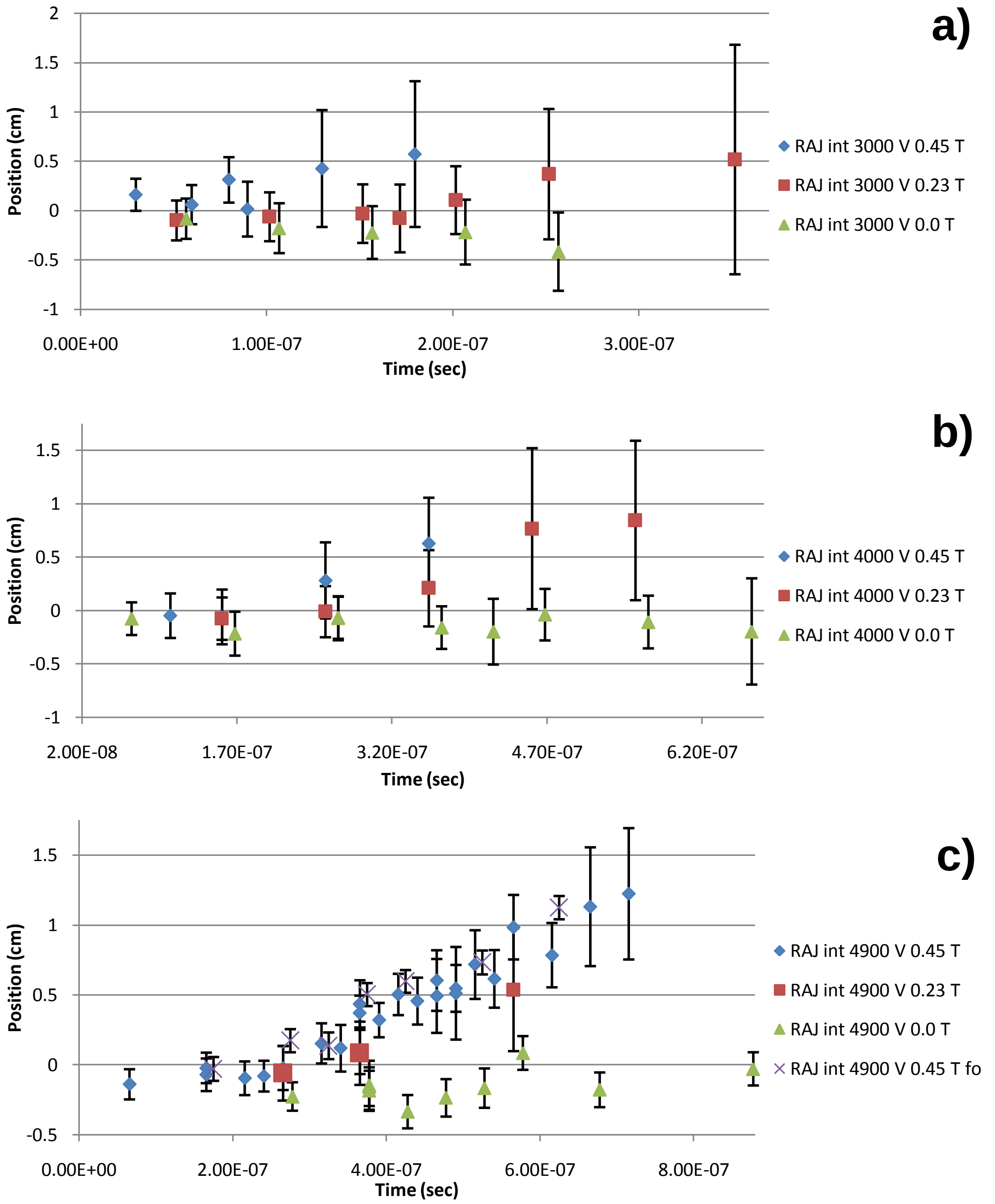

Figure 5.36: RAJ jet axis intercept progressing with time, a) 3000 V, b) 4000 V, and c) 4900 V

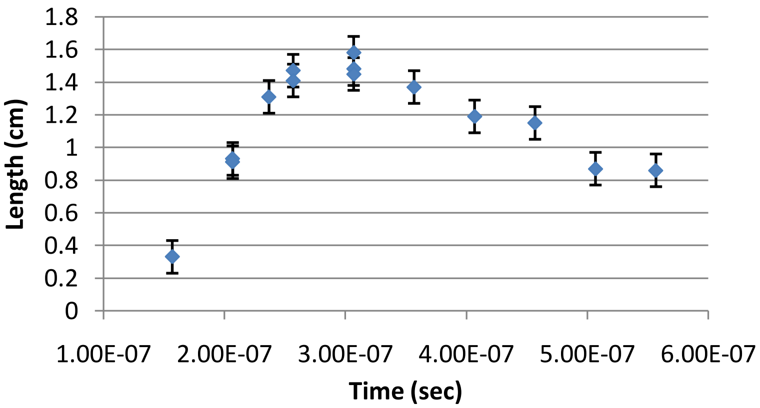

Figure 5.37: Tip of the flare in a magnetosphere experiment as it progresses in time with 3000 V initial charge. See figures 6.10 and D.4.

gaussian

$$y = y_0 + A_1 e^{\left(\frac{(x-x_0)^2}{Wid_1}\right)} - A_2 e^{\left(\frac{(x-x_0)^2}{Wid_2}\right)}. \tag{5.43}$$

The percent of the area of the minor gaussian to the area of the major gaussian was recorded. A table listing these fits is presented in the appendix in table C.2. In figure 5.32 the progression of the divot in time was reported. The measurement in this figure was the percent of the subtracted gaussian area from the positive gaussian area in the fits above. This showed a relative increase of the divot in the jet throat. For the 3000 V case there was a strong dip in the divot and as the overall intensity of the jet throat decreased the divot ratio increased again, but not to the original levels.

In these data figures and tables one can see that the jet throat progressed at roughly the same speed of about 4.0×10^6cm/s and the jet tips progressed at more than double this speed. When there was a background magnetic field the intercepts of the RAJ evolved with the jet throat material at approximately the same speed as in tables 5.1 and 5.2, and the angle of the

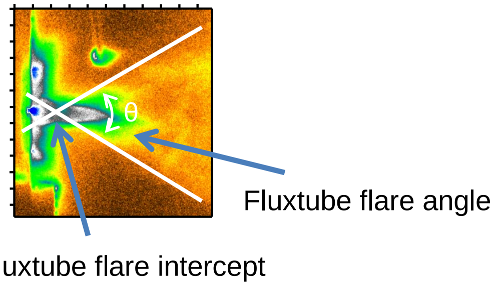

Figure 5.38: The definition of the RAJ intercept and angle.

RAJ cone increased with time in higher voltages as illustrated in figure 5.35. With no magnetic field the RAJ angle stayed the same or even decreased in the case of the 3000 V jet. The RAJ intercept speed reflected on this behavior. Many of these measured quantities will be analyzed and compared with models in the next section.

5.5 Schlieren and Interferometry Measurements of Laboratory Produced Jets

I took Schlieren and interferometric measurements of the plasma jets using the capacitor charged to 4900 kV and in .45 T magnetic field with the purpose of measuring the density. I used the same setup for this measurement as we did for laser-produced plasmas in chapter 4. Optical measurements for this jet were difficult to differentiate from the background. There was concern that the discharge from the capacitor would induce too much noise in the system to take the needed data. The interferometric data's integrity was tested by taking interferometric measurements of the laser-produced plasma while the discharge was taking place. There was a clear interferometric signal of the anode jet before our usual cathode jets began to form. I took only one

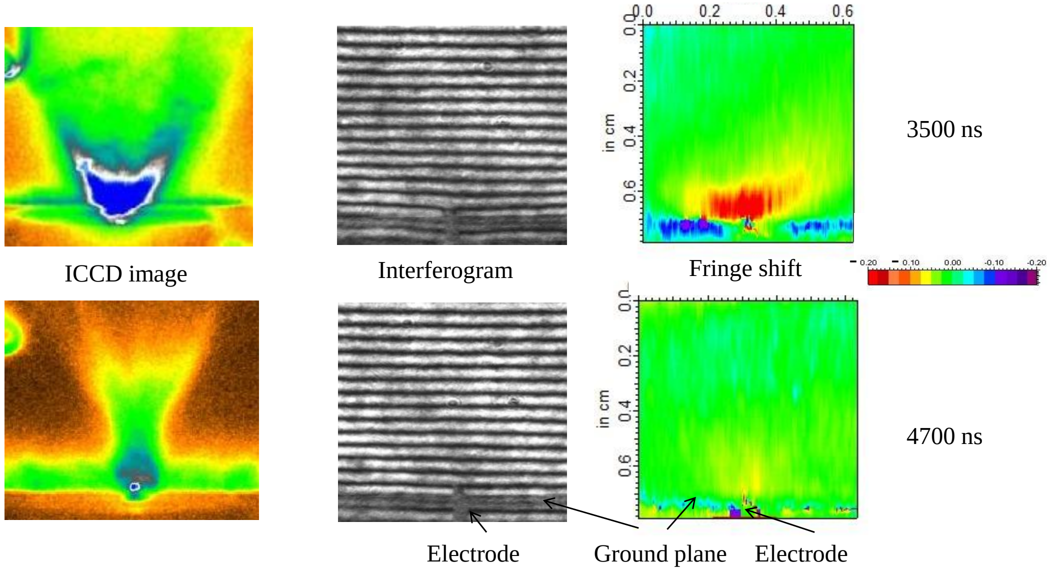

Figure 5.39: Interferometric images of jets with .45 T B field with the capacitor charged initially to 4900 V compared with ICCD images at the same time on the left.

set of this data.

The interferometric data does give valuable information about the jet density. The Schlieren data gives an indication of plasma density gradients around the electrode. I could calculate the density from the interferograms using equation 3.47. For probing frequencies of $\lambda = 532nm$ equation 3.47 becomes

$$N = -2.38 \times 10^{-18} cm^2 \int n_e dl. \tag{5.44}$$

Assuming that the plasma is cylindrical, has constant density and the diameter can be obtained from the ICCD images the density will be $n_e \approx 2.84{\times}10^{17} cm^{-3}$ for 3500ns and $n_e \approx 1.9{\times}10^{17} cm^{-3}$ for 4700ns. This gave insight into the anode jet boiling off molybdenum vapor before it settles down into the remnant anode jet. By the time the jet develops at 4700 ns the interferometric signal greatly decreases, at the same time the ICCD camera plasma signal narrows, which would also decrease the signal. This does give a measurable density, and after the jet has expanded beyond this time the signal drops below the noise of the interferogram.

5.6 Modeling and Analysis of the Laboratory Produced Jets

As shown in section 5.4 there are several quantities in these jets that are distinct, repeatable and quantifiable. The repeatability of the ICCD images of essential jet phenomena from shot to shot enables the measurement of jet dynamics using a compilation of single shot images from each jet measurement. Specifically these quantities include a distinct supersonic jet structure, jet spatial density profile, jet velocity, jet morphology, RAJ progression, jet divot formed in the throat of the jet and a high velocity jet that emanates in the front of the jet. There are many comparisons that can be made between the theoretical ideas outlined in section 5.2 and these various quantities. The measurement of these jet properties are limited to ICCD radiance profiles, current, voltage, and magnetic field measurements, and limited interferometric density measurements of the a small number of jets. From these measurements I compared with the theoretical calculations deriving a range of values for temperature and density.

This analysis section ties together many different interrelated pieces of information. The first investigations in section 5.6.1 will be looking at the supersonic nonmagnetic anode jets in this experiment. This analysis revealed the processes of the initial conditions of the magnetic jets. Bellan's formulation outlined in the theory section 5.2.3 give a calculation of the pressure balance with a known current distribution and flux tube envelope. This formulation calculates density profiles that are comparable to the measured ICCD images. Estimations from the anode jet analysis give approximate temperatures for these calculations from which density calculations can be made and compared to the interferometric measurements of the jets. Spatial calculations can be made using Maxwell SV to calculate the spatial distributions of the current as reported in section 5.6.2. This provides an idea of what the current is doing and how it is distributed throughout the jet. Bellan's formulation can calculate the dynamics of an evolving flux tube as reported in section 5.6.3. The velocities and morphologies are calculated using one dimensional MHD codes. Comparisons are measured between measured and observed velocities and RAJ angles.

Bellan's formulation also includes provisions for calculating the rotation of the fluxtube. This gave an estimate of the formation of the divot in the jet throat as reported in section 5.6.3. The spike at the beginning of the jet can be explained using the Maxwell SV calculations and the dynamical Bellan theory. Finally in section 5.6.4 the kinking of the flux tube can be calculated using the Krusckal-Shafranof theory.

5.6.1 Supersonic Anode Jets

The initial conditions of the measured magnetic jets in this experiment were the remnants of an anode jet from the electrode setup bounded by a barrel shock. To get a good idea of the initial conditions of the magnetic jets I analyzed the information measured related to the anode jet physics. This included reviewing what vacuum arc technology has studied on the subject.

The anode jet flow is affected by a flared nozzle that will produce a supersonic flow into the chamber. The characteristic signature of a supersonic flow into a vacuum was measured with negative biased jets in the jet forming time region. Rate flow analysis provided a model describing the density of the electrode cavity as a function of ablated material and the ejected jet material. This provided a linear relationship at early times between the pressure and the integral of the current squared. This quantity was measured and then used to calculate a range of initial conditions for the RAJ. The boundary of the RAJ was then characterized as a barrel shock which the conditions across the barrel shock can be described by the Rankine-Hugoniot equation.

The discussion of the supersonic nonmagnetic anode jets begins with anode jet physics. The current electrode configuration allows very little heat conduction from the center wire to its surroundings. This was apparent in the case of the Mo wire. The wire was small and does not deform when fastened against the copper electrode block. This provided very little surface area contact to drain heat away from the Mo wire. The only other physical contact the center electrode has was minor contact with the plastic bottom of the electrode holder.

According to Boxman [13] when an anode is thermally isolated from its surroundings the anode can heat up to high temperatures quickly. This was the case with these jet experiment and this property was useful in studying magnetic jets. With the majority of the center electrode placed in a small cavity with a small exit aperture, the cavity filled to high pressures of Mo gas and expelled into the vacuum with high velocities. The exit aperture of the cavity became flared due to heating of the wire. This flaring part of the aperture caused the exiting flow to become supersonic and form a barrel shock as the anode jet exits the aperture and this flow persisted for some time after the anode cycle has completed due to the pressure build up in the cavity. The anode jet did not show significant differences with and without a magnetic field, likely due to the high pressures involved. The anode jet also did not show characteristics of being influenced by currents. This was most likely due also to the high pressures involved that then connect the grounding block to the molybdenum ring. This then provided a much less restricted path for the current to flow through the plasma. With the high temperatures and densities of the plasma the conductivity of the plasma will be much less anisotropic with the magnetic fields involved, which will alow the current to flow between the coper lug and the grounded ring without forming a magnetized jet.

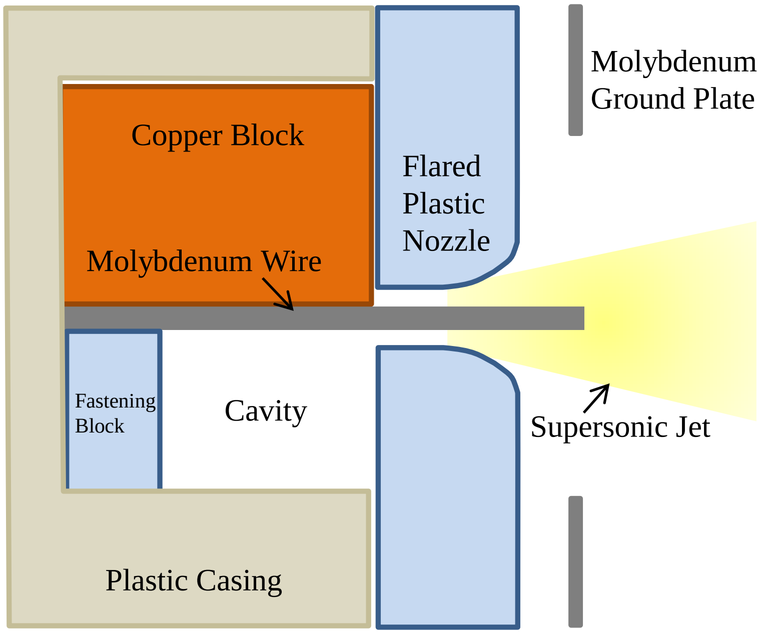

Figure 5.40: Diagram of the physical set up of the electrode configuration allowing for the escaping of hot Mo gas out of a flared nozzle.

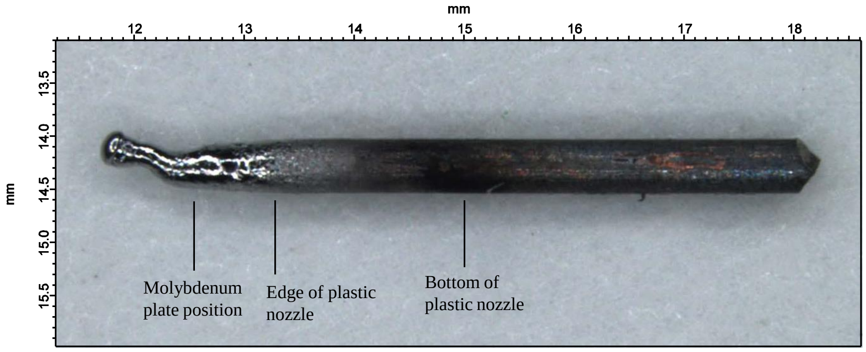

Figure 5.41: Picture of a used Mo center electrode showing various positions in the holder set up.

With the geometry setup as outlined in figure 5.40 calculated the velocity flow using the equation 5.7. The dimension of the flare outlined in figure 5.40 was approximated by the area flaring in a hemispherical curve. This was integrated over the dimensions measured. This calculation was dependent on the geometry of the electrode set up. The wire radius of the Mo wire was 2.5×10^{-4} m. The radius of the cavity side of the nozzle was 7.62×10^{-4} m. The thickness of the nozzle was 1.73×10^{-3} m. The nozzle flare was assumed to be circular with a radius of $\ell = 7.2 \times 10^{-4}$ m. The outer radius of the circular aperture was measured to be 1.48×10^{-3} m. I assume due to evaporation that there was a slight slope on the wire of .0001. With these parameters I numerically calculated the Mach number of the flow from equation 5.7 assuming that the Mach number at the throat was 1.73 (derived from Hagena's fromulation in section 5.2.2). This Mach number was the standard Mach number of a circular converging nozzle and a monatomic gas. The integration assumed that the radius of curvature was $R = 1.001 \times \ell$, and was integrated from 0 to ℓ or the radius of curvature above. The results of this calculation are in figure 5.42. They gave a reasonable result for a Mach number of 3.5. The effective radius for further calculations of the throat of the nozzle will be the radius of the approximated area of the throat or $r_{eff} = \sqrt{(7.26 \times 10^{-4})^2 - (2.5 \times 10^{-4})^2} m = 6.8 \times 10^{-4} m$. The volume of the cavity as estimated from the engineering drawings was $1.2 \pm 0.5 \times 10^{-8} m^3$.

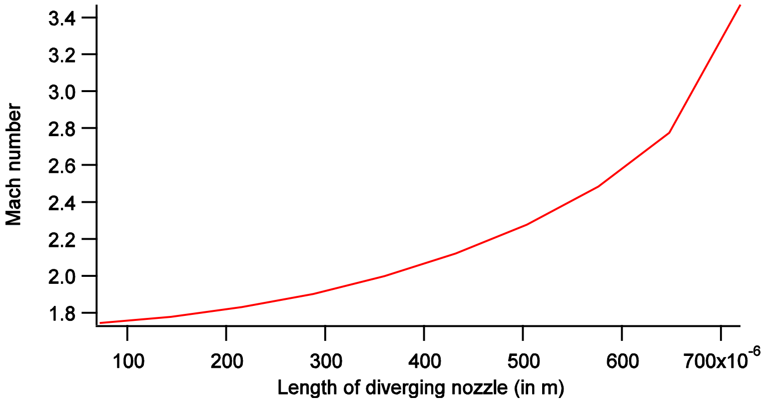

Figure 5.42: This is an integration of the converging-diverging nozzle. The x axis is the length of the nozzle from the diverging point.

The problem with this type of nozzle setup was that a lot of Mo material was boiling off in front of the nozzle creating a region of high pressure. This high pressure region will dissipate between the anode cycle and the cathode cycle. I do have density measurements of the anode cycle jet from interferometry, as the jet converts from an anode jet to a cathode jet, but this measurement was undoubtedly be dominated by the boiling off of the material form the unenclosed wire. The material outside the nozzle was expelled much faster than the gas inside the cavity, and the material in the cavity built up enough pressure to create a sustained supersonic jet. A microscope picture of the wire is in figure 5.41. This shows the area where the wire was exposed to the chamber's vacuum. The vaporpressure was high enough at this point that the wire began to boil off molybdenum. But inside the cavity the pressure exceeded the vaporpressure of the wire and the wire did not boil. This gave further evidence of a high pressure region inside of the cavity which will then create a supersonic flow out of the nozzle.

There was a distinct supersonic jet signature during the second phase anode jet in this setup, or in other words where the electrode was initially a cathode then became an anode. This was the reverse situation to the magnetic jets. This signature was illustrated in figure 5.43. Compare this with figure 5.6. This signature gave important information about the supersonic jet parameters, as the parameters were matched up with $(x_m/d) = 0.67(P_0/P_b)^{1/2}$ where x_m is the distance from the nozzle to the Mach disk, d is the diameter of the nozzle, P_0 is the pressure in the enclosed chamber, and P_b is the background pressure. As discussed in section 5.2.2 the other dimensions can be described by $x_b = 0.63x_m, D_m = 0.5x_m$, and $D_b = 0.75x_m$ with a 25% margin of error. These dimensions were measure and are reported in figure 5.44 and table 5.4. The pressure ratio was also compared to the current in figure 5.45. This gave very good agreement between the empirical theory and the jet measurements with most cases being within the 25% error range. The discrepancy may be found in the “aerospike” or plug nature of the jet nozzle, which is the condition with a tapered spike in the center of a nozzle that creates a lot of turbulence [21].

Now I discuss modeling of the cavity density as related to the ablation of the wire and the output of the supersonic flow. This was necessary for estimating the densities in the RAJ and for establishing how long the RAJ will last after the anode cycle. Lebedev, in his magnetic tower paper [20], gave a formula to describe the mass ablation off of wires in a z pinch. The

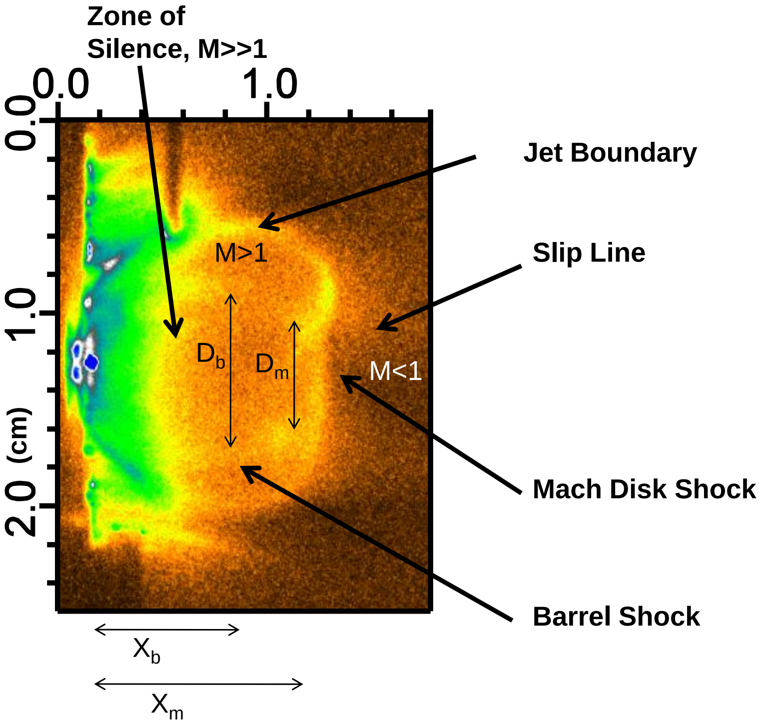

Figure 5.43: Anode jets in this experiment had a distinctive morphology that can be compared to the supersonic diagram 5.6.

formula is

$$\frac{dm}{dt} = \frac{\mu_0 I^2}{4\pi V r} \tag{5.45}$$

where m is the ablated mass per unit length, I is the current through the wire, V is the ablation velocity, and r is the radius of the wire. The ablated mass was related to the chamber pressure by $P = nkT$ due to the saturation of the ablated material in the chamber.

The density evolution of a cavity containing this wire with a volume Vol, length ℓ, and nozzle area A was calculated in appendix C.4.1 by analyzing the particles entering the cavity through ablation and leaving the cavity by

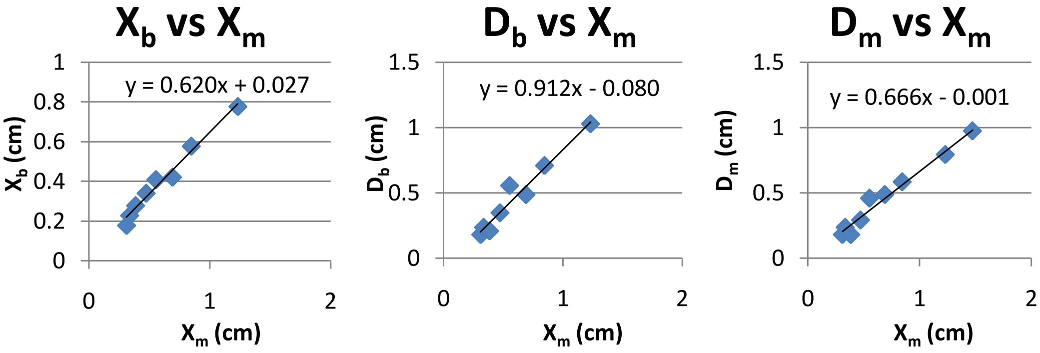

Figure 5.44: The relationships between x_b,D_b,D_m, can be related to x_m by $x_b = 0.63x_m$, $D_m = 0.5x_m$, and $D_b = 0.75x_m$. This was then compared with the measure values in the experiment.

	Xb	Db	Dm
3000v	0.62 ± 0.04	0.91 ± 0.08	0.67 ± 0.04
4900v	0.73 ± 0.06	1.08 ± 0.07	0.89 ± 0.04
empirical	0.63 ± 0.16	0.75 ± 0.19	0.5 ± 0.13

Table 5.4: The values of the proportionality constants between x_b,D_b,D_m, and x_m are reported. The literature reported empirical values are within 25% [125].

the supersonic flow through the nozzle. The relation for the density in relation to time was given with $c_1 = 0.514\hat{v}_0 AVol$ and $c_2 = \frac{\ell}{m}\frac{\mu_0}{4\pi VrVol}$ (where m is the mass of the molybdenum ions) as

$$n = \int_0^t c_2 I(t)^2 dt + \frac{c_1 \int_0^t \int_0^t c_2 I(t')^2 dt' e^{-c_1 t} dt}{e^{-c_1 t}}. \quad (5.46)$$

This can then be related to the ratio of pressures through equation 5.11 for early times by the equation (also derived in appendix C.4.1)

$$\frac{p_{cavity}}{p_{background}} = \frac{kT}{p_{background}} \frac{\ell}{m} \frac{\mu_0}{4\pi VrVol} \left(\frac{1}{1 + 0.514 n_0 \hat{v}_0 A \frac{t}{Vol}} \right) \int I^2 dt. \quad (5.47)$$

This quasi-linear relationship with the integral of I^2 was measured. The integral of I^2 was obtained by summing the product of the measured I^2 with the time steps between the measurements. The measured ratio as illustrated in figure 5.46 was 299.2 ± 8.9. This number can then be related to the unknowns in our formulation, temperature, background pressure, and the ablation velocity by the equation

$$299.2 = 9187.38(\frac{mPa}{Ksec})\frac{T}{p_{background}V} \tag{5.48}$$

or

$$\frac{T}{p_{background}V} = 0.033(\frac{Ksec}{mPa}). \tag{5.49}$$

Unfortunately V is not known. Lebedev lists the ablation velocity for his experiment to be $\sim 100\ kms^{-1}$. He used much higher current than was used in this experiment. Fortunately the measurement between the ratio of pressures and the integral of the current squared swallows up the need to know T and V for pressure calculations. This was then a model from which the ratio of pressures between the cavity and the background gas can be estimated. Although the chamber was initially pumped down to 1 mTorr the background pressure as experienced by the cavity may not be this pressure due to ablation material from the electrodes, and left over laser plasma material. Thus to calculate various parameters I used a range of possible background pressures from 10 mTorr to 1 Torr.

The density in the cavity can then be calculated with this formulation as a function of time using the measured current. Assumptions of the background pressure and the temperature need to be made. A typical plot of the density can be seen in figure 5.47. This showed that a continual flow of mass will occur into the cathode jet region even as the current went to zero between cycles. Lebedev's formula may not be applicable in the cathode jet case, because the entire electrode will not heat up as is does in the anode case. Lebedev's formula is for a z-pinch where the wire was connected across the electrodes.

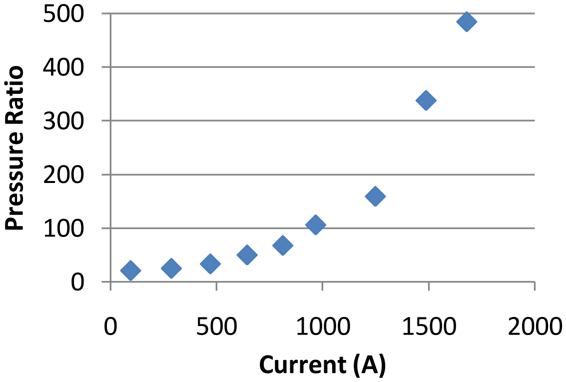

Figure 5.45: The measured pressure ratio as compared to the measured current.

This seems to be more indicative of the HAVA anode phenomena than that of the cathode. The main point then is that when the cathode jets formed there was a remnant anode jet present from the material stored in the cavity from the anode cycle.

Parameters based on Hagena's model (as stated in section 5.2.2) at 5 mm away from the cavity and based on the cavity calculation above are in table 5.6. Possible parameters in the cavity for various background pressures and temperatures are in table 5.5. The ratio of pressure was 3430.5 according to this calculation at the null point of the current oscillation. This would give a Mach disk distance of 5.3 cm. A Mach disk was not clearly observed at this distance as the RAJ becomes increasingly turbulent as time increases. The nozzle setup in this experiment was similar to the aerospike nozzle, a type of plug nozzle, that is known for its turbulent behavior [21].

Interferometric measurements of this density were measured. With the density calculated from the interferometry being $n_e \approx 2.84 \times 10^{17}\ cm^{-3}$

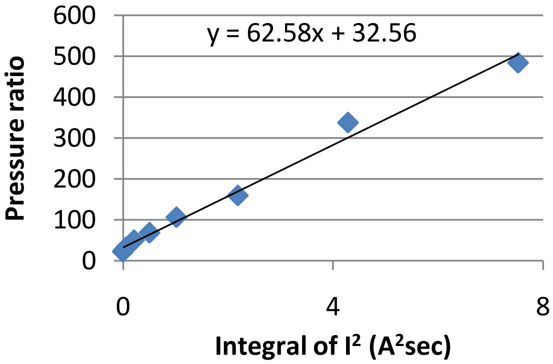

Figure 5.46: The measured pressure ratio between the cavity and background gas has a linear relationship with the integral of the current squared.

Density (m^3)	.1 eV	1 eV	10 eV
10 mT	5.9×10^{23}	5.2×10^{22}	3.5×10^{21}
100 mT	5.9×10^{24}	5.2×10^{23}	3.5×10^{22}
1 T	5.9×10^{25}	5.2×10^{24}	3.5×10^{23}

Table 5.5: The density measurement of the cavity at 4.3×10^{-6}sec with the electrode biased to 4900 V is reported.

at 3500ns with $I = 3440$ A into the cycle the pressure will be $p(Pa) = n_e(cm^{-3})1.6 \times 10^{-13}(Pa/(eVcm^{-3}))\ T(eV)$ For 1 eV $p = 4.5 \times 10^4\ Pa = 341.0\ Torr$. The magnetic pressure for .45 T is 600 Torr. At 2000 ns with $I = 6610$ A $n_e \approx 1.90 \times 10^{18}\ cm^{-3}$ which gave $p = 3.0 \times 10^5\ Pa = 2277\ Torr$ at 1 eV The density measurement from the interferometry are not an accurate measurement of the pressures coming from the cavity due to Hagena because the electrode was boiling off a lot of molybdenum in front of the cavity. This may increase the temperatures and densities into the RAJ because of the jet stream blowing over this hot portion of the wire. The length of this wire did grow over time, possibly due to the flow of this supersonic jet over this wire. This also brings up a discussion of the magnetic field. With the pressures being

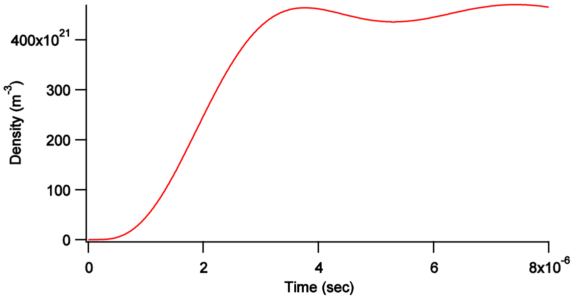

Figure 5.47: The cavity model predicts the density in the cavity as a function of time.

	.1 eV	1 eV	10 eV
10 mT	$6.5 \times 10^{21} m^{-3}$	$5.8 \times 10^{20} m^{-3}$	$3.9 \times 10^{19} m^{-3}$
	0.005eV	0.05eV	0.5eV
100 mT	$6.5 \times 10^{22} m^{-3}$	$5.8 \times 10^{21} m^{-3}$	$3.9 \times 10^{20} m^{-3}$
	0.005eV	0.05eV	0.5eV
1 T	$6.5 \times 10^{23} m^{-3}$	$5.8 \times 10^{22} m^{-3}$	$3.9 \times 10^{21} m^{-3}$
	0.005eV	0.05eV	0.5eV

Table 5.6: The density and temperature calculation of the jet .5 cm away from the cavity according to Hagena's equations with the electrode biased to 4900 V are reported.

comparable to the magnetic field pressure and the velocity being very high, this expansion will be able to overcome the magnetic field enough that the shocks will be largely unaffected as observed in the data. The lines defining these shocks for the early anode jets were more defined in the magnetic field case as seen in figure 5.18. This is most likely due to magnetic effects breaking the flow in slight ways.

I have presented evidence that the anode jet cycle produced a supersonic expansion into the chamber with the positions of the barrel shock measured from the ICCD images. I thus conclude that the boundary associated with the RAJ before the magnetic jets begin to form was a barrel shock associated with supersonic expansions between the jet ejecta and the background gas. The difference then between the jet ejecta and the background gas will be governed by the Rankine-Hugoniot equation [156] as discussed in 5.2.2.

For a Mach number of 3.7 as calculated by the afore mentioned calculation these relationships will be $n_1 = 3.28n_2$ and $T_1 = 5.13T_2$. As the temperature drops as the jet progresses out into the chamber the Mach number will rise. At 5mm the Mach number according to Hagena will be 16.6. This will give $n_1 = 3.95n_2$ and $T_1 = 87.0T_2$. This showed that therewas a definite and significant temperature and density difference between the inner jet cone and the chamber gas. This was significant in section 5.6.2 when discussing the distribution of currents throughout the jet region.

The wrap-up of this section describes a range of possible initial conditions for the RAJ. The information obtained by the supersonic anode jet analysis gave a relation between the pressure ratios and the current. From this discussion I conclude that, within error, the ICCD images of the developing anode jet are within the empirical calculations provided by Miller in [125]. This was used to calculate the cavity pressure as a function of time. The Hagena formulations gave the jet parameters as a function of distance at the time the magnetic jets begin. This allowed for estimation of the ambient temperatures and densities to be as in tables 5.5 and 5.6. These estimates are most likely low because of the material evaporated off of the tip of the electrode. The boundary of the RAJ was the barrel shock from the supersonic jet emanating from the cavity that can then be described by the Rankine-Hugoniot equations. This concludes that there was a distinct boundary in the jet region and a range of estimates can be made about the density and temperatures in these regions. This RAJ cone within the barrel shock then serves as the initial conditions for the magnetic cathode jets discussed in this chapter.

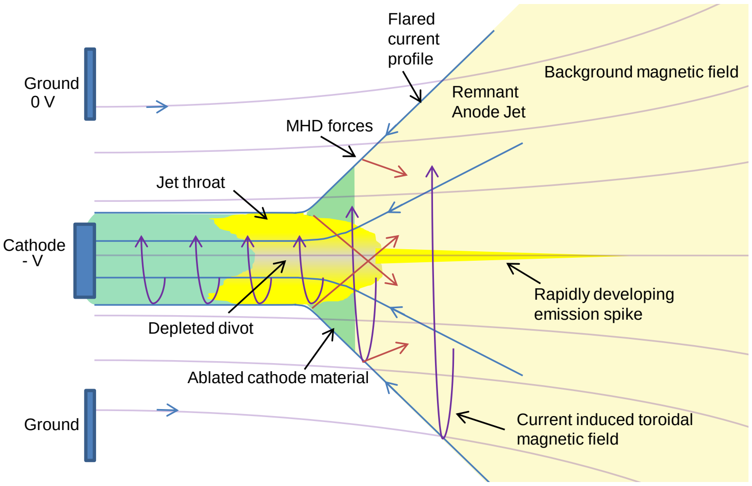

Figure 5.48: Schematic of dynamical processes within the jet.

5.6.2 Pressure Balance and Maxwell SV Conduction Calculations

In this section I discuss the pressure balance from Bellan's discussion in section 5.2.3 and how it related to the measured density distribution. Then I discuss current calculations made using Maxwell SV and how they are related to the current distributions in Bellan's theory and also the measured density distribution. Bellan describes a pressure balance between the current and the thermal pressure as described in section 5.2.3. If one has information on the current distribution the pressure distribution can be calculated. If the temperature is known the density distribution can also be calculated. As discussed in section 3.3.2 the plasma radiance from the plasma in the form of bremsstrahlung emission is a function of the temperature and density. Thus the radiance distribution in the plasma jets are related to the density and temperature distribution. Assuming a value for the temperature, if the current density and distribution are known a three-dimensional density distribution can be calculated and compared with the ICCD images. In this section the densities of the jet throat were calculated using this formulation with the currents measured from the Pearson transformer and the fluxtube dimensions obtained from the ICCD images. These density distributions were spatial compared with the ICCD emission distribution. Interferometric data that was taken for the 4900 V as in section 5.5 had a measured density of $1.9 \pm 0.2 \times 10^{17}\ cm^{-3}$. With an assumed temperature of 6.0 eV (taken from vacuum arc literature in section 5.2.1), and with the measured current of 791 A, the density calculated from Bellan's formation was $2.1 \times 10^{16} cm^{-3}$.

From the ICCD images and from the characteristic shock related to the RAJ I conclude that the fluxtube is hyperbolic. Hyperbolic here means that the radius of the fluxtube is defined by two asymptotes as seen in figure 5.51. The RAJ and the cathode ablated material act as a funnel for the current in a hyperbolic profile. The enhanced throat density will be in the region with the highest flare or or da/dz and the smallest a. This will give the highest force and pressure along the axial direction according to Bellan's equation 5.40.

Bellan's equations use the current derived from a constant current density, which integrates to $I = (r^2/a^2)I_0$ where a is the flux tube outline. This then generates a density or pressure profile that will have the most dense regions when a is small as in

$$P(r,z) = n(r,z)kT = \frac{\mu_0 I_0^2}{4\pi^2 a^2}\Big(1 - \frac{r^2}{a^2}\Big) \tag{5.50}$$

As seen in figures 5.50 and 5.51 the images of the plasma density show an enhancement of density at the throat region similar to the throat region in the

ICCD images. The outline of the flux tube was taken to be the outline of the luminous material boundary along the entire jet in the ICCD images.

Maxwell SV was used to calculate the distribution of currents in the plasma distributions inferred from the plasma emission distributions in the ICCD images and the inferred plasma distribution from the RAJ. Maxwell SV, as explained in section 5.2.3, calculated the AC current distribution on a two dimensional grid with a manually imputed anisotropic conductivity field. The reason for this calculation was to understand the distribution of currents in the fluxtube to know how Bellan's formulation should be used in this situation. The major result showed that the RAJ bounded by the barrel shock had a current that quasi-uniformly funneled through the RAJ to the electrode which was calculated with conductivities defined by densities and temperatures similar to that given by the Rankine-Hugoniot equations and the magnetic fields. These calculations also yielded a density distribution derived from Bellan's pressure balance. These density distributions were compared with the constant current case discussed above and the ICCD measured plasma emission.

To make the Maxwell SV calculation more interesting I estimated the geometries involved and used the measured resistance of the plasma of $.22\Omega$ to get an independent measurement of temperature and density. The value of this calculation is still qualitative in nature, and not meant to be rigorous. The conductivities imputed into Maxwell SV were based on temperature, density, and the magnetic field. Therefore estimating the resistance of the plasma in different regions will yield a temperature for the plasma assuming the density.

I modeled the conductivity through the jets with three separate regions instead of just two. The third region consists of the hot plasma being ablated from the cathode. The three regions are then the background gas, the RAJ, and the jet column containing the cathode ablation. I made basic models of physical configurations of these regions to get an idea of the conductivities required in these regions for Maxwell SV to calculate the current distribution. I constructed three geometrical blocks of different plasma conditions to calculate the resistances in the jet as illustrated in figure 5.49. A hollow cylinder connected the grounded ring to the RAJ (region 1). A triangular cylinder that had two axis of conduction modeled the RAJ (region 2). Then a simple cylinder connected the RAJ to the center electrode (region 3). The resistance in each of these objects was given by the equation

$$R = \int \frac{\eta d\ell}{A}. \tag{5.51}$$

Because of the anisotropy in the RAJ I separated resistance calculation into the two axis and integrate them separately. The two resulting resistances were then calculated in series. The total resistance calculated by the discharge was about $.22\Omega$ as discussed earlier in this section. The total resistance of the plasma must be less than this

$$R_{groundcolumn} + R_{RAJ} + R_{jetcolumn} \leq 0.22\Omega. \tag{5.52}$$

for simplicity I assume

$$R_{groundcolumn} = R_{RAJ} = R_{jetcolumn} = 0.22/3\Omega. \tag{5.53}$$

Using this estimate for the resistance I calculated the temperature in each region, assuming the density of the plasma, and calculated the parallel and perpendicular conductivities in the plasma for each section. I then used these numbers to calculate the current distribution in Maxwell SV.

For region 1 the parallel resistivity was $.00172\Omega m \Rightarrow T_e \approx .712eV$. For region 3 the parallel resistivity was $5.2 \times 10^{-5}\Omega m \Rightarrow T_e \approx 7.38eV$. For region

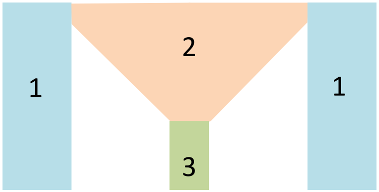

Figure 5.49: Cartoon of the three regions for a general resistivity calculation.

2 the calculation of the resistivity involved a complicated anisotropic calculation of the resistance of the cone described above. The temperature was calculated for two values of n_0 which were $1 \times 10^{15}\ cm^{-3}$ and $5 \times 10^{14}\ cm^{-3}$. These yielded two temperatures 1.21 eV and 3.06 eV respectively. The conductivities calculated for each are in table 5.7 under σ_2. These temperature calculations are according to $\eta_\perp = 1.03 Z ln\Lambda T^{-3/2}\ \Omega m$ with Z=1 and $ln\Lambda = 10$. These measurements for temperature and density are similar in nature to the Rankine-Hugoniot relations as discussed in section 5.6.1.

I chose three different conditions to run the Maxwell SV calculation, these include the inferred temperatures from above and various guesses on the density. These different conditions were three jets with different initial voltages and times. I chose the three conductivity regions to match the assumed regions in the ICCD data. Some of these jets had "spikes" in the middle-front of the jet that were given the high conductivity parameters. The calculation of current density and integrated current from Maxwell SV are reported in figures 5.50 and 5.51. The current flow for the 4900 V 4700 ns example from situation 2 in table 5.7 is in figure 5.52. This shows a current flow toward the center electrode as soon as the current crosses the RAJ boundary. This is significant because the fluxtube is then well defined by the axial current and the RAJ boundary. These calculations showed a radially uniform current

	$\parallel$	$\perp$	T_e	n_e
Situation 1				
σ_1	581.4 siem./m	.9 siem./m	.712 eV	$10^{13} cm^{-3}$
σ_2	1293.5 siem./m	968.3 siem./m	1.214 eV	$10^{15} cm^{-3}$
σ_3	19230.8 siem./m	10968.6 siem./m	7.38 eV	$10^{17} cm^{-3}$
Situation 2				
σ_1	581.4 siem./m	74.8 siem./m	.712 eV	$10^{14} cm^{-3}$
σ_2	1293.5 siem./m	968.3 siem./m	1.214 eV	$10^{15} cm^{-3}$
σ_3	19230.8 siem./m	10968.6 siem./m	7.38 eV	$10^{17} cm^{-3}$
Situation 3				
σ_1	581.4 siem./m	74.8 siem./m	.712 eV	$10^{14} cm^{-3}$
σ_2	5173.8 siem./m	230.0 siem./m	3.06 eV	$5 \times 10^{14} cm^{-3}$
σ_3	19230.8 siem./m	10968.6 siem./m	7.38 eV	$10^{17} cm^{-3}$

Table 5.7: This is a list of parameters used for the calculation of current density in Maxwell SV.

density unless there was a "spike" of higher temperature plasma imputed into the front of the jet. The increased current density in this spike was due to the same funneling phenomena, with the current focussing into the tip of the spike. In regard to the axial current density, the boundary of the jet showed a very sharp boundary in the current density. The current density was negative outside the jet boundary and positive inside the jet boundary showing a clean regional separation of the fluxtube as defined by the barrel shock an boundary of the jet. The integrated current along the boundary of the fluxtube is in figure 5.53 for situation 3 in table 5.7. This showed that the current was roughly constant (around 25%) in the fluxtube for about half of the fluxtube region. Hence assuming a constant current bounded by the barrel shock for the Bellan's dynamical calculations in section 5.6.3 was appropriate for matching observations in section 5.6.3.

With a current density distribution calculated from Maxwell SV the

	sit. 1	sit. 2	sit. 3
3000V	80.2 A	387.2 A	350.9 A
4000V	166.1 A	795.5 A	732.17 A
4900V	824.1 A	808.1 A	808.1 A

Table 5.8: Maximum amperage of the simulations from Maxwell SV.

	sit. 1	sit. 2	sit. 3	Constant Current
3000V	$1.4 \times 10^{14} cm^{-3}$	$1.8 \times 10^{15} cm^{-3}$	$1.1 \times 10^{15} cm^{-3}$	$1.5 \times 10^{15} cm^{-3}$ (248 A,6 eV)
4000V	$5.6 \times 10^{14} cm^{-3}$	$6.6 \times 10^{15} cm^{-3}$	$4.3 \times 10^{15} cm^{-3}$	$1.2 \times 10^{16} cm^{-3}$ (630 A,6 eV)
4900V	$1.3 \times 10^{16} cm^{-3}$	$1.3 \times 10^{16} cm^{-3}$	$1.3 \times 10^{16} cm^{-3}$	$2.1 \times 10^{16} cm^{-3}$ (791 A,6 eV)

Table 5.9: The maximum density of the jet throat is given as calculated by Maxwell SV and from Bellan's equation using radially constant current density.

pressure and density can be calculated doing a numerical formulation of the procedure outlined above. The current density is symmetrized and set in cylindrical coordinates. For each z value of the current density the current density is integrated to get the current. Then squared and integrated to obtain the pressure.

The density calculations give a maximum density for each situation at the throat of the flux tube are in table 5.6.2. and the maximum integrated current for the Maxwell SV calculations are in table 5.8. This was not a reliable calculation of the density it was just a check on how each of these calculations in this section related to each other. A density estimate was used to calculate the conductivity of the plasma for the Maxwell SV calculations. This reported data gives consistent measurements of current and density with the rest of this chapter.

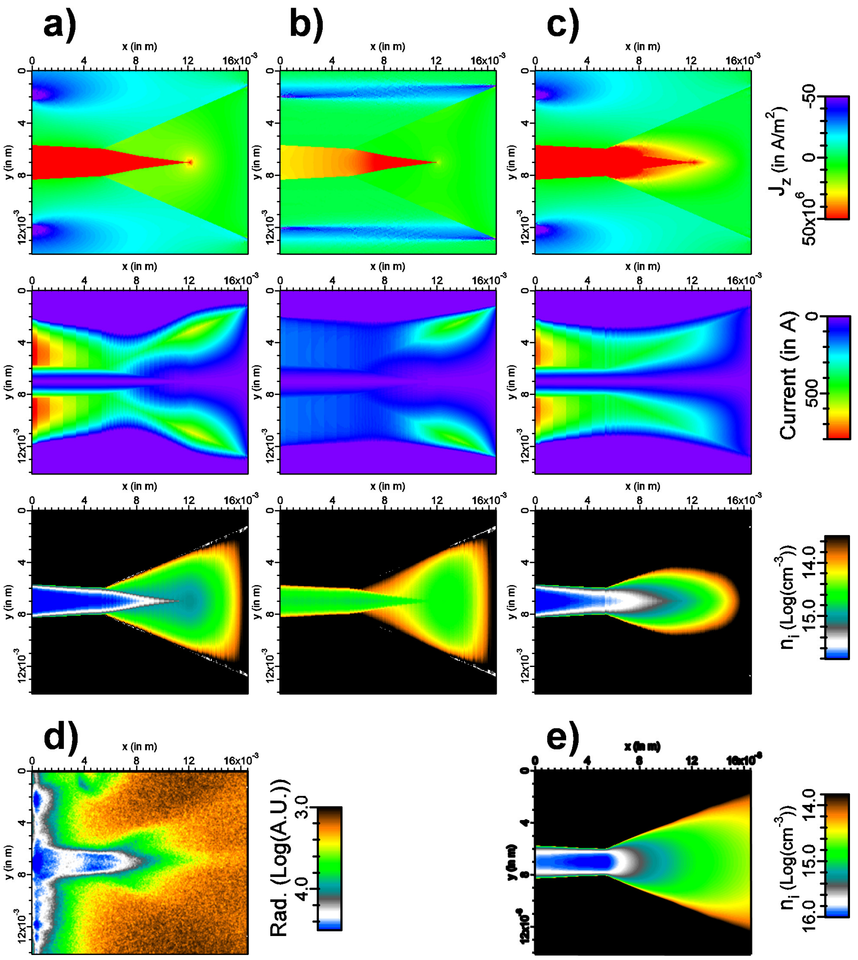

Figure 5.50: The conductivities listed in table 5.7 are represented in this figure by the current density, integrated current, and calculated density profiles with a) situation 2, b) situation 1, and c) situation 3. The equivalent ICCD image at 4000 V and 4700 ns is in d) and the density profile as calculated from Bellan pressure balance is in e) with a current of 630 A and 6 eV.

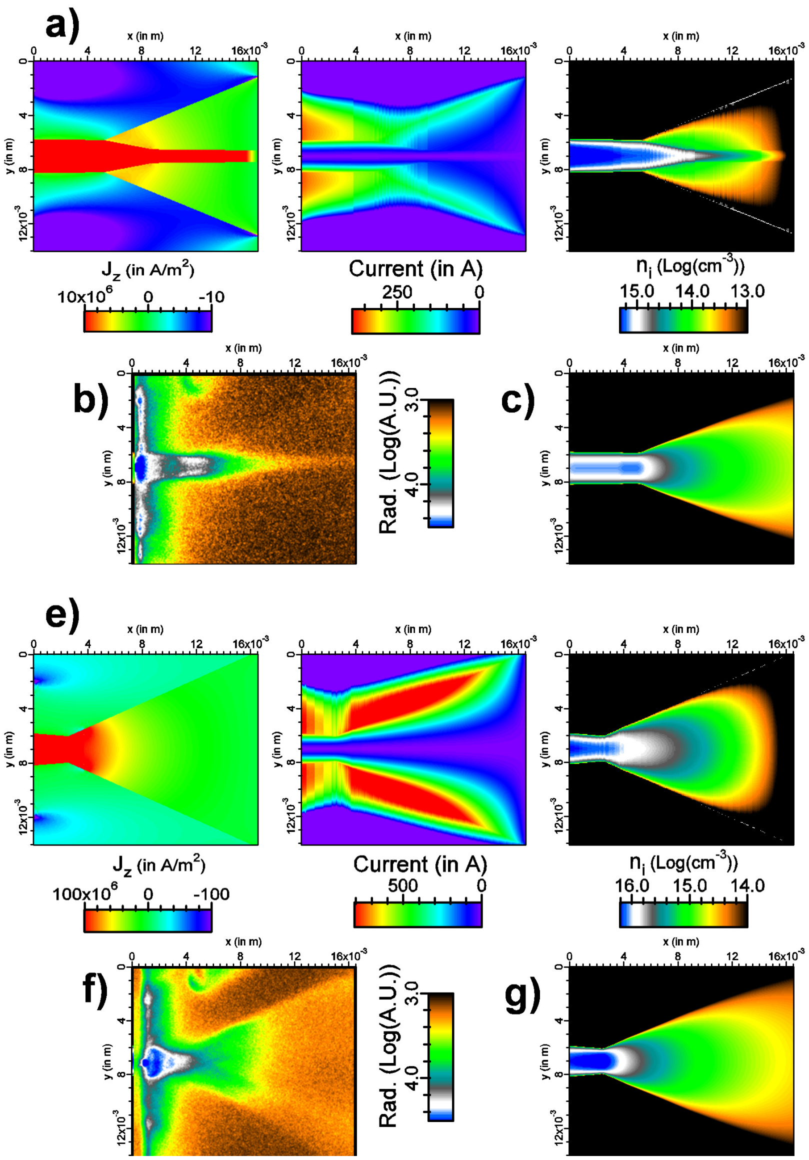

Figure 5.51: The current density, integrated current, and calculated density profiles with conductivities listed in situation 2 from table 5.7 are in a) for 3000 V and 4600 ns with b) the equivalent ICCD image and c) the Bellan formulation calculated density profile for a current of 248 A and 6 eV. Similar for e), f) and g) with 4900 V and 4700 ns. A current of 791 A and 6 eV used in g).

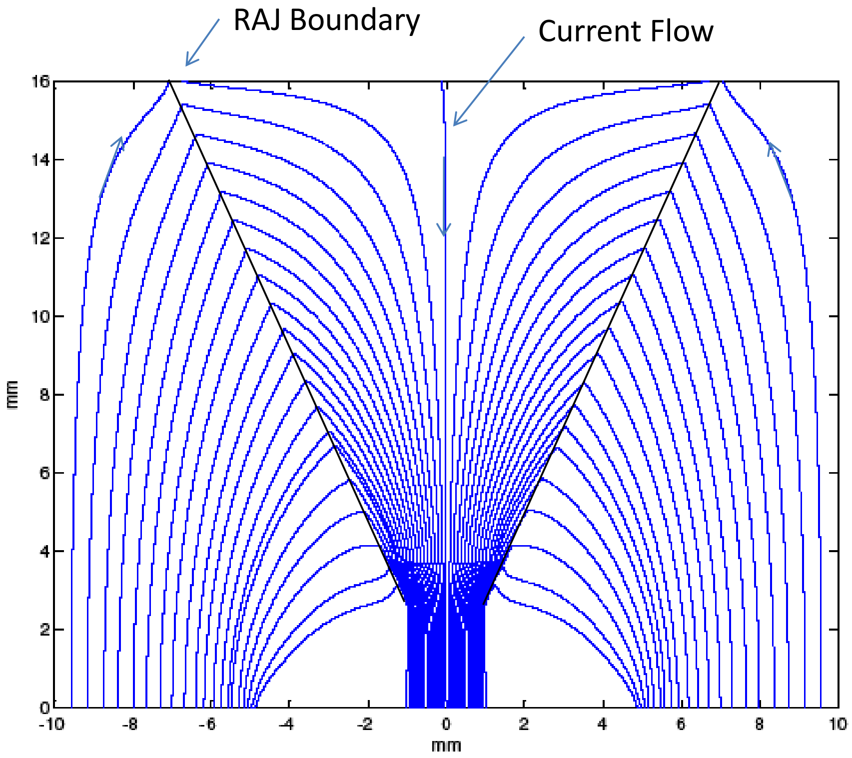

Figure 5.52: The current flow lines from conductivities listed in situation 2 from table 5.7 for 4900 V and 4700 ns.

The Maxwell SV results show that when a higher conducting spike is imbedded in the lower conduction RAJ region that the current density will concentrate in the tip. The dynamical equations show that increased flow was due to a flared current profile. This implied that there are two flared current profiles when a spike forms in the front of the jet. This will be discussed later in section 5.6.3. Thus we see that the density can reasonably be compared with Bellan's formulation, suggesting that there is a pressure balance in the corresponding fluxtubes measured in this experiment. Also Maxwell SV showed that the current density, without a spike, was quasi-uniform and thus

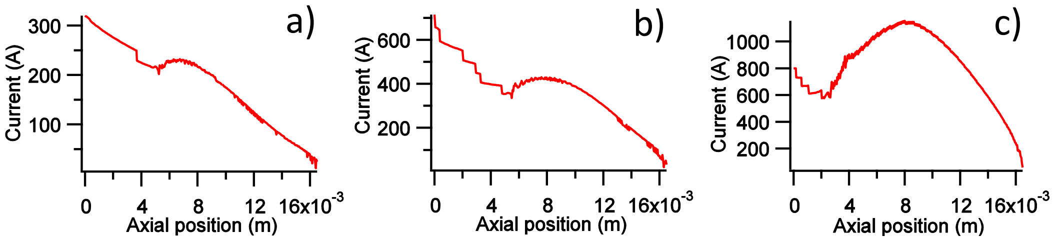

Figure 5.53: This is the line out of the integrated currents along the fluxtube boundary. The conductivities are situation 3 in table 5.7. a) is 3000 V, b) is 4000 V and c) is 4900 V.

Bellan's original formulation, using a radially constant current density, will be sufficient to simulate the corresponding data measured in this thesis in section 5.6.3.

5.6.3 Modeling of dynamical processes in magnetic jets

In this section I modeled the dynamical processes in the Jets. This mostly focused on one-dimensional PDE simulations describing the evolution of the jet throat. These numbers compared favorably with the measured values in section 5.4. They also predicted growth in the evolution angle as measured in section 5.4. The high velocity emission spike or jet tip was postulated to be a second current flare within the total fluxtube. The divot discussed in section 5.4 compared favorably as a result of rotation occurring in the jet throat as predicted by Bellan's formulation.

The dynamical processes in magnetic jets have been modeled using simpler one dimensional models than a full 3D MHD calculation. Bellan's theory, assuming a pressure balance reduces the three dimensional process into a one dimensional partial differential equation system. This has many advantages in both reduced computational complexity and a clear illustration as to the causes of the dynamical evolution. Bellan's theory does have many draw backs because of this simplicity. Bellan, in his theory, also separates the dynamics caused by $I = 0$, $dI/dt \neq 0$ and $I \neq 0$ and $dI/dt = 0$. The first case causes a rotation in the fluxtube column and the second causes axial acceleration. The two cases simplify when separated from each other to give a readily calculatable result, but loose their simplicity when they are combined. In the case of the magnetic jets under study both $I >> 0$ and $dI/dt >> 0$. Although this case falls out of the realm of Bellan's result, approximate calculations can be made to give explanation to the processes going on in the magnetic jet formation. The rotation portion in Bellan's theory assumes rotation as an initial condition for the $I = 0$, $dI/dt \neq 0$ case and provides no provision for acceleration of the plasma. These formulations also do not take into account the heating of the plasma and other ultimate effects of the progression of the plasma. I show that the time the plasma will take to radially accelerate will be less than the time for the plasma to axially accelerate. This shows that the axial motion will be dominant in the calculations.

The dynamical evolution of a flared fluxtube can be calculated using Bellan's formulation for $I > 0$, $dI/dt = 0$. Bellan's formulation assumes a pressure balance in the radial direction. This enables the calculation of the pressure, which will simplify the governing equations. This enables the reduction of a three dimensional system of MHD equations to a one dimensional MHD system. With the pressure balance discussed in section 5.6.2 above the force in the equation can be calculated to give

$$F_z = (\mathbf{J} \times \mathbf{B})_z - \frac{\partial P}{\partial z} = \frac{\mu_0 I_0^2}{2\pi^2 a^3}\left(1 - \frac{r^2}{a^2}\right)\frac{\partial a}{\partial z}. \tag{5.54}$$

With this force equation the dynamics of the fluxtube evaluation can be modeled with a one dimensional hydrodynamic code using a 4th order Runge-Kutta integration method. The MHD equations to integrate are

$$\frac{\partial \rho}{\partial t} + v_z \frac{\partial \rho}{\partial z} + \rho \frac{\partial v_z}{\partial z} = 0 \tag{5.55}$$

$$\rho\left(\frac{\partial v_z}{\partial t} + v_z \frac{\partial v_z}{\partial z}\right) - F_z = 0 \tag{5.56}$$

$$\frac{\partial p}{\partial t} + v_z \frac{\partial p}{\partial z} + \frac{5}{3} p \frac{\partial v_z}{\partial z} = 0 \tag{5.57}$$

with $p = \rho kT/m$. These systems of equations are discussed in section 3.1.1. The fluxtube outline was chosen to be a hyperbolic function defined by the barrel shock slope and a line parallel to the axis. The equation for this was

$$a(z) = .5(((m_1 + m_2)z + b_1 + b_2) +$$

$$\sqrt{((m_1 + m_2)z + b_1 + b_2)^2 - 4((m_1 z + b)(m_2 z + b_2) - c)}) \tag{5.58}$$

where m_1 and m_2 were the slopes of the two lines, b_1 and b_2 were the y intercepts of the lines, and c was the measure of how the two lines connect hyperbolically. The radius of the calculation was the distance between this axial axis and the origin. The slope of the barrel shock line was generally kept at .62 which was observed in the experiments. The hyperbolic distance to the origin was kept very small. The dimensions of the fluxtube were designed to reflect the observations. The simulations were made in the IGOR programming language and the source code is in appendix G

In addition to the time step of 3.0×10^{11} sec in each iteration the fluxtube envelope was modified to keep a radial pressure balance. The equation

$$P(r, z) = \frac{\mu_0 I_0^2}{4\pi^2 a^2}\left(1 - \frac{r^2}{a^2}\right) \tag{5.59}$$

was solved a after each iteration with r=0. This gave

$$a = \sqrt{\frac{\mu_0 I_0^2}{4\pi^2 P(0,z)}} \tag{5.60}$$

after each iteration.

The evolution of the fluxtube involved a "pinching" of the fluxtube that propagated in the direction of flaring. An example of the evolution is given in figure 5.54. In this figure the fluxtube envelope was calculated by the Runge-Kutta method and the density was calculated by requiring a pressure balance as described earlier in the previous subsection.

The calculation was completed under several different configurations. A sample of these conditions are reported in tables 5.10 to 5.16. For a fixed fluxtube radius a given current will dictate the density and pressure required for the calculation. For a calculation with constant current, the dynamics will be the same regardless of the initial current-pressure conditions that are given for the problem. For a basic calculation that had a uniform initial temperature and hyperbolic profile the dynamics will be entirely dependant on temperature, throat radius of the fluxtube, and the shape of the fluxtube. Other variations of the problem included a temperature variation in the z direction, different flared profiles, and different current density distributions. I present various tables with velocity calculations and other measurements in this section with a range of possible parameters.

These calculations show that the velocity of the pinch (the region of the jet with the most curvature and smallest radius, or the jet throat) increased with decreasing initial radius and increased with higher temperatures. Since the pressure of the fluxtube was locked in with the current of the fluxtube the only way to adjust the relative mass of the flux tube was to vary the

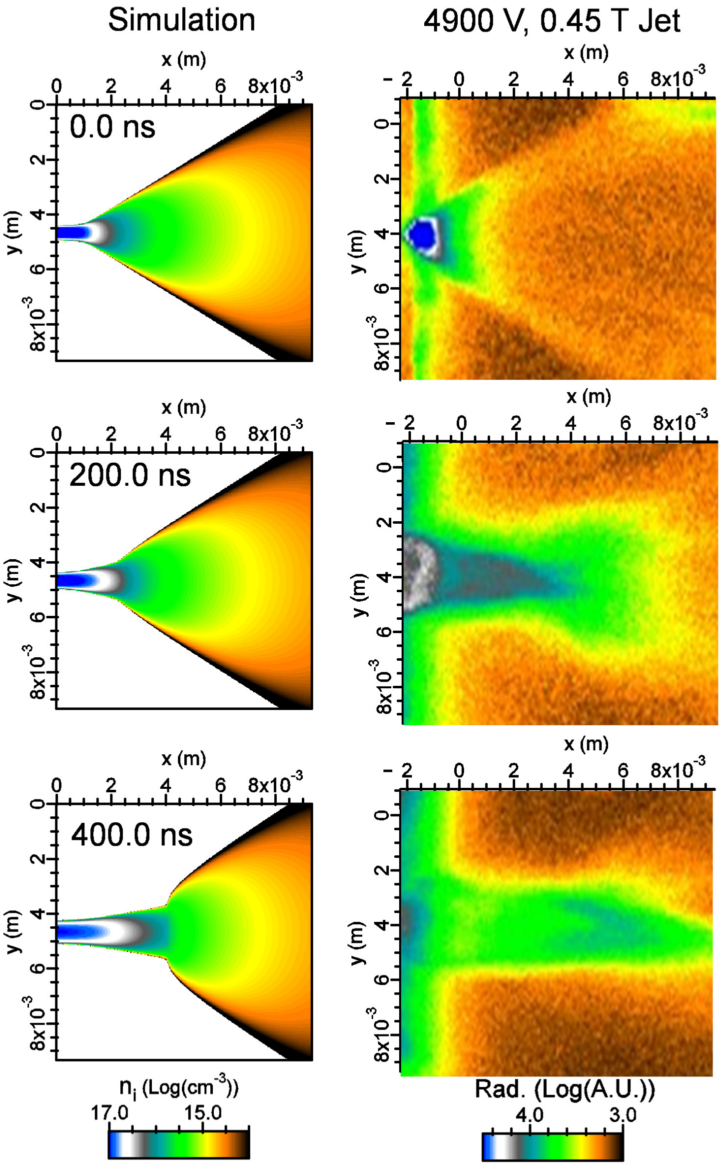

Figure 5.54: PDE simulation of the jet progression, shown with ICCD images with similar conditions. The density calculations are calculated using a pressure balance.

Velocity in m/s	r=5e-05 m	r=0.0001 m	r=0.00025 m	r=0.0005 m
T=1eV	19778	18021	19399	20397
T=10eV	24490	27280	26776	25363
T=50eV	44455	39469	36680	32947
T=100eV		49496	46386	41708

Table 5.10: The current is 1000 A, exponential spatial temperature decay T*exp(-i/100), the initial velocity is 1.8e4 m/s, time is 200 ns.

Velocity in m/s	r=5e-05 m	r=0.0001 m	r=0.00025 m	r=0.0005 m
T=1eV	2304.5	2129.9	2129.9	1978.6
T=10eV	9229.6	7902.6	8012	6900.2
T=50eV		27688	21506	17722
T=100eV			34046	31569

Table 5.11: The current is 1000 A, constant temperature , the initial velocity is 0.0 m/s, the flare slope is .62 (the observed slope), time is 200 ns.

Velocity in m/s	r=5e-05 m	r=0.0001 m	r=0.00025 m	r=0.0005 m
T=1eV	784.34	627.2	410.78	270.74
T=10eV	6217.1	4973.5	3375.1	2323.5
T=50eV			14082	9379.2
T=100eV				17171

Table 5.12: Maximum velocity of the calculation. The current is 1000 A, constant temperature , the initial velocity is 0.0 m/s, the flare slope is .62 (the observed slope), time is 200 ns.

Velocity in m/s	r=5e-05 m	r=0.0001 m	r=0.00025 m	r=0.0005 m
T=1eV	2302	2297.9	1974.8	629.29
T=10eV	7581.9	7958.9	5967.9	5541.3
T=50eV	21532	19639	16819	15843
T=100eV	35932	31460	27689	24742

Table 5.13: The current is 1000 A, constant temperature , the initial velocity is 0.0 m/s, the slope of the flare is .3, time is 200 ns.

Velocity in m/s	r=5e-05 m	r=0.0001 m	r=0.00025 m	r=0.0005 m
T=1eV	2310.9	2307.4	1977.8	1845.6
T=10eV	12024	11409	9083.3	8239.7
T=50eV			38165	23493
T=100eV				40342

Table 5.14: The current is 1000 A, constant temperature , the initial velocity is 0.0 m/s, the slope of the flare is 1.2, time is 200 ns.

Velocity in m/s	r=5e-05 m	r=0.0001 m	r=0.00025 m	r=0.0005 m
T=1eV	1457.3	1538.3	1538.3	1628.7
T=10eV	5268.6	5267.4	4604	3953
T=50eV	18765	12594	10313	9229.6
T=100eV			13944	12095

Table 5.15: The current is 1000 A, Hagena temperature decay as in equation 5.9, the initial velocity is 0.0 m/s, the slope of the flare is 0.62, time is 200 ns.

Velocity in m/s	r=5e-05 m	r=0.0001 m	r=0.00025 m	r=0.0005 m
T=1eV	2517.2	2310.9	2128.5	1845.9
T=10eV	18765	10741	9229.6	7809.6
T=50eV				24581

Table 5.16: The current is 1000 A, constant temperature , the initial velocity is 0.0 m/s, the flare slope is .62 (the observed slope),time is 400 ns.

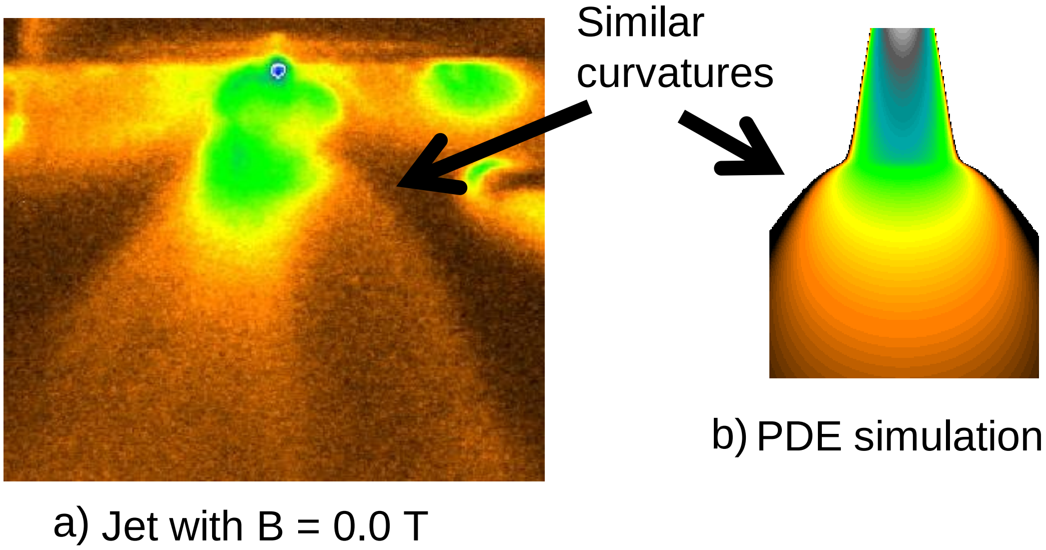

Figure 5.55: While the RAJ's of the jets without a background magnetic field do not evolve with time as dramatically as the RAJ's in a background magnetic field, they do show curvature that is similar to the PDE calculations.

temperature. Thus with higher temperature the mass of the flux tube will be less and will be able to be accelerated more. The addition of an initial velocity on the pinch progression had only an additive effect. The numbers calculated in these tables are much lower than the numbers measured because the initial velocity was taken to be zero. From Mesyatz [94] the velocity of a cathode jet from molybdenum is about 1.8×10^6 cm/s under similar conditions. As discussed in section 5.2.1. This may or may not have any magnetic effects associated with it, but we do know from the anode jet section 5.6.1 that the RAJ is progressing with speeds comparable to 1.0×10^6 cm/s. With this as an initial velocity the numbers reported in these table are comparable to the numbers measured for the jet throat velocity in table 5.1. With these velocity calculation there were several problems. With higher temperatures and smaller

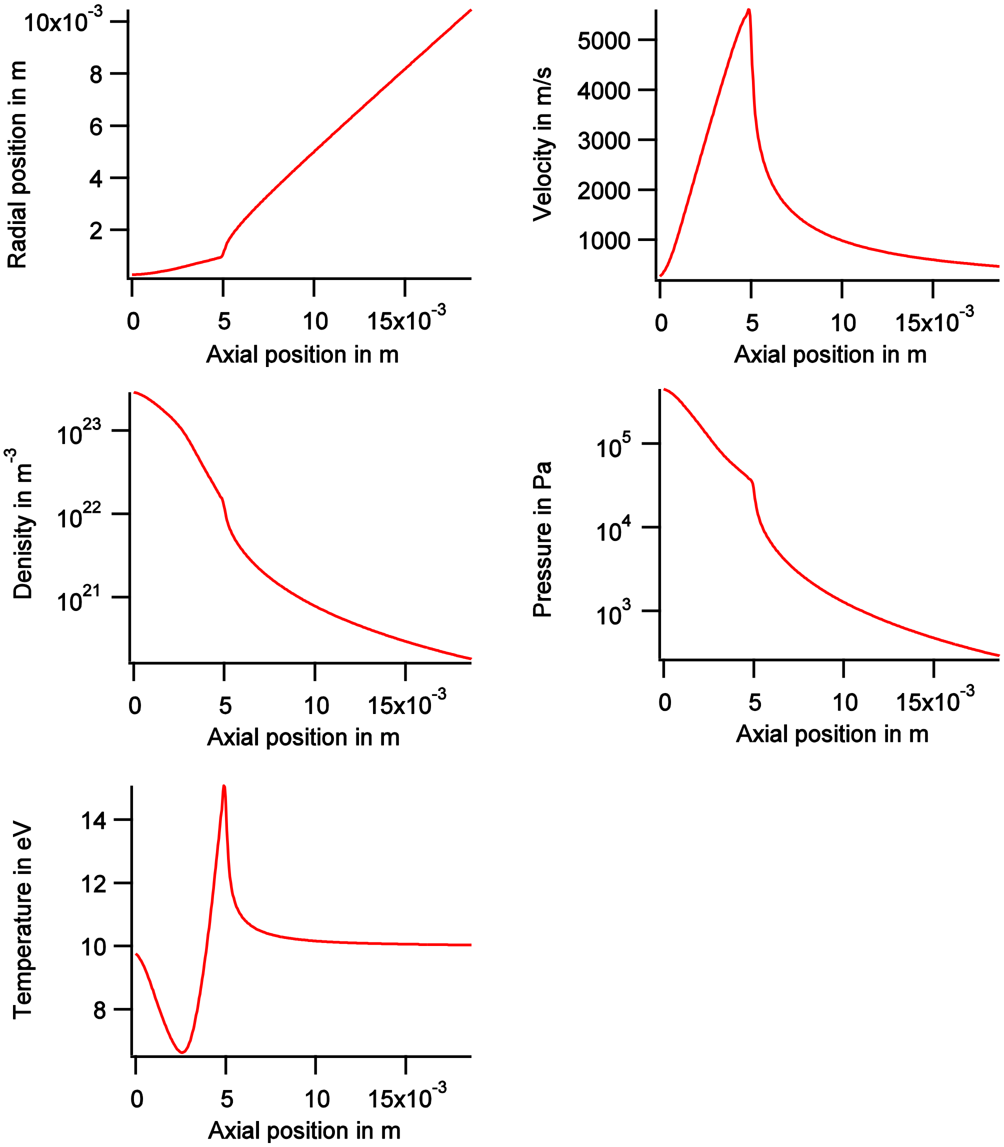

Figure 5.56: Physical parameters for a calculation involving I=1000 A, the initial throat width .25 mm, zero initial velocity, and at 400 ns

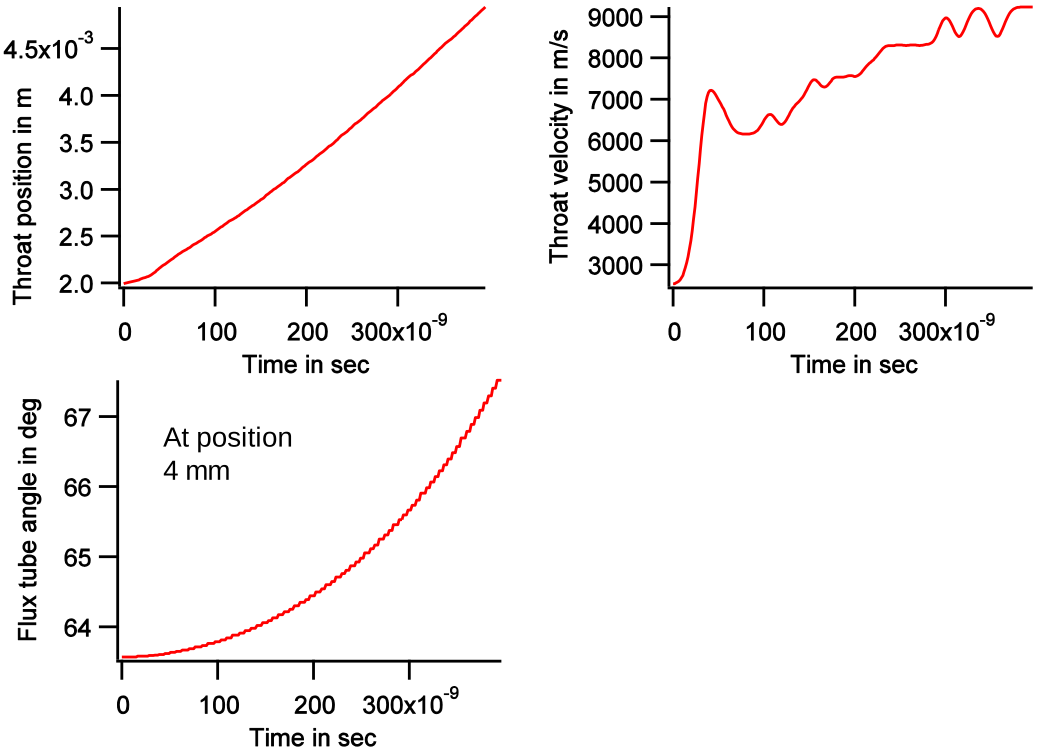

Figure 5.57: Parameters of the jet envelope as a function of time with I=1000 A, the initial throat width .25 mm, and zero initial velocity. Compare this with the data measured in figures 5.33 and 5.35.

throat diameters the calculations would become numerically unstable, and the calculations where unable to complete themselves. This is represented in the blank entries in the above tables. In calculating the velocity of the jet throat pinch I followed the highest second derivative potion of the flux tube envelope. This provided a position verses time history progression. Because of the discrete nature of this progression, the data was smoothed in order to take the derivative for the velocity. This introduced some error.

The parameter figures in this calculation also showed that the maximum flow velocity was much less than the pinch velocity as in figure 5.56. This also shows that the maximum velocity of the jet was at the pinch of the flux tube, as was expected. The temperature showed compression down stream of the jet and expansion up stream of the jet, which was also expected. Since the plasma was acted upon with a force one would expect that the acceleration of the jets would be nonzero. This was not observed in the measured jet data. These simulations gave an explanation for this by showing that the flow velocity is constantly accelerating but the jet throat pinch velocity as in figure 5.57 showed that the acceleration of the jet pinch was close to zero, as observed in the data. The simulations also resulted in measurements of the RAJ angle. This angle increased as time increased as in figure 5.57, although the angle increase was not as dramatic as in the data in figures 5.35. This demonstrated a qualitative and quantitative explanation for the increased RAJ angle due to differential "pinching" of the fluxtube due to the morphology of the fluxtube. The simulated morphology did not share the same morphology seen with the magnetic field jet examples. The simulated pinch was more dramatic than the measured ICCD data in magnetic fields. Although the RAJ did not evolve the same way without magnetic fields as with magnetic fields, they did exhibit, at an early part of their evolution, the same curvature found in the simulations, as in figure 5.55.

To take this idea of flared fluxtube acceleration further I discuss the filamentary spike measured in the data as the jet tip in section 5.4. The long filamentary feature in the front of the jet has very curious origins in the presence of a magnetic field as seen in figures 5.48, 5.27, and 5.61. This feature grows with a much higher speed than the rest of the jet. The feature forms as a spike in the front of the flat luminous profile when in the presence of a magnetic field. As shown in the previous subsection 5.6.2, when there is a protrusion in the density profile, current will funnel into that protrusion and increase the current density. This can therefore create a second fluxtube flare in the middle of the magnetic jet, that will accelerate the material along the axis with higher velocities. The radius of this secondary flux tube will be much smaller and because of the increase of current density the plasma can locally heat up much more, thus increasing the velocity of the jet according to the PDE modeling. The fact that the filamentary jet was moving relative to the jet throat means that the velocity for calculation need only involve the relative velocity between the two. Hence the velocity calculations from the PDE simulations would involve an initial velocity of not only the additional 1.8×10^6 cm/s, but the velocity gained from the full flux tube calculation, and with a smaller jet radius, this value could become very high. It would be of value for future studies to see how this behavior is similar to a plasma instability.

With these comparisons one might be tempted to assume that the jet was hotter than the $\sim 6eV$ that I have been assuming. With higher temperatures the jet will obtain a higher velocity. There was no evidence yet that the temperatures are higher than this. There are other processes that may hinder the acceleration of the jet, such as a small magnetic Reynolds number and the introduction of rotation forces from $dI/dt \neq 0$ that will weaken the pinch of the flux tube. There is therefore much more that needs to be measured about these jets in the future, to explain the high velocities.

I discuss now the rotation of the fluxtube in relation to Bellan's rotation formulation and to the divot observed in the jet throat. The luminosity of the jet throat decreases uniformly over time, and a divot or depletion of luminosity in the center of the luminosity profile increases over time to about 50% in the log scale as seen in figure 5.31 and measured in figure C.6. This divot formed in all cases in a magnetic field ≥ 0.23 T, initially charged capacitor of ≥ 3000 V. This divot formed in cases where the magnetic field is less and even zero, but it was more distinct in the higher magnetic field case. The ICCD images of the divot are integrated images over the entire luminosity of the jet collum. So with the divot luminosity decrease of 50% the actual decrease of luminosity in the center of the jet is much less. Figure 5.58 shows the comparison of the an actual profile with the line integrated profile. This shows that a very significant depletion of radiating material was needed to produce an integrated divot of about 50%. I propose that this divot in the luminosity was due to the depletion of plasma from the higher density throat region due mainly to the increase of rotation due to $abs(dI/dt) >> 0$ and somewhat due to the depletion of the jet throat from the high velocity spike.

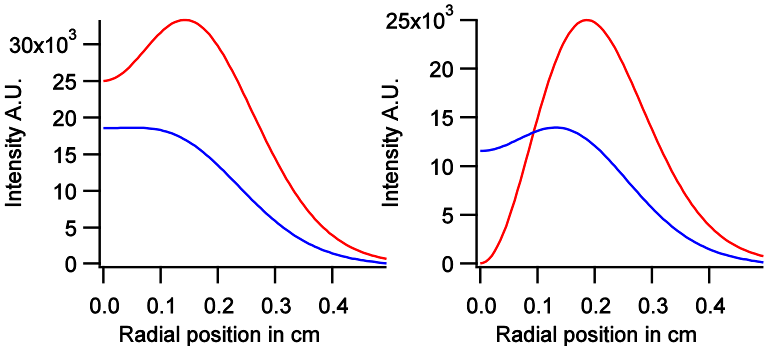

Figure 5.58: In order to get an integrated divot the actual intensity divot must be very strongly divoted. Red - actual radial intensity, Blue - line integrated intensity to the ICCD camera.

The filamentary jet can deplete the center throat region to be a cause of the divot formation. This can be modeled by counting the particles as in the equation

$$\frac{dn}{dt} = -\frac{(nf)vA}{Vol} \tag{5.61}$$

where A is the area of the effective aperture of the filamentary jet, Vol is the volume of the throat cavity, v is the velocity and f is the fraction of the density that gets expelled. In this case $A/Vol = \ell$ where ℓ is the length of the cavity. Integrating this will then yield

$$n = n_0 e^{-(fv/\ell)t}. \tag{5.62}$$

For typical parameters believed to be involved with the filamentary jet and the jet throat we have $n = 10^{14}\ cm^{-3}$ for the jet and $n_0 = 10^{16}\ cm^{-3}$ for the jet throat. This will gave f=.01. V was on the order of $10^7\ m/s$ and $\ell \approx 0.2\ cm$ for the jet throat cavity. This then gave a decay constant of 5.0×10^5 1/sec. This required 4.6 μs to drop n_0 by 10%. If the filamentary jet was $10^{15}\ cm^{-3}$, the time constant would be 5.0×10^6 1/sec. This would require only 461 ns to reduce the cavity at least 10%. This implies that the filamentary spike would reduce the density of the cavity, but since the cavity density needed to be reduced was much greater than 10%, this will be not nearly enough density depletion to match observations. Thus rotation must be taken into account.

Bellan's theory gave a provision that the flux tube will rotate if $dI/dt \neq 0$ as discussed in the theory section 5.2.3. This was due to the axial magnetic field twisting because of the toroidal magnetic field developing. The plasma will rotate because the plasma is frozen into the magnetic field. In a non-ideal case where the magnetic Reynolds number is low, this rotation will take time to develop. The rotation of the plasma column was related to the distance of the plasma from the electrode as in section 5.2.3. Thus as the jet throat expanded away from the electrode the angular velocity increased in time. This

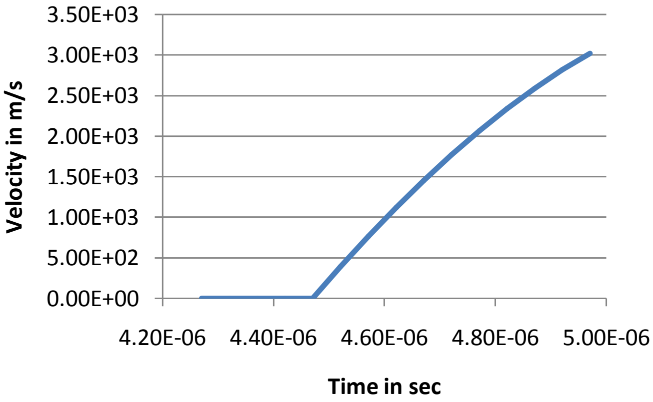

Figure 5.59: This is the velocity in the θ direction for a 4900 V jet at the jet throat radius of .5 mm, with the total jet radius 2.0 mm, as a function of time.

will cause the material to move out of the column. This will be a factor in the creation of the divot.

The centripetal force density, $\rho U_\theta^2/r$, can be compared with Bellan's $\mathbf{J} \times \mathbf{B}$ force which is $\mathbf{J} \times \mathbf{B} = -\frac{\mu_0 r I_0^2}{2\pi^2 a^4}$. This is reported in figure 5.60. The density for the centrifugal force calculation was taken to be the density given by the pressure balance given by Bellan's equations this will give a greater centrifugal force near the center of the jet and a greater $\mathbf{J} \times \mathbf{B}$ force near the edge of the jet as shown in the figures. The rotational velocities obtained are on the order of 1000 m/s. An example of the calculation of the rotational velocity is in figure 5.59 where the angular velocity at a radius of .5 mm was calculated in the jet throat as the jet throat progressed in time. The radial expansion velocities would be on the order of the rotational velocities if the rotation was not rigidly confined, which would be the case if $\mathbf{J} \times \mathbf{B} \ll \rho U_\theta^2/r$ The radial displacement of the divot was on the order of a 5×10^{-4} m over a time of about 200 ns. This gave a displacement velocity of 2500 m/s which was comparable

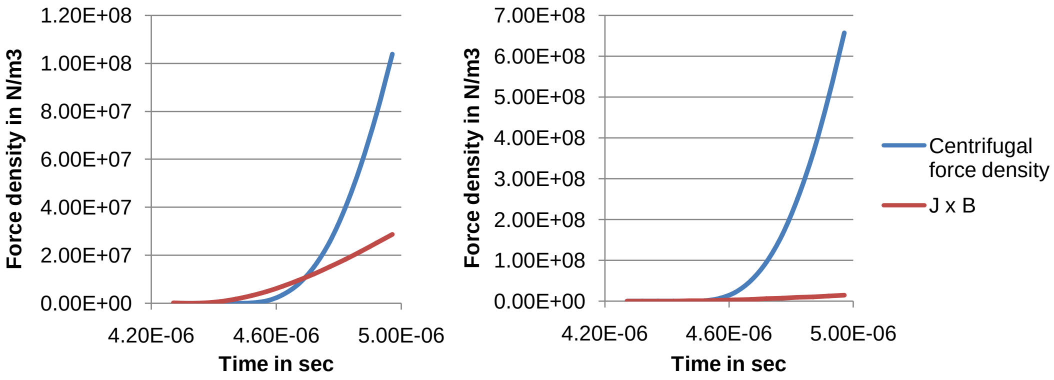

Figure 5.60: This is the centrifugal force compared with the $J \times B$ force using current information from a 4900 V jet. The radius of the fluxtube is 2.0 mm. On the left the calculation is made at r=1.0 mm, and on the right the calculation is made near the edge at r=1.95 mm.

to the rotational velocities obtained using Bellan's formulation. This suggest that rotation of the fluxtube was likely to have the ability to form a divot in the density profile. This would also suggest that rotation was important in the jet evolution dynamics. This is important because astrophysical jets are subject to rotational forces and rotation is important in their collimation. This warrants future study. The rotational velocities were much smaller than the axial velocities suggesting that the rotation does not adversely affect the axial acceleration as formulated by Bellan, suggesting that the assumptions made about the current limits were valid.

I placed the jet electrode in the presence of the old Faraday rotator magnet with field of .1 T at the interaction region. There was a very surprising helical structure that formed out of the electrode while charged to 3000 V. The structure formed very quickly and lasted only a short time and then became less helical (see figure 5.61). This feature lasted only 70 ns, but was very

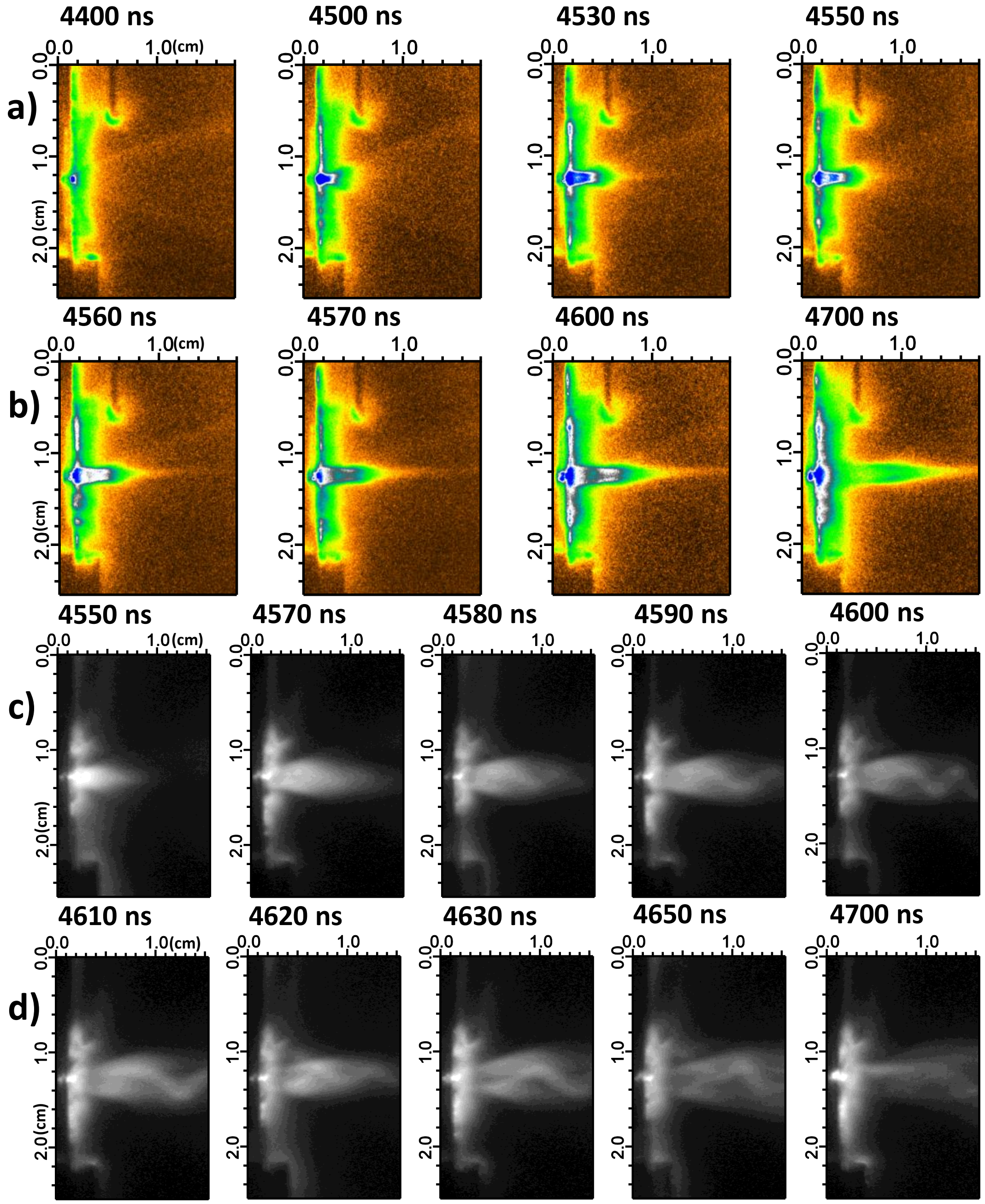

Figure 5.61: Fine Mo jet progressions with a)-b) 3000 V and ∼.45 T magnetic field, and c)-d) 3000 V and ∼.1 T magnetic field.

repeatable. This helical structure seems too uniform to be entirely a kink instability. This could be a result of Bellan's dynamical rotation where the week magnetic fields give the appropriate rotation while not confining the flux tube to the field lines.

The dynamical process of the jet progression have been compared with numerical partial differential equation modeling of Bellan's formulation and other similar models. The progression of the flaring pinch of the flux tube has been modeled and the velocity has been correlated to the temperature, and initial radius of the flux tube. The formation of the divot has also been linked to rotational forces and to the depletion of the jet throat caused by the filamentary jet.

5.6.4 Analysis of the Jet Kinking

The kinking parameter was an important part of our analysis. This gave a benchmark in comparing our jets to relevant z-pinch and fluxtube phenomena. As stated in section 3.1.2, all fluxtubes without an external magnetic field will be unstable to the m=1 mode. This was certainly true of the kink instability criteria outlined in equation 5.42. All jet-like structures in this experiment formed kink modes when there was no external magnetic field as discussed above. And for high currents in magnetic fields there are kinks that formed in the region between the jet throat and the electrode.

Determining the kinking parameter was subject to many uncertainties. The length and the width of the fluxtube were not well defined. For the length, the distance between the jet throat and the electrode was taken as a likely definition of jet length. Beyond the jet throat the fluxtube flared and may become a different dynamical region in reference to the kink instability. If the kink instability behaved as a typical boundaryvalue problem both the electrode and the jet throat were likely candidates for boundaries of the kink instability. The best examples of kinking with large magnetic field are in figures 5.25 and 5.26 where the field of view is larger for a 4900 V discharge in a .45 T magnetic field. The kinks appeared in these images as heightened intensity blobs on the edges of the luminescent cylinder connecting the electrode with the jet throat. In other images of this phenomenon with a smaller field of view, clear helical modes were seen in this region but they were not as reproducible. The instability appeared to have a wavelength of the distance between the electrode and the jet throat. The fluxtube formed in the fully enclosed magnetic field also has this structure of a full period oscillation mode, except that there were two fluxtubes in this case. The case where a helical fluxtube was seen in this cylinder also had the same spatial frequency. Hsu also reports a single axial wave length in Bellan's jets where there is no solid boundary [63]. The reasoning behind this is a strong axial gradient for $Bn^{-1/2}$ associated with their flare at the "mushroom" part of the fluxtube system that acts as an Alfven speed discontinuity. This was true in my setup in that there in a steep rise in density at the jet throat similar to Bellan's jet. Thus the jet throat acted as an effective boundary for the fluxtube to give a defined spatial wavelength for the jet.

The radius of the fluxtube was another difficult quantity to measure. The radius was also the most critical measurement to make for the kinking instability because of the a^2 dependence. Measuring this quantity required careful examination of the data. This quantity need not be the entire fluxtube radius, but the region in the fluxtube that will eventually kink. The jet throat may be wider than the "kinking" part of the fluxtube. Diameters of the fluxtube most likely can be determined by the fluxtube diameter without a magnetic field, or in the rare cases where a twisted fluxtube can be measured between the electrode and the jet throat. This diameter is quite small, much smaller than the jet throat. The kinking in the 4900 V, larger field of view case as in figures 5.25 and 5.26 (or in more compact form figure 5.62) was most likely the fluxtube helix nodes interacting with the boundary of the cylinder between the electrode and the jet throat.

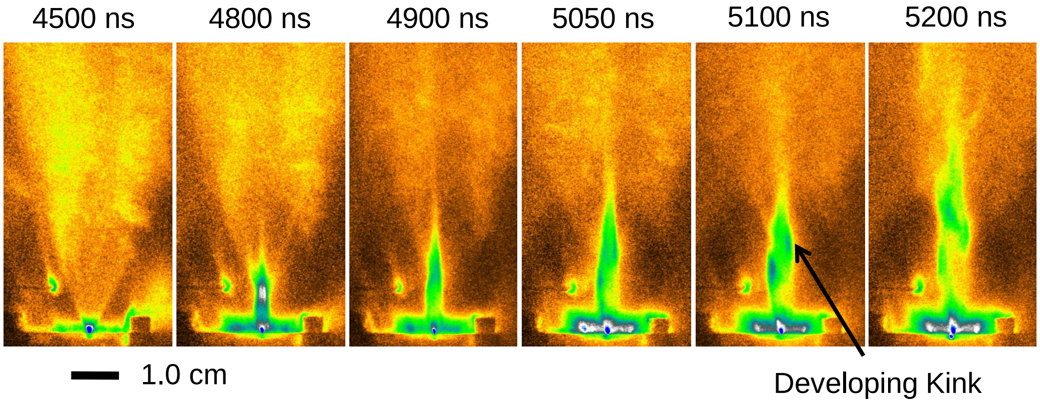

Figure 5.62: Development of a kink structure in an 4900 V Mo jet.

In calculating the kinking parameter I took into account these uncertainties to get a probable range of the kinking parameter. This included the uncertainty of the current, length, magnetic field, and diameter. The diameter was the dominant factor in the uncertainty from the uncertainty equations. In figure 5.63 the kinking parameter was calculated for a 4900 V jet in a magnetic field of 0.45 T. I took the mean radius for the jet to be 2.0 mm. The average kinking parameter dropped close to unity and the error bars encompass the value unity during the later times. As seen from the graph the values that kink correspond to the kinking values close to unity. In graph 5.64 the jet the pa-

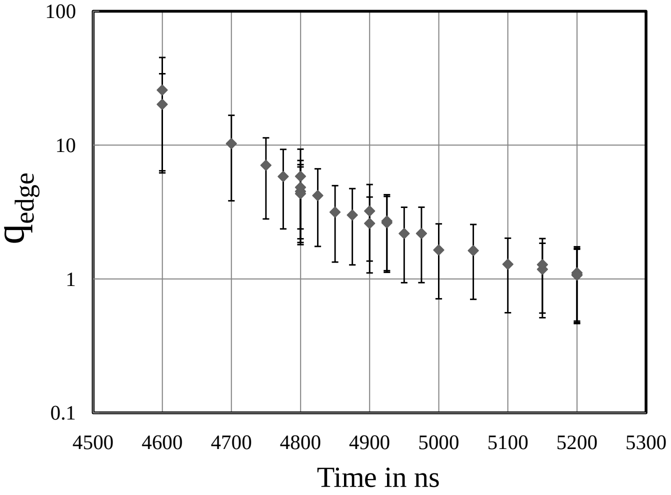

Figure 5.63: Estimate of the kink parameter for the jets we measure, with q_{edge} being the kink parameter. Kinking begins to form in the ICCD images after 5100 ns.

rameter λ verses the jet length was reported as described in section 5.2.3. The curved line represents where the kinking instability is unity. The graph shows the progression of two jets describing their values as kinked or not. This corresponded to the same graph for Bellan's jets in Hsu's paper [63]. Their value for λ is much lower than these values, which is to be expected because their jet diameters are much larger that mine. This showed good agreement with Kruskal-Shafranov theory, which supports the claim that these jets were developed by fluxtubes, and that the numbers for these experiments correspond to a well developed and respected theory of z-pinches.

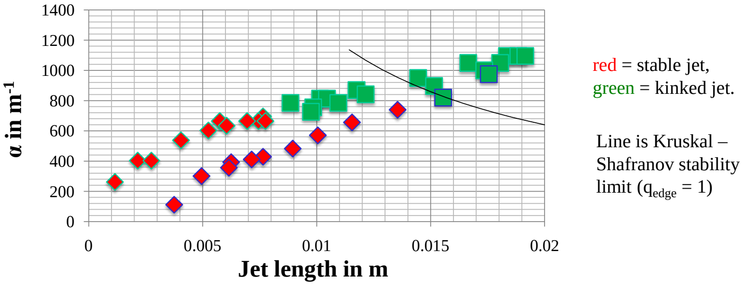

Figure 5.64: Graph of the quality parameter against the estimated jet length, and show jets that are kinked in green and jets that are not kinked in red. The curved line has the value where the kink parameter is one.

5.7 Relevance to Astrophysical Jets and other Magnetic Laboratory Jet Experiments

I compared the parameters we have inferred or measured from our jets with jets found in YSO, Bellan's jet and Lebedev's jet in table 5.7. The calculated Euler numbers inferred by these parameters all match very closely. Many of the parameters have been assumed and approximated, but these comparisons show good correlation among other laboratory astrophysics experiments and YSO's.

This experiment measured collimated fluxtube jets with flared current profiles using a relatively simple and inexpensive setup. This supports the notion of the ubiquitousness of the jet phenomena. Although our jets were produced in a magnetic field much greater than that found in scaled amounts in nature there were still similar features found in astrophysical jets, including long collimated flows, and the onset of kinking type nodes in the astrophysical jets.

A major difference between the magnetized jets in this experiment and

Parameters	YSO	our jet	Lebedev	Bellan
h(cm)	10^{11}	1	1	10
t(s)	10^{4}	10^{-7}	10^{-8}	10^{-6}
P(dyne/cm^2)	10^{-8}	10^{5}	10^{9}	10^{5}
$n(cm^{-3})$	10^{3}	10^{16}	10^{19}	10^{15}
T(eV)	1	5	100	10
B(G)	10^{-4}	10^{4}	10^{5}	10^{3}
v(cm/s)	10^{7}	5×10^{6}	10^{7}	10^{7}
Euler number	40	9	13	13

Table 5.17: Comparison of parameters between various jet frames, both laboratory and astrophysical [85][154][4][135]. The pressures are calculated from the other parameters.

galactic jets was that the laboratory jets have a distinct “turn on” time, and the astrophysical jets have essentially obtained a steady state. Comparing the collimation of the two jets is a little tricky. The data shown in figure 1.5 shows the collimation of the M87 jet as a function of distance from the origin. This can be related to the time evolution of the collimation of the jet with by relating each of these points to the dynamical collimation. The position of the jet can be related to the time of the evolution of the collimation of the jet through the velocity which is on the order of 10^8 m/s. Thus finding the appropriate scaling between these two frames will be related to the length scale and the velocity. I will take the length scale of the M87 jet as the order of magnitude length it takes to collimate or 10^{17} m. The corresponding length scale in the laboratory jets is 0.01 m. Thus the scaling parameter as discussed in section 3.2 is $a = 10^{19}$. The velocity scale parameter is, with the laboratory jets being 5×10^4 m/s, $\sqrt{c/b} = 2000$ (see section 3.2 for details). Thus the time scale parameter is $a\sqrt{b/c} = 5 \times 10^{15}$. This scaling is then reflected in the collimation of the jet as compared with the laboratory frame in figure 5.65. The collimation in the laboratory frame is measured at .005 m from the

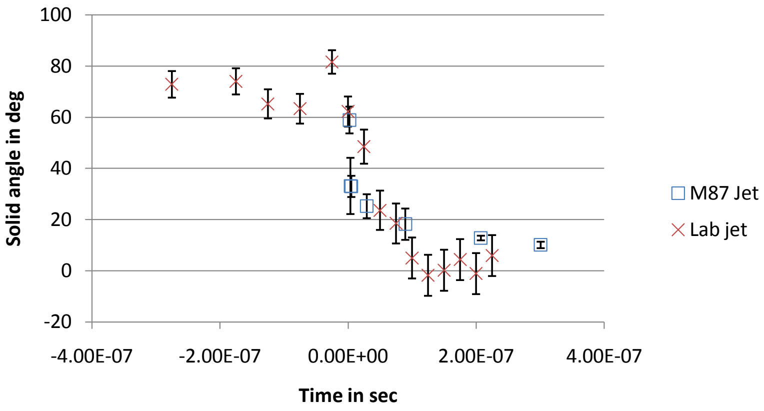

Figure 5.65: Comparison of the collimation of the laboratory jet with the scaled collimation of the M87 in figure 1.5.

electrode, and the time comparison was taken when the laboratory jet began to collimate. This then showed a very close comparison of the collimation of the jet with the collimation rate for the laboratory jet being -5×10^8 deg/sec compared with the scaled M87 jet being -8×10^7 deg/sec.

Comparing this result to both Lebedev and Bellan shows that there are many similarities between the experiments, but there are some distinct differences worth mentioning. First one difference is that the cost of this experiment is much lower than both of these two experiments. This opens up the possibility of spending more resources on diagnostics. With the occurrence of the RAJ and the barrel shock there was a novel distribution of gases for the initial condition. Our background magnetic field was much stronger than both experiments. This gave unique insight at the quasi-hyperbolic flared current profile that neither of these two experiments had. This gave a unique situation to study fluxtube dynamics to contribute to what Bellan and Lebedev have already contributed. These jets also add to the parameter space of similar jet experiments.

5.8 Conclusion

I created laser-triggered jets using a single capacitor charged to high voltage connected directly to the electrode. I have shown that the jet evolution and velocity could be measured using an ICCD camera. Measurements for anode jet behavior revealed nonmagnetic supersonic expansions, that can be correlated to the current flowing through the electrode. This gave initial conditions for the magnetically controlled cathode jet behavior. The cathode jets showed evidence of being a quasi-hyperbolically flared fluxtube and subject to acceleration mechanisms outlined by Bellan [6]. This has been confirmed using numerical simulations of Bellan's theoretical formulations. I have shown that the onset of the kinking instability is consistent with Kruskal - Shafranov theory. The scaling between this experiment and YSO astrophysical jet conditions are reported to be similar with Euler numbers 9 and 40 respectively.

Chapter 6

Laboratory Experiments Simulating Magnetosphere Physics

6.1 Introduction

The magnetosphere has been observed and studied for much of the past century. Space scientist have launched satellites such as the Advanced Composition Explorer at the L1 libration point to give real time data of incoming coronal mass ejections (CMEs) to aid in magnetosphere research and protection for communication systems [130]. This has added tremendously to the area of magnetosphere research. Researchers have also studied the magnetosphere using scaled laboratory techniques in recent studies such as Zakharov [112] to studies performed at the turn of the 20th century by Kristian Birkeland [11]. Refer also to the discussion in section 1.4 for more background on magnetospheres.

I present an experiment with the goal of simulating magnetosphere dynamics in the laboratory using the unique capabilities outlined in previous chapters of this thesis. Theoretical formulations of magnetospheres were applied to a laboratory setting. The experiments were performed using magnetic dipoles and aluminum blocks with the same geometry for comparison with plasma winds created by lasers and laboratory jets as described in chapters 4 and 5. These laboratory simulations were compared with simulations given by the hydrodynamic code HYADES and the stand off distance of the magnetosphere related to these simulations was discussed.

6.2 Theoretical Aspects of Magnetospheres Relevant to this Experiment

Laboratory astrophysical experiments need magnetohydrodynamic scaling to justify comparison physics [60][61]. Gravity is a key physical force in astrophysical problems which is not present in laboratory simulations. In laboratory simulations of the solar wind driven magnetospheres gravity plays no important role. The scaling factor from the laboratory to the astrophysical realm is relatively small compared to other astrophysical phenomena. The geophysical space scale, for instance is 10^9 compared to a magnetic white dwarf (10^{12}) and a supernova (10^{40}). Using the ideal MHD equations the parameters can be scaled between a laboratory experiment and the magnetosphere as in table 6.1.

In table 6.1 I list parameters of the Earths magnetosphere frame from literature [18][77] and the experimental frame as simulated with the hydrodynamic code HYADES, which will be discussed in section 6.5. The earths magnetosphere is a high temperature low density plasma, that flows with large velocities. The length scale is the distance of the magnetopause to the dipole center. The time scale is taken as the length scale divided by the velocity of the solar wind. The solar wind plasma consists mainly of protons, and the experimental density consisted aluminum ions. This must be taken into account when comparing densities. This discussion of the parameters will be revisited, in the context of scaling, in the analysis section 6.5.

Various physical characteristics about magnetosphere physics were discussed in section 1.4. The dynamics of the magnetopause are governed by the

	Earth's Magnetosphere	Experiment
h(cm)	10^9	1
t(s)	10^2	10^{-7}
P(dyne/cm^2)	10^{-8}	5×10^4
$n(cm^{-3})$	10	10^{14}
T(eV)	10	5
B(G)	10^{-4}	10^3
v(cm/s)	10^7	5×10^6
Euler	.4	1.5

Table 6.1: These are the scaling relations for the earths magnetosphere and the experimental setting as calculated by HYADES (see section 6.5). The scaling parameters as defined in section 3.2 are $a \approx 10^9$ (length scale parameter),$b \approx 10^{-15}$ (ρ scale parameter),and $c \approx 10^{-13}$ (pressure scale parameter). [18][77]

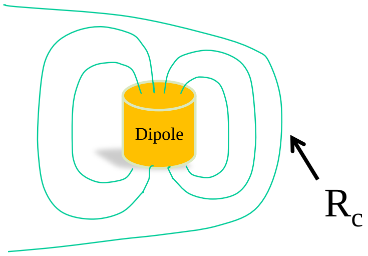

Figure 6.1: The R_c term for the governing magnetohydrodynamic equations is the radius of curvature of the magnetic field along the equatorial plane.

magnetohydrodynamic equations [129] which were discussed in section 3.1.1. The following magnetohydrodynamic equations are a one-dimensional simplification of the global model:

$$\frac{\partial \rho_e}{\partial t} = -\frac{\partial}{\partial x}(\rho_e u) \tag{6.1}$$

$$\frac{\partial (\rho_e u)}{\partial t} = -\frac{\partial}{\partial x}\left(\rho_e u^2 + p + \frac{B_{dp}^2}{2\mu_0}\right) - c \tag{6.2}$$

These equations were derived from variations of the MHD equations 3.12 through 3.15 with the addition of the magnetic field tension term $\frac{B_{dp}^2}{2\mu_0 R_c}$. When

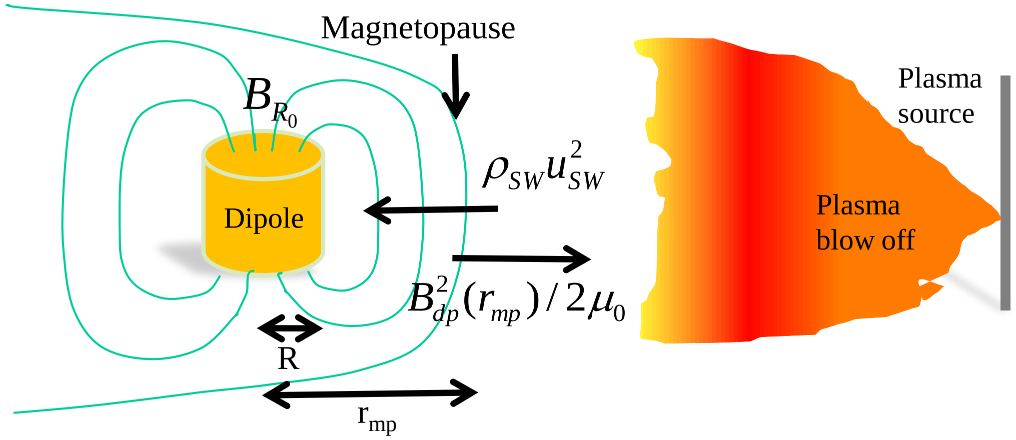

Figure 6.2: The magnetopause is the boundary between the magnetosphere and the solar wind, which is where the magnetic pressure balances with the solar wind pressure.

formulating the one dimensional dynamics of the magnetosphere one needs to include a term for the magnetic tension, where R_c is the radius of curvature of the magnetic field on the equatorial plane of the magnetosphere (see figure 6.1) and B_{dp} is the magnetic field strength.

The standoff distance of the magnetopause, or the distance between the magnetopause and the magnetic dipole center, can by calculated by investigating the pressure balance of the solar wind and the dipole magnetic field

$$\rho_{SW} u_{SW}^2 = B_{dp}^2(r_{mp})/2\mu_0 \tag{6.3}$$

as illustrated in figure 6.2. The dipole magnetic field dies off as the cubed power of the distance

$$B_{dp} = B_{R_0}(R/d)^3. \tag{6.4}$$

As the solar wind interacts with the dipole magnetic field it induces a force on

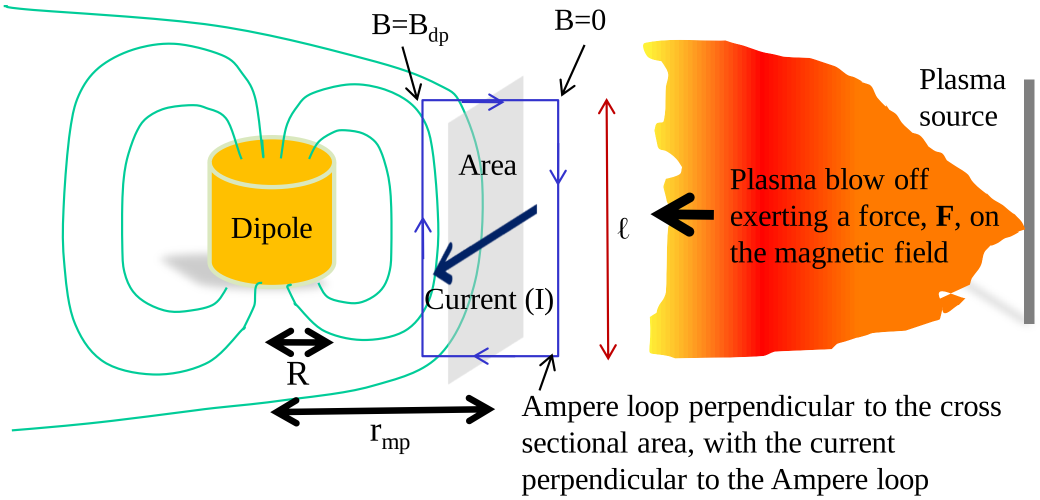

Figure 6.3: The solar wind action on the magnetic field cause a current to form on the magnetopause.

the field. This causes a current to flow called the Chapman-Ferraro current (see figure 6.3)[150]. This current alters the magnetic field in the magnetosphere and such changes in the magnetic field can be detected on the earths surface. This can be formulated by noting that the magnetic field has a sharp boundary at the magnetopause, quickly going to zero up stream from the solar wind. The Chapman-Ferraro current can be estimated using the force-current equations, by defining a fictitious flat area of the magnetopause cross section, and using the solar wind pressure on this area to obtain

$$F = AreaP_{SW} = I\ell B_z. \tag{6.5}$$

The Chapman-Ferraro current can also be calculate from Ampere's law as $\ell \Delta B_z = \mu_0 I_{CF}$ where ℓ is the length of the side of an idealized Ampere rectangle encompassing the magnetopause as in figure 6.3. The ΔB_z is the jump in the magnetic field on the magnetopause, which will be B_{dp} since there is no magnetic field upstream of the magnetopause, and I_{CF} is the Chapman-Ferraro current.

Using the mirror method formulation [115] the magnetic field at the magnetopause will be twice the magnetic field as there would be without a solar wind interaction. Then one can calculate the standoff distance of the magnetopause as:

$$B_{dp} = 2B_{R_0}(R/d)^3 \Rightarrow d = R\Big(\frac{2B_{R_0}^2}{\mu_0 \rho_{SW} u_{SW}^2}\Big)^{1/6}. \tag{6.6}$$

Thus we see that the standoff distance increases with increasing dipole fields and decreases with increased solar wind velocity and density as was expected.

6.3 Experimental Details

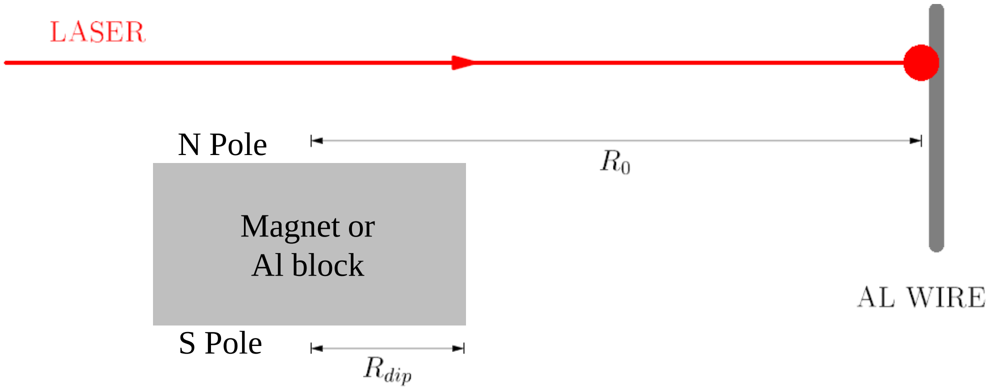

Figure 6.4: Position of the laser, target and magnetic dipole or aluminum block.

I designed a laboratory experiment to test the feasibility of studying scaled planetary magnetosphere physics in the laboratory. Laser-produced plasma and laser triggered jets simulated a “solar wind” in the experiment.

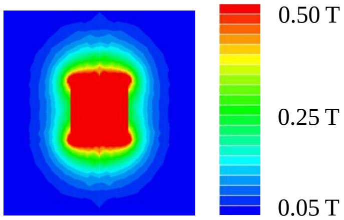

Figure 6.5: Simulation of the magnetic field of the dipole from the electrostatic simulation program Maxwell SV.

Permanent magnetic dipoles and non magnetic objects of the same size and shape were inserted in the path of this plasma wind as in figure 6.4. The goal of the experimental investigation was to investigate the creation of a shock in the magnetosphere, the boundary of the magnetopause, the plasma wind-magnetosphere interaction, and electron acceleration mechanisms.

I performed this magnetosphere laboratory experiment using the YOGA laser. A Princeton Instruments ICCD camera was the main diagnostic as discussed in section 4.3.8. Other experimental details were similar to the details outlined in chapters 2, 4, and 5.

When I used a laser-produced plasma as our solar wind the magnetic dipole or non magnetic obstacle was placed in front of the aluminum laser target as in fig 6.4. I situated the obstacles so that the laser passed the closest possible distance above the obstacle with the laser beam being able to pass onto the target. The laser-produced plasma then flowed back onto the obstacles along the same path that the laser traced out.

The magnetic dipoles consisted of a permanent magnet cylinder with a 4.5 mm radius and a 9 mm length and another with a 6.35 mm radius and a 6.35 mm length. The magnetic field strength as measured by a hall probe on the top of the poles was .5 T and .35 T respectively of these two magnets. The non magnetic obstacles were made out of aluminum and had the same dimensions. The 4.5 mm radius magnets were placed about 28.5 mm away from the target. The 6.35 mm radius radius magnets were placed about 15 mm away from the target.

I attached the magnetic dipole magnetically to small iron wire or to iron screws. These iron objects were connected to large copper wire to attach to a stand in the vacuum chamber. They were too small to perturb significantly the magnetic field. The University of Texas physics machine shop build aluminum blocks with the same dimensions as the dipoles, with taped holes on the sides to attach the blocks directly to screws. These blocks were then attached in the same way to the copper wire as the magnetic dipole for alignment. When I used the laser triggered jets as the plasma wind the obstacles were placed in the paths of the jets the same way. For alignment techniques see appendices E.6 and E.5.

6.4 Magnetosphere Data

I obtained data using an ICCD camera using various plasma wind sources. As previously described I used laser-produced plasma as a plasma wind source using 200 mJ, 500 mJ and 2 J of energy in the laser pulses. laser triggered plasma jets were also used as plasma wind sources using 3000 V and 4900 V with a molybdenum electrode as parameters for the jets.

I originally used the larger dipole magnet for the magnetic obstacle in the laser produced plasma experiment. But this data was flawed as there was a shockwave that formed due to the proximity of the dipole with the plasma wind (See appendix D for details). I placed the smaller magnetic dipole's

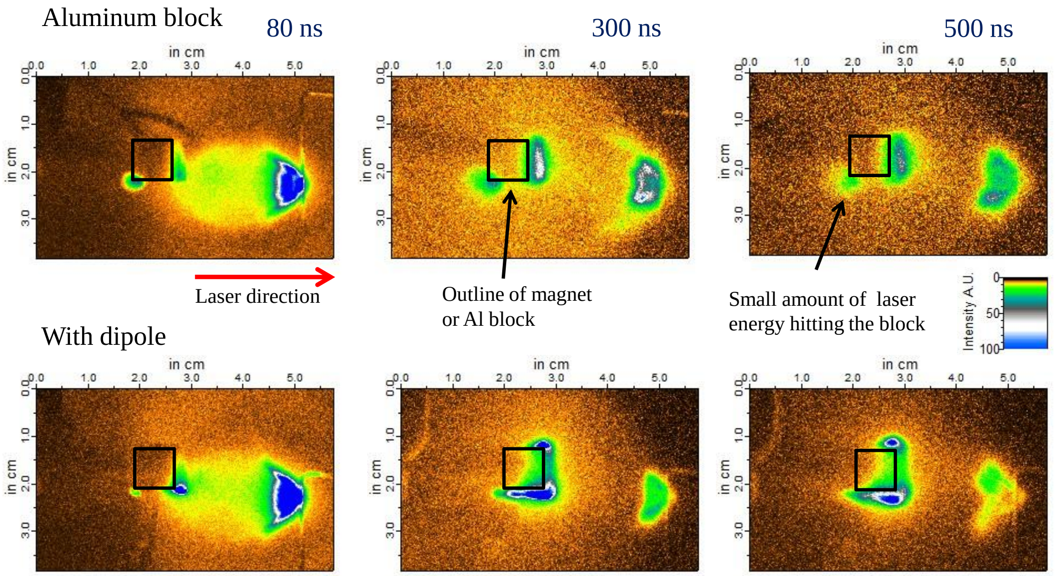

Figure 6.6: Data for the magnetosphere experiment using a 200 mJ laser pulse to create a plasma wind.

center about 2.8 cm away from the target interaction as in figures 6.4 and 6.6. At this distance the shockwave buildup was not present as it was in the previous example. The data showed, more clearly, the plasma accumulation on the poles of these magnets. The aluminum block had the plasma accumulation on the face of the block directly facing the target interaction. This was seen in figures 6.6, 6.8, and D.3 (in appendix D). Plasma buildup along the poles also occurred with the larger dipole magnet. This plasma buildup signified plasma buildup in the cusp region of a magnetosphere system. The figures showed that the laser hit the back of the magnet as it progressed towards the target. This should not be confused with a night side aurora. It is key to note that many planets do not have magnetic fields to protect them from the solar wind such as Venus. Thus the blocks with no magnetic fields represented

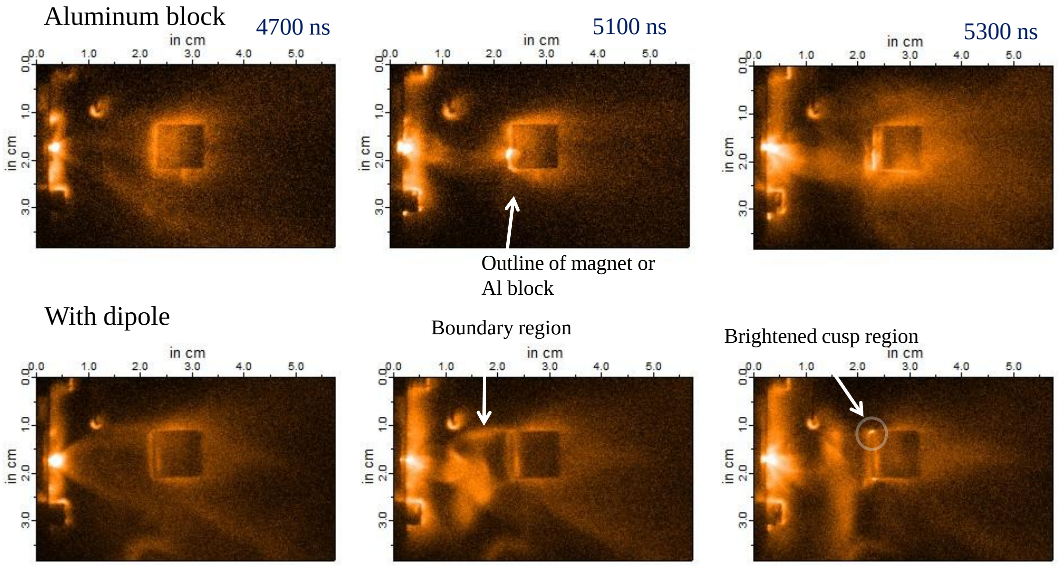

Figure 6.7: Data for the magnetosphere experiment using the jet formulation described in chapter 5 as the plasma wind.

unmagnetized planetary ionospheric physics as on Venus. There were features in these images that suggest a boundary in the luminescent background plasma (as in figure 6.12) that were suggestive of a magnetopause boundary that will be discussed in section 6.5. This is similar to other faintly visible boundaries, such as the RAJ, discussed in this thesis.

With jets as a plasma wind source (taken during the jet forming region), more distinct features appeared that on first inspection appeared more similar to magnetosphere structures than those derived in the laser-wire blow off plasma experiment. The physics was much more complicated in these examples. With a jet formed using a molybdenum electrode biased at 4900 V as explained in chapter 5 there were similar features in this experiment that resembled the jet experiments in chapter 5. The remnant anode jet and the

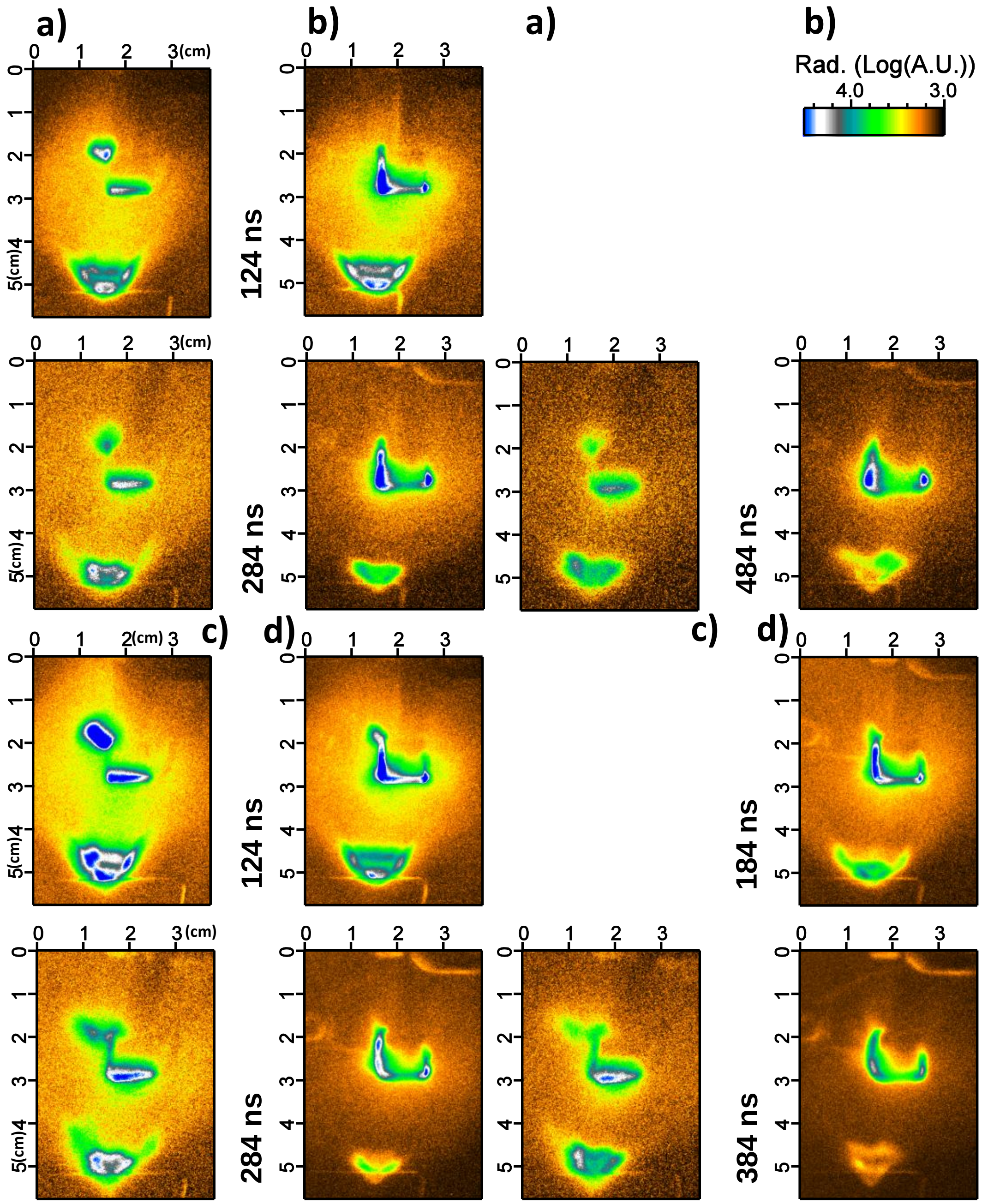

Figure 6.8: 200 mJ laser pulse impinging on an Al target next to a) a 4.5 mm radius Al block and b) a 4.5 mm radius magnetic dipole. c) and d) have similar conditions as a) and b) respectively with a 500 mJ laser pulse.

ablated material progressed towards the block or magnet. While using an aluminum block the jet formed between the block and the electrode. Luminescent material built up on the block facing the electrode. A halo of plasma surrounded the aluminum block and currents progressing through this halo plasma forming kinks in the fluxtube (see figures 6.7,6.9 and 6.10).

More distinct features formed with a magnetic dipole. The ablated material, in a blobular, form progressed towards the magnet. The jet material did not penetrate beyond a certain radius from the magnet. Plasma formed in a cusp region on the dipole and at a certain time in the progression the cusp tips of the magnet became briefly, intensely illuminated. As the jet progressed this defined radius fluctuated, but a boundary of plasma always held away from the face of a magnet. Visible lobes that appeared to be return currents formed along this boundary and connected approximately to the grounded part of the electrode. The current found least resistance propagating along the magnetic field lines of the magnet. A plasma tail formed behind the magnet throughout the duration of the jet. Unidentified plasma lines emanated from the center of the poles of the magnet toward the night side of the magnet.

I investigated the residue deposited on the magnet and blocks by investigating the physical block its self. The jet experiments deposited much more material onto the block than the laser-wire blow off experiments. With the jet example the jet material plated half of the face of the poles of the magnet facing the jet, while the jet material plated only the surface of the side of the aluminum block facing the jet. This gave more evidence that the jet material evolves according to magnetosphere dynamics.

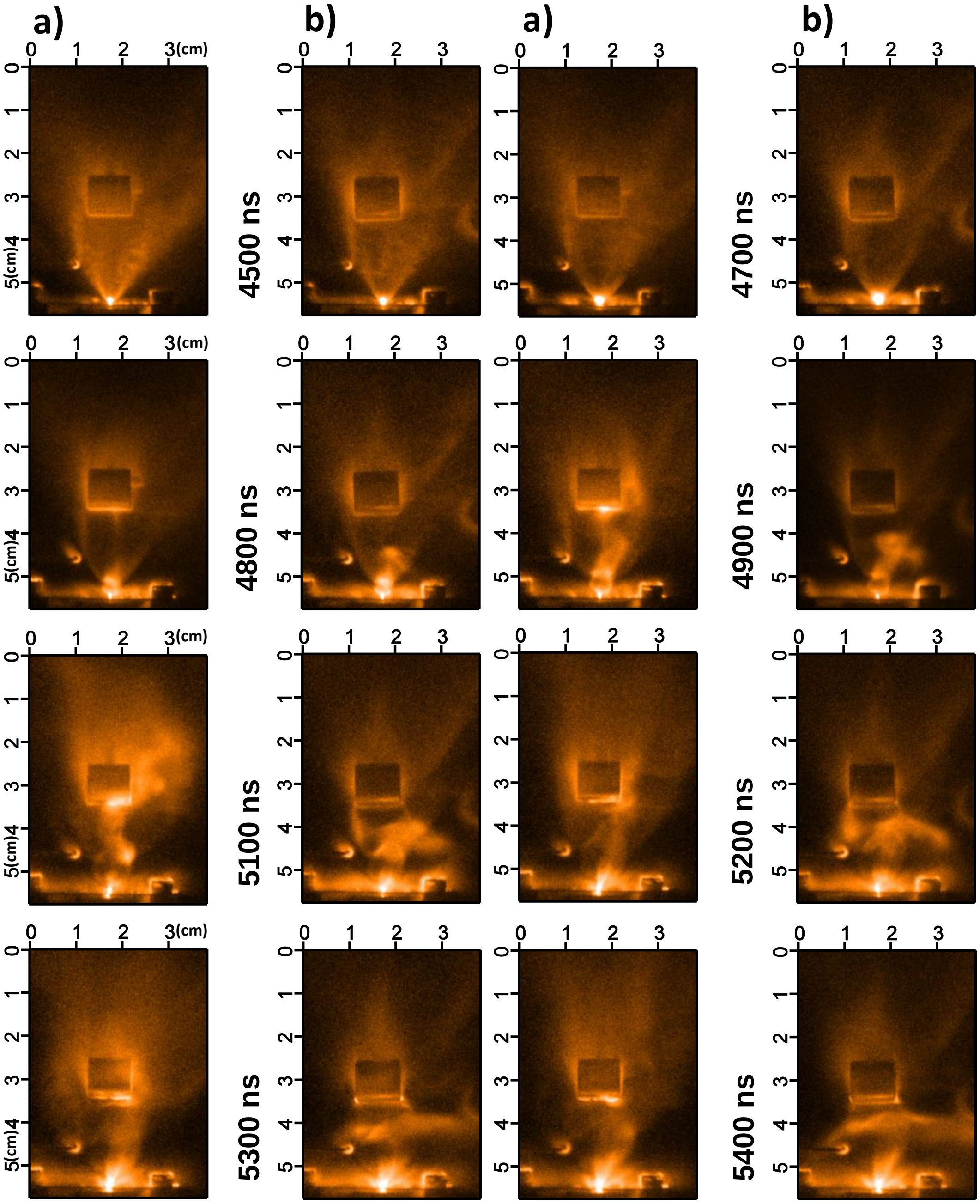

Figure 6.9: ICCD image of a 4900 V Mo jet impinging on object a) an Al block and b) a magnetic dipole.

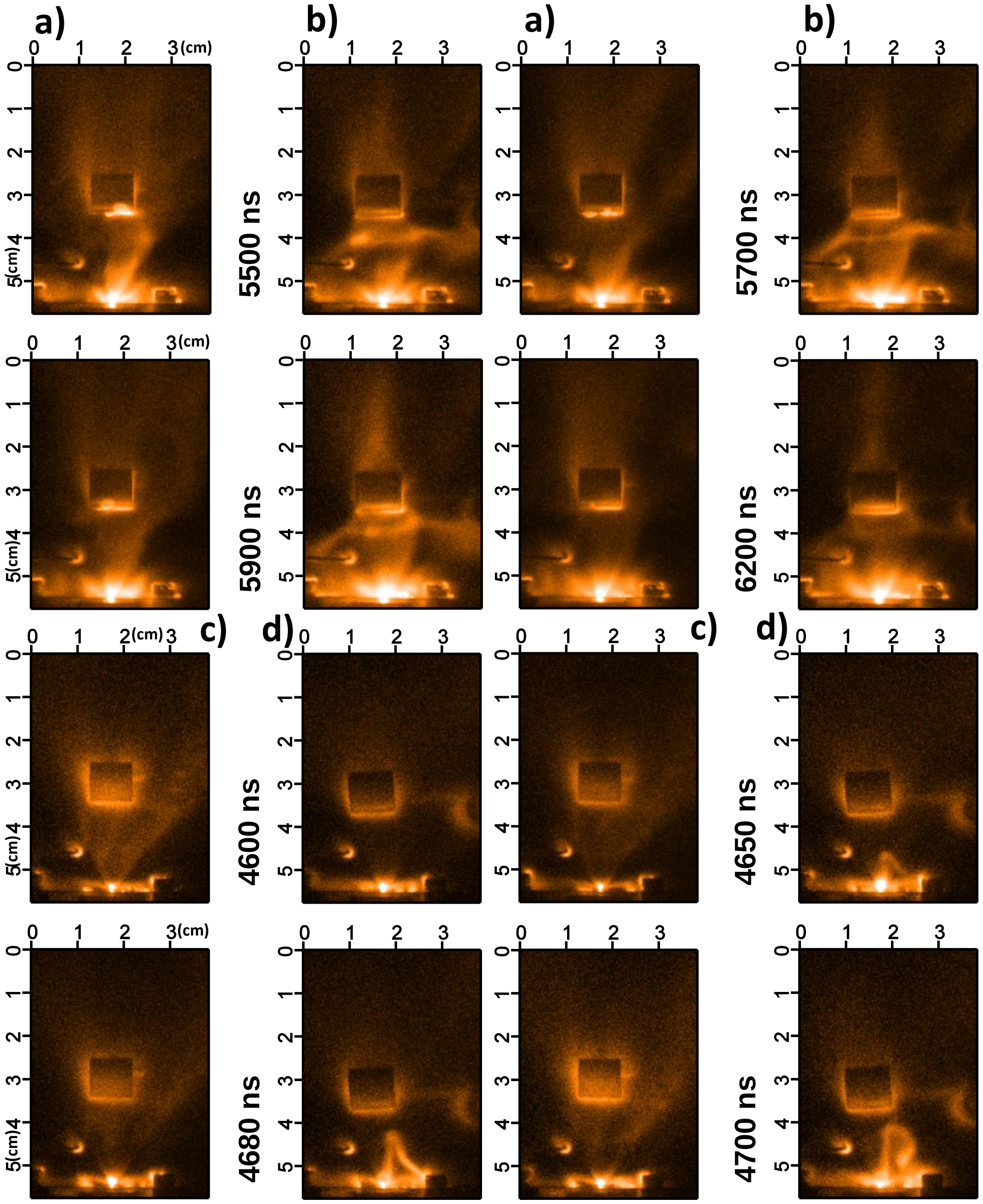

Figure 6.10: ICCD image of a 4900 V Mo jet impinging on object a) an Al block and b) a magnetic dipole.ICCD image of a 3000 V Mo jet impinging on object c) an Al block and d) a magnetic dipole.

6.5 Analysis with HYADES Simulations

I used HYADES [82], a one dimensional hydrodynamic code developed at LLNL as described in chapter 4, to estimate parameters about our plasma wind. The calculations were confined to one-dimensional calculations in linear, cylindrical, and spherical geometries.

The HYADES code calculated the plasma parameters at 2 cm away from an Al target that had been ablated with a 200 mJ 1064 μm laser source using cylindrical geometry. The results are in figure 6.11 with a) the plasma pressure, b) the plasma velocity, c) the ion density, d) the mach number, and e) the electron density. This required some extrapolation from the output of HYADES. HYADES outputs parameters vs. mesh point number. Hence to get a precise number for a consistent distance I had to infer the data from the mesh point output. This was done for several parameters as reported in figure 6.11. Take notice here that the solar wind mach number was about 4 to 10 which was consistent with these calculations. This was an artifact of using aluminum ablation plasma. If a lighter ion material such as hydrogen was used the mach number would be much higher.

From these parameters I calculated the standoff distance using equation 6.6 in figure 6.12. This calculation showed that the magnetopause should hit the magnet briefly. In the example, outlined in figure 6.12, at 300 ns, the calculated magnetopause will be at $\sim$.75 cm away from the axis of the dipole. There was, in this ICCD figure, a diffuse boundary in the luminescent material surrounding the magnet at a distance of approximately 1.5 cm away from the axis of the dipole. This boundary was interpreted as the magnetopause of the system. The boundary was expected to be diffuse due to the finite value of the electron mean free path and the transient nature of the event. In which

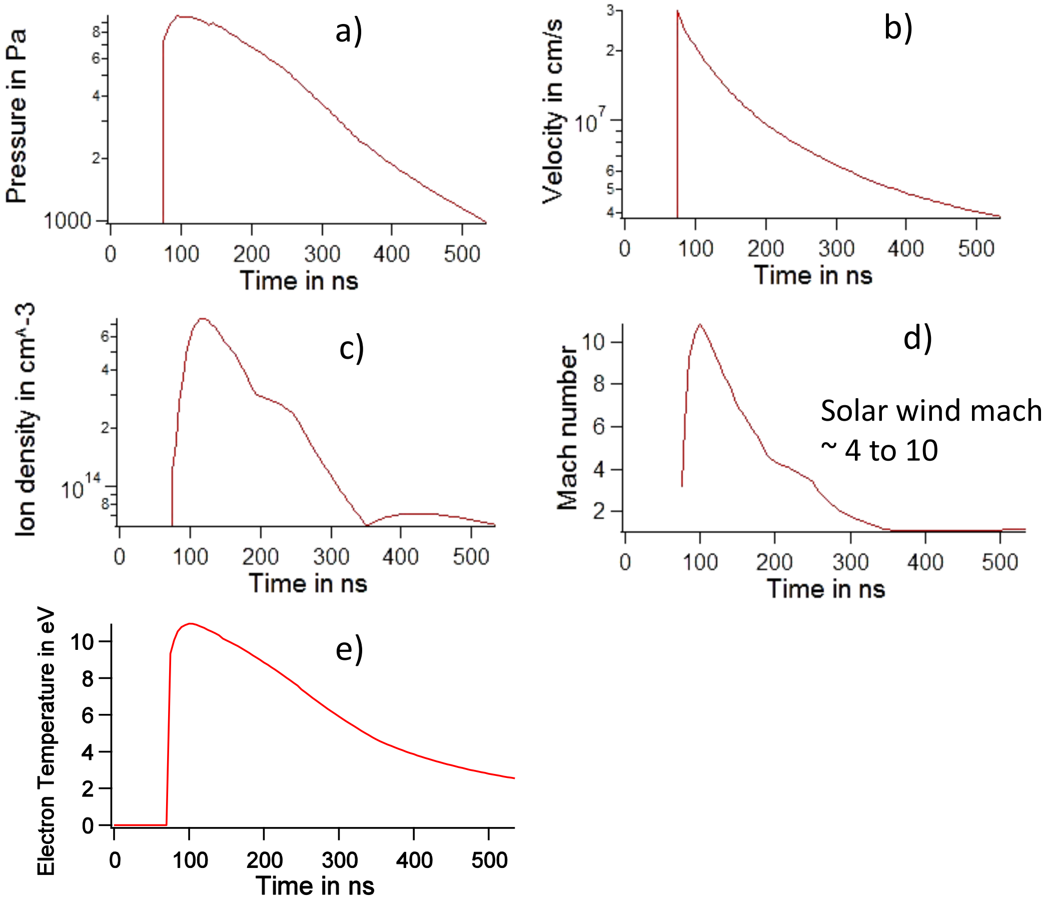

Figure 6.11: Simulation results for the five key plasma parameters for the plasma wind from a 200 mJ laser pulse impinging on an Al target at a distance 2.0 cm away from the ablated target. The simulation was in cylindrical geometry.

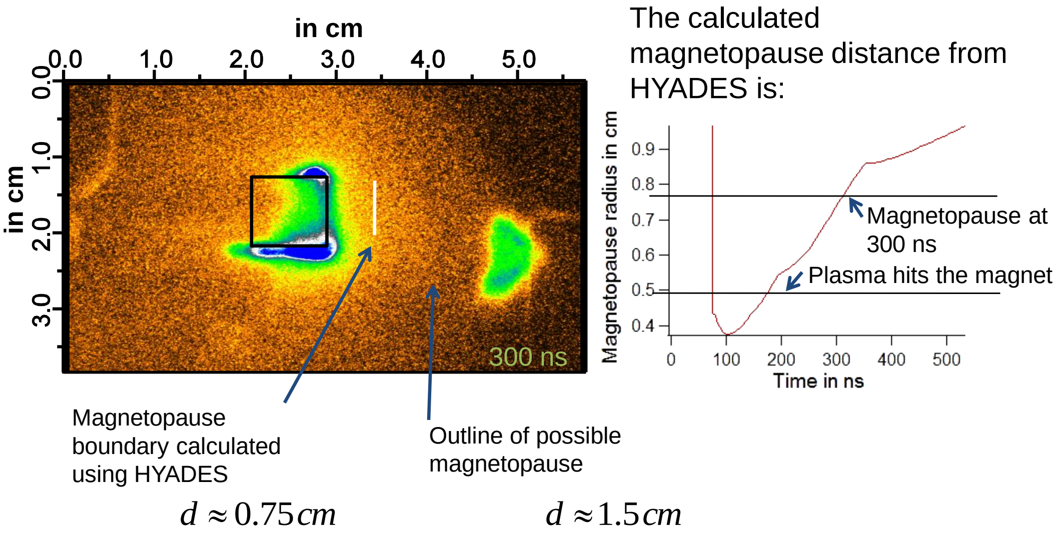

Figure 6.12: I compared the magnetopause distance calculated from HYADES with the ICCD image of the plasma wind-dipole interaction at the same time.

case the calculation matched closely with what was observed.

Data from HYADES can be used to calculate the force of the plasma wind on the magnets magnetosphere. If the magnetopause effective cross section was estimated to be 4 cm^2 then the force on the magnetopause at 300 ns, in the case presented in figure 6.12, would be

$$F_{pw} = A_m P_{pw} \approx 1.2\ N.$$

This would be a measurable force and certain collaborations are interested in measuring this force. Measuring this force would give important information about the size and effect of the magnetopause. As discussed in section 6.2 this force caused the Chapman-Ferrero current to flow. The value of this current for the force calculated above will be 350 A using equation 6.5.

I also derived information about the magnetosphere from the jet-magnetic

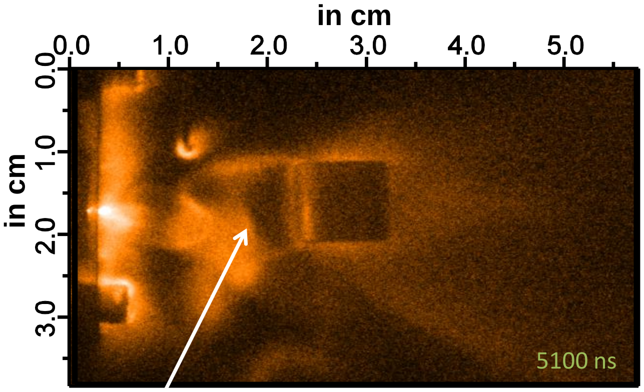

$V \approx 4\times10^{6} cm/s$

$n_i \approx 10^{15} cm^{-3}$

$\Rightarrow d \approx .5cm$

Boundary region

$d \approx 1.0\, cm$

Figure 6.13: The standoff distance for the jet flow was comparable to our calculations.

dipole experiment from the parameters of the experiment as illustrated in figure 6.13. The velocity of the plasma wind from the jet was about $V \approx 4 \times 10^6\ cm/s$. The initial density of the jet, as in chapter 5, was on the order of $10^{16}\ cm^{-3}$. If I allowed for the expansion of the material in the radial direction one order of magnitude over the time the jet reached the magnetic vicinity the density will drop to the order of $10^{15}\ cm^{-3}$. This gave a standoff distance of $d = 0.5\ cm$ from equation 6.6. The boundary of the standoff plasma measures to about 1.0 cm. This showed further correlation between theory and experiment.

In laboratory comparisons with planetary magnetospheres, one concern is that planetary magnetospheres are a collisionless phenomena and that the laboratory experiments are very collisional. For many of the effects in the magnetosphere there would not be a good comparison of effects, but is this case the magnetopause and the Chapman-Ferrero current were investigated. These effects were only dependant on the magnetization of the plasma and the effects of the flow of the plasma. Hence the degree of magnetization was the issue. As discusses in previous sections (ie. section 5.2.3) the ions in these laser-produced plasmas jet will not necessarily be magnetized but the electrons will be magnetized and will bind the ions to the magnetic fields through electrostatic forces. Thus, as seen in with other magnetic effects of this thesis, the experimental plasma wind will be affected by the magnetic dipole approximately to that described in section 6.2. Hence the physics of the magnetopause between the two frames will be similar. Also the Chapman-Ferrero current only needed a "jump" in the magnetic field to be produced, which will be provided by the laser-plasma wind compressing the magnetic field with the magnetized electrons.

The comparison between the magnetosphere frame and the experimental frame as calculated by HYADES is in table 6.1. There were no direct plasma parameter measurements in this experiment, but as discussed in section 4.5, HYADES calculated reasonable values for density and front velocity in the laser-produced plasma. With this credibility, the scaling between the two frames was similar with Euler numbers being .4 and 1.5 for the earths magnetosphere and the laboratory respectively. With this similarity and the geometrical similarity of the set up, further investigations into the dynamics of the laboratory magnetosphere plasma are warranted.

6.6 Conclusion

I developed and performed repeatable laboratory experiments simulating plasma wind incident on a magnetic dipole target. The dynamics of wind-magnetosphere interaction were measured with both spatial and temporal resolution, opening up the possibility of direct investigation of relevant plasma dynamics of plasma wind on planetary and astrophysical objects. Features were found that were consistent with solar wind-magnetosphere interactions, including creation of a magnetopause in front of the magnetosphere, and brightening visible at poles with associated deposition on the polar caps of the targets. The observed diffuse magnetopause visible at the standoff distance consistent with calculations of the standoff distance theory. Continued development of these techniques may provide valuable data for testing our current understanding of solar wind - magnetosphere and ionosphere interactions.

Chapter 7

Conclusion and Future Directions

7.1 Summary

This thesis has discussed topics relating to laboratory astrophysics involving laser-produced plasmas, currents, and magnetic fields. Matters involving laser-produced plasmas and the creation of lasers to instigate these plasmas have been discussed. Several measurements and models have been made to investigate laboratory simulations of magnetized jets and magnetospheres.

To create laser-produced plasmas lasers with high energy and moderate pulse lengths are required. This instigated the creation of a glass amplified laser system called YOGA. The YOGA laser was built with 19mm Nd-glass rods pumped with 1200 J pulse forming networks. The laser pulse was 8 ns long at 1064 nm and had pulse energies up to 3.7 J.

Using the YOGA laser, measurements of laser-produced plasmas were performed. The laser targets used were aluminum and copper wire embedded with and without magnetic fields. These plasma interactions were measured using main diagnostics of Schlieren, interferometry, and ICCD photography. Quantifiable differences with and without magnetic fields were measured with ICCD photography, but some differences were measured with interferometry. These differences and other plasma characteristics were modeled using self-similar equations and HYADES simulations. Very agreeable comparisons were made between plasma expansions with cylindrical HYADES calculations and ICCD measurement.

Magnetized plasma jets were created with a novel experiment based on vacuum arcs for the purpose of laboratory simulations of astrophysical jets. Vacuum arc technology was used to construct plasma jets where a supersonic unmagnetized anode jet remnant served as the initial conditions for a magnetized cathode jet. The electrode geometry was axisymmetric with a grounded outer ring. The applied bias on the center electrode was reversed directions during the measurement due to a capacitor discharge. The reaction of an electrode to a vacuum arc is inherently antisymmetric between cathode and anode modes, enabling different responses of the electrode to an alternating current discharge.

The anode jet created a non-magnetized supersonic flow into the chamber through a flared nozzle and a small cavity encompassing the electrode. This supersonic flow created a measurable barrel shock in an axial magnetic field. The supersonic flow had a Mach number of ~ 3.5 as calculated from the geometry of the nozzle. The barrel shock bounded a cone of higher densities and temperatures overlaid in a colder background gas. The Rankine-Hugoniot equations [59] predicted, for a Mach number on this order, the density drop across the shock will be on the order of a factor of four and the temperature will drop a factor on the order of ten.

With this barrel shock cone embedded in an axial magnetic field, the currents upon reversing direction funneled down the cone due to the anisotropic conductivity in the magnetized plasma and the differences in plasma conductivity between the two regions. Maxwell SV software calculated the current distribution under similar conditions and showed that the axial current in the cone was quasi-uniform as outlined with the fluxtube. This created a fluxtube outlined by the barrel shock where the current was approximately $I = \left(\frac{r}{a(z)}\right)^2 I_0$ where $a(z)$ is the radius of the barrel shock and I_0 is the total current. This type of fluxtube was subject to Bellan's MHD based fluxtube model [6].

Modeling of Bellan's MHD based fluxtube model [6] showed a dynamical progression of a jet-throat pinch similar to the measured jet progression. The simulation tracked the velocity of the jet throat as it progressed in time. The throat velocity increased with plasma temperature and inversely with the jet radius in the calculation. The velocity of the throat was additive to the velocity of the plasma being emitted by ablation on the electrode which was on the order of 10^6 cm/s. The velocity calculated with this formulation was 8.0×10^5 cm/s with no initial velocity, the temperature at 10 eV, and the current at 1000 A. The measured throat velocity under the corresponding conditions was $4.44 \pm 0.94 \times 10^6$ cm/s. With the velocity of thermal expansion of the cathode jet material assumed to be 1.8×10^6 cm/s (as reported from vacuum arc literature for cathode jets under similar voltage and amperage conditions [94]) the additive Bellan calculated velocity was 2.6×10^6 cm/s.

Bellan's equations predicted the distribution of mass within the fluxtube similar to the plasma emission distribution in the ICCD images. Interferometric data was taken in an early stage of the jet progression that measured a density of $1.9 \pm .2 \times 10^{17}$ cm^{-3}. With an assumed temperature of 6.0 eV (Taken from vacuum arc literature with similar conditions [94]), and with the measured current of 791 A, the density calculated from Bellan formation was 2.1×10^{16} cm^{-3}.

Bellan's equations predicted rotation occurring in the fluxtube [6]. This rotation created a centrifugal force that expelled mass from the center of the jet throat. Evidence of this was measured in the distribution of plasma emission in the throat of the jet having a significant divot in plasma emission. The calculated radial displacement velocity was on the order of 10^5 cm/s which was the same order of magnitude of the emission displacement velocity in the divot. Kinks in the plasma tube column were measured in the jets and were compared favorably with Kruskal-Shafranov theory [64]. The scaling parameters of the jet were similar to the parameters in YSO astrophysical jets [4][135] with the Euler numbers being 9 and 40 respectively.

Several investigations were made into measurement of laser-produced plasmas and laser-triggered jets interacting with magnetic dipoles with the purpose of simulating magnetosphere physics in the laboratory. Measurements of the standoff distance of the magnetopause were measured and compared with the magnetopause measurement calculated with HYADES. Rough agreement between visible boundaries in the plasma and this standoff distance suggest that this experiment may eventually give viable information concerning magnetosphere physics.

7.2 Future Directions

Exciting measurements have been made of various phenomena that relate to laboratory simulation of astrophysics. The phenomena and tools developed in this thesis are just the beginning of future possibilities for subsequent researchers. There are many possible investigations that can be derived from this work.

7.2.1 Future Directions for the Laser-produced Plasma Experiment

ICCD images of aluminum plasma show intense boundaries in magnetic fields that could possibly be measured with interferometry. This measurement would be worth taking to give more useful tools in optical probing, and to complete the investigations made in this thesis. Modeling in HYADES can be developed using magnetic fields. There would be academic value in testing HYADES magnetic capabilities in comparison with the measured laser-produced plasmas in magnetic fields presented in this thesis. Also small plasma probes can be tested using laser-produced plasmas for use in future plasma jet experiments.

7.2.2 Future Directions for the Laboratory Produced Jet Experiment

There are many exciting and interesting directions the experiment concerning magnetized jets can take. The use of a variety of direct plasma probes to measure the plasma parameters of the jet will give more accurate and complete measurements of the plasma density, temperature, current, and magnetic fields. It would not be difficult to make a B-probe on the order of 3 mm to use in this experiment. 3 mm is a little too large for the fine detail over jets, with more effort B-probes can be made down to 1 mm. Small Langmuir probes can also be made to measure the plasma density and temperature on a small scale. It would be wise to collaborate with Gekelman's group at the LAPD. They have experience in measuring small laser-produced plasmas with direct plasma micro-probes [113]. Faraday cups would be an effective way to measure the velocity of ions expelled from the jets.

The use of spectroscopic measurements would be very beneficial for this experiment. One could place a filter in front of the ICCD camera to measure the spatial distribution of a specific spectral line on the jet progression. This could tell us much about the composition and temperature of the jets. Challenges in spectroscopic measurements include finding ways to be more proximate to the plasma to increase the radiation solid angle for spectroscopic measurements taken using a spectrometer backed by the same ICCD camera. Laser spectroscopic measurements such as laser induced fluorescence and Thompson scattering can reveal more information about the temperature and density of the plasma, although these are generally difficult measurements to make.

There are plans to solicit a group at Sandia National Labs to make full three dimensional simulations of the set up. Full MHD simulations will complement the reduced MHD simulations performed in this thesis. Full MHD simulations have the potential of revealing how all the parameters, such as unmagnetized supersonic flow and the current being both large and nonconstant, interact together whereas in this thesis all of these parameters were treated separately.

There is academic interest in the interaction of plasma jets with other materials such as plasma winds and denser gases. Collaborators have suggested impinging these jets into ultra low-density foams to simulate jets interacting with the interior of stars. Different pulse power systems can be developed to investigate the possibility of using the laser-produced plasma as a medium for jet formation. If a faster rise time of current could be induced more dynamics in a hotter laser-produced plasma might be observed. With the mechanism for producing these jets being relatively simple more resources could be used to develop these different detection systems and improvements to compete in the field of laboratory astrophysics.

7.2.3 Future Directions for Experiments Involving Magnetospheres

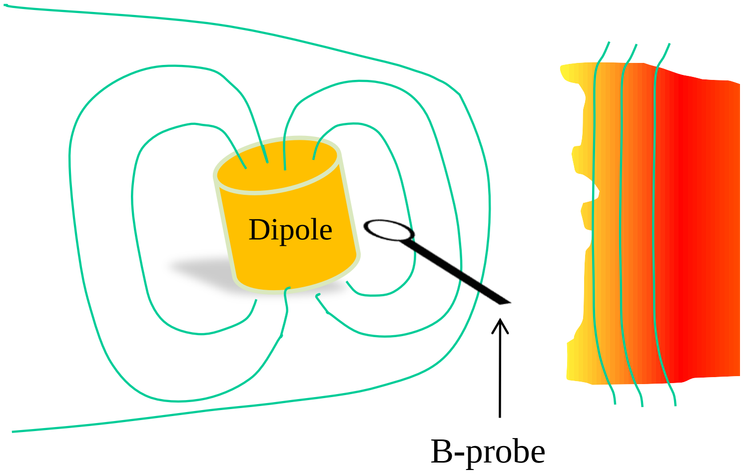

Figure 7.1: Future experiment would include adding magnetic fields to the plasma wind and measuring the plasma with B-probes and other plasma probes.

I propose future experiments for studying laboratory magnetosphere as outlined in figure 7.1. In future experiments the induction of a tilt in the magnetic dipole similar to the earth-sun relationship will be made. Different tilts in the earth-sun system create different distributions of plasma around the magnetosphere, and these differences would be sought in the laboratory model.

The incoming solar wind has an imbedded magnetic field that produces vastly different effects in the magnetosphere depending on whether the plasma wind's magnetic field is aligned or anti-aligned with the magnetosphere's magnetic field [58][28]. I propose to add magnetic fields in the laser-produced plasma by creating the plasma in a weak magnetic field. Differences would be expected in the plasma distribution around the dipole magnet with different directions of magnetic fields in the incoming plasma wind. This would be similar to that in the earth-sun system. Using B-probes in this experiment would be a valuable use of the B-probes developed for other similar experiments proposed in this chapter. This would give direct information about the magnetic field interactions with the plasma wind, magnetopause magnetic fields, and would potentially measure the effects of the Chapman-Ferrero current.

7.3 Conclusion

New technologies have increased the possibilities of studying astrophysics in the laboratory. There is a wealth of unanswered questions given to the body of science from astronomers that cannot be answered without direct probing of the phenomena [117]. Making such conditions in the laboratory can help give insight to these interesting and varied questions. This thesis poses experiments that may bring us intellectually closer to the stars through work done in a humble laboratory.

Appendices

Appendix A

Figures and procedures associated with the YOGA laser development

A.1 Instructions for the Assembly of the Glass Laser Heads

Assembling the glass laser head is very difficult due to the construction of the glass laser head and the fragility of the components involved. Taking apart and reassembling the heads should be done with the most careful and controlled circumstances. To assemble the glass laser heads you need the following list of materials as illustrated in figure A.1:

- The steel casing
- the macor diffuse reflector
- six flashlamps
- the 19 mm glass laser rod
- two stainless steel casing covers that have holes for the flashlamps and the glass rods
- two plastic covers that will seal the head
- two smaller plastic covers that seal the flashlamps on the plastic cover

- four 11/16” X 7/8” S70 silicone o-rings
- 12 5/16” X 1/2” S70 fluorosilicone o-rings

Make sure that all the materials are clean before assembly. The flashlamp’s lifetime will dramatically decrease if there is any finger oil or other impure substance on them. The macor reflector needs to be extremely clean and white in order to reflect uniformly onto the laser rod. Keeping all the materials clean will greatly increase the lifetime of the head assembly.

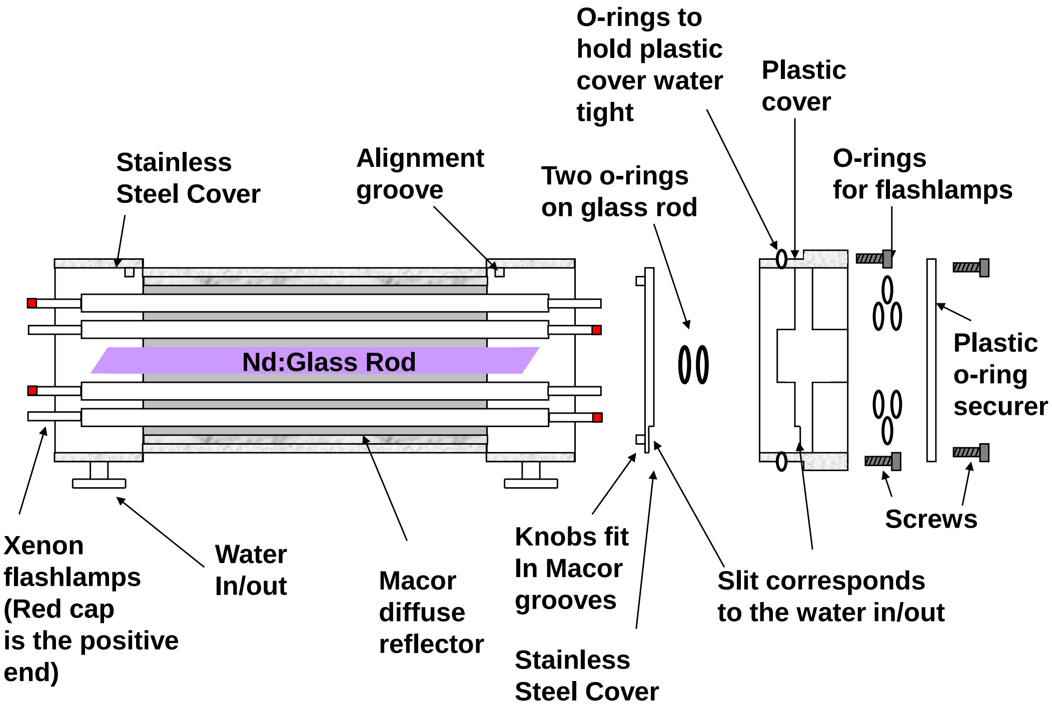

Figure A.1: Side view assembly diagram of the glass rod and flashlamp configuration in the laser head.

With all of the materials clean and ready to assemble, choose a comfortable place with plenty of room to be able to assemble the head with as

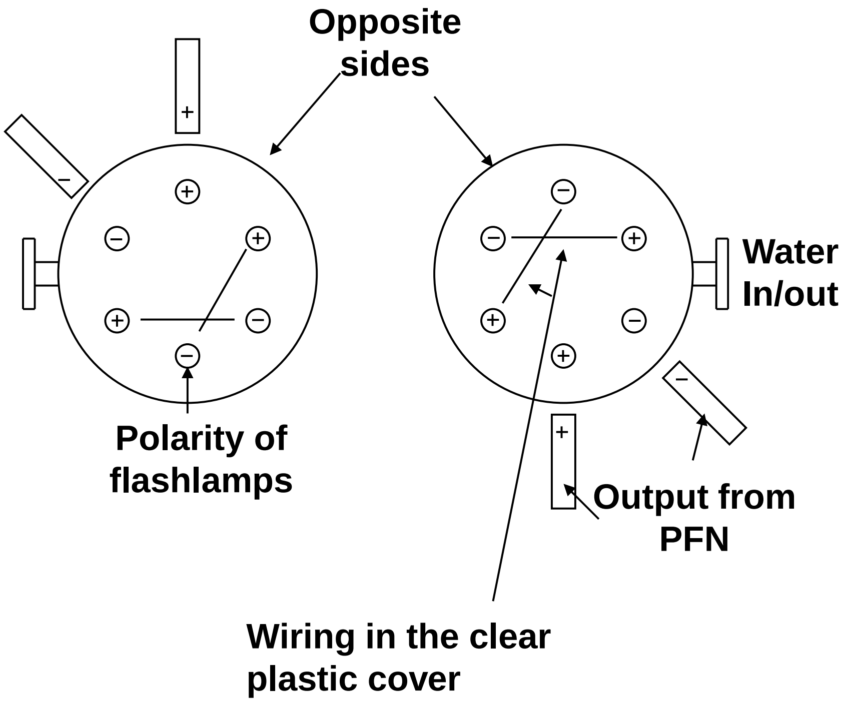

Figure A.2: Head on assembly diagram of the laser head showing the electrical connections of flashlamps.

minimal outside stress as possible. Make sure all the tools are available and within reach. This is tedious, fragile work and if you are in the middle of a fragile procedure and you can not get what you need to finish the procedure, I advise working backward to bring the project back into a safe comfortable position. You will risk breaking the laser rod and the flashlamps which are very expensive.

Lay the stainless steal housing down on a flat space. Slide the macor reflector into the housing and place the stainless steel covers onto the the macor reflector with the groves of the cover sliding in place with the macor reflector. Remember that macor is glass and can shatter if dropped, or chipped if handled improperly. Once the cover is in place carefully slip the glass rod through the center hole, making sure you do not chip the rod as it slides though the hole. Have the larger o-rings ready to slip onto the rod. Slip the o-rings onto the glass rod; this will enable the glass rod and a stainless steel cover to stay firmly in place. You will need to put two o-rings on each end of the glass rod so that the plastic covers will be able to press the o-rings onto the stainless steel cover. Make sure that the glass rod is in the center of the device.

With both o-rings on the sides of the glass rod and stainless steel covers firmly in place you are ready to put the larger plastic covers onto the stainless steel enclosure. This procedure is difficult because of the tight fit these plastic covers with the accompanying o-rings provide for the enclosure. It is helpful to have two sets of screws. The first set will be very long for the purpose of getting the plastic covers into the enclosure past the o-ring. You will have six screws on each side. Alternate screwing the screws diagonally, screwing each screw a quarter turn until the cover is close to the glass rod. Before clamping the cover onto the glass rod make sure that both covers are equally in place. At this point alternate screwing the screws on both sides of the head, using quarter turns each time. Keep screwing until the covers are firmly on the enclosure.

With the plastic covers firmly in place you are now ready to slide flashlamps through the device. Each flashlamp has a defined polarity marked with a red marking on one of its electrodes. When you slide in the flashlamps make sure that the red markings are the same in figure A.2. Slide in the flashlamps using rubber gloves. Again make sure not to break the flashlamps during this procedure. You then place the small o-rings on each end of the flashlamps to hold the flashlamps in place. Make sure that the flashlamps are centered in the device. Now screw on the small plastic cover that will clamp the o-rings in place. Again alternate the screws you screw on in a diagonal fashion to make sure the applied pressure is even, and screw on both covers at the same time. With this cover on the edges of the laser head you now have a watertight seal.

Carefully slip the electrical connections over the flashlamp leads as shown in figure A.1. Be careful of the electrical connectors, as they are brittle. The last part of the assembly is to slip the laser head end cap insulators over the flashlamp leads. The laser head end cap insulators have two electrical connectors that connect the flashlamps to the PFN's. These electrical connectors must be extended while the laser head end cap insulators are being put on. Put the electrical connectors onto the leads of the flash lamps as shown in figure A.2. Slowly move on the laser head end cap insulators while slowly pulling back the electrical connector leads. Make sure you put no torque on the system. If there is even a small amount of torque on the flashlamps they will break. If the flashlamp does break you must undo the entire head and clean out the glass. Screw on the end cap insulators using nylon screws. Screw the protective plastic coverings along the insulated leads onto the end cap insulators. Check the success of the assembly by using a tesla coil on the flashlamp leads to see if they glow. If they do not glow, then one of the flashlamps has broken and will need to be replaced.

Taking apart the laser heads uses the same instructions for assembly but in reverse order, with one exception. Taking off the black plastic cover is very tricky and risky. With the flashlamps and screws removed, take off the black plastic covers by inserting two flathead screwdrivers on opposite sides of the black plastic cover where the cover meets the laser head assembly. Torque the screwdrivers in the same relative clockwise direction so that the screwdrivers twist in opposite directions relative to each other, causing the black plastic cover to pop up a small amount. Continue around a laser head lifting up the black plastic cover in a way that reduces the torque on the glass rod from the black plastic cover.

A.2 YOGA laser S.O.P.

1. **Startup**
2. Turn on the GCR; make sure that the cooling water is flowing. (The cooling water does not shut off with the laser, so I usually turn off the water manually after shutting off the laser.) On the power supply, turn the key and flip the white breakers to the “On” position.

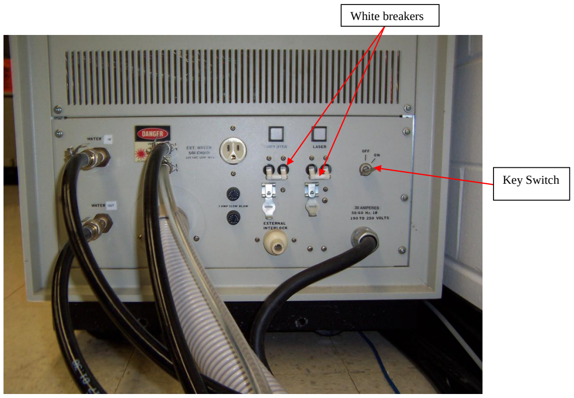

Figure A.3:

3. Set the GCR (both the oscillator and the amplifier) to simmer. To do this, press and momentarily hold the green buttons for both the oscillator and the amplifier at the same time
4. Identify where the waveplate positioned at the exit from laser is set.

- 25° is full energy
- 341° deg lets the minimum amount of energy through

The stray light goes into a beam dump from a polarizer. Make sure that the spatial filter pump is on and that all telescopes in the laser are under vacuum.

5. Check that the beam output is blocked. Set the waveplate to the desired setting, and turn the GCR to full energy. Let the laser warm up for one hour.

Figure A.4:

6. Measure the output energy once a week by setting the waveplate at 25° (full energy setting) and placing the power meter before the shutter.
7. Turn on the PFN cooling water at least fifteen minutes before aligning the laser, so that the pump has time to filter the water to a de-ionized state. (A green light means that the water is ionized.) The PFN cooling water remains on during laser operation. (This does not change the thermal properties of the rods.)
8. **Alignment**
9. Turn the waveplate to 341°. Open the shutter, and align the laser system.

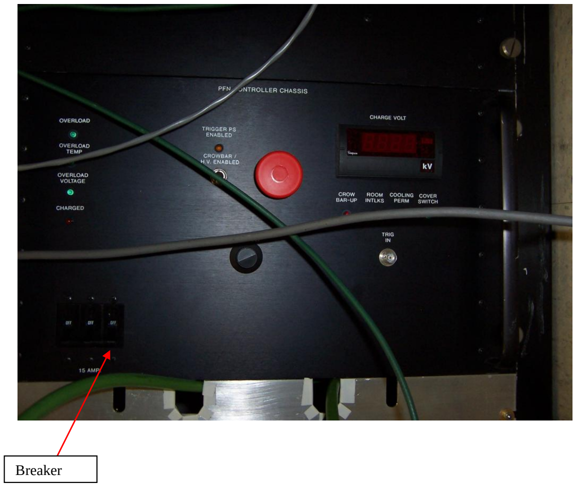

Figure A.5:

10. On the laser table, there are two cross hairs: one encompasses the spatial filter, and the other separates the two laser heads. Use the laser camera to manage the progression of the cross hairs. After using the first two cross hairs for alignment purposes (spatial filter), remove them. Optimize the spatial filter by looking at the monitor. Before aligning the back mirror of the first laser head, adjust the waveplate to maximize the energy that is back reflected ($\sim 145^{\circ}$ is max energy,$\sim 10^{circ}$ is alignment). Change the waveplate back to 145.5° and remove iris. Align the back mirror with the iris and the IR viewer so that two-pass head is aligned.

11. When the shutter is open, keep the waveplate on the low energy setting ($340^{\circ} < 351^{\circ}$).

12. Once the laser is aligned using the cross hairs, check to see if the laser heads are not clipping the beam too much. The laser beam cannot

completely bypass the laser heads, so minimizing the amount of beam that is clipped remains the standard operating procedure.

13. Use burn paper to see the soft diffraction. Set the waveplate to 353° for the smaller beam (lower energy setting) and 16° for the larger beam (high energy setting).

14. Make sure the soft diffraction is okay. Check to see if the diffraction is symmetric or not. Also, make sure that there are no dust spots that are too large.

15. **Full System Operation**

16. Turn on the PFN (located underneath the laser table), by flipping the circuit breakers, and other power inducing switches. For the red PFN, first hit the crowbar switch, followed by the Charge button. For the black PFN, flip the breaker first, and then hit the crowbar switch.

17. Set the voltage for the red PFN to 3200 V and the black PFN to 3400 V.

Figure A.6:

18. Because the shutter needs to warm up before it fires consistently, the beam should be blocked and the shutter fired before firing the laser. The laser is then operational with the removal of the beam block.
19. Do not fire the PFN more than once every 30 seconds.
20. When finished with the laser, turn the GCR to simmer. Let the PFN water continue to flow for a few minutes. Let the GCR cool for 10 minutes. Turn off the simmer, and then turn off the laser body. Turn off the cooling water.

A.3 Changing water and Filters on the GCR

1. Unplug chord for laser
2. Open door/check water level.
3. Pull cover off front.
4. Siphon water out of containment vessel
5. Unscrew holder for DI filter
6. Exchange DI filter
7. Replace clamps
8. Similarly, replace particulate filters
9. Run a couple different cycles of water through
10. Check for leaks
11. Replace tubing if needed. Use only New Age brand tubing.

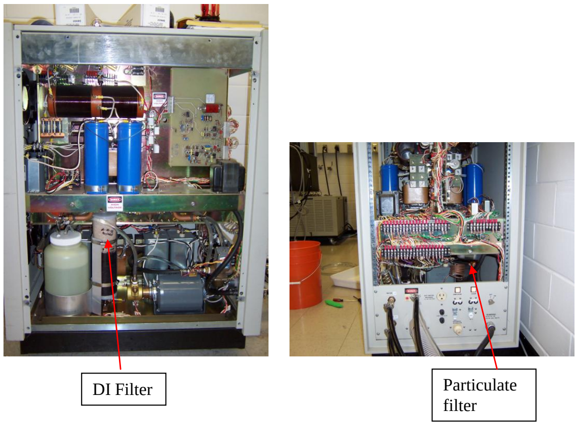

Figure A.7:

A.4 Change Flashlamps

1. **Removal**
2. Turn laser off and unplug.
3. Open cover for laser
4. Unplug water from top and allow to drain in back -Clean up leftover water
5. Remove lamp leads from heads -Unscrew black caps -Remove red wire -Remove black wires
6. Remove lamp holder thumb screws, both left and right side (loosen evenly) , and small plastic white blocks.
7. Withdraw lamp from the right side of the lamp housing.
8. **Installation**

9. Insert new lamp. The Flashlamp cathode goes into the housing first, i.e. as you face the laser the cathode is on the left side of the housing. The anode end of the flashlamp is indicated by a red mark on the anode electrode. The cathode electrode is segmented but the anode electrode is one solid piece. Flashlamp envelope tip-off is at cathode end of flashlamp.
10. Rotate flashlamp envelope tip-off toward the laser rod.
11. Tighten thumb screws evenly. Do not over tighten. To insure a positive seal, rub a little vacuum silicone grease on the o-ring surface. Use grease very sparingly.
12. Connect Lamp leads.
13. Replace cover.

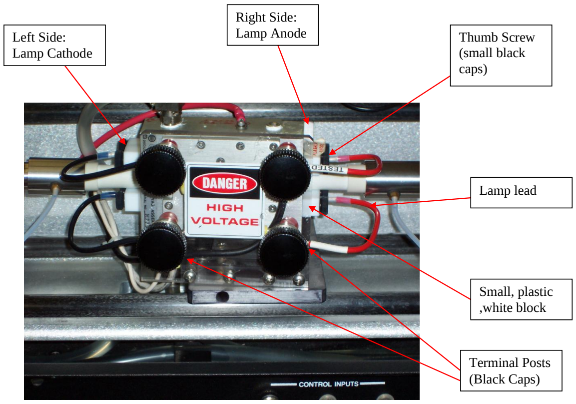

Figure A.8:

A.5 Trouble Shooting with the GCR

Using the wrong plastic hoses in the water cooling part of the power supply caused one of these pipes to burst under operation. The water released by this rupture spouted water on the large high power resistors on the simmering circuit. This caused the resistors to fail. Fortunately the resistors were still commercially available and replaced by myself.

I have found that the water flow must be carefully monitored through the GCR laser assembly to make sure that the water was flowing well, or else the mode quality diminished and can form a distinct four lobe feature. This included making sure that the hoses are not kinked, and that the hoses were clean. When possible all the hoses, especially those connected to the house water, were light tight hoses. This ensured that algae did not build up in the system. A major algae build up occurred in the house water that nearly stopped the flow of house water through the system. While cleaning the system a part from the Penn-valve broke. This part was fixed by the machine shop. During the warm summer months the house water was not cool enough to cool the laser. We fixed this by replacing a panel of the power supply housing with a sturdy mesh that evacuated more heat from the system. One unexplained problem with the laser is the sudden occurrence of a cross in the reflection of the beam off the first polarizer. Cooling problems often create heat induced birefringence in the rods. This birefringence is responsible for the cross pattern in the reflected beam, but the source of the cooling problem and its sudden onset is unknown. The reflected beam has 60 mJ of energy which makes it an eye hazard and could take energy away from the main beam. We tried resolving this problem by changing the repetition rated to 2 Hz; while this resolved the cross pattern reflection the imaging of the rest of the system changed. We resolved the problem at 10 Hz by carefully blocking the rejected beam and setting aside the cooling problem. This did however leave the throughput GCR beam at a lower energy.

Appendix B

Historical Progression of the Jet Experiment

I originally started this project by assessing what project I could undertake with our resources that would allow us to contribute to the field involving magnetohydrodynamics combined with laser-produced plasmas. I originally was going to bring the Thor laser beam to Professor Bengtson's plasma rotation device to increase the density in the rotation experiment. I progressed with this experiment only to the point of putting a connection between Professor Ditmire's and Professor Bengtson's lab with ceiling connections to attach optics due to a new project idea proposed by Dr. Prashant Valanju.

Dr. Prashant Valanju proposed an experimental project to Professor Ditmire about a laser plasma experiment combined with electric and magnetic fields to produce a laboratory simulation of an astrophysical jet. This proposed experiment was more in line with the goals of Professor Ditmire's group. As a consequence the experiment combining Professor Bengtson's rotation chamber and the Thor laser has not yet progressed.

Dr. Valanju's experimental proposal consisted of creating a laser-produced plasma in the presence of an axial magnetic field and a radial electric field supplied by a biased pin as in figure B.1 where we would hope to see an experimental signature as illustrated in figure B.2.

I initially started this experiment using lasers from the Thor laser such as the Quanta-ray GCR as a drive beam, and the Big Sky laser as a probe

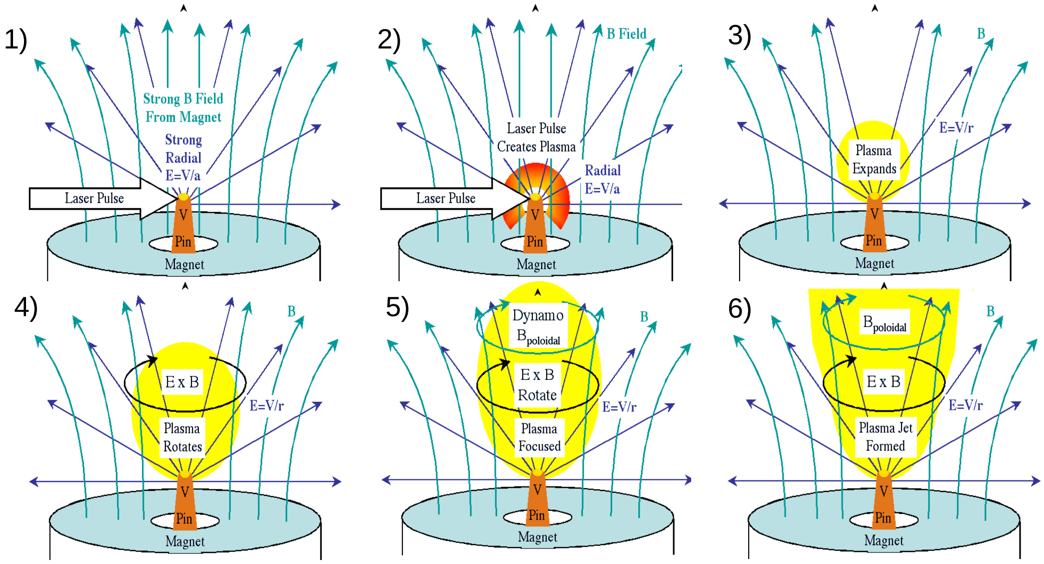

Figure B.1: Dr. Valanju's original idea to create jets using static $\mathbf{E} \times \mathbf{B}$ fields. These illustrations were made by Dr. Valanju.

beam. I used a gas jet chamber in the target room of the Thor and laser lab. The design of this experiment is very similar to the laser-produced plasma experiment in chapter 4. In fact the Thor laser experiment was in effect a trial and testing experiment that gave me the details I needed to construct the current experiment. So many of the techniques I used for the YOGA experiment flow out of the Thor experiment. Pictures of parts of this set up are in figure B.3. This experiment used Schlieren imaging to image the plasmas. The Big Sky laser was ideal for the Schlieren imaging because the Big Sky laser had a clean Gaussian profile. I used various sizes of copper wire as targets from 1.0 mm to 50 μm. The minimum background pressure was 15 mTorr. I used a Faraday rotator magnet for the magnetic field to enclose laser-produced plasmas in the experiment. This magnet only had value of 0.1

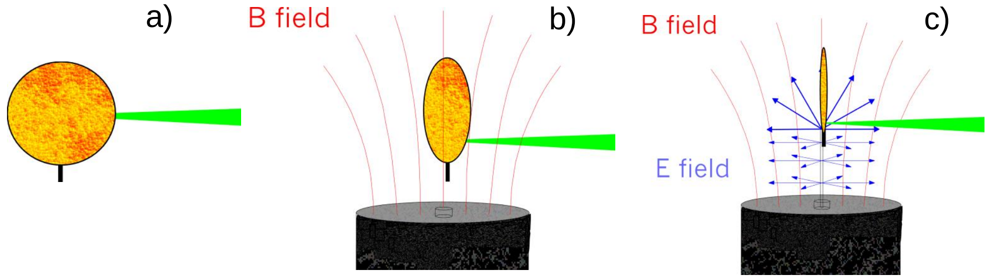

Figure B.2: The original experimental signature: a) without magnetic fields we should see a spherical expansion, b) With a background magnetic field we would see elongation along the field lines, c) With background magnetic and electric fields we would see more elongation along the field lines.

T and the magnetic field was divergent.

The main problem that with this experiment was that the Quanta Ray laser would not give the energies in single shot mode that the laser would give in the 10 Hz mode. The collimation properties were also different between the 10 Hz mode (the mode for the alignment) and the single shot mode (the mode for the experimental shots). This problem could not be fixed because the laser was not designed to be alternated between modes. Both optics and electronics had to maintain the same thermal properties to keep uniform laser properties. I used both the fundamental and the second harmonic Quanta Ray laser pulse for the drive beam in our experiment. When I used the fundamental mode I constructed an optical isolator to protect the Quanta Ray laser from retroreflections out of a 1/4 wave plate and a polarizer.

I had to develop techniques for target alignment that included viewing telescopes and HeNe lasers. I assessed that the HeNe laser was the best way for alignment. I also used the probe imaging system and the Schlieren break

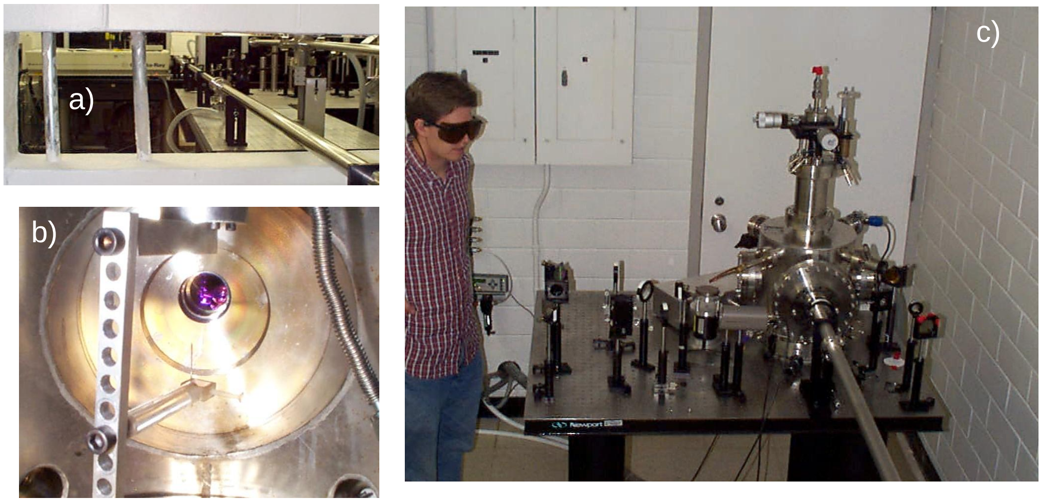

Figure B.3: Pictures of the laser-produced plasma probing experiment on the Thor laser. a) is the beam path from the laser room to the target room, b) is inside the chamber with the target holder, and c) is the target chamber set up.

down in air to aline the target with the drive laser focus. The first Schlieren data of this experiment is in figure B.4

I constructed a high voltage circuit with a $1.0\mu F$, 5000 V capacitor that would connect directly to the electrode as in figure B.5. The circuit consisted of this capacitor that was connected to a SRS high voltage power supply through a shunt resistor. One end of the capacitor was grounded and the other end connected directly to the electrode. The capacitor had shunt resistors across to keep the capacitor discharged when not in use. I put a simple wire loop on the capacitor output electrode to measure the current carried through the wire, but we were never able to obtain viable measurements from this loop configuration. With this circuit I calculated what velocities the $\mathbf{E} \times \mathbf{B}$ drift would obtain assuming the E field penetrated the plasma in figure B.6.

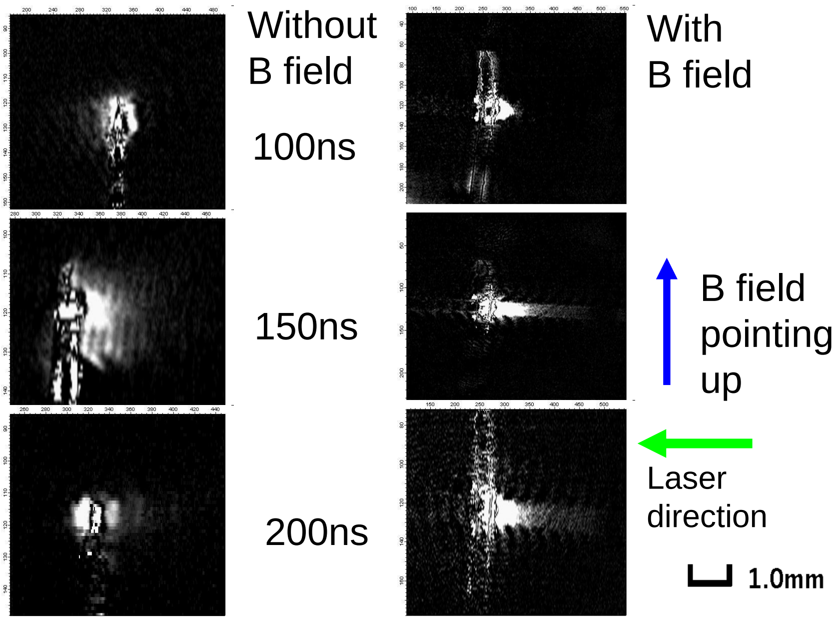

Figure B.4: The first Schlieren images on the Thor laser.

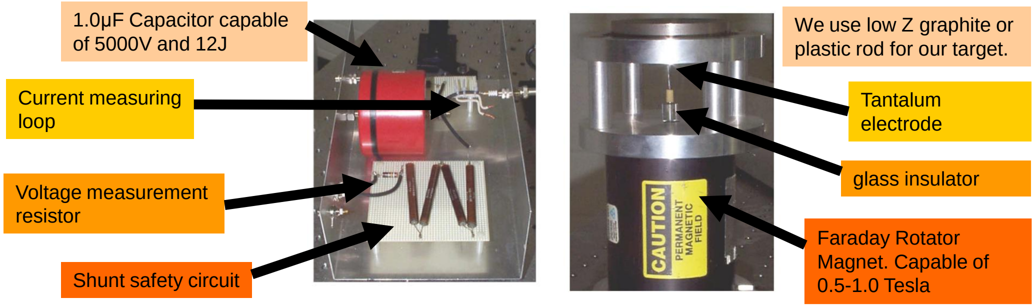

Figure B.5: We used a capacitor shunt circuit to supply potential to the electrode and a faraday rotator magnet to supply the magnetic field.

The discharge results in the Thor lab did not produce the desired results. The laser produced plasma seemed to cool too quickly; and no quantifiable difference was seen with or without magnetic fields. The discharge between the electrode and the laser produce plasma was sometimes observed as in figure B.7.

We assessed that this experiment would not be viable in the Thor lab. We concluded that more energy was needed in the laser pulse to create a laser-produced plasma that could be measured with our diagnostics and that would be more in line with what we hoped to obtain from the experiment. This suggestion was coupled with the fact that Professor Ditmire had the parts for an amplified glass laser and wanted this laser to be constructed. We then changed our direction to constructing the YOGA laser.

We decided, with the completion of the YOGA laser, to modify the experiment partially to shoot a 25 μm wire to increase the temperature of the laser-produced plasma. This also had the advantage of symmetry in the experiment and would also serve as the electrode.

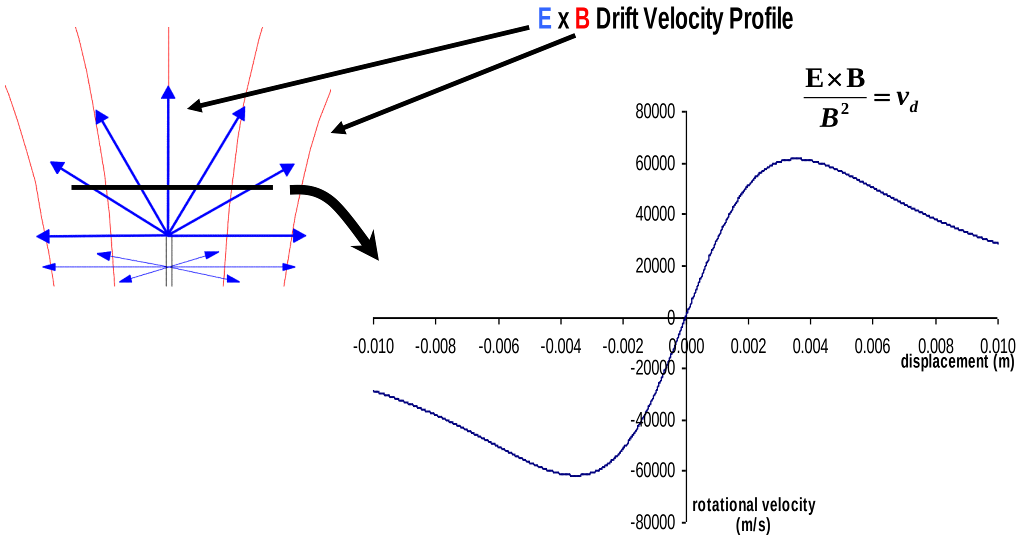

Figure B.6: We calculated the velocity a static $E \times B$ field would give.

I designed a device that the machine shop built that would hold a $25\mu m$ wire to a $1.0mm$ wire in electrical contact with the capacitor. I wanted the wire and the target to be removable. The holder consisted of a flat plastic block with a hole at the end where the wire rests in. The plastic was a material known as PEEK, a plastic good for high temperature applications. This was used because electric discharges and laser-produced plasmas can be high temperatures. A hollow shaft bores down the length of the block to this hole. A copper rod in this shaft pressed against the electrical lead from the capacitor and pressed onto the target wire standing in the hole with a plastic screw. Great care was taken to keep the rod ends clean from oxidation to make good electrical contact. The electrical lead from the capacitor was a small rectangular copper lug to produce a uniform electrical contact from this lug to the rod.

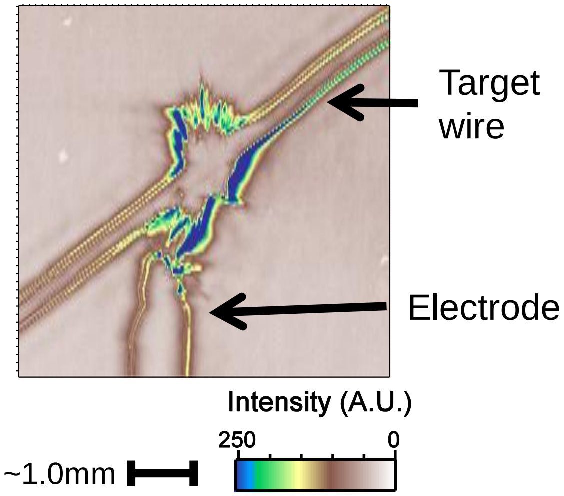

Figure B.7: Interaction of the electrode with a laser-produced plasma from the Thor experiment. The electrode has discharged through the laser plasma forming a plasma bridge between the two.

I used Keith Carter's small triggerable-pulsed power supply originally designed for use with a tokamak. The power supply gave a pulse with a voltage of about $2500V$ and had a pulse duration of $\sim 13.2\mu s$. The pulser had a thyratron that triggered with another $200V$ trigger box. This thyratron connected the discharge of the capacitor to though an isolator transformer into the experiment. This pulser created a lot of noise and was very susceptible to noise. A lot of effort went into cutting out the noise for this device. There was 3.09 μs jitter shot to shot for this pulser, so we had to perform the experiment several microseconds after the pulser fired. This jitter came from the device and from the Stanford boxes shot-to-shot timer.

I took Schlieren and interferometric measurements of laser-produced plasmas, and made some progress in making these measurements while the target was biased with the electrical pulser. The first complete set Schlieren

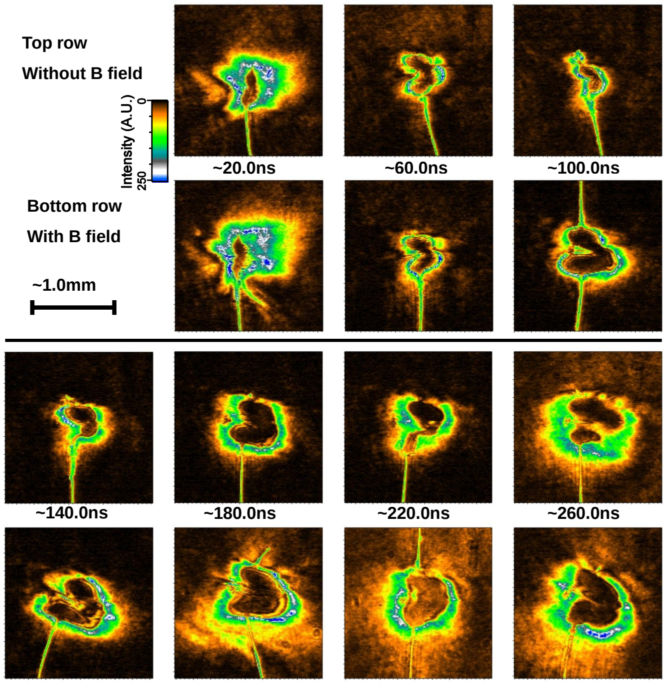

Figure B.8: Schlieren images of laser produced plasma progression where the input laser energy is ~4.7 J and the target is ~25 μm thick Cu wire. The magnetic field is a one sided magnet that give ~0.09 T at the interaction region. The pressure is also different between the two cases.

images of this experiment is in figure B.8, and other Schlieren images were discussed in chapter 4. I encountered many problems with this experiment when introducing voltage on the target. Once the pulser fired, the $25\mu m$ wire target made electrical contact to ground, and the wire would evaporate. This was a big problem because of the time involved in setting up the experiment. Loading the target took a lot of time and the experiment often missed shots. The pulser had the triggering noise that added to the uncertainty of this one shot procedure. The pulser produced a lot of noise that interfered with the camera systems making the possibility of recording this event low. The few shots that were measured are in figure B.9.

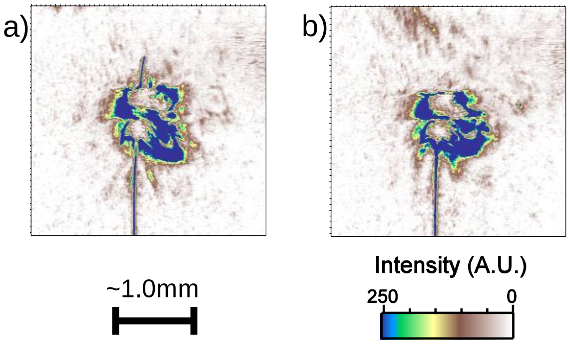

Figure B.9: Schlieren images of a laser-produced plasma at 60 ns with a 3.7 J laser pulse. a) is in a .85 T magnetic field and b) is in a .85 T magnetic field and the wire is biased to 2500 V. There is a visible but not quantifiable signal above the interaction in the biased case that is not in the unbiased cases.

I looked at the possibility of using a Langmuir probe in the laser-produced plasmas without an voltaic bias to aid to the Schlieren images. To test this idea a vacuum rated coaxial cable with .06” outer diameter and .028” inner diameter wire was used to place next to the laser-produced plasma produced with a 3.7 J YOGA laser pulse on a 25 μm copper wire. The inner wire was braided and hence would not give accurate quantifiable results, but the purpose of this study was more qualitative in nature. An oscilloscope measured the bias on the wire as it interacted with the plasma. I measured interesting qualitative results for both the magnetic and nonmagnetic cases, but I did not pursue this idea further. I present the data in figure B.10 without explanation for reference purposes.

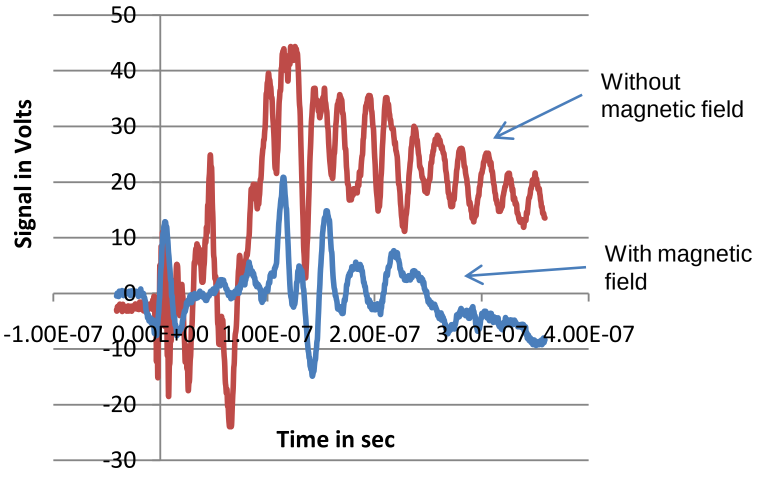

Figure B.10: Makeshift Langmuir probe data with and without a magnetic field with a 3.7 J laser pulse on a 25 μm copper target. The probe was about 2 cm away from the interaction. The reading was measured with 1 MΩ termination and the "without" B field case was measured through a high voltage probe.

At the time I had thoroughly studied the expansion of the $4.0J$ shots on the $25\mu m$ wire with the Schlieren imaging, Professor Bengtson suggested that the experiment should be altered. We calculated that the expanding plasma in a vacuum could not carry the amount of current necessary to induce significant rotation of the plasma in the magnetic field from a biased electrode. The current would be limited to the amount of charge that could be stored on a spherical capacitor as it expanded. This would be less than one 1.0 A which would provide insignificant rotation from $\mathbf{J} \times \mathbf{B}$. One of the original assumptions was that the E field from the pin would be enough to rotate the plasma with $\mathbf{E} \times \mathbf{B}$ drift, but it turns out that the plasma will be conductive enough to short the E field out. Thus current flow must be supplied to keep the E field from shorting out.

Dr. Valanju suggested changing the system to a coaxial system to induce current flow in the laser-produce plasma. I changed the experiment from a voltage-based system to a current-based system, and with this change came many complications. A current based system can be as detailed as one has resources to make it. The impedance of the system and the wave nature of the alternating current were now important, especially if one wanted to deliver a current into a plasma that had the lifetime of a laser-produced plasma, which is on the order of a 200 ns.

One can construct a pulsed power device that has higher impedance than the experimental region which would have a fast rise time, but such a device would be expensive and extremely time consuming to build. We decided that it would not be expedient at this particular time to build such a device and this would be left for future researchers to consider. Instead I would connect a capacitor directly to the experiment, with no special pulsed power technology, to measure the effect of current discharge in a laser-produced plasma.

The Paschen curve is a relation of the breakdown voltage of a spark gap to the length of the gap of the spark gap and the back ground pressure [13]. I relied on the Paschen curve for our current related experiment. The pressure needed to be low enough so that when the capacitor was connected to the electrode the voltage would not break down. I decided to abandon the electrical pulser, and instead pump the chamber down to $1.0mTorr$ to take advantage of the Paschen curve for several 1000 volts.

I used the capacitor set up from the Thor experiment. This was a 5000 V, 1 μF, 1.302 μH valued capacitor. The current detection device used a Pearson transformer (model number 411) that converted $10A$ to $1V$ and had a sufficient rise time to work for the experiment to measure the current. I designed an experiment to test out the effect of the discharge in a laser-produced plasma using the ICCD camera. This used the electrical contact holder with a $1.0mm$ diameter Al wire as a target for the laser shown in figure B.11.

The Al wire electrode experiment gave very interesting results. I used the same set up as in chapter 3, except with an electrically contacted holder that was connected with a wire through an electrical feed through on the chamber. The enclosures of the magnet and the Al can (refer to chapter 4 for descriptions of these objects) were grounded. There are clearly differences between these conditions as in figures B.12 and B.13. The current does have an effect on the laser-produced plasma. Without a magnetic field the current diffuses through the system and cathode spots form on the aluminum enclosure. With a magnetic field the plasma can be seen to rotate around the pin by showing the pin shadow in the figure B.12. This could be from $\mathbf{J} \times \mathbf{B}$ forces and the current being forced to move across the field lines before aligning with them. Plasma radiation occurs long after the observed laser-produced plasma's lifetime. The Pearson reading of the current is shown in figure B.14.

With the interest generated by the Al wire electrode experiment I wanted to make a coaxial electrode experiment in the least time consuming and costly way possible. I used a 4.0 mm in diameter solid copper coaxial

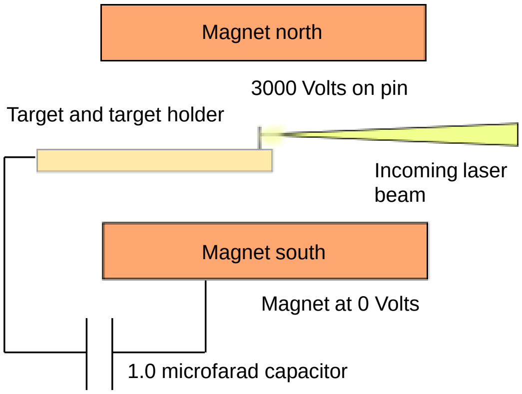

Figure B.11: The experiment included a biased pin enclosed in a grounded magnetic enclosure. A laser impinged on this pin which created a plasma.

cable, and shaped it in such a way that we could fit it in our chamber. The tip was bent up in the tightest possible radius of curvature that would not kink the cable. Then with a jewelry file the tip was cut off so there was a flat cross section of the coaxial cable exposed. The result was a flat coaxial face that would be parallel to the magnet face and was roughly half way between the two faces of the enclosed magnet. I taped a hole in the feed-through that could attach the ground cover of the coax directly to the chamber near the feed-through. The goal was to preserve the wave-guide from the coaxial cable coming from the capacitor, and also reduced impedance to the electrodes.

I put the Al target near this coaxial system in the enclosed magnetic field, and performed the experiment, measuring the interaction with the ICCD camera and the Pearson transformer. The electrode was charged to only $1000V$ because the cable was not rated for higher voltages. There was a jet-like feature observed as illustrated in figure B.15 and B.16, but I saw this feature without

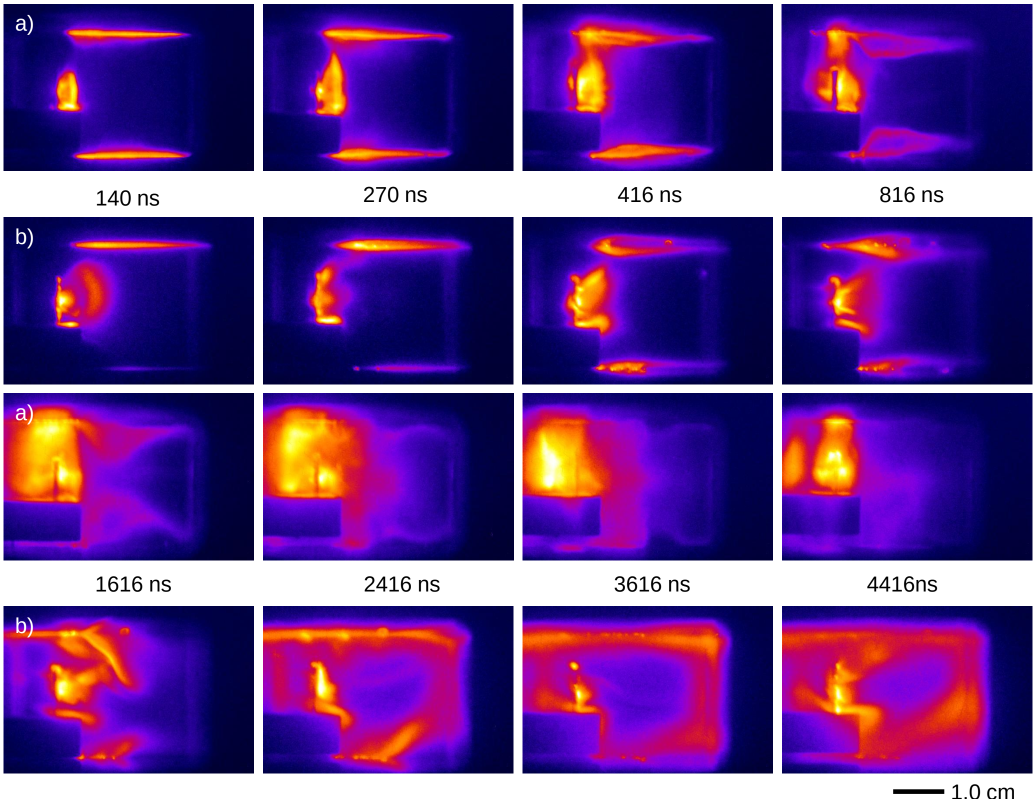

Figure B.12: This shows the discharges of the pin as outlined in figure B.11

any voltage on the electrodes. The jet was a result of the laser-produced plasma reflecting off of the coaxial cable and then streaming along the magnetic field lines. There is also some injection of material from the coaxial cable discharge itself.

While this jet may not be produced by electric and magnetic fields, it is a collimated stream of plasma bounded by magnetic fields. This is reminiscent of the second jet model discussed by Remington about jet collimation though hydrodynamic flow through constricting lobes in an accretion disk [117]. The

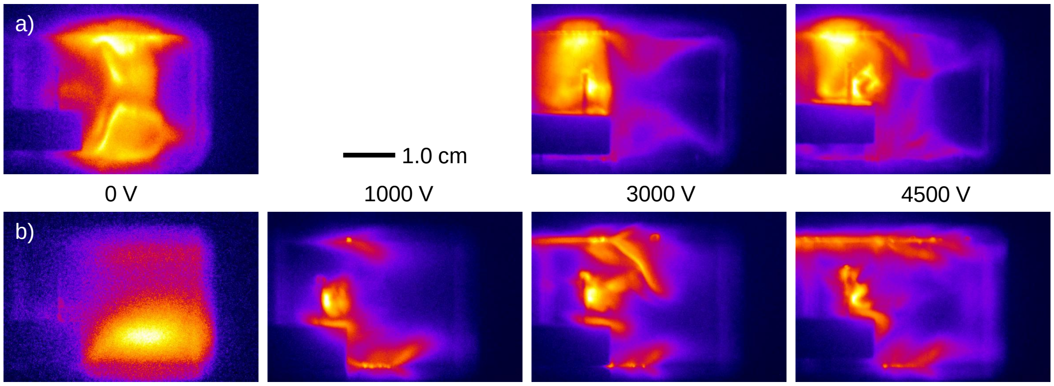

Figure B.13: This shows differences in voltage on the discharge.

magnetic field in this case could provide radial pressure to the expanding plasma in a way similar to the lobes in an accretion disk. This could be a subject of future study.

While this jet may be of significance to astrophysical jets, I chose not to pursue the study of these phenomena with this coaxial cable configuration. The coaxial cable only survived about 10 shots before it would not hold voltage at $1000V$. This was due most likely to carbonization of the inter coaxial material, teflon, which quickly turned from an insulator to a resistor. Carbonization was observed by microscope on the coaxial electrode.

I wanted to build a very flat configuration that had a grounded ring with an electrode in the center. I didn't want any dielectric directly connecting the center electrode with the grounded ring, or at least a configuration where any dielectric that connects the two would not be able to be carbonized due to arcing. I also wanted to keep the impedance of the electrode configuration to a minimum by keeping the configuration compact. The carbonization problem was solved by having a plate with a hole in it covering the area where the

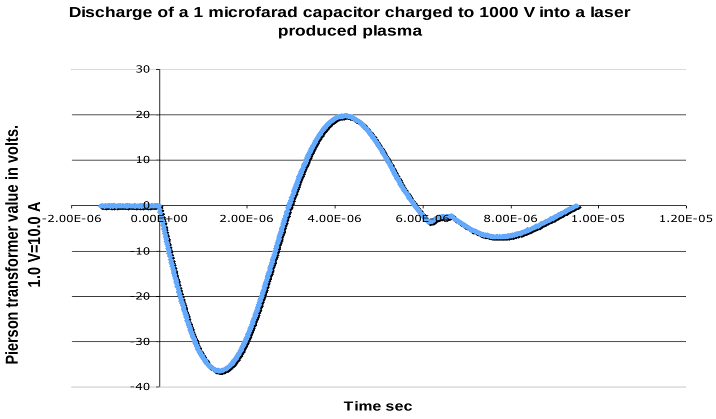

Figure B.14: A Pearson transformer to measured the discharge of the capacitor though the plasma.

electrode was, and having enough space underneath the ring to cast a shadow on the dielectric so that laser-produced plasma would not build up on the dielectric. This new electrode design provided the conditions needed to produce viable plasma-jet phenomena.

The discovery of what I refer to as “jets” in the experiment was almost accidental. I originally postulated that the laser-produced plasma would be self-organized into a jet by the induced currents. The laser-produced plasma was only experimentally viable for about 600 ns. After this time the plasma radiance become too week to measure. This initial time frame produced no clear phenomena that resembled jets. Further exploration reveled an anvil shaped plasma structure that grew out of the center of the electrode when measured in a .85 T magnetic field (see figure B.17). This anvil structure formed when the current flow reversed direction with the center electrode originally positive biased. This anvil structure occurred at different times

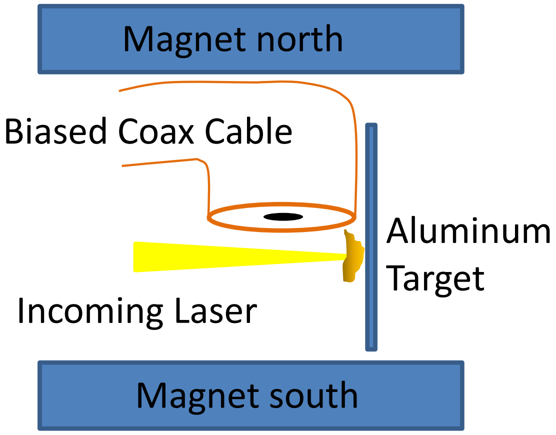

Figure B.15: Diagram of the biased coaxial cable laser plasma experiment. The coaxial cable is bent, placed between magnets and the laser passes over the cable face to impinge on a thick Al target.

of the discharge when similar conditions were met and with applied voltages between 2000 to 5000 V.

When I investigated this behavior without a magnetic field and with the aluminum enclosure something unexpected was observed. Under the same voltage conditions I didn't see an anvil structure or what I could recognize as a jet, but when the voltage was set to 3000 V a jet-like structure emanated off of the center electrode and hit the top of the aluminum scaffolding. Without the aluminum scaffolding the jet evolved into the chamber. This was the first encounter of the phenomena that I call laser-triggered jets. From this point on I conducted most of the investigations without an enclosed magnetic field. The machine shop disassembled the MCE magnet so that one side could be used. After this long progression of the evolution of this experiment viable and repeatable plasma jets could be measured under a variety of conditions.

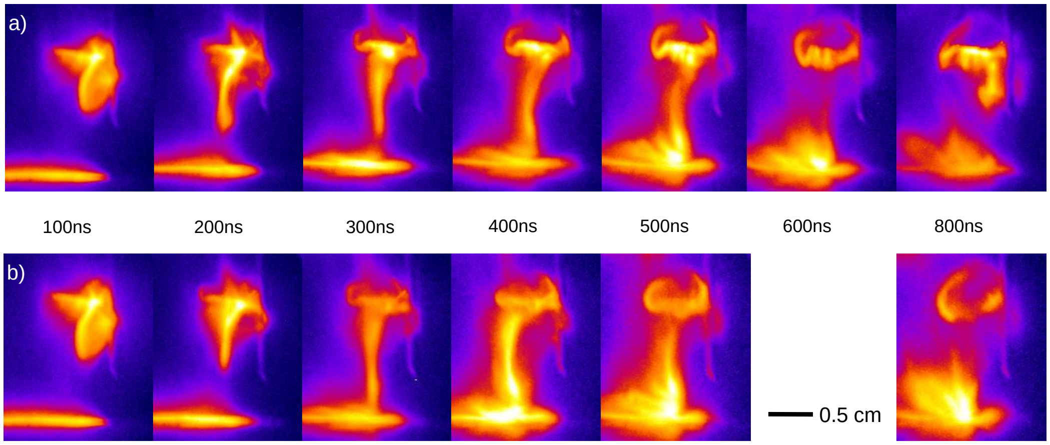

Figure B.16: Jet caused by laser-produced plasma reflecting off of a coaxial electrode. a) is with the center pin biased to 1000 V and b) is without voltage.

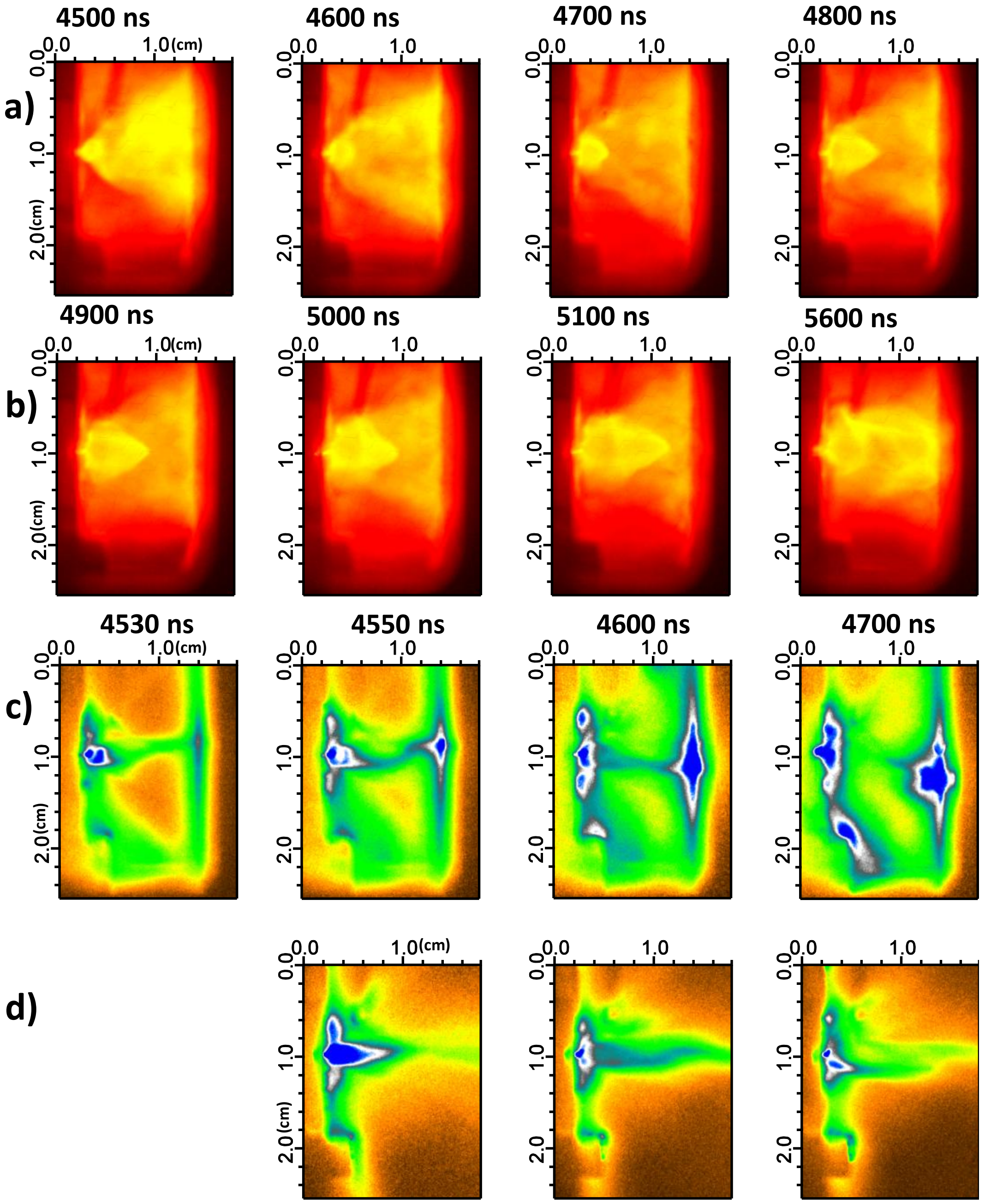

Figure B.17: Jet with Mo electrode in a 0.85 T enclosed magnetic field. For c) there is a 3000 V discharge jet enclosed in an aluminum enclosure, and in d) is the same jet without an enclosure.

Appendix C

Appendix for Laser Triggered Laboratory-Produced Jets

In this appendix I discuss additional information concerning the jet experiment discussed in chapter 5. There were many more parameters that were explored than were reported in chapter 5. I also give more detailed information for concerning several points of analysis outlines in chapter 5.

C.1 Jet Theory Appendix

The original idea for this experiment was to use the laser-produced plasma as the medium for jet production. The set up was then more similar to Lebedev's set up [20], by inducing current flow through a laser-produced plasma in the presence of a cylindrically symmetric electrode configuration with varying background magnetic field strengths. A simplistic overview of the theoretical ideas behind magnetic jet formation is described in this way. As current discharges through this electrode configuration, the plasma will experience dynamic $\mathbf{J} \times \mathbf{B}$ forces. The current will form a toroidal magnetic field, which combined with the radial current will cause the plasma to flow perpendicular to the plane of the electrode configuration as shown in figure C.1. Plasma in the presence of the center electrode will experience a $\mathbf{J} \times \mathbf{B}$ force causing the plasma to pinch into a central column. The plasma at this point will have a flared current profile, which according to Bellan will cause collimated flow to form. This effect will be altered and confined to more symmetrical conditions with a background magnetic field. With the presence of a background magnetic field the plasma will also rotate in the plasma region above the column. The ideas that shaped the jet explanation in chapter 5 came from a complex web of different aspects of the experiment as in figure C.2.

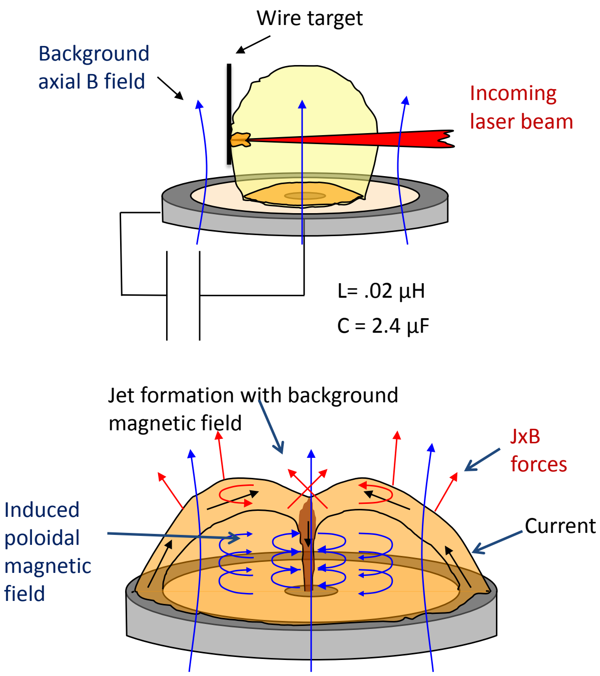

Figure C.1: We create an experimental model of a magnetically propelled jet using crossed electric and magnetic fields. The laser plasma completes the circuit and builds up a current that will blow the plasma off of the disk and form a jet. Current interactions with background and self-induced magnetic fields collimate and accelerate the jet.

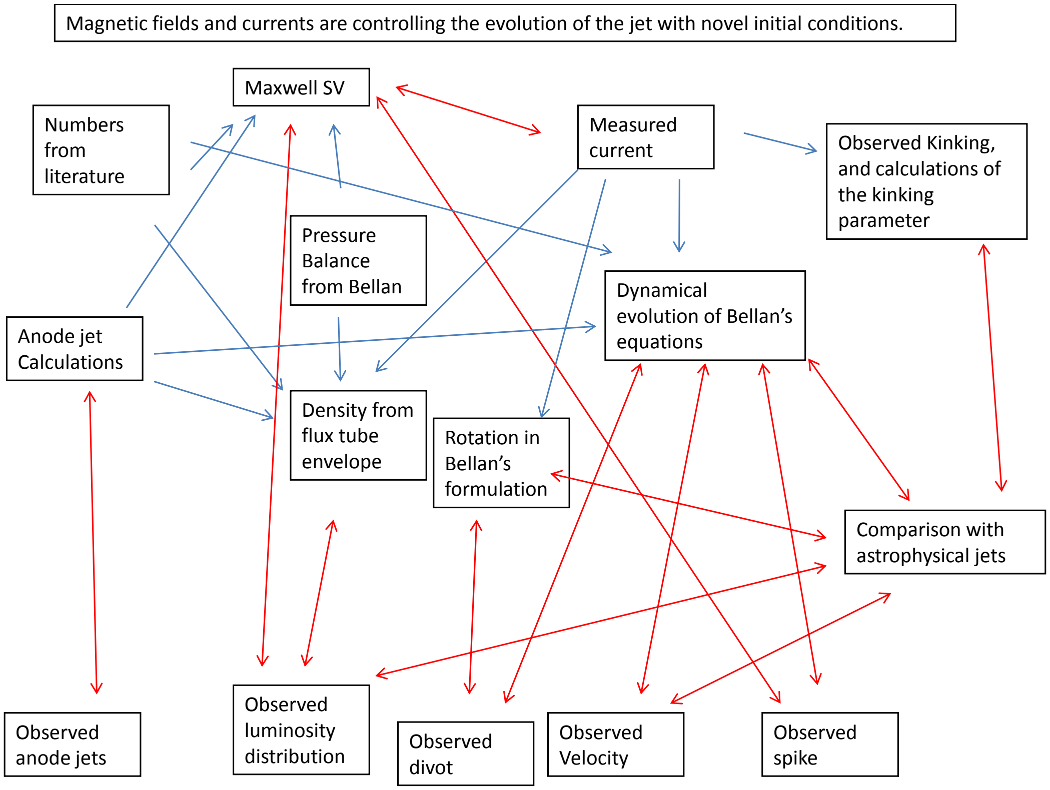

Figure C.2: Logic diagram of the jet experiment.

C.2 Jet Experimental Appendix

The entire experimental setup contained more parameters than described in chapter 5 The electrode configuration consisted of a thin molybdenum plate with a 0.5 or 1.0 cm hole with a wire aligned perpendicularly to the plate in the center of the hole as in figure 5.12. The wire was replaceable. The tip of the wire was coplanar with the molybdenum plate. I used 0.5 mm molybdenum wire and 1.0 mm aluminum wire in our experiment.

The capacitor in this set up was a physically large, 2.4 μF, 30 kV rated capacitor that had a measured internal inductance of .02 μH. I used the same circuit box as in the older experiment, but Matt McCormick cut a hole in the bottom of the box to fit the capacitor to the box. He also reduced the size of the shunt resistor so that the capacitor would charge faster.

The SRS high voltage power supply was a PS300 series 25 W, ±5000 V power supply. I applied an appropriate shunt resistor to limit the current output from the power supply. I also attached a ferrite coil on the cable between the HV power supply and the capacitor to limit spikes in the current caused by discharges. The power supply was short protected but the ferrite coil gave the power supply more protection. The charging took around two minutes. The power supply gave the current reading of the charging process. This reading was used to judge when the capacitor was charged.

I used various magnets for this jet setup. The magnet that was most useful was the MCE magnet taken apart. I used the intact MCE magnet during this experiment, but I found that an open magnet would be more useful than a closed magnet. I employed the University of Texas physics machine shop to take apart this magnet because the forces holding the magnetic scaffolding together were on the order of 200 lb. The Maxwell SV calculations of this magnet are in figure 5.14. Kevin Burnett measured the open magnetic field and the results are in figure 5.13 using a hall probe. An aluminum casing protected the magnet, as it was very brittle. I had to be much more safety conscious when dealing with this magnet because there was a lot more exposed magnetic fields. Three positions were used with this magnet in the following experiments, to test out different magnetic fields. The magnetic fields at the center electrode were roughly $\sim$0.45 T and $\sim$0.23 T for the first two positions. The other position was a tilted position of the electrode. The magnetic field at the electrode was difficult to measure with a hall probe, but I estimate that the magnetic field was on the order of ~0.4 T. I also used the Faraday rotator magnet with a hall probe measured magnetic field of ~0.1 T at the electrode.

C.3 Extra Jet Data Discussion

I took over 400, 4.0 ns exposure ICCD images of electrical discharges from this electrode configuration. The experimental conditions varied with the use of different electrode wires, ground ring diameters, magnetic field, fields of view, bias voltages, etc.. In this section I discuss relevant data to the jet experiment, that was not discussed in chapter 5. Many measurements that have not been quantized, but could be useful for future investigations are discussed in this section. Table C.1 lists the important electrical discharge evolutions and their experimental conditions. The program that recorded the ICCD camera data saved the jets as TIFF files with a dynamic range in intensity of 0 to 65000 au. In many of the images there were different regimes of structure depending on the intensity in the images. Physical features seen in the electrode configuration provided the spatial information for calibrating the ICCD images.

In images early in the discharge cycle there were remnants of the laser-produced plasma from the laser target interaction. There was evidence of the interaction of this plasma with the current discharges but nothing easily quantifiable as in figure C.8. The electrical discharges lasted up to and beyond 10 μs. The discharge cycle period was about 8.8 μs. This included several different cycles of discharge. There were specific features for all different regimes within the discharge time.

During the peak of the first cycle this central anode jet was at its peak

Hole Diam.	Wire Diam.	Wire Material	V	B Field	enclosed	Laser Energy
0.5 cm	0.5 mm	Mo	4.9 kV	0.85 T	yes	200 mJ
0.5 cm	0.5 mm	Mo	-4.9,3,4.9 kV	0.85 T	yes	mix
0.5 cm	0.5 mm	Mo	-4.9 kV	0.0 T	yes	mix
0.5 cm	0.5 mm	Mo	-4.9 kV	0.0 T	yes	mix
0.5 cm	0.5 mm	Mo	-4.9,3,4.9 kV	0.0 T	no	200 mJ
0.5 cm	0.5 mm	Mo	3,4.9 kV	0.12 T	no	mix
1.0 cm	1.0 mm	Al	-4.9,3,4.9 kV	0.0 T	no	mix
1.0 cm	1.0 mm	Al	-1.5,3,4.9 kV	0.85 T	yes	mix
1.0 cm	0.5 mm	Mo	-1.5,-3 kV	0.45 T	no	20 mJ
1.0 cm	0.5 mm	Mo	2,3,4,4.9 kV	0.45 T	no	20 mJ
1.0 cm	0.5 mm	Mo	2,3 kV	0.0 T	no	20 mJ
1.0 cm	1.0 mm	Al	2,3,4,4.9 kV	0.45 T	no	20 mJ
1.0 cm	1.0 mm	Al	2,3,4,4.9 kV	0.23 T	no	20 mJ
1.0 cm	0.5 mm	Mo	2,3,4,4.9 kV	0.23 T	no	20 mJ
1.0 cm	0.5 mm	Mo	-3,3,4,4.9 kV	0.45 T	no	20 mJ
1.0 cm	0.5 mm	Mo	4.9 kV	0.45 T	no	20 mJ
1.0 cm	0.5 mm	Mo	3,4.9 kV	0.0 T	Tilt	20 mJ
1.0 cm	0.5 mm	Mo	3,4.9 kV	0.23 T	Tilt	20 mJ

Table C.1: Table of all jets and physical conditions in which they were taken.

radiative intensity. It was at this point that the data from the interferometry measurements give the greatest signal. There was no measurable difference in this jet with or without magnetic fields. The remnant anode jet that was still visible at the time the jet forming region occurred usually had relatively sharply defined boundaries. There were differences in the evolution of this remnant anode jet (or RAJ) with or without magnetic fields that will be analyzed in section 5.6. It appeared that with a strong background magnetic field the current moved this RAJ along with the jet throat. The aluminum laser target often deflects this RAJ. There appeared to be a wind that was not luminous that causes a corona to form around this target when the target was not in the RAJ.

With the polarity reversed the cathodes spots formed on the molybdenum plate as seen in figure C.3. Cathode spots each had about 150 amps maximum [81], and so counting the cathode spots could give an estimate of the current. The remnant cathode jet in these shots was much different than the remnant anode jets seen with the opposite polarity. The remnant cathode jets are much less uniform and are not defined by distinct lines.

I investigated the differences in jet formation in many different situations with a positive initial bias. As discussed previously there are two different wires used as central electrodes. Both the Al and Mo wires gave different results. The Mo wire was able to get much hotter than Al [81] and was therefore able to create a much more distinct RAJ. In the Mo case there was much more qualitative information available about the remnant anode jet than in the Al case. Jet-like features formed in all of these different cases, which will be called magnetic jets. The jet-like features were much more distinct in the Mo cases as in figure C.3. A map of the various features seen in these magnetic

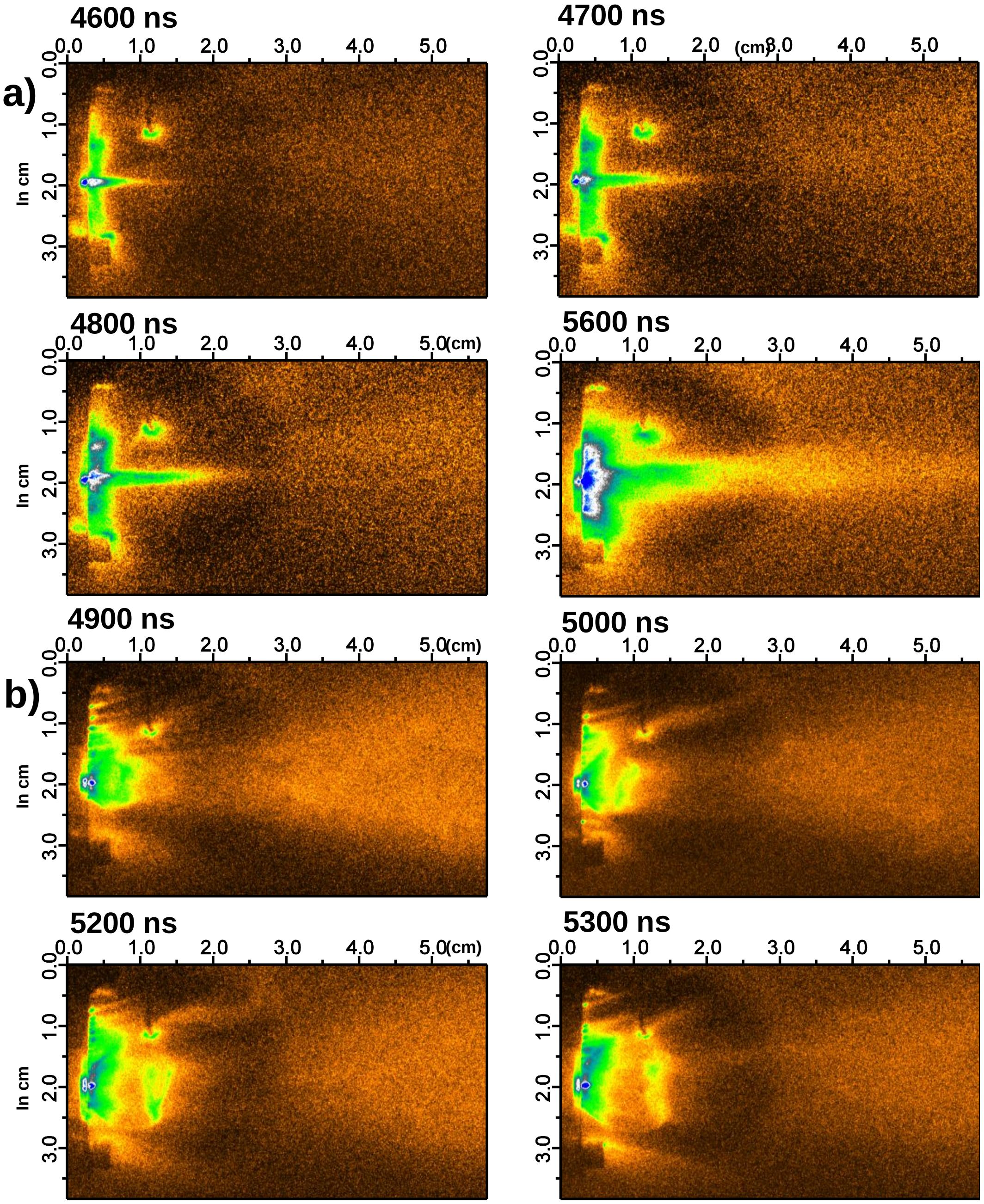

Figure C.3: a) Jet sequence with Mo electrode biased to 3000 V in a ∼.45 T open magnetic field. b) is the same except the electrode was biased to -4900 V. The field of view has been extended. For figure details see figure 5.15.

jets is in figure 5.15. When Al is used the jets are much more broad and less distinctly defined than in the Mo case (see figures C.4 and C.5). When the jet measurements were taken with lower voltages, jets could still be seen as in figure C.7, but finer features such as the divot and the RAJ could not be seen.

There was one interesting feature in the Al case that was not in the Mo case. It is that a "bubble" formed and emanated from the central electrode. This was similar to the ablated material that emanates in the Mo jets, but expands semi-spherically and a brightened region formed in certain regions of this bubble that then resemble jets. This was quite different than in the reversed polarity case in Mo described above. This feature progressed over hundreds of nanoseconds.

The luminosity of this ablated material decreased uniformly over time, and a divot in the luminosity increased over time to about 50% in the log scale as in figure C.6. This divot formed in all of the Mo cases in a magnetic field above and including 3000 V. This divot formed also in cases where the magnetic field is less and even zero, but it is more distinct in the higher magnetic field case. A table listing fits to the double gaussian discussed in section 5.4 is presented in table C.2.

There were several observations to be made in the jets produced without magnetic fields. The kinking that took place without a magnetic field usually seemed to preference kinking away from the electrode arm. This could be a case of the fluxtube interacting with the magnetic field of the electrical lead that connected directly to the central electrode and was perpendicular to the central electrode. The ablated material was less clearly defined in the nonmagnetic field case. It did seem to expand away from the jet axis much more than the ablated material in the magnetic field case. This would be expected because

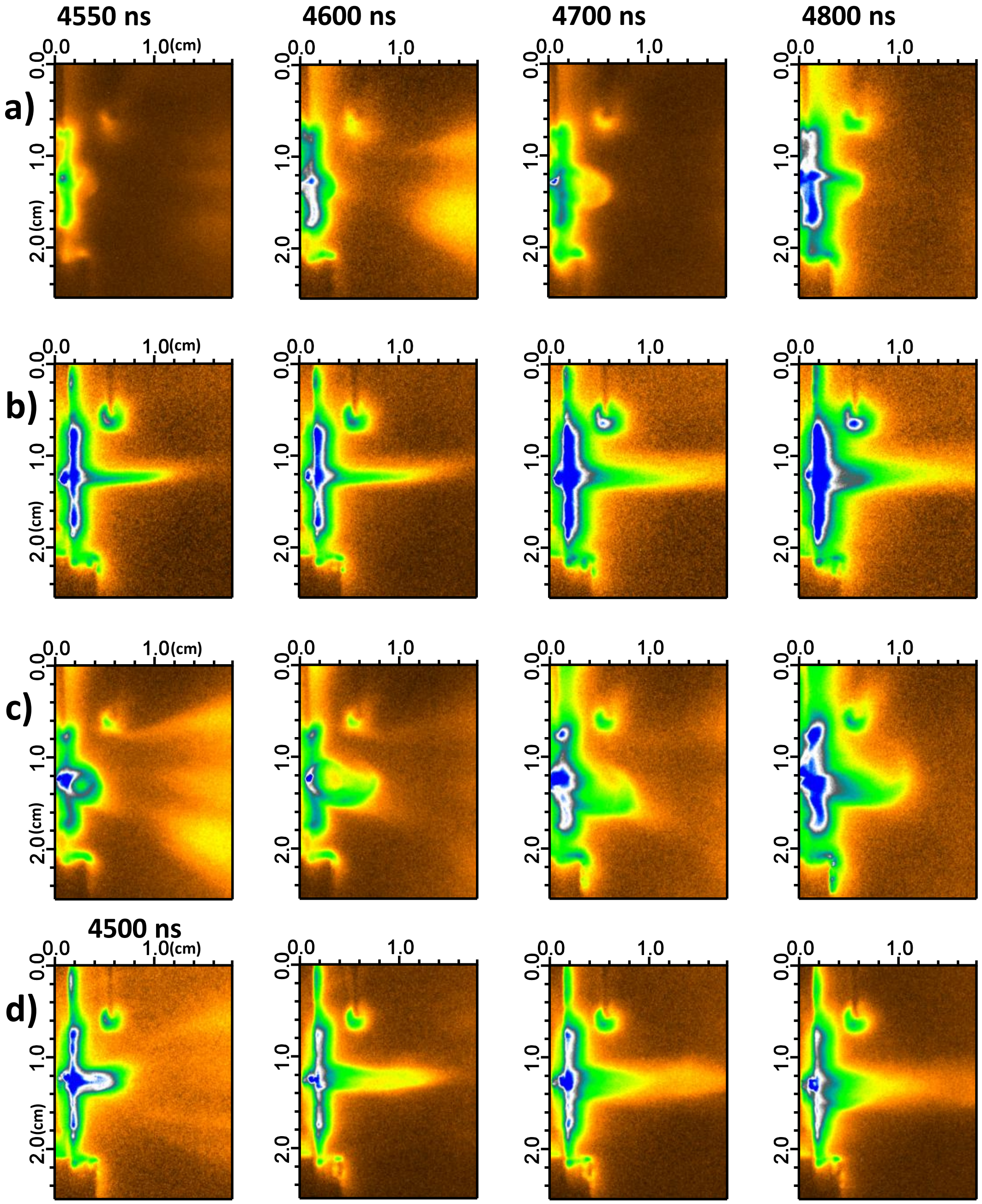

Figure C.4: Jets with Al center electrode with conditions a) 3000 V and ~0.0 T, b) 3000 V and ~.45 T, c) 4900 V and ~0.0 T, and d) 4900 V and ~.45 T. For figure details see figure 5.15.

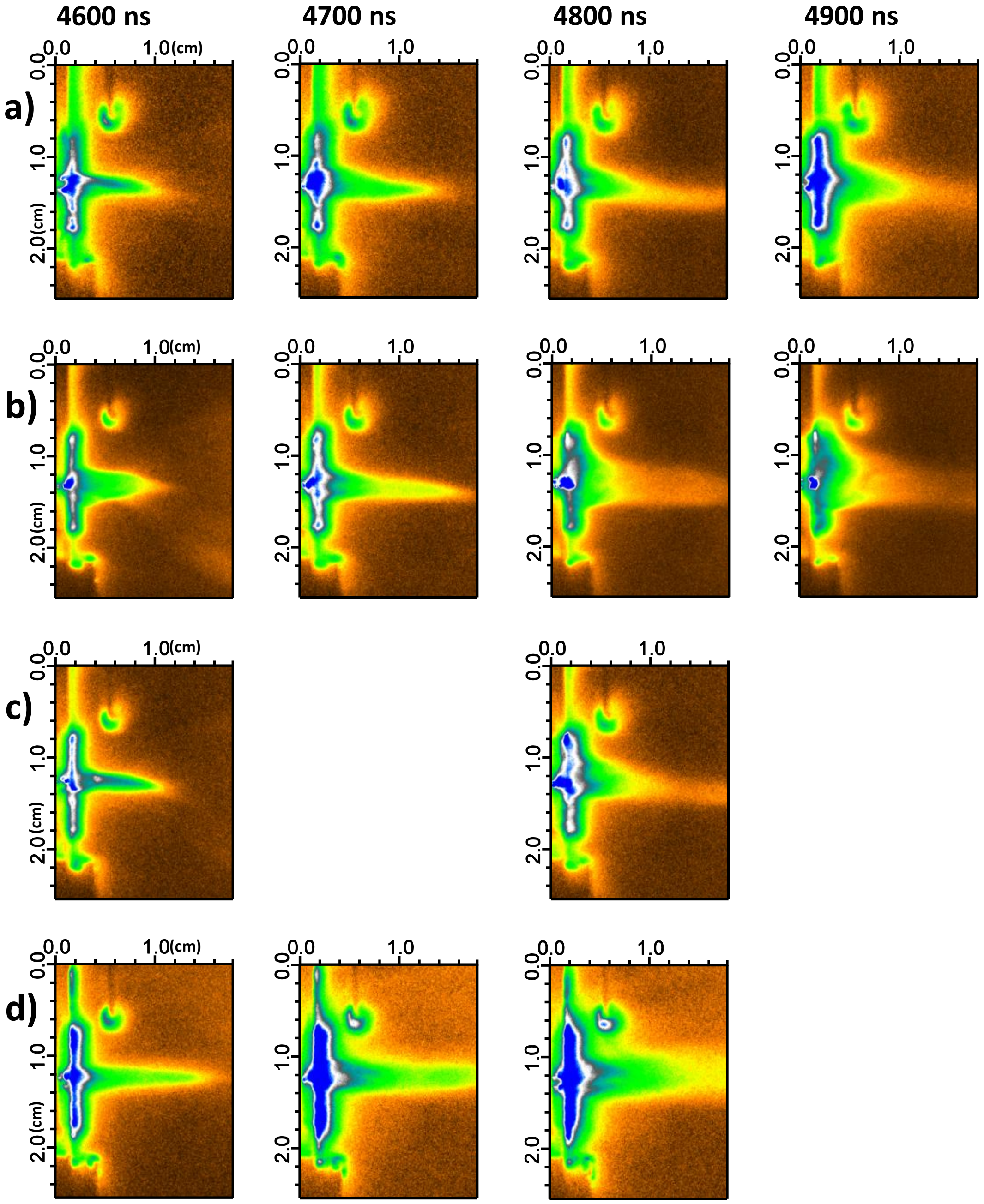

Figure C.5: Jets with Al center electrode with conditions a) 3000 V and ∼.23 T, b) 4900 V and ∼.23 T, c) 4000 V and ∼.23 T, and d) 4000 V and ∼.45 T. For figure details see figure 5.15.

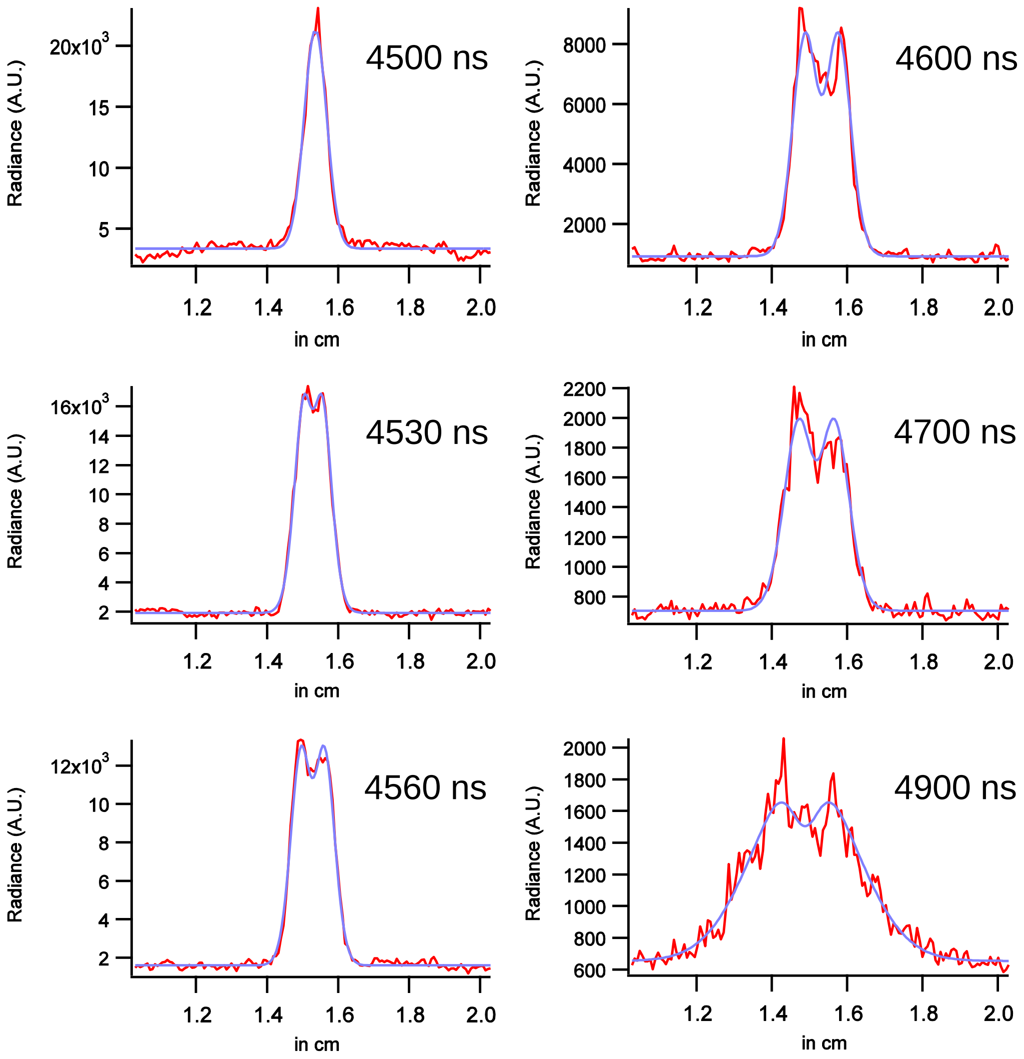

Figure C.6: Here is a progression of line profiles of the jet throat in log scale where a divot may form as in figure 5.31. The line profiles were fit to the double gaussian equation $y = y_0 + A_1 e^{\left(\frac{(x-x_0)^2}{Wid_1}\right)} - A_2 e^{\left(\frac{(x-x_0)^2}{Wid_2}\right)}$.

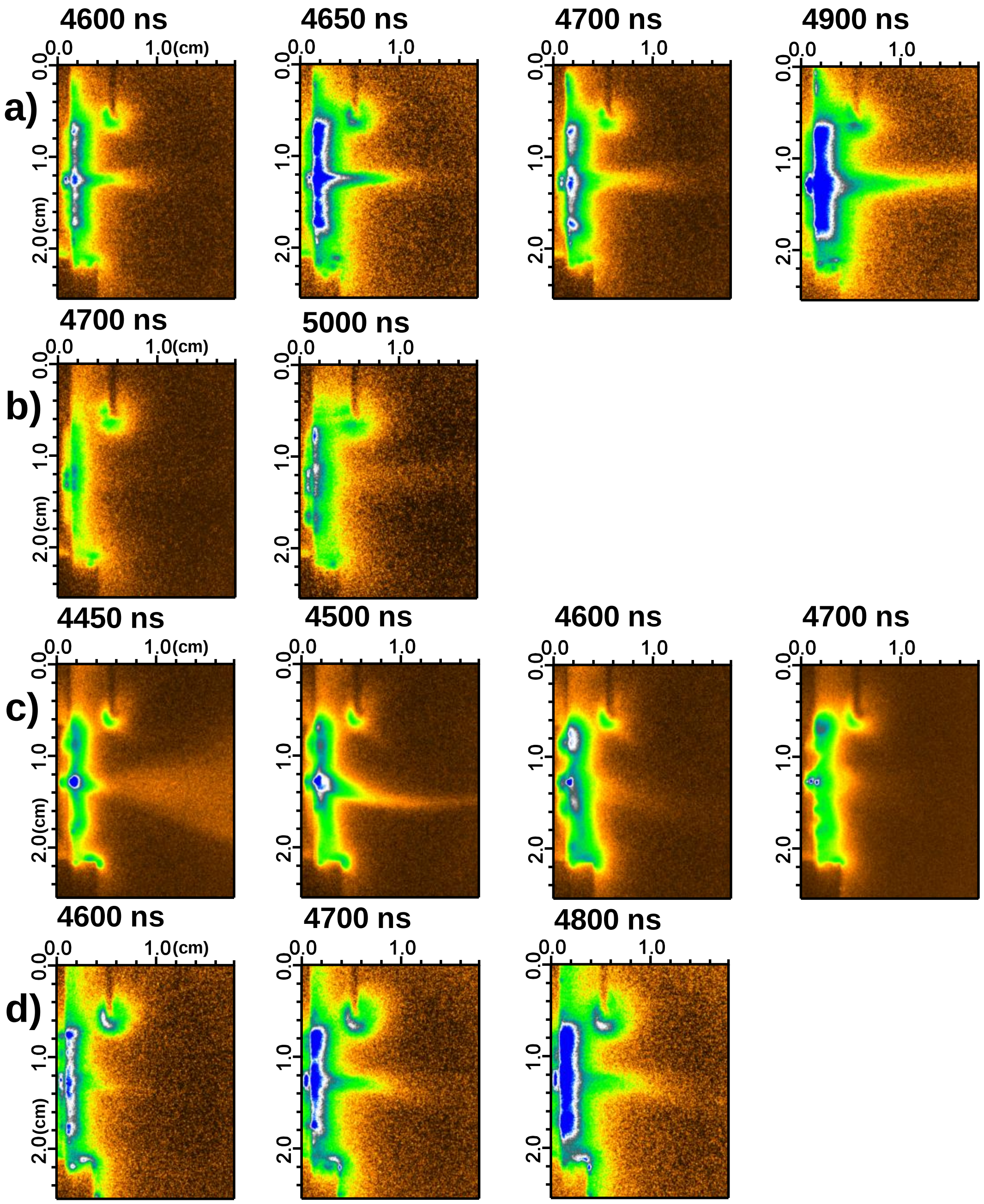

Figure C.7: Jets with Mo electrode and: a) 2000 V and ∼.45 T magnetic field, b) 1000 V and ∼.45 T magnetic field, c) 2000 V and ∼0.0 T magnetic field, and d) 2000 V and ∼.23 T magnetic field. For figure details see figure 5.15.

ablated material would be a hot plasma and therefore would be confined in the magnetic field. The divot seemed to form much faster without the magnetic field, but it was difficult to make out precise features in the ablated material. It was very difficult to see the filament forming without the magnetic field. This could be because the speed at which it does so was much too quick to be seen with our methods. There did seem to see a possible progression of this filament in in figure 5.21.

I ran an experiment to see if a jet would form with the initial laser plasma. I searched in the first half cycle of the discharge when the capacitor was initially charged to a negative 1500 V in a .45 T magnetic field. This gave approximately the same current as the 3000 V case on the second half cycle. There was evidence of the jet forming though the laser-produced plasma (see figure C.8). There are anode jets that formed around the ring as they stream along the magnetic field. I performed this same experiment with a .85 T enclosed magnetic field, or the magnet used before I took it apart (see figure C.8). There was a current flowing from the grounded ring through the laser-produced plasma to the top of the magnet, through the magnet and down the center of the magnet onto the electrode. A fluxtube formed in the middle with several tiny fluxtubes forming around it. There was not a jet seen progressing from the electrode to the top of the magnet. The fluxtube just appeared. The fluxtube also developed kinks as it progressed. There was even the development of a double fluxtube feature at 1000 ns (see figure C.8).

I performed jet experiments without magnetic fields in the enclosure used for the laser-produced plasma experiment in section 4. The jet hit the top of this enclosure and left a bright feature on the top of the enclosure as in figure B.17. The jet had the same morphology with and without the enclosure.

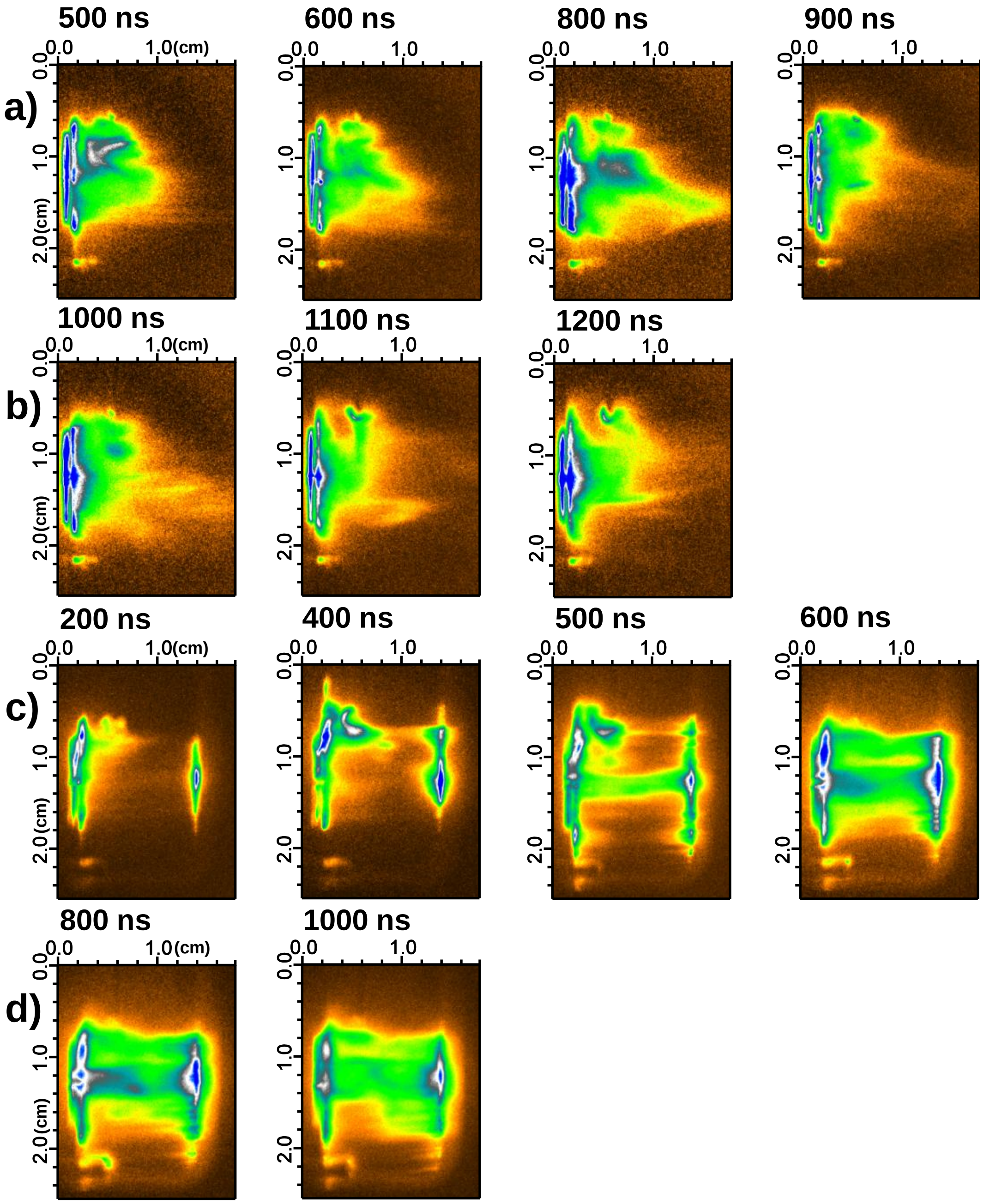

Figure C.8: Jets with Mo electrode biased to -1500 V. The varying magnetic field strength are a)-b) unenclosed ∼.45 T magnetic field and c)-d) enclosed ∼.85 T magnetic field. For figure details see figure 5.15.

I assumed that this bright feature could be material being deposited on the surface of the enclosure. It could also be the currents flowing through the enclosure and the currents themselves ablating the top of the enclosure.

I noted that the center electrode was very ablated after its use. The initial electrode is sanded to a flat top. The jets features take about 4 shots to form into appropriate repeatability. After the initial 4 shots the jets were extremely repeatable for a long use of the electrode, with both aluminum and molybdenum. The electrodes actually grew in height during the course of their use in the experiment because of the melting and reforming of the material. There were periodic sparks that fly off of the electrode so that the electrode is constantly loosing material. I noted that by eye (using safety goggles) one could see a glow emanating from the electrode system. I did not see a collimated jet form by sight but a cone of material emanated from the central electrode. Ablated features formed all around the grounded ring. This combined with the fact that there was no noticeable difference between using a .5 cm and 1.0 cm diameter rings imply that the diameter of the ring (between these two choices) was not important to the jet formation, except for establishing the Paschen effect.

I used two laser energies for the experiment, 200 mJ and 20 mJ. The 20 mJ was used as much as possible to reduced the strain on the damage spot on the laser rod. I observed no spatial differences in the jets between the two energies. This suggested that the capacitor discharge was doing all the work. The only difference between these two energies was that the time that the jet started to form was different. The effect of time on the discharge was measured using photodiodes and the oscilloscope, and the discharge started $\sim$30 ns after the pulse with the 200 mJ pulse and $\sim$130 ns after the 20 mJ

Jet	A1 (A.U.)	A2(A.U.)	W1 (cm)	W2 (cm)
3000 V,4500 ns	17955.0	259.4	0.045	0.0017
3000 V, 4530 ns	27509.0	13619.0	0.050	0.029
3000 V, 4550 ns	11273.0	4792.6	0.054	0.041
3000 V, 4550 ns	8549.2	364.5	0.056	0.010
3000 V, 4550 ns	25114.0	12857.0	0.048	0.029
3000 V, 4560 ns	32374.0	22647.0	0.053	0.038
3000 V, 4570 ns	27146.0	20644.0	0.061	0.042
3000 V, 4600 ns	36293.0	30920.0	0.060	0.049
3000 V, 4700 ns	3504.8	2495.4	0.074	0.051
3000 V, 4750 ns	3389.6	1025.6	0.084	0.026
3000 V, 4800 ns	2543.6	766.1	0.086	0.041
3000 V, 4900 ns	1214.5	365.2	0.185	0.052
4000 V 4600 ns	18724.0	0	0.075	0
4000 V 4700 ns	25102.0	14391.0	0.074	0.045
4000 V 4800 ns	27395.0	20410.0	0.090	0.062
4000 V 5000 ns	9265.5.0	7817.8	0.18	0.12
4900 V 4700 ns	17112.0	1344.3	0.094	0.021
4900 V 4800 ns	11305.0	968.6	0.10	0.0055
4900 V 5000 ns	9365.4	4410.9	0.17	0.070

Table C.2: Table of divot fits as in figure 5.32.

pulse. This would be expected because the 20 mJ laser-plasma moves much slower than the 200 mJ laser-plasma. This had to be taken into account when specifying the time of the jets.

C.4 Jet Analysis Appendix

C.4.1 Supersonic Jet Analysis Appendix

The relationship between n and m, as discussed in section 5.6.1, can be seen in the following formulation. The density build up in the cavity is calculated by summing the amount of particles being ablated into the cavity and the amount of particles leaving the cavity, or

$$\frac{dn}{dt} = \frac{J_a}{Vol} - \frac{J_o}{Vol} \tag{C.1}$$

where J_a is the rate of ablation and J_o is the rate that the mass is leaving the cavity. According to Hagena [49] $J_o = 0.514 n \hat{v}_0 A$ where A is the area of the nozzle and $\hat{v}_0 = \sqrt{2kT/m}$, and n is the density. J_a can be found as

$$J_a = \frac{\ell}{m} \frac{dmass}{dt}. \tag{C.2}$$

Thus

$$\frac{dn}{dt} = \frac{\ell}{m} \frac{dmass}{dt} \frac{1}{Vol} - 0.514 n \hat{v}_0 \frac{A}{Vol} \Rightarrow \tag{C.3}$$

$$\frac{dn}{dt} = \frac{\ell}{m} \frac{\mu_0}{4\pi V r Vol} I^2 - 0.514 n \hat{v}_0 \frac{A}{Vol} \Rightarrow \tag{C.4}$$

$$n = \frac{\int_0^t e^{-0.514 \hat{v}_0 A Vol t} \frac{\ell}{m} \frac{\mu_0}{4\pi V r Vol} I^2 dt}{e^{-0.514 \hat{v}_0 A Vol t}}. \tag{C.5}$$

If we let $c_1 = 0.514 \hat{v}_0 A Vol$ and $c_2 = \frac{\ell}{m} \frac{\mu_0}{4\pi V r Vol}$ then

$$n = \int_0^t c_2 I(t)^2 dt + \frac{c_1 \int_0^t \int_0^t c_2 I(t')^2 dt' e^{-c_1 t} dt}{e^{-c_1 t}} \tag{C.6}$$

now from the Schwartz inequality [120]

$$\left| \frac{c_1 \int_0^t \int_0^t c_2 I(t')^2 dt' e^{-c_1 t} dt}{e^{-c_1 t}} \right| \leq \frac{\left(\int \left(\int_0^t c_2 I(t')^2 dt' \right)^2 dt \right)^{1/2} \left(\int_0^t (c_1 e^{-c_1 t})^2 dt \right)^{1/2}}{e^{-c_1 t}} = \tag{C.7}$$

$$\left(\int_0^t \left(\int_0^t c_2 I(t')^2 dt' \right)^2 dt \right)^{1/2} \frac{c_1^{1/2}}{2} \sqrt{e^{c_1 t} - 1} \leq \tag{C.8}$$

$$c_2 I^2(t) t^{3/2} \frac{c_1^{1/2}}{2} \sqrt{e^{c_1 t} - 1} \tag{C.9}$$

which holds when I is monotomic.

So if $0.514\hat{v}_0 A \frac{t}{Vol} \ll 1$ then a linear relationship holds. In this situation $0.514\hat{v}_0 \frac{A}{Vol} \approx 6.2 \times 10^5 1/sec$ and the anode jets measured are on the order of $t \approx 1 \times 10^{-6} sec$ which gives $c_1 t = .62$ which would be a limit of linearity. So in the region measured the relationship should be linear.

C.4.2 Jet Current Discussion

I discuss the results of the current measurements by fitting the current discharge obtained from the Pearson transformer to the equation:

$$I(t) = ae^{(t-c)/b} sin(\omega(t-c)). \tag{C.10}$$

Various results from this fit are in table C.4.2. Note the quality of the fits due to the small error bars on each parameters. This gave more confidence in the repeatability of the experiments. The resistance in the plasma and the inductance of the system are given by the equations

$$\omega = \sqrt{\frac{1}{CL} - \left(\frac{R}{2L}\right)^2}$$

and

$$\frac{1}{b} = \frac{r}{2L}.$$

The fit data suggests slight differences in the various parameters in different situations as in table C.3. The inductance was most likely dominated by the capacitance connection in the circuit box. There was an essential loop with a parameter of about 18 inches that connects the capacitor to the box, electrode and ground. This would gave an inductance of ~ $.25\mu$H assuming a square loop for simplicity and a wire thickness of .25". This was comparable to the inductances measured in table C.3. The resistance did measurably change in a predictable way between different conditions. The resistance increased with

various conditions	L	R
Mo 3000 V .23 T	$7.59 \pm .01 \times 10^{-7} H$	$.236 \pm .006\Omega$
Mo 3000 V .45 T	$7.63 \pm .01 \times 10^{-7} H$	$.244 \pm .006\Omega$
Mo 4000 V .0 T	$7.57 \pm .01 \times 10^{-7} H$	$.219 \pm .001\Omega$
Mo 4000 V .23 T	$7.59 \pm .01 \times 10^{-7} H$	$.231 \pm .003\Omega$
Mo 4900 V .0 T	$7.559 \pm .005 \times 10^{-7} H$	$.228 \pm .002\Omega$
Mo 4900 V .45 T	$7.572 \pm .007 \times 10^{-7} H$	$.2360 \pm .0003\Omega$

Table C.3: A table showing the various L and R for discharges involving a Mo wire with charged to various voltages and placed in different magnetic fields

an increase in magnetic fields, and the resistance decreased with an increase in initial voltage. The increase of resistance with a magnetic field was likely explainable because of the resistance of the plasma across a magnetic field. The decrease of plasma resistance due to the increase of voltage was due to the increased heating of background plasma due to the higher currents. The high resistance was likely due to the low temperature background gas.

C.5 Other Jet Experiments that May Relate to the Experiment

Other jets experiments, using lasers and z-pinches, have created jet-like structures unrelated to astrophysical phenomena, but it may be useful to investigate if these jets could also be used to study astrophysical jet phenomena. Mostovych et al. [98] measured a jet-like filament emanating from a foil that was backlit with a high energy laser. Xu et al. [153] measured jet-like filaments emanating from laser line focused ablation off of solid targets. Mitchell et al. [96] measured jet-like structures emanating from an X-pinch plasma using interferometry. An X-pinch is similar to a Z-pinch. It has a configuration with two wires that touch in the middle and the current flows from the top of

Conditions	Amplitude (Amps)	Exponential decay (Sec)	Omega (Rad/sec)	Offset (Sec)
Mo wire,.45 T, +4900 V	-9.0E+03	6.6E-06	7.3E+05	-4.6E-06
Error	1.4E+02	4.8E-08	4.2E+02	2.1E-08
Tilt with B field, +3000 V	-5.5E+03	6.7E-06	7.3E+05	-4.8E-06
Error	1.5E+01	3.1E-08	4.5E+02	9.1E-08
Tilt with B field, +4900 V	-8.9E+03	7.1E-06	7.3E+05	-4.6E-06
Error	4.3E+01	2.5E-08	3.2E+02	2.7E-08
Tilt no B field, +4900 V	-8.8E+03	7.2E-06	7.3E+05	-4.6E-06
Error	5.2E+01	4.7E-08	4.2E+02	1.8E-08
tilt no b field, +3000 V	-5.4E+03	6.9E-06	7.3E+05	-4.8E-06
Error	2.3E+01	6.4E-08	5.7E+02	3.0E-08
Al wire, 0.45 T, +3000 V	-5.5E+03	6.4E-06	7.2E+05	-4.8E-06
Error	2.2E+01	6.6E-08	1.6E+03	3.0E-08
Al wire, 0.45 T, +4900 V	-9.1E+03	6.9E-06	7.3E+05	-4.6E-06
Error	3.6E+01	3.6E-08	1.1E+02	2.8E-08
Al wire, 0.23 T, +3000 V	-5.4E+03	6.8E-06	7.3E+05	-4.6E-06
Error	1.6E+01	5.2E-08	1.0E+03	1.3E-08
Al wire, 0.23 T, +4900 V	-8.9E+03	7.2E-06	7.3E+05	-4.5E-06
Error	2.0E+01	2.6E-08	2.0E+02	3.7E-08
Mo wire, 0.23 T, +3000 V	-5.4E+03	6.4E-06	7.2E+05	-4.6E-06
Error	1.9E+01	1.7E-07	9.9E+02	8.5E-08
Mo wire, 0.23 T, +4000 V	-7.3E+03	6.6E-06	7.3E+05	-4.5E-06
Error	6.3E+01	8.3E-08	1.7E+02	2.0E-08
Mo wire, 0.0 T, -3000 V	-1.0E+04	6.7E-06	7.3E+05	-4.6E-06
Error	5.8E+00	4.1E-09	5.4E+02	2.4E-08
Mo wire, 0.0 T, +4000 V	-7.2E+03	6.9E-06	7.3E+05	-4.5E-06
Error	3.2E+01	3.4E-08	3.8E+02	2.3E-08
Mo wire, 0.0 T, +4900 V	-8.8E+03	7.0E-06	7.3E+05	-4.5E-06
Error	4.1E+01	2.6E-08	2.6E+02	3.5E-08

Table C.4: This is a list the fit parameters for the Pearson reading of the current. The fit parameters are of the form in equation C.10.

the “X” to the bottom. Jets emanate from this crossing point. None of these experiments were designed to measure astrophysical jet phenomena

The x-pinch mentioned at above seems to have a decidedly hyperbolically flared profile similar to the discussion in section 5.6.3, which would explain its occurrence [96]. The x-pinch would be the most similar to this experiment. The x shape in the wires is most definitely hyperbolic, in the sense of the term that I use. The interaction point would then accelerate material in the same way as I have prescribed for my jet.

Appendix D

Appendix for the Magnetosphere Experiment

In this appendix I present extra data obtained in the pursuit of magnetosphere physics. I originally used the larger dipole magnet for the magnetic obstacle in the laser produced plasma experiment. The center of this magnet was placed about 1.5 cm away from the target interaction. The same dimension block was used composed of aluminum for comparison. With a 2 J laser pulse an intense shockwave progressed towards the magnet shown in figure D.1. For comparison, other laser energies are shown in this configuration in figures D.2 and D.3. This shockwave formed from the plasma and gas buildup between the target interaction and the block or magnet. The shockwave in the magnetic field seemed to follow magnetic field lines in its outer extremities. But no significant differences were seen between conditions with these high energies.

With a molybdenum 3000 V jet in this experiment where no magnetic fields were used have many of the same features similar to the jet experiments without background magnetic fields in chapter 5. In the magnetic field case a flux loop formed out of the electrode system and progressed toward a magnet at extremely high velocities of $\sim 10^7$ cm/s. When the flux loop reached a certain radius away from a magnet the fluxtube stopped and reversed direction back toward the electrode as in figure 5.37. A twist in the flux loop formed as it progressed back towards the electrode. This may be explained by currents in magnetic field dynamics. As the current progressed toward the magnet the current will be propagating perpendicular to the magnetic field. This plasma current twisted due to the $\mathbf{J} \times \mathbf{B}$ force and cause the current eventually to reverse direction. This also gave important information about speed of the progressing jet since the flux loop boundary progression can be clearly seen in space and time (see figures D.4 and 6.10 (in section 6.4).

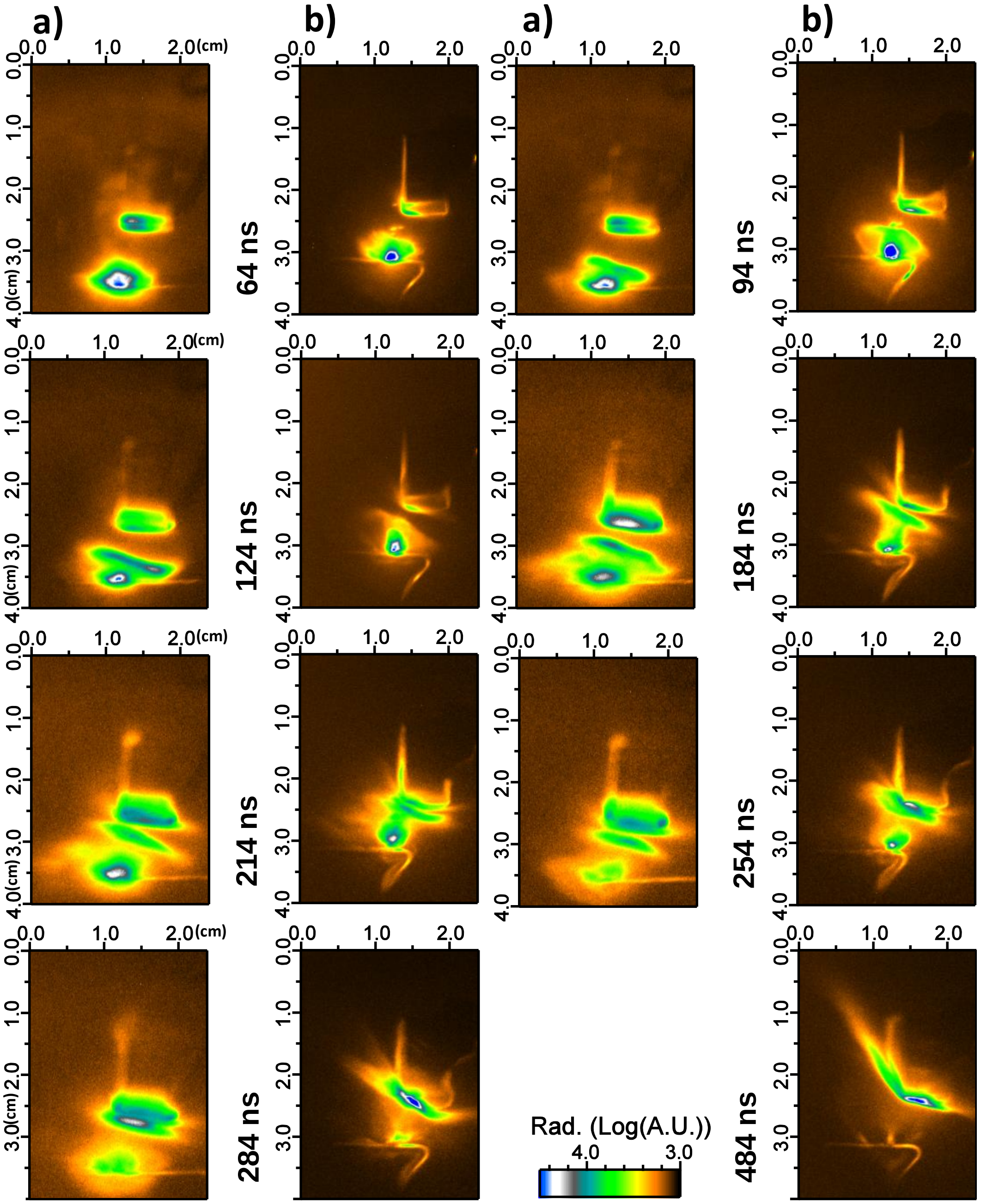

Figure D.1: 2 J laser pulse impinging on an Al target next to a) a .25" radius Al block and b) a .25" radius magnetic dipole.

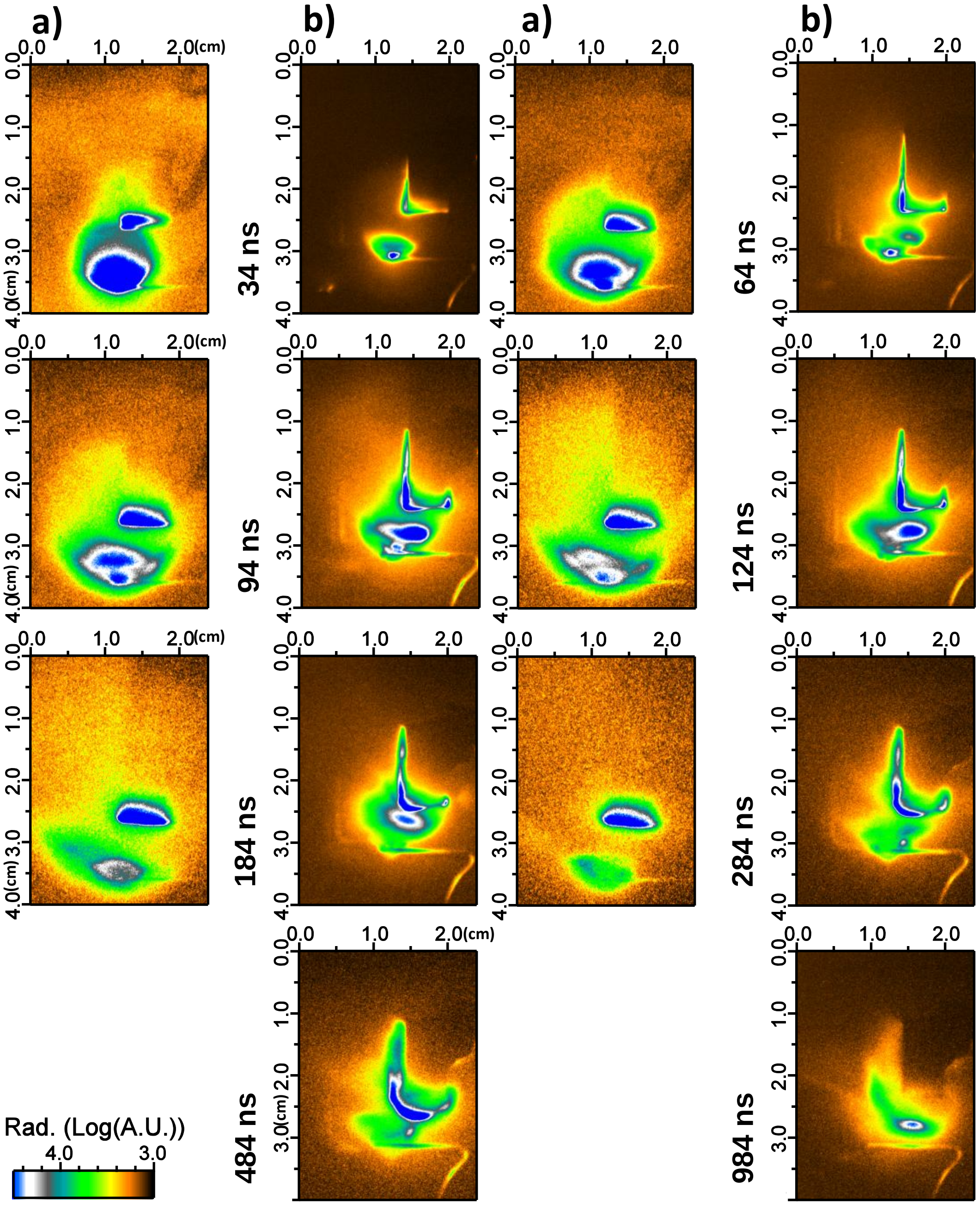

Figure D.2: 200 mJ laser pulse impinging on an Al target next to a) a .25" radius Al block and b) a .25" radius magnetic dipole.

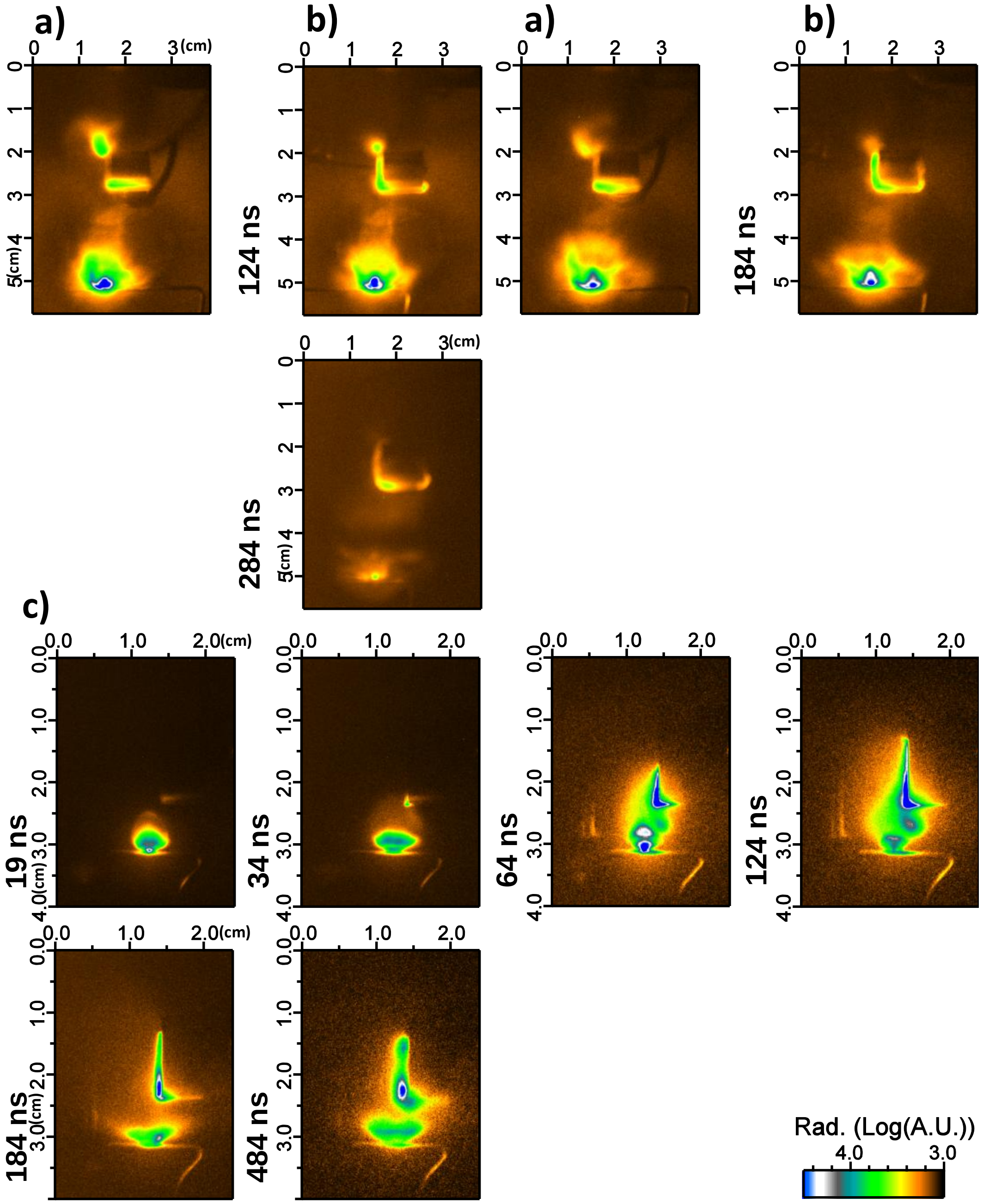

Figure D.3: 2 J laser pulse impinging on an Al target next to a) a 4.5 mm radius Al block and b) a 4.5 mm radius magnetic dipole. In c) a 20 mJ laser pulse impinging on an Al target next to a .25" radius magnetic dipole.

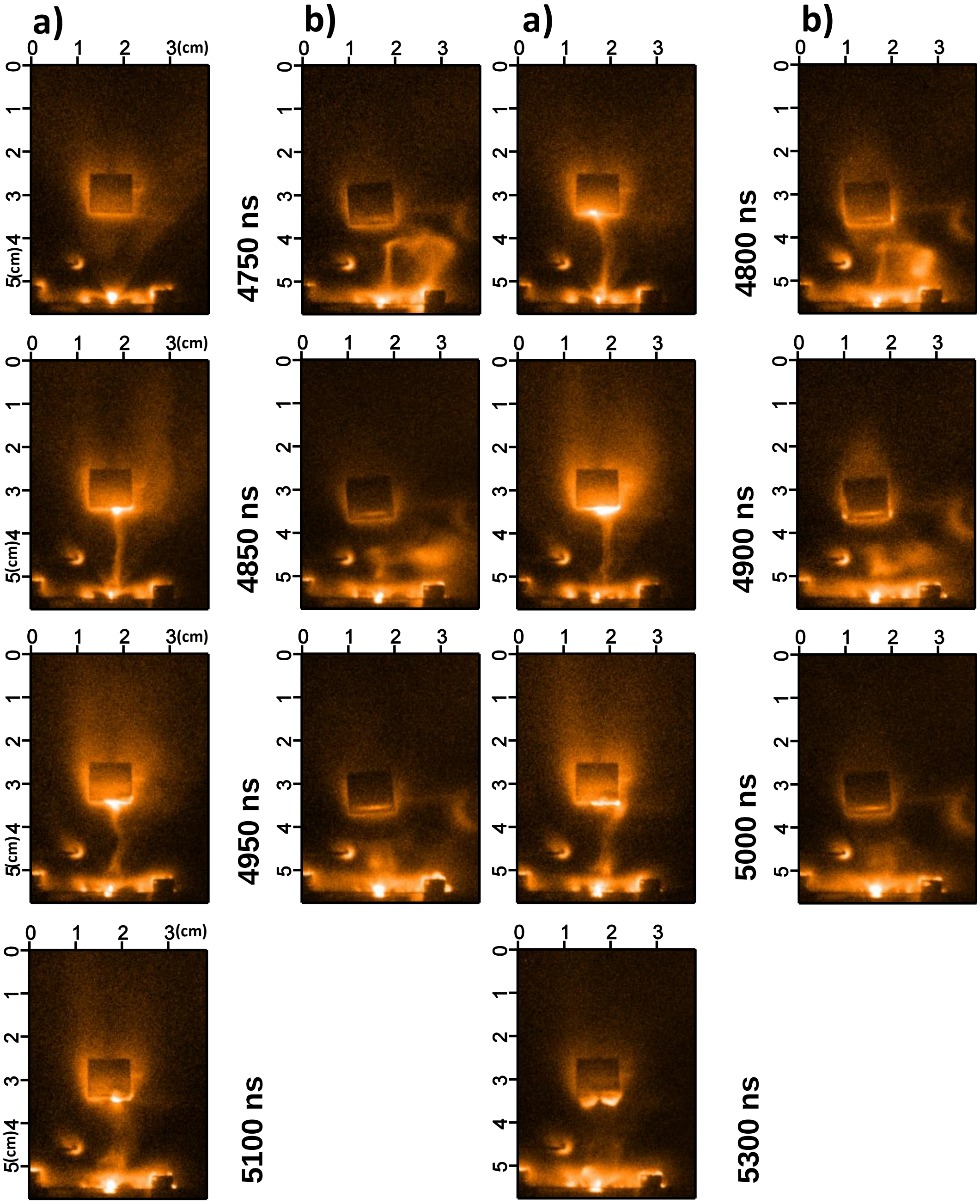

Figure D.4: ICCD image of a 3000 V Mo jet impinging on object a) an Al block and b) a magnetic dipole.

Appendix E

Procedures for Taking Data Outlined in this Thesis

E.1 Procedure for Taking LPP Data with Optical Probing

1. I warmed up and aligned the YOGA laser, by following the YOGA laser S.O.P. in appendix A.2.

2. I warmed up the Quantel Laser. I kept the Quantel firing on lamps only mode until I was ready to use the laser beam to reduce the eyehazard.

3. The YOGA laser focus needed to be aligned with the HeNe laser focus for target alignment purposes. The CCD camera used for the YOGA alignment was used to align the HeNe and YOGA laser. I imaged the laser foci onto the camera using a 20× microscope objective. The microscope objective mounted on a special mount that attached to the arm breadboard in the chamber.

4. With the microscope objective set up the camera was placed in a premarked location that was about 16 cm away from the microscope objective. I used the HeNe without ND filters to get an approximate position for the alignment of the camera. For imaging on the camera a ND 2 gelatin filter attenuated the HeNe beam. With the camera placed on the pedestal I found the image of the HeNe on the camera and moved the

microscope objective back and forth along the laser path until the tightest focus was found. A thin set of two ND 4 gelatin filters attenuated the YOGA beam for safe camera viewing. The ND filters needed to be thin because the thinner the filter the less distortion will be present for beam alignment.

5. I adjusted the YOGA beam intensity so that there was appropriate illumination on the camera. The microscope objective was adjusted to get to the desired focus of the YOGA beam. The YOGA beam was astigmatic which will give a vertical and horizontal line focus. I usually chose the vertical focus or the line focus that was aligned with a thin target to get more material heated by the laser.

6. Once both beams were on the field of view of the camera, I adjusted the HeNe beam so that it overlaps with the focus of the YOGA laser. The YOGA laser flashed at 10 Hz on the monitor when compared with the HeNe, without triggering the camera. The grid program marked where the YOGA focus was, which, because of the 10 Hz repetition rate, could then be blocked and the HeNe focus could be aligned with the grid marker.

7. I put the camera back to its original position, removed the microscope objective, blocked the YOGA beam and removed the ND filters.

8. The magnet and the aluminum scaffolding both fasten to a stand. This stand was designed to be roughly in the center of the chamber at a 45° angle in the chamber, starting on the left side moving out into the chamber on the right. Screw the magnet or the aluminum scaffolding on the stand with the vented screws. The magnet will be slightly movable

and will need to be placed in the position needed for the experiment. Using half of the magnet had the same procedure, but there was more space to maneuver. This half of the magnet was more dangerous to work with because of its unclosed magnetic fields lines.

9. Placing the target in the chamber depended on the type of target used.
    (a) With a 25 μm wire that was not connected electrically to a capacitor, I placed the wire in the ceramic straw and capped the end of the straw with a copper wire plug. With my fingers I straightened the wire as much as possible. The ceramic straw was placed in a specially designed plastic connector. I carefully put the unit into the chamber, being careful not to bend the wire or break the ceramic straw, and screwed the unit onto the shaft. Fine adjustments were made to the wire, while putting pressure on the xyz-stage, to make sure the wire was perfectly vertical. Care was taken to make sure that the subsequent adjustments on the holder will have full mobility in the chamber and will not get caught on any chamber obstruction.
    (b) If the target is a thick wire, I straightened out the wire by pulling on both ends of the wire with pliers until it was straight. The wire was shaped so that a $\sim$ 1 cm straight portion of this wire will be perfectly vertical in the chamber. The rest of the wire was bent so a horizontal arm could be connected to the shaft. The wire should be shaped so that the straight part of the wire will have full mobility in the enclosure when adjusted vertically. I cut the wire arm at about 5 cm to attach to plastic holder. The target unit was placed into the chamber following the same procedure for the smaller wire.

    (c) For a target electrically connected to a current source, I used the special holder designed to deliver high potentials to the wire. The copper shaft of this device was placed through the holder far enough in to touch the wire. The lead from the vacuum feed through was placed into the holder and a plastic screw clamped this wire holder onto the copper rod and onto the wire target. I connected the holder onto the xyz-stage shaft making sure that the electrical lead would not get caught on anything in the subsequent alignment process.

10. To operate the Schlieren for the probe laser, I placed the wire beam block into the appropriate probe beam focus using the wire beam block's xyz-stage. With the beam hitting the tip of the wire I observed how well the beam was blocked by looking at the shadow of the laser beam after the focus and looking for good symmetry.

11. To operate the interferometry mode of the probe beam, I sent the probe beam through the Wollaston prism and the subsequent polarizers using the appropriate angular polarization settings.

12. In order to position the YOGA focus on the camera, I moved the target wire out of the way of the focus, both on the YOGA axis and the probe axis. This position was judged in relation to the HeNe beam. Then with the Quantel beam running, the mechanical shutter operating, and the YOGA laser set with wave plate setting 330 the detecting system was ready to image the laser focus in air. The YOGA beam was fired to mark the position of the focus. I adjusted the camera to place the focus at the desired position on the field of view. This is an approximate alignment the actual alignment is discussed later.

13. I started the chamber pump down process by faceting the 8” CF flange with an o-ring onto the chamber with three screws. The o-ring was first stretched so that the o-ring could be placed on the o-ring grove and held in place with tension. The vacuum pump was turned on with the inlet valve and all other valves on the chamber closed. The inlet valve was slowly opened so that the outgoing air flow would not be strong enough to blow out oil from the diffusion pump. This was about about 20 Torr/sec. With the pump and the GCR on, the noise level was very high, and to reduce risk of hearing loss I wore earplugs.

14. With the pressure at 18 Torr I took a Schlieren measurement of the full YOGA energy breakdown in air at 0.0 ns for the purpose of identifying the position of the focus to use for alignment. The Schlieren image of the focus was in the form of an elongated dumbbell shape. I set the position of the focus to be in the middle of the downstream side of the focus. This is the side of the focus where, because of the astigmatism, the focus will be a line focus aligned vertically with the wire. A grid marker was placed on this part of the focus and saved with the grid program.

15. With the pressure below 1 Torr I opened the inlet valve all the way. When the pressure had reached 100 mTorr the diffusion pump could be turned on; both the fan and the oil heater. The valve should be closed almost all the way, so that the pressure was kept more or less constant in the chamber. When the diffusion pump heats up there is a point where the pumping retrogrades back into the chamber, hence I kept the valve closed as much as possible. Four minutes after turning on the diffusion pump the valve could be op all the way and wait for the pressure to get to $1.0 mTorr$.

16. To finely align the target, the probe beam was changed to Schlieren mode. I then brought the target into the focus of the HeNe. This was the hardest part, and I took notes of where the wire was in relation to the HeNe beam before pumping down. A common mistake was having the target below the HeNe laser beam. The target was moved until it blocked the HeNe beam, and gave a central diffraction pattern with small wires. The target was aligned so that it was centered on the gird marker on the computer screen. This process was iterated until the target was aligned.

17. With the YOGA beam aligned to the photodiode, I aligned the YOGA beam onto the energy meter just before the target chamber. The probe laser pulse and the scattered light from the energy meter was blocked from the photodiode. The photodiode response was recorded with an oscilloscope coincident with the energy reading on the energy meter. About three measurements were taken for statistics.

18. I had the following procedure for taking the experimental data. The extravagant nature of this procedure existed because of the finicky nature of some of the experimental equipment. The camera alternated between half frame and full frame at 30 sec intervals. So I choose to wait until the camera began to take full frame shots to take the data. The shutter worked best when it had been fired close to the time it was used for data taking, so a warm up shot was used before the data was taken. The flash lamps also seemed to work better when they had been warmed up before the data was taken. So the procedure for taking the shot was: put a beam block in the beam path just after the shutter, enable the PFNs, fire the PFNs with the shutter, remove the beam block, wait at

least thirty seconds before the PFNs are fired again. The procedure continues: while waiting for the flash lamps to cool down make note of the full camera exposure periodicity, when the camera begins have full exposures a background shot should be taken, and then set the camera trigger and fire the shot. The data was then saved on both the camera card and the oscilloscope.

19. To position the target to take another shot go to steps 16 and 18.

20. To change the targets bring the chamber was brought to air by closing the valve that connects the chamber to the diffusion pump. The chamber was then vented slowly (10 Torr/sec) to avoid condensation on the optics. I turned off the diffusion pump immediately to save time for the diffusion pump to cool down before pumping again. The target was replaced and prepare for the next run by following steps 8 to 18, excluding the steps required for alignment of the probe laser. The probe laser would still be aligned.

21. The shut down started by turning off the diffusion pump and closing the value between the vacuum chamber and the diffusion pump. The PFNs were discharged and turned off. The GCR was turned off by following the laser S.O.P.. The Quantel was turned off by shutting off the lamps, and letting the Quantel cool down for ten minutes. I turned off the shutter and unplugged all such electrical devices. Cables that could be a tripping hazard were removed. Once the diffusion pump was cooled down (after 20 minutes) the roughing pump was turned off and the vacuum line at the diffusion pump was vented.

E.2 Procedure for Taking LPP Data with the ICCD Camera

1. I warmed up and aligned the YOGA laser, by following the YOGA laser S.O.P. in appendix A.2.

2. The cool down process for the ICCD camera was an important process to follow both for the quality of the images and for the health of the camera. This process began by turning on the water chiller and setting the chiller to about 5°C. The chiller barley reached this base temperature. Before I turned on the electronic camera cooling system, for which the water chiller is used to cool, I made sure that the temperature of the water chiller was at least 10°C. With this water chiller system the electronic cooling system could be set at -30°C. When an ice bath was used to chill the electronic cooling system the electronic cooling system could be set at -35°C, but the ice bath system was less reliable and the ice had to be replenished quite often. The indicator light on the electronic cooling system would turn green after a few minutes indicating that the minimum temperature had been reached, but to get the clearest picture the temperature must stabilize for a half hour.

3. Items 3 to 8 from section E.1 were followed.

4. The focus of the drive laser needed to be located in the ICCD camera field of view for positioning. I took pictures of the laser breakdown in the air with the ICCD camera. The camera was set to take gated shots. The gate was set to 4.0ns wide and a delay of 60.0ns. The camera lens was set to f22 and the gain was set to 10. The gain dial had a maximum of 100 and not 10, and the major dial was read at × 10 and the minor

dial was read at × 1. I set the wave plate on YOGA to 330 to get an adequate breakdown in air.

5. I set the camera on external mode with the Winspec camera program. The programm was set to acquire and would wait for an input trigger from the YOGA laser pulse. The laser was fired and Winspec would take the image. I made sure that the photodiode trigger for the ICCD camera was attached to the camera system before making the shots. Several images were taken and the coordinates for the spark center, as in figure E.1, were recorded. The average of this measurement was taken to be the target alignment position.

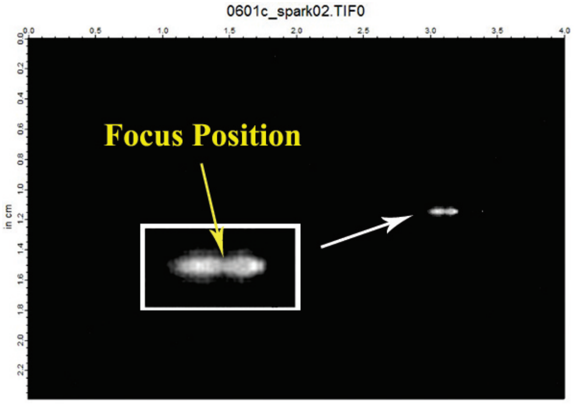

Figure E.1: An ICCD image of laser breakdown in air. This is how the positioning for aligning targets on the ICCD camera was obtained.

6. Steps reported in items 13 and 15 in section E.1 were followed.

   Fine target alignment techniques followed item 16 in section E.1 except the ICCD camera image under the free acquiring setting was used to position the target in the right place.

7. With the targets illuminated with an appropriate amount of light images of the target area with the ICCD camera were taken. I used the free shutter option from the program with a 1 ms setting. The focus of the camera was adjusted with the purpose of getting the target wire in best focus.

8. With low energy (non PFN) shots the target was adjusted and a laser shot was fired using the push button trigger circuit with the shutter warmed up. I set the pressure to a desired setting. If the PFNs were used I followed the procedure in item 18 from section E.1.

9. Finding the right gain was important because of the ease of destroying the camera in laser plasma systems. When first firing the system using a particular set of parameters for the experiment, I started with the lowest gains possible and worked my way up by increasing the gain and f-number on the lens. The f-number on the lens was kept constant throughout a particular experiment. Using the smallest f-number gave the sharpest image. I used f-numbers 1.4-4 with most of the experiments. The gain was changed in the experiments between shots because of the dramatic change of luminosity corresponding to different experimental parameters. This sacrificed making absolute gain measurement, but I did not find that necessary for this experiment. I choose an f-number and then increased the gain until the desired exposure was found. The gain was recorded to aid in finding the correct gain for subsequent experiments.

10. If I was interested in precise measurements of the energy then I followed item 17 from section E.1. Without the PFNs firing the energy measurements are much more stable. Averages were measured for each energy

setting, and the energy was inferred from those measurements.

11. To position the target to take another shot I used steps 16 and 18 in section E.1.
12. I shut the system down by turning off the diffusion pump and closing the value between the vacuum chamber and the diffusion pump. Then the PFNs were discharged if they were used. The GCR was turned off by following the laser S.O.P.. The electrical cooling supply for the camera was turned off and the chiller flowed through the ICCD camera for another 10 minutes. The electrical power supplies to the camera were then turned off. I made sure that there was enough nitrogen flowing through the camera after the camera was turned off. The mechanical shutter was turned off and all such electrical devices were unplugged. Cables that were a tripping hazard were removed. Once the diffusion pump was cooled down (after about 20 minutes) the roughing pump was turned off and the vacuum line was vented at the diffusion pump.

E.3 Procedure for Taking Jet Data with Optical Probing

1. I followed the steps in items 1 to 7 in section E.1.
2. I followed step in item 8 in section E.1. I most often used just half a magnet and no Al scaffolding in these experiment. I positioned the magnet so that the center of the magnet would be where the jet would take place, or in other words, where the center electrode was.
3. I connected the electrode to the breadboard in the arm of the chamber where the main entry flange was. I put insulating thin plastic sheets

between the electrode holder and the magnet or what ever was used to prevent the magnet from becoming grounded. Using the HeNe beam and the ICCD camera as guides, the electrode was aligned to the desired place in the chamber. The tilt of the electrode holder was adjusted so that the electrode was level or had the tilt angle desired for the experiment.

4. I made an Al wire target in the same way as in step 9b in section E.1. The wire was bent so that the perfectly straight part of the wire, being about 2.0 cm, could be laid almost horizontally over the electrode. The target had to be adjusted horizontally instead of vertically for the jet experiments. Adjustments were made so that this straight part of the target was aligned parallel to the probe beam.

5. I followed steps 10 to 17 of section E.1.

6. Once the pressure had fallen below 1.0 mTorr, the power supply to the electrode could then be turned on. I made sure, before I did this, that all high voltage electrical connections were securely in place, and that all the electrical devices and optical tables were properly grounded. The power supply was turned on to the desired setting and there was a 2-3 minute wait for the capacitor to charge. The current on the power supply was monitored for the charging rate. I choose a base current for each high voltage setting to run the experiments at.

7. I followed steps 18 to 21 of section E.1, with the added condition of waiting for the capacitor to charge between each shot, and I did not use the PFN mode. When shutting down, the high voltage was shut off first, and after the high voltage had discharged the capacitor was disconnected from the chamber.

E.4 Procedure for Taking Jet Data with the ICCD Camera

1. I followed the steps from sections E.2 and E.3 to take the jet data with an ICCD camera.

E.5 Procedure for Taking Magnetosphere Data with LPP Wind

1. I followed procedures from section E.2 for this experiment with the following extra step.

2. The dipole magnet was attached via magnetic attraction onto a iron wire holder, which was connected to a copper positioning wire. This combination was placed in the desired place for the experiment. The Al block was screwed onto the positioning wire and placed in the desired place for the experiment. The desired place in the experiment was having the flat part of the block parallel to the drive beam and upstream from the target. The drive beam would pass directly above the block. Care needed to be taken to align the magnet or the Al block so that the laser would be close, but not hit these objects. I made sure that the magnet or Al blocks were centered with the drive beam. The blocks were adjusted by bending the positioning wire in slight ways, until the alignment was adequate. A large field of view on the ICCD camera was necessary for this experiment.

Box type	Channel	width	delay	purpose
SRS				
	Ch 0			GCR lamps
	Ch A		0.003193	GCR Q-switch
	Ch B		0.002993106	Quantel lamps
	Ch C		B+0.0002	Quantel q-switch
	Ch D		0.050026	To BNC
BNC				
	Ch A	0.019	0.018	Camera and Sutter
	Ch B	0.000001	0.052831	Black PFN
	Ch C	0.001	0.052725	Red PFN
	Ch D	0.001		Blank

Table E.1: This was the timing diagram for the experiment. There were two timing boxes; the SRS and the BNC box. Each had four channels. The BNC box had a width of the pulse associated with each channel whereas the SRS box did not.

E.6 Procedure for Taking Magnetosphere Data with Laboratory Produced Jet Wind

1. I followed sections E.4 and E.5 to complete this set up with the addition that the blocks were placed above the center electrode well out of the way of the incoming YOGA drive beam.

E.7 Timing Chart for the Laser System

Appendix F

HYADES Information Files

```
wireal- Ablating 25um Aluminum wire with the YOGA laser.
c
c  Purpose:
c        To simulate the expansion of the plasma ablated
c    by the YOGA laser.
c
c
c cylindrical
geometry 2
c
mesh 1 100 0.0 .00125 .95
region 1 99 1 2.7
material 1 13. 26.982 1.
c
c we will use the qeos for Aluminum
c
qeos 1 7e11 2.7
c
c
c    The laser source:
```

```
c        laser delivers .5 Joules in about 8
c    nanoseconds FWHM at 1.064 micrometers.  The
c    focal spot I estimate to be 3.14e-4cm^2. Our
c    laser then has 2.5*2.5e7W in it and
c    2.5*1.412e9 W/cm or 2.5*1.412e16 ergs/sec cm^2.
c
c
source laser 1.0 -99
gauss 10e-9 3.53e16 8e-9
c
pparray r rcm rho pres te ti u csi dene
pparray deni elecon0 zbar vol ucm xmass
parm postdt 50.e-10
c
parm editdt 100.e-10
parm tstop 130.e-9
parm nstop 100000000
parm itmcyc 100
```

Appendix G

Igor fluxtube simulation source code

```
#pragma rtGlobals=1// Use modern global access method.
function pderkan()
variable x,i,j,k,kb,T,delt,xo,delx,xoo,bo,
 noo,mass,Nn,tick, tickt,y1,y2
variable pii,Cur, upper, lower,c,b,m,r,da,a,z,
imax, gam, vmax, dvmax, dvmaxx, rhom, drhom, drhomx
variable c1,c2,noo1,noo2, x1,x2,jj, x3,ii,ddelx,
mrho,rhofor,ni,current,tsin
variable pdei1,pdei2,fullt,tinit,xpek,xpeki,bi,
bii,ticktt,bb,aa,wr,zof,vi,am,dam,zmf,dmdt,
dmdt1,peekh,peekfal
variable xminp,xrhosum,xrhosumm,b2,m2,vpek,hh,
tablei,tablej,ti,tj,wavmax,timeh,vpekn
variable tt

ni=3
Nn=150*ni
make /D/O/N=(Nn) rho=0
make /D/O/N=(Nn) rhov=0
make /D/O/N=(Nn) xco=0
```

```
make /D/O/N=(Nn) vel=0
make /D/O/N=(Nn) rhoi=0
make /D/O/N=(Nn) pre=0
make /D/O/N=(Nn) prei=0
make /D/O/N=(Nn) preii=0
make /D/O/N=(Nn) pprei=0
make /D/O/N=(Nn) rhoii=0
make /D/O/N=(Nn) veli=0
make /D/O/N=(Nn) curi=0
make /D/O/N=(Nn) force
make /D/O/N=(Nn) forcez=NaN
make /D/O/N=(Nn) forcezi=NaN
make /D/O/N=(Nn) xpo=NaN
make /D/O/N=(Nn) arad
make /D/O/N=(Nn) rhovel
make /D/O/N=(Nn) temp=0
make /D/O/N=(Nn) tempi=0
make /D/O/N=(Nn) RR
make /D/O/N=(Nn) rhofun
make /D/O/N=(Nn) velfun
make /D/O/N=(Nn) prefun
make /D/O/N=(Nn) F2
make /D/O/N=(Nn) F1
make /D/O/N=(Nn) F3
make /D/O/N=(Nn) F4
make /D/O/N=(Nn) rrhoi=0
make /D/O/N=(Nn) vveli=0
```

```
make /D/O/N=(Nn) aaa=0

make /D/O/N=(Nn) aaai=0

make /D/O/N=(Nn) acc=0

make /D/O/N=(1) ang=0

make /D/O/N=(1) vpe=0

make /D/O/N=(1) pet=0


// constants for the force equation


timeh=0

vpekn=0

pii=3.1415926

Cur=1000

z=-.01

imax=100000

b=.00001

m=.62

//m=.62

b2=b

m2=0

//m=2

c=1e-8

r=.0*b


vmax=1e6

dvmax=1e6

drhom=1e-8
```

```
//constants for hydrodynamics and similar conventions.
gam=5/3
xo=0
// for tiff lineouts
//delx=0.0000623
delx=2*0.0000623
// the delta t for the pde
//tinit=2e-7
tinit=0
delt=3e-11
fullt=2e-7
pdei2=50
pdei1=floor(fullt/(delt*pdei2))
hh=0
//more hydro with Mo
T=100000
kb=1.38e-23
mass=95.94*1.66e-27
tick=0

for(i=0;i<Nn;i+=1)

tempi[i]=T*exp(-i/100)
//tempi[i]=T
```

```
endfor

for(i=0;i<Nn;i+=1)

//curi[i]=cur*exp(-i/50)
curi[i]=cur

endfor

variable me,cl,ee,pi,hp,nu1,nu2,ZZ
ZZ=1
me=9.108E-31
cl=2.998E8
ee=1.602E-19
pi=3.1415926

hp=6.625E-34
nu1=3.75E14
nu2=1.0E15

// the x initialization

for (i=0;i<Nn;i+=1)
xco[i]=xo+i*delx/ni
endfor

ddelx=delx
```

```
for (i=0;i<Nn;i+=1)
z=xco[i]-0.002
aaa[i]=.5*(((m+m2)*z+b+b2)+sqrt(((m+m2)*z+b+b2)^2-
4*((m*z+b)*(m2*z+b2)-c)))

endfor

Differentiate /EP=0 aaa /X=xco /D=daaa

aaai=aaa

forcez=((4E-7*pii)/(2*pii^2*aaa^3))*(1-r^2/aaa^2)*daaa

prei=((4E-7*pii)*curi^2/(4*pii^2*aaa^2))*(1-r^2/aaa^2)

wavestats /Q forcez
jj=V_maxloc

rhoi=prei/(kb*tempi/mass)

//rhoi=prei/(kb*T/mass)

// more force redef
rho=rhoi
rhoii=rhoi
```

```
vi=1.8e4
//vi=0
veli=vi

vel=veli

// for current
//make /O/N=4 coef={-545.805*10,6.25E-06,7.21E+05,-4.848E-06}
//make /O/N=4 delcoef={7.9198*10,3.48E-08,346,2.829E-08}

make /O/N=4 coef={-729.8433333*10,0.000006782,727570,
-4.6658E-06}

//current=coef[0]*exp(-(t-coef[3])/coef[1])*
sin(coef[2]*(t-coef[3]))


Differentiate /EP=0 rhoii /X=xco /D=drhoii
preii=prei

//  The PDE
xpek=.000/(delx/ni)
xpeki=xpek

bi=0
tickt t=0
for(i=0;i<pdei1;i+=1)
```

```
//The unrecorded  sub loop
for(k=1;k<pdei2;k+=1)
tick=tick+1

// current and time definition


tickt=tick*delt
tsin=tickt+pii/coef[2]+coef[3]+tinit
 current=cur+coef[0]*exp(-(tsin-coef[3])/coef[1])*
sin(coef[2]*(tsin-coef[3]))
current=cur



aaa=sqrt(pi*4e-7*Cur^2/(4*pi^2*prei))



Differentiate /EP=0 aaa /X=xco /D=daaa


Differentiate /EP=0 daaa /X=xco /D=ddaaa
//for (ii=0;ii<Nn;ii+=1)


aa=.001
bb=.001
wr=.0008
```

```
forcez=(current^2)*((4E-7*pii)/(2*pii^2*aaa^3))*
(1-r^2/aaa^2)*daaa
prei=((4E-7*pii)*curi^2/(4*pii^2*aaa^2))*(1-r^2/aaa^2)
rhoi=prei/(kb*T/mass)

rhofunca(rhoi,veli,rhofun)
F1=rhofun*delt
rrhoi=(rhoi+F1/2)
rhofunca(rrhoi,veli,rhofun)
F2=delt*rhofun
rrhoi=(rhoi+F2/2)
rhofunca(rrhoi,veli,rhofun)
F3=delt*rhofun
rrhoi=(rhoi+F3)
rhofunca(rrhoi,veli,rhofun)
F4=delt*rhofun

rho=rhoi+(1/6)*(F1+2*F2+2*F3+F4)

velfunca(rhoi,veli,prei,forcez,velfun)
F1=velfun*delt
vveli=veli+F1/2
velfunca(rhoi,vveli,prei,forcez,velfun)
F2=velfun*delt
vveli=veli+F2/2
velfunca(rhoi,vveli,prei,forcez,velfun)
F3=velfun*delt
```

```
vveli=veli+F3
velfunca(rhoi,vveli,prei,forcez,velfun)
F4=velfun*delt


vel=veli+(1/6)*(F1+2*F2+2*F3+F4)



prefunci(veli,prei,prefun,current)
F1=prefun*delt
pprei=prei+F1/2
prefunci(veli,pprei,prefun,current)
F2=prefun*delt
pprei=prei+F2/2
prefunci(veli,pprei,prefun,current)
F3=prefun*delt
pprei=prei+F3
prefunci(veli,pprei,prefun,current)
F4=prefun*delt

pre=prei+(1/6)*(F1+2*F2+2*F3+F4)


//rho[0]=dmdt
vel[0]=vi
//pre[0]=preii[0]
//vel[Nn-1]=0
```

```
//acc=(vel-veli)/delt


rhoi=rho
veli=vel
prei=pre
endfor
dowindow /k Graph3
temp=pre/(rho*kb/mass)
// emission:
//  RR=-(32*pi/3)*sqrt(2*pi/(3*kb*temp*me))*
(ZZ^2*ee^6/(me*cl^3))*(rho/mass)^2*(kb*temp/hp)*
(exp(-hp*nu2/(kb*temp))-exp(-hp*nu1/(kb*temp)))
rhov=rho/(mass*1e6)
display /k=1 vel vs xco
// wavestats /Q vel
wavestats /Q ddaaa
vpek=V_maxloc
wavestats /Q vpe
wavmax=V_npnts
if (vpekn == 0)
vpe[0]=vpek
pet[0]=0
else
if (abs(vpekn-vpek)>(delx/(ni*10)))
insertpoints wavmax, timeh+1, vpe
// insertpoints wavmax, timeh, ang
```

```
insertpoints wavmax, timeh+1, pet

for(tt=0;tt<(timeh+2);tt+=1)

 vpe[wavmax-1+tt]=((vpek-vpekn)*delx/ni/(timeh+1))*tt
+xo+vpekn*delx/ni
 pet[wavmax-1+tt]=pdei2*(tt-(timeh+1))*delt+pdei2*
hh*delt

endfor

timeh=0
else

timeh=timeh+1
endif
endif

wavestats /Q vpe
wavmax=V_npnts

hh=hh+1

vpekn=vpek

differentiate vpe /X=pet /D=vvpe
smooth 50,vvpe
```

```
// ModifyGraph log(left)=1

mrho=0
for(ii=0;ii<Nn;ii+=1)
mrho=mrho+rho[ii]*ddelx
endfor
//V_LeadingEdgeLoc
print tickt, mrho, current,xpek,xminp
label left "time="+num2str(tickt)

endfor
end

function rhofunca(rrhoi,vveli,rhofun)
wave rrhoi,vveli,rhofun
Differentiate /EP=0 vveli /X=xco /D=ddveli
Differentiate /EP=0 rrhoi /X=xco /D=ddrhoi
rhofun=-(vveli*ddrhoi+rrhoi*ddveli)
end

function velfunca(rrhoi,vveli,pprei,fforcez,velfun)
wave rrhoi,vveli, pprei, fforcez,velfun
Differentiate /EP=0 vveli /X=xco /D=ddveli
// Differentiate /EP=0 pprei /X=xco /D=ddprei
//velfun=(-(vveli*ddveli+ddprei/rrhoi)+fforcez/rrhoi)
velfun=(-(vveli*ddveli)+fforcez/rrhoi)
end
```

```
function prefunci(vveli,pprei,prefun,curre)
wave vveli, pprei,prefun
variable curre
Differentiate /EP=0 vveli /X=xco /D=ddveli
Differentiate /EP=0 pprei /X=xco /D=ddprei

prefun=-(vveli*ddprei+(5/3)*pprei*ddveli)
end
```

Bibliography

[1] H. Alfvén. On the Importance of Electric Fields in the Magnetosphere and Interplanetary Space. *Space Science Reviews*, 7:140–148, October 1967.

[2] D. J. Ampleford, S. V. Lebedev, A. Ciardi, S. N. Bland, S. C. Bott, J. P. Chittenden, G. Hall, C. A. Jennings, J. Armitage, G. Blyth, S. Christie, and L. Rutland. Formation of Working Surfaces in Radiatively Cooled Laboratory Jets. *Astrophysics and Space Science*, 298:241–246, July 2005.

[3] D. T. Attwood, J. M. Auerbach, P. H. Y. Lee, and D. W. Sweeney. Interferometric confirmation of radiation-pressure effects in laser-plasma interactions. *Physical Review Letters*, 40:184–187, January 1978.

[4] F. Bacciotti and J. Eislöffel. Ionization and density along the beams of Herbig-Haro jets. *Astronomy and Astrophysics*, 342:717–735, February 1999.

[5] F. Bacciotti, T. P. Ray, R. Mundt, J. Eislöffel, and J. Solf. Hubble Space Telescope/STIS Spectroscopy of the Optical Outflow from DG Tauri: Indications for Rotation in the Initial Jet Channel. *Astrophysical Journal*, 576:222–231, September 2002.

[6] P. Bellan. Why current-carrying magnetic flux tubes gobble up plasma and become thin as a result. *Physics of Plasmas*, 10, January 2003.

[7] R. Benattar and C. Popovics. Interaction and transport processes illustrated by measurement of the electron-density profile of a laser-irradiated microsphere. *Physical Review Letters*, 45:1108–1111, September 1980.

[8] R. Benattar, C. Popovics, and R. Sigel. Polarized light interferometer for laser fusion studies. *Review of Scientific Instruments*, 50:1583–1585, December 1979.

[9] I. B. Bernstein and W. J. Fader. Expansion of a Resistive Spherical Plasma in a Magnetic field. *The Physics of Fluids*, 11:2209–2217, October 1968.

[10] D. K. Bhadra. Expansion of a Resistive Plasmaid in a Magnetic Field. *The Physics of Fluids*, 11:234–239, January 1968.

[11] Kristian Birkeland. *The Norwegian Aurora Polaris Expedition 1902-1903*. 1908.

[12] R. D. Blandford and D. G. Payne. Hydromagnetic flows from accretion discs and the production of radio jets. *Royal Astronomical Society, Monthly Notices*, 199:883–903, June 1982.

[13] Raymond L. Boxman, Philip J. Martin, and David M. Sanders. *Handbook of Vacuum Arc Science and Technology Fundamentals and Applications*. Noyes Publications, Park Ridge, New Jersey, U.S.A., 1st edition, 1995.

[14] R. W. Boyd. *Nonlinear Optics*. Academic Press, San Diego, CA, 2st edition, 2003.

[15] S. H. Brecht and N. T. Gladd. Structuring of a plasma shell expanding into a magnetized plasma at sub-Alfvenic speed. *IEEE Transactions on Plasma Science*, 20:678–690, December 1992.

[16] J. Briand, V. Adrian, M. El. Tamer, A. Gomes, Y. Quemener, J. P. Dinguirard, and J. C. Kieffer. Axial magnetic fields in laser-produced plasmas. *Physical Review Letters*, 54:38–41, January 1985.

[17] The Netherlands) Garrelt Mellema (Stockholm University) Bruce Balick (University of Washington), Vincent Icke (Leiden University and NASA. Hubble witnesses the final blaze of glory of sun-like stars, stsci-prc1997-38. Internet, December 1997.

[18] H. V. Cane and I. G. Richardson. Interplanetary coronal mass ejections in the near-Earth solar wind during 1996-2002. *Journal of Geophysical Research (Space Physics)*, 108:1156–+, April 2003.

[19] J. P. Chittenden, A. Ciardi, C. A. Jennings, S. V. Lebedev, D. A. Hammer, S. A. Pikuz, and T. A. Shelkovenko. Structural Evolution and Formation of High-Pressure Plasmas in X Pinches. *Physical Review Letters*, 98(2):025003–+, January 2007.

[20] A. Ciardi, S. V. Lebedev, J. P. Chittenden, D. J. Ampleford, S. N. Bland, B. S. Bott, and J. Rapley. Modeling Magnetic Tower Jets in the Laboratory. *Astrophysics and Space Science*, 298:277–286, July 2005.

[21] C. Debeer. Study on the plug nozzle propulsion system. Web, May 2000.

[22] R. Decoste and B. H. Ripin. High-energy ion expansion in laser-plasma interactions. *Phys. Rev. Lett.*, 40(1):34–37, Jan 1978.

[23] G. Dimonte. A magnetooptic imaging probe for continuous magnetic field profiles. In R. J. Leeper, editor, *Presented at the 9th Topical Conference on High-Temperature Plasma Diagnostics, Santa Fe, NM, 15-19 Mar. 1992*, pages 15–19, March 1992.

[24] G. Dimonte and L. G. Wiley. Dynamics of exploding plasmas in a magnetic field. *Physical Review Letters*, 67:1755–1758, September 1991.

[25] T. Ditmire, A. Rubenchik, V. V. Mirnov, and D. Ucer. Modeling of the Expansion of Ultra-Short-Pulse Laser-produced Plasmas in Magnetic Fields. *The Astrophysical Journal, Supplement*, 127:293–297, April 2000.

[26] T. R. Ditmire. *Soft X-Ray Generation in Gases with an Ultrashort Pulse Laser*. PhD thesis, Univesity of California at Davis, December 1995.

[27] M. G. Drouet, R. Bolton, G. Saint-Hilaire, P. Kieffer, Z. Szili, H. Pepin, B. Grek, A. Thibaudeau, and K. Trepanier. Simultaneous measurements of current and magnetic field in laser-produced plasmas. *Applied Physics Letters*, 29:469–471, October 1976.

[28] J. W. Dungey. Interplanetary Magnetic Field and the Auroral Zones. *Physical Review Letters*, 6:47–48, January 1961.

[29] G. M. Dyer. *Experimental Study of the Equation of State of Isochorically Heated Warm Dense Matter*. PhD thesis, Univesity of Texas at Austin, August 2007.

[30] A. D. Edens. *Experimental Study of the Hydrodynamics of High Mach Number Blast Waves*. PhD thesis, Univesity of Texas at Austin, August 2005.

[31] A. D. Edens, T. Ditmire, J. F. Hansen, M. J. Edwards, R. G. Adams, P. Rambo, L. Ruggles, I. C. Smith, and J. L. Porter. Study of high Mach number laser driven blast waves. *Physics of Plasmas*, 11:4968–4972, November 2004.

[32] J. A. Biretta et al., Hubble Heritage Team (STScI /AURA), and NASA. M87 galactic jet, 3c279. Internet, July 2000.

[33] D. R. Farley, K. G. Estabrook, S. G. Glendinning, S. H. Glenzer, B. A. Remington, K. Shigemori, J. M. Stone, R. J. Wallace, G. B. Zimmerman, and J. A. Harte. Radiative Jet Experiments of Astrophysical Interest Using Intense Lasers. *Physical Review Letters*, 83:1982–1985, September 1999.

[34] R. Fedosejevs, M. D. Burgess, G. D. Enright, and M. C. Richardson. Supercritical density profiles of CO2 laser-irradiated microballoons. *Physical Review Letters*, 43:1664–1667, November 1979.

[35] C. Fendt. Collimation of Astrophysical Jets: The Role of the Accretion Disk Magnetic Field Distribution. *Astrophysical Journal*, 651:272–287, November 2006.

[36] J. M. Foster, B. H. Wilde, P. A. Rosen, T. S. Perry, M. Fell, M. J. Edwards, B. F. Lasinski, R. E. Turner, and M. L. Gittings. Supersonic jet and shock interactions. *Physics of Plasmas*, 9:2251–2263, May 2002.

[37] J. M. Foster, B. H. Wilde, P. A. Rosen, R. J. R. Williams, B. E. Blue, R. F. Coker, R. P. Drake, A. Frank, P. A. Keiter, A. M. Khokhlov,

J. P. Knauer, and T. S. Perry. High-Energy-Density Laboratory Astrophysics Studies of Jets and Bow Shocks. *Astrophysical Journal, Letters*, 634:L77–L80, November 2005.

[38] J. Frank, A. R. King, and D. J. Raine. *Accretion power in astrophysics.* Cambridge and New York, Cambridge University Press, 1985, 283 p., 1985.

[39] Jeffrey P. Freidberg. *Idea Magnetohydrodynamics.* Plenum Press, New York, New York, 1987.

[40] D. Fried, G. P. Reck, T. Kushida, and E. W. Rothe. Electric field enhancement of optical emission from plasma plume generated during ArF excimer photoablation of BaO_2, Y_2O_3, CuO and $YBa_2Cu_3O_7$. *Journal of Physics D Applied Physics*, 24:1065–1071, July 1991.

[41] T. A. Gardiner, A. Frank, E. G. Blackman, S. V. Lebedev, J. P. Chittenden, D. Ampleford, S. N. Bland, A. Ciardi, M. Sherlock, and M. G. Haines. MHD Models and Laboratory Experiments of Jets. *Astrophysics and Space Science*, 287:69–74, 2003.

[42] W. Gekelman, A. Collette, and S. Vincena. Three-dimensional current systems generated by plasmas colliding in a background magnetoplasma. *Physics of Plasmas*, 14, 2007.

[43] W. Gekelman, M. Van Zeeland, S. Vincena, and P. Pribyl. Laboratory experiments on Alfvén waves caused by rapidly expanding plasmas and their relationship to space phenomena. *Journal of Geophysical Research (Space Physics)*, 108:1281–+, July 2003.

[44] D. B. Geohegan. Fast intensified-CCD photography of $YBa_2Cu_3O_{(7-x)}$ laser ablation in vacuum and ambient oxygen. *Applied Physics Letters*, 60:2732–2734, June 1992.

[45] Allan Greenwood. *Vacuum Switchgear.* The Institution of Electrical Engineers, London, United Kingdom, 1st edition, 1994.

[46] G. R. Grigsby. *Development of Broad Spectrum Technologies for High Energy Chirped Pulse Amplification.* PhD thesis, Univesity of Texas at Austin, August 2007.

[47] W. R. Grigsby. *Experimental Studies of High Energy Density Silicon Using Ultra-Fast Lasers.* PhD thesis, Univesity of Texas at Austin, August 2007.

[48] M. A. Hafez, M. A. Khedr, F. F. Elaksher, and Y. E. Gamal. Characteristics of Cu plasma produced by a laser interaction with a solid target. *Plasma Sources Science Technology*, 12:185–198, May 2003.

[49] O. F. Hagena. Nucleation and growth of clusters in expanding nozzle flows. *Surface Science*, 106:101–116, 1981.

[50] S. S. Harilal, C. V. Bindhu, R. C. Issac, V. P. N. Nampoori, and C. P. G. Vallabhan. Electron density and temperature measurements in a laser produced carbon plasma. *Journal of Applied Physics*, 82:2140–2146, September 1997.

[51] S. S. Harilal, C. V. Bindhu, M. S. Tillack, F. Najmabadi, and A. C. Gaeris. Internal structure and expansion dynamics of laser ablation plumes into ambient gases. *Journal of Applied Physics*, 93:2380–2388, March 2003.

[52] S. S. Harilal, B. O'Shay, Y. Tao, and M. S. Tillack. Ambient gas effects on the dynamics of laser-produced tin plume expansion. *Journal of Applied Physics*, 99:3303–+, April 2006.

[53] S. S. Harilal, B. O'Shay, and M. S. Tillack. Debris mitigation in a laser-produced tin plume using a magnetic field. *Journal of Applied Physics*, 98:6102–+, August 2005.

[54] S. S. Harilal, M. S. Tillack, B. O'Shay, C. V. Bindhu, and F. Najmabadi. Confinement and dynamics of laser-produced plasma expanding across a transverse magnetic field. *Physical Review E*, 69(2):026413–+, February 2004.

[55] A. B. Hassam and J. D. Huba. Magnetohydrodynamic equations for systems with large Larmor radius. *Physics of Fluids*, 31:318–325, February 1988.

[56] Richard D. Hazeltine and Francois L. Waelbroeck. *The Framework of Plasma Physics*. Perseus Books, Reading, Massachusetts, 1998.

[57] E. Hecht. *Optics*. Addison Wesley Longman, Inc., 3rd edition, 1998.

[58] T. W. Hill. Generation of the magnetospheric electric field. *Washington DC American Geophysical Union Geophysical Monograph Series*, pages 297–315, 1979.

[59] Heinrich Hora. *Nonlinear Plasma Dynamics at Laser Irradiation*. Springer-Verlag, 1979.

[60] W. Horton and C. Chiu. Laser Z-pinch dipole-target experiments to simulate space physics acceleration processes. *Physics of Plasmas*, 11:1645–1654, April 2004.

[61] W. Horton, C. Chiu, T. Ditmire, P. Valanju, R. Presura, V. V. Ivanov, Y. Sentoku, V. I. Sotnikov, A. Esaulov, N. Le Galloudec, T. E. Cowan, and I. Doxas. Laboratory simulation of magnetospheric plasma shocks. *Advances in Space Research*, 39:358–369, 2007.

[62] S. C. Hsu and P. M. Bellan. A Laboratory Plasma Experiment for Studying Magnetic Dynamics of Accretion Disks and Jets. In *Bulletin of the American Astronomical Society*, volume 34 of *Bulletin of the American Astronomical Society*, pages 760–+, May 2002.

[63] S. C. Hsu and P. M. Bellan. Experimental Identification of the Kink Instability as a Poloidal Flux Amplification Mechanism for Coaxial Gun Spheromak Formation. *Physical Review Letters*, 90(21):215002–+, May 2003.

[64] S. C. Hsu and P. M. Bellan. On the jets, kinks, and spheromaks formed by a planar magnetized coaxial gun. *Physics of Plasmas*, 12:2103–+, March 2005.

[65] J. D. Huba. Hall magnetohydrodynamics in space and laboratory plasmas. *Physics of Plasmas*, 2:2504–2513, June 1995.

[66] J. D. Huba. Nrl plasma formulary. Naval Ressearch Laboratory, Wasington, DC, 2006.

[67] J. D. Huba, J. G. Lyon, and A. B. Hassam. Theory and simulation of the Rayleigh-Taylor instability in the limit of large Larmor radius. *Physical Review Letters*, 59:2971–2974, December 1987.

[68] V. Icke, G. Mellema, B. Balick, F. Eulderink, and A. Frank. Collimation of astrophysical jets by inertial confinement. *Nature*, 355:524–526, February 1992.

[69] F. E. Irons. Radiative transfer across expanding laser-produced plasmas. I - Line profiles. *Journal of Physics B Atomic Molecular Physics*, 8:3044–3068, December 1975.

[70] G. Jellison and C. R. Parsons. Resonant shadowgraph and schlieren studies of magnetized laser-produced plasmas. *Physics of Fluids*, 24:1787–1790, October 1981.

[71] H. Ji, M. Burin, E. Schartman, and J. Goodman. Hydrodynamic turbulence cannot transport angular momentum effectively in astrophysical disks. *Nature*, 444:343–346, November 2006.

[72] R. Jordan, D. Cole, and J. G. Lunney. Pulsed laser deposition of particulate-free thin films using a curved magnetic filter. *Applied Surface Science*, 109, 1997.

[73] W. Junor, J. A. Biretta, and M. Livio. Formation of the radio jet in M87 at 100 Schwarzschild radii from the central black hole. *Nature*, 401:891–892, October 1999.

[74] A. Kasperczuk, P. Pisarczyk, T. Pisarczyk, B. Králiková, K. Mašek, M. Pfeifer, K. Rohlena, J. Skála, J. Ullschmied, and M. Kálal. Interferometric Investigation of an Early Stage of Plasma Expansion with

the High-Power Laser System PALS. *Czechoslovak Journal of Physics*, 52:395–404, March 2002.

[75] A. Kasperczuk and T. Pisarczyk. Interferometric investigations of laser-produced plasma in strong external magnetic field. *Physica Scripta*, 53:503–+, April 1996.

[76] A. Kasperczuk, T. Pisarczyk, S. Borodziuk, J. Ullschmied, E. Krousky, K. Masek, K. Rohlena, J. Skala, and H. Hora. Stable dense plasma jets produced at laser power densities around $10^{14} W/cm^2$. *Physics of Plasmas*, 13:2704–+, June 2006.

[77] M.G. Kivelson and C.T. Russell, editors. *Introduction to Space Physics*. Cambridge Univ. Press, 1995.

[78] F. Kokai, Y. Koga, and R. B. Heimann. Magnetic field enhanced growth of carbon cluster ions in the laser ablation plume of graphite. *Applied Surface Science*, 96, 1996.

[79] D. W. Koopman. High-beta effects and anomalous diffusion in plasmas expanding into magnetic fields. *Physics of Fluids*, 19:670–674, May 1976.

[80] William L. Kruer. *The Physics of Laser Plasma Interactions*. Westview Press, Boulder, Colorado, 2003.

[81] J. M. Lafferty. *Vacuum Arcs Theory and Application*. John Wiley & Sons, 1st edition, 1980.

[82] J. T. Larsen and S. M. Lane. HYADES - a plasma hydrodynamics code for dense plasma studies. *Journal of Quantitative Spectroscopy and Radiative Transfer*, 51:179–186, February 1994.

[83] S. V. Lebedev, J. P. Chittenden, F. N. Beg, S. N. Bland, A. Ciardi, D. Ampleford, S. Hughes, M. G. Haines, A. Frank, E. G. Blackman, and T. Gardiner. Laboratory Astrophysics and Collimated Stellar Outflows: The Production of Radiatively Cooled Hypersonic Plasma Jets. *Astrophysical Journal*, 564:113–119, January 2002.

[84] S. V. Lebedev, A. Ciardi, D. J. Ampleford, S. N. Bland, S. C. Bott, J. P. Chittenden, G. N. Hall, J. Rapley, C. Jennings, M. Sherlock, A. Frank, and E. G. Blackman. Production of radiatively cooled hypersonic plasma jets and links to astrophysical jets. *Plasma Physics and Controlled Fusion*, 47:B465–B479, December 2005.

[85] S. V. Lebedev, A. Ciardi, D. J. Ampleford, S. N. Bland, S. C. Bott, J. P. Chittenden, G. N. Hall, J. Rapley, C. A. Jennings, A. Frank, E. G. Blackman, and T. Lery. Magnetic tower outflows from a radial wire array z-pinch. *Monthly Notices of the Royal Astronomical Society*, 361(1):97–108, 2005.

[86] L. M. Logory, P. E. Stry, and P. L. Miller. Nova High-Speed Jet Experiments. *The Astrophysical Journal, Supplement*, 127:423–428, April 2000.

[87] Ralph H. Lovberg and Hans R. Griem. *Methods of Experimental Physics, Volume 9-Part B Plasma Physics.* Academic Press, Inc., New York, New York, 1st edition, 1971.

[88] K. J. Mason and J. M. Goldberg. Characterization of a laser plasma in a pulsed magnetic field. Part II: Time-resolved emission and absorption studies. *Applied Spectroscopy*, 45:1444–1455, November 1991.

[89] T. Matoba and S. Ariga. Motion and Collision of Plasma Blobs Produced by Giant Pulse Laser in a Transverse Magnetic Field. *Journal of the Physical Society of Japan*, 30:1477–+, May 1971.

[90] S. Matt, A. Frank, and E. G. Blackman. Astrophysical Explosions Driven by a Rotating, Magnetized, Gravitating Sphere. *Astrophysical Journal, Letters*, 647:L45–L48, August 2006.

[91] M. L. Mays, W. Horton, J. Kozyra, T. H. Zurbuchen, C. Huang, and E. Spencer. Effect of Interplanetary Shocks on the AL and Dst Indices. *Geophysical Research Letters*, 34:11104–+, June 2007.

[92] E. A. McLean, J. A. Stamper, B. H. Ripin, C. K. Manka, D. W. Droemer, and H. R. Griem. Observation of magnetic fields in laser-produced plasma using the Zeeman effect. *Physics of Fluids*, 27:1327–1335, May 1984.

[93] D. L. Meier, S. Koide, and Y. Uchida. Magnetohydrodynamic Production of Relativistic Jets. *Science*, 291:84–92, January 2001.

[94] Grannady A. Mesyats. *Cathode Phenomena in a vacuum Discharge: The Breakdown, the Spark and the Arc.* Nauka Publishers, Moscow Russa, 1st edition, 2000.

[95] G. Michael. Space weather. Internet.

[96] I. H. Mitchell, R. Aliaga-Rossel, R. Saavedra, H. Chuaqui, M. Favre, and E. S. Wyndham. Investigation of the plasma jet formation in X-pinch plasmas using laser interferometry. *Physics of Plasmas*, 7:5140–5147, December 2000.

[97] A. Mizuta, S. Yamada, and H. Takabe. Numerical Analysis of Jets Produced by Intense Laser. *Astrophysical Journal*, 567:635–642, March 2002.

[98] A. N. Mostovych, B. H. Ripin, and J. A. Stamper. Laser-produced plasma jets - Collimation and instability in strong transverse magnetic fields. *Physical Review Letters*, 62:2837–2840, June 1989.

[99] D. Mourenas, F. Simonet, Y. P. Zakharov, A. G. Ponomarenko, V. M. Antonov, E. L. Boyarintsev, A. V. Melekhov, V. G. Posukh, and I. F. Shaikhislamov. Laboratory and PIC simulations of collisionless interaction between expanding space plasma clouds and magnetic field with and without ionised background. *Journal de Physique IV*, 133:1025–1030, June 2006.

[100] Paul Murdin and Margaret Penston. *The Firefly Encyclopedia of Astronomy.* Firefly books, Buffalo, New York, 2004.

[101] M. Nakamura, H. Li, and S. Li. Stability Properties of Magnetic Tower Jets. *Astrophysical Journal*, 656:721–732, February 2007.

[102] NASA and B. Reipurth. Three stars blast 12-light-year-long jets of gas into space. Internet, March 2000. STScI-2000-05.

[103] A. Neogi and R. K. Thareja. Dynamics of laser produced carbon plasma expanding in a nonuniform magnetic field. *Journal of Applied Physics*, 85:1131–1136, January 1999.

[104] A. Neogi and R. K. Thareja. Laser-produced carbon plasma expanding in vacuum, low pressure ambient gas and nonuniform magnetic field. *Physics of Plasmas*, 6:365–371, January 1999.

[105] A. Neogi and R. K. Thareja. Instabilities in laser-produced carbon plasma expanding in a nonuniform magnetic field. *Applied Physics B: Lasers and Optics*, 72:231–235, 2001.

[106] Newport. *The Newport Resource 2004*. Newport Corperation, 2004.

[107] NASA/JPL-Caltech/J. Bally (Univ. of Colorado) et al. Cosmic tornado. Internet.

[108] S. Okada, K. Sato, and T. Sekiguchi. Behaviour of laser-produced plasma in a uniform magnetic field - Plasma instabilities. *Japanese Journal of Applied Physics*, 20:157–165, January 1981.

[109] R. Ouyed, R. E. Pudritz, and J. M. Stone. Episodic jets from black holes and protostars. *Nature*, 385:409–414, January 1997.

[110] G. Pelletier and R. E. Pudritz. Hydromagnetic disk winds in young stellar objects and active galactic nuclei. *Astrophysical Journal*, 394:117–138, July 1992.

[111] T. A. Peyser, C. K. Manka, B. H. Ripin, and G. Ganguli. Electron-ion hybrid instability in laser-produced plasma expansions across magnetic fields. *Physics of Fluids B*, 4:2448–2458, August 1992.

[112] A. G. Ponomarenko, Y. P. Zakharov, V. M. Antonov, E. L. Boyarintsev, A. V. Melekhov, V. G. Posukh, I. F. Shaikhislamov, and K. V. Vchivkov. Laser Plasma Experiments to Simulate Coronal Mass Ejections During Giant Solar Flare and Their Strong Impact on Magnetospheres. *Plasma Science, IEEE Transactions on*, 35:813–821, August 2007.

[113] P. Pribyl, W. Gekelman, M. Nakamoto, E. Lawrence, F. Chiang, J. Stillman, J. Judy, N. Katz, P. Kintner, and P. Niknejadi. Debye size microprobes for electric field measurements in laboratory plasmas. *Review of Scientific Instruments*, 77:3504–+, July 2006.

[114] V. N. Rai, A. K. Rai, F.-Y. Yueh, and J. P. Singh. Optical emission from laser-induced breakdown plasma of solid and liquid samples in the presence of a magnetic field. *Applied Optics*, 42:2085–2093, April 2003.

[115] J. A. Ratcliffe. *An Introduction to the Ionosphere and Magnetosphere.* Cambridge University Press, Great Britain, 1972.

[116] A. Raven and O. Willi. Electron-density structures in laser-produced plasmas at high irradiances. *Physical Review Letters*, 43:278–282, July 1979.

[117] B. A. Remington, R. P. Drake, and D. D. Ryutov. Experimental astrophysics with high power lasers and Z pinches. *Reviews of Modern Physics*, 78:755–807, 2006.

[118] B. H. Ripin, J. D. Huba, E. A. McLean, C. K. Manka, T. Peyser, H. R. Burris, and J. Grun. Sub-Alfvénic plasma expansion. *Physics of Fluids B*, 5:3491–3506, October 1993.

[119] B. H. Ripin, E. A. McLean, C. K. Manka, C. Pawley, and J. A. Stamper. Large-Larmor-radius interchange instability. *Physical Review Letters*, 59:2299–2302, November 1987.

[120] W. Rudin. *Principles of Mathematical Analysis.* McGraw-Hill, 3rd edition, 1976.

[121] P. T. Rumsby and J. W. M. Paul. Temperature and density of an expanding laser produced plasma . *Plasma Physics*, 16:247–260, March 1974.

[122] D. Ryutov, R. P. Drake, J. Kane, E. Liang, B. A. Remington, and W. M. Wood-Vasey. Similarity Criteria for the Laboratory Simulation of Supernova Hydrodynamics. *Astrophysical Journal*, 518:821–832, June 1999.

[123] D. D. Ryutov, R. P. Drake, and B. A. Remington. Criteria for Scaled Laboratory Simulations of Astrophysical MHD Phenomena. *The Astrophysical Journal, Supplement*, 127:465–468, April 2000.

[124] C. Burrows (St Scl), J. Hester (AZ state U.), J. Morse (ST Scl), and NASA. Jets from young stars, prc95-24a. Internet, June 1995. ST Scl OPO.

[125] G. Scoles, D. Bassi, U. Buck, and D. Laine. *Atomic and Molecular Beam Methods*, volume 1. Oxford University Press, 1988.

[126] X. K. Shen, Y. F. Lu, T. Gebre, H. Ling, and Y. X. Han. Optical emission in magnetically confined laser-induced breakdown spectroscopy. *Journal of Applied Physics*, 100:3303–+, September 2006.

[127] K. Shigemori, R. Kodama, D. R. Farley, T. Koase, K. G. Estabrook, B. A. Remington, D. D. Ryutov, Y. Ochi, H. Azechi, J. Stone, and N. Turner. Experiments on radiative collapse in laser-produced plasmas relevant to astrophysical jets. *Physical Review E*, 62:8838–8841, December 2000.

[128] N. M. Short. Novae, supernovae; neutron stars and pulsars; quasars and black holes; gamma ray bursts; and star collisions. Internet.

[129] J. R. Spreiter and A. Y. Alksne. Plasma flow around the magnetosphere. *Reviews of Geophysics and Space Physics*, 7:11–50, 1969.

[130] E. C. Stone, A. M. Frandsen, R. A. Mewaldt, E. R. Christian, D. Margolies, J. F. Ormes, and F. Snow. The Advanced Composition Explorer. *Space Science Reviews*, 86:1–22, 1998.

[131] J. M. Stone, N. Turner, K. Estabrook, B. Remington, D. Farley, S. G. Glendinning, and S. Glenzer. Testing Astrophysical Radiation Hydrodynamics Codes with Hypervelocity Jet Experiments on the Nova Laser. *The Astrophysical Journal, Supplement*, 127:497–502, April 2000.

[132] S. Suckewer, C. H. Skinner, H. Milchberg, C. Keane, and D. Voorhees. Amplification of stimulated soft-X-ray emission in a confined plasma column. *Physical Review Letters*, 55:1753–1756, October 1985.

[133] S. Sudo, K. N. Sato, and T. Sekiguchi. Re-thermalisation and flow of laser-produced plasmas in a uniform magnetic field. *Journal of Physics D Applied Physics*, 11:389–407, February 1978.

[134] D.R. Symes, J. Osterhoff, R. Faustlin, M. Maurer, A.C. Bernstein, A.S. Moore, E.T. Gumbrell, A.D. Edens, R.A. Smith, and T. Ditmire. Production of periodically modulated laser-driven blast waves in a clustering gas. *High Energy Density Physics*, 3:353–357, October 2007.

[135] T. Tajima and K. Shibata. *Plasma Astrophysics*. Addison-Wesley, 1st edition, 1997.

[136] G. Tomassetti and G. Sanna. *Introduction To Molecular Beams Gas Dynamics* . World Scientific, 2005.

[137] Y. Y. Tsui, H. Minami, D. Vick, and R. Fedosejevs. Debris reduction for copper and diamond-like carbon thin films produced by magnetically guided pulsed laser deposition. *Journal of Vacuum Science Technology*, 20:744–747, May 2002.

[138] Y. Y. Tsui, D. Vick, and R. Fedosejevs. Guiding and confinement of a laser produced plasma by a curved magnetic field. *Applied Physics Letters*, 70:1953–1955, April 1997.

[139] F. S. Tsung, G. J. Morales, and J. N. Leboeuf. Dynamics of a Supersonic Plume Moving along a Magnetized Plasma. *Physical Review Letters*, 90(5):055004–+, February 2003.

[140] R. G. Tuckfield and F. Schwirzke. Dynamics of a laser created plasma expanding in a magnetic field . *Plasma Physics*, 11:11–18, January 1969.

[141] G. V. Ustyugova, A. V. Koldoba, M. M. Romanova, V. M. Chechetkin, and R. V. E. Lovelace. Magnetocentrifugally Driven Winds: Comparison of MHD Simulations with Theory. *Astrophysical Journal*, 516:221–235, May 1999.

[142] G. V. Ustyugova, R. V. E. Lovelace, M. M. Romanova, H. Li, and S. A. Colgate. Poynting Jets from Accretion Disks: Magnetohydrodynamic Simulations. *Astrophysical Journal, Letters*, 541:L21–L24, September 2000.

[143] T A Pikuz I Yu Skobelev A Ya Faenov T Pisarczyk A Kasperczuk J Wolowski E Zielinska V M Dyakin, A I Magunov. Observation of the characteristics of laser-plasma expansion in a strong transverse magnetic field on the basis of x-ray emission spectra. 27, 1997.

[144] M. Vanzeeland, W. Gekelman, S. Vincena, and G. Dimonte. Production of Alfvén Waves by a Rapidly Expanding Dense Plasma. *Physical Review Letters*, 87(10):105001–+, September 2001.

[145] M. Vanzeeland, W. Gekelman, S. Vincena, and J. Maggs. Currents and shear Alfvén wave radiation generated by an exploding laser-produced plasma: Perpendicular incidence. *Physics of Plasmas*, 10:1243–1252, May 2003.

[146] J. C. Wheeler, D. L. Meier, and J. R. Wilson. Asymmetric Supernovae from Magnetocentrifugal Jets. *Astrophysical Journal*, 568:807–819, April 2002.

[147] L. M. Wickens and J. E. Allen. Ion emission from laser-produced, multi-ion species, two-electron temperature plasmas. *Physics of Fluids*, 24:1894–1899, October 1981.

[148] L. M. Wickens, J. E. Allen, and P. T. Rumsby. Ion emission from laser-produced plasmas with two electron temperatures. *Physical Review Letters*, 41:243–246, July 1978.

[149] O. Willi, P. T. Rumsby, and S. Sartang. Optical probe observations of nonuniformities in laser-produced plasmas. *IEEE Journal of Quantum Electronics*, 17:1909–1917, September 1981.

[150] D. J. Williams. The earth's ring current: Causes, generation, and decay - /Tutorial Lecture/. *Space Science Reviews*, 34:223–234, 1983.

[151] J. Woitas, F. Bacciotti, T. P. Ray, A. Marconi, D. Coffey, and J. Eislöffel. Jet rotation: Launching region, angular momentum balance and magnetic properties in the bipolar outflow from RW Aur. *Astronomy and Astrophysics*, 432:149–160, March 2005.

[152] J. Wolowski, A. Kasperczuk, P. Parys, T. Pisarczyk, E. Woryna, and Y. P. Zakharov. Laser-produced plasmas interaction with high pulsed magnetic field. *Plasma Physics and Controlled Fusion*, 41:A771–A778, March 1999.

[153] Z.-Z. Xu, S.-S. Chen, L.-H. Lin, Z.-M. Jiang, and W.-Q. Zhang. Characteristics and evolution of plasma-jet-like structures in line-focused laser-produced plasmas. *Physical Review A: General Physics*, 39:808–815, January 1989.

[154] S. You, G. S. Yun, and P. M. Bellan. Dynamic and Stagnating Plasma Flow Leading to Magnetic-Flux-Tube Collimation. *Physical Review Letters*, 95(4):045002–+, July 2005.

[155] Y. P. Zakharov, A. V. Melekhov, V. G. Posukh, and I. F. Shaikhislamov. Direct conversion of the energy of laser and fusion plasma clouds to electrical energy during expansion in a magnetic field. *Journal of Applied Mechanics and Technical Physics*, 42:185–195, March 2001.

[156] I. A. B. Zeldovich and I. U. P. Raizer. *Physics of shock waves and high-temperature hydrodynamic phenomena*. Academic Press, New York, 1966.

Vita

Parrish Clawson Brady was born on July 26, 1975 to Don and Cathy Brady. He began attending the University of Utah in the summer of 1990 concurrently with high school. While in college Parrish Brady took two years off to serve a full-time mission for the Church of Jesus Christ of Latter-Day Saints in Norway at his own expense. He graduated from the University of Utah in spring of 2000 cum laude, with a major in Math, Physics and almost a major in music. He began at the University of Texas at Austin in the fall of 2000 where he joined Professor Ditmire's group to study laser plasma laboratory astrophysics. Parrish's dissertation centered around novel laboratory simulations of astrophysical jets. Parrish was awarded Doctor of Philosophy in May, 2008.

Permanent address: 1811 Marcus Abrams Blvd.
Austin, Tx 78748

This dissertation was typeset with LaTeX[†] by the author.

[†] LaTeX is a document preparation system developed by Leslie Lamport as a special version of Donald Knuth's TeX Program.